THE UNIVERSITY OF CHICAGO

NANOSCALE METAL–ORGANIC FRAMEWORKS FOR CANCER THERAPIES

A DISSERTATION SUBMITTED TO

THE FACULTY OF THE DIVISION OF THE PHYSICAL SCIENCES

IN CANDIDACY FOR THE DEGREE OF

DOCTOR OF PHILOSOPHY

DEPARTMENT OF CHEMISTRY

BY

ZIWAN XU

CHICAGO, ILLINOIS

AUGUST 2023

© 2023

ZIWAN XU

ALL RIGHTS RESERVED

Table of Contents

List of Figures

List of Tables

List of Schemes

List of Abbreviations

2D	two dimensional
3D	three dimensional
APF	aminophenyl fluorescein
ATP	adenosine triphosphate
BDC	benzene dicarboxylate
BET	Brunauer–Emmett–Teller
BPDC	biphenyl dicarboxylate
bpy	2,2′-bipyridine
BPY	4’,6’-dibenzoato-[2,2’-bipyridine]-4-carboxylate
BRD	bromodomain
CBI	checkpoint blockade immunotherapy
CLSM	confocal laser scanning microscope
COF	covalent organic framework
CRT	calreticulin
CT	computerized tomography
DAB	3,3′-diaminobenzidine
DAPI	4’,6-diamidino-2-phenylindole
D-Arg	D-arginine
DBA	2,5-di(p-benzoato)aniline
DBAn	9,10-di(*p*-benzoato-)anthracene
DBB-Ir	bis(2,2’-bipyridine)(5,5’-di(4-benzoato)-2,2’-bipyridine)ruthenium(II) chloride
DBCO	dibenzylcyclooctyne

DBP	5,15-di(p-benzoato)porphyrin
DC	dendritic cell
DCFH-DA	2’,7’-dichlorodihydrofluorescein diacetate
DCFH	2’,7’-dichlorodihydrofluorescein
DCF	2',7'-dichlorofluorescein
DEF	dose enhancement factor
DHBC	3,5-dihydroxybenzyl carbamate
DLS	dynamic light scattering
DMF	*N*,*N*-dimethylformamide
DMR	dose modifying ratio
DSB	double-strand break
EPR	enhanced permeability and retention
EDCI	1-(3-dimethylaminopropyl)-3-ethylcarbodiimide hydrochloride
FFT	fast Fourier transform
FITC	fluorescein isothiocyanate
$GIF_{10\%}$	growth inhibition factor at 10% growth rate inhibition
GR	growth rate
GRI	growth rate inhibition
H&E	hematoxylin-eosin
H_2QP	2"-((4-(hydroxymethyl)-2,6-dimethoxybenzamido)methyl)-[1,1':4',1":4",1"'-quaterphenyl]-4,4"'-dicarboxylic acid
H_2TP-OH	2’-((4-(Hydroxymethyl)-2,6-dimethoxybenzamido)methyl)-[1,1’:4’,1’’-terphenyl]-4,4’’-dicarboxylic acid

HOBt	hydroxybenzotriazole
HMGB-1	high mobility group box 1
HPF	hydroxyphenyl fluorescein
HRTEM	high-resolution transmission electron microscopy
HSAB	hard and soft acid and base
IC_{50}	half-maximal inhibitory concentration
ICP-MS	inductively coupled plasma-mass spectrometry
IMD	imiquimod
LA	lattice
LC-MS	liquid chromatography-mass spectrometry
LINAC	linear accelerator
MC	Monte Carlo
MDR	multiple drug resistance
MFI	mean fluorescence intensity
MOF	metal–organic framework
MOL	metal-organic layer
mPEG-PO_3H_2	phosphate-functionalized methoxy polyethylene glycol
nMOF	nanoscale metal–organic framework
NMR	nuclear magnetic resonance
NP	nanoparticle
PBS	phosphate buffer solution
PCP	porous coordination polymers
PEG	polyethylene glycol

PI	propidium iodide
POM	polyoxometalate
ppy	2-phenylpyridine
PROTAC	proteolysis targeting chimera
PXRD	powder X-ray diffraction
QPDC	quaterphenyl dicarboxylate
RDT	radiodynamic therapy
RFI	relative fluorescence intensity
ROS	reactive oxygen specie
RT	radiotherapy
SBU	secondary building unit
SEM	scanning electron microscopy
SF	survival fraction
SiRNA	small interfering RNA
SN38	7-ethyl-10-hydroxycamptothecin
TBP	5,10,15,20-tetra(p-benzoato)porphyrin
TBS	*tert*-butyldimethylsilyl
TEM	transmission electron microscopy
TFA	trifluoroacetate
TGF-β	transforming growth factor-beta
TGI	tumor growth inhibition index
TME	tumor microenvironment
TPDC	terphenyl dicarboxylate

UV-Vis	ultraviolet-visible
Vc	vitamin C
αPD-L1	anti-programmed death-ligand 1 antibody
γ-H2AX	phosphorylated H2A histone family member X

Abstract

Ziwan Xu: Nanoscale Metal–organic frameworks for Cancer Therapies

Under Direction of Professor Wenbin Lin

Metal–organic frameworks (MOFs) are crystalline molecular materials constructed by metal ions or metal-oxo secondary building units (SBUs) and multidentate organic ligands. Nanoscale metal–organic frameworks (nMOFs) have demonstrated significant potential for biomedical applications by leveraging their high porosity, structural regularity and tunability for multifunctionality and biodegradability. In particular, nMOFs with heavy metal-based SBUs have exhibited extraordinary radiosensitizing abilities owing to the large X-ray attenuation coefficient of the electron-dense SBUs. Furthermore, rational design of the organic ligands enables photosensitizing functionality or X-ray triggerable drug release. In this dissertation, we have further demonstrated the design and development of nMOFs for cancer therapies including radiotherapy (RT), radiodynamic therapy (RDT), chemotherapy, and immunotherapy.

Chapter 1 introduces nMOFs and their potential applications with emphasis on heavy metal-based nMOFs in radiotherapy and radiodynamic therapy, and nMOFs as drug delivery systems for chemotherapy.

Chapter 2 reports Monte Carlo simulations comparing the radiosensitization effects of nonporous nanoparticles (NPs) and nMOFs when exposed to X-rays or γ-rays. The simulations demonstrate that lattices, constructed with nanoscale SBUs, outperform solid NPs via enhanced scatterings of electrons. The optimization of SBU size and ligand length allows for maximum dose enhancement in nMOFs.

Chapter 3 details the rational design of a bismuth-based nMOF, Bi-DBP, for synergistic checkpoint-blockade and radiotherapy–radiodynamic therapy (RT–RDT). Bi-DBP incorporates $Bi_{10}O_8$ clusters and photosensitizing 5,15-di(*p*-benzoato)-porphyrin (DBP) linkers. Following low-dose X-ray irradiation, Bi-DBP mediates strong RT–RDT effects to reverse immunosuppressive tumor microenvironments by decreasing intratumoral transforming growth factor-beta (TGF-β), thus enhancing the therapeutic effects of checkpoint blockade immunotherapy.

Chapter 4 describes the design of a thorium-based nMOF, Th-DBP, composed of $Th_6O(OH)_4$ SBUs and DBP linkers, to further enhance RT–RDT guided by MC simulation. Th-lattice outperform Hf-lattice in radiation dose enhancement owing to higher mass attenuation coefficient. Upon irradiation, Th-DBP exhibited enhanced cytotoxicity against cancer cells and significantly suppressed tumor growth in two mouse models.

Chapter 5 reports the design of a Hf-based nMOF, Hf-TP-SN (SN = 7-ethyl-10-hydroxycamptothecin, SN38), for synergistic radiotherapy and chemotherapy. Hf-TP-SN contains an X-ray triggerable SN38 prodrug. Upon X-ray irradiation, electron-dense Hf_{12} SBUs enhances hydroxyl radical generation for the triggered release of SN38, leading to 5-fold higher release of SN38 from Hf-TP-SN than its homogeneous counterpart. As a result, Hf-TP-SN plus X-ray irradiation induced significant cytotoxicity to cancer cells *in vitro* and efficiently inhibited tumor growth *in vivo* in a murine colon carcinoma model.

Chapter 6 discloses the development of Hf-DBP-QP-SN mixed-ligand nMOF for synergistic RT–RDT and chemotherapy. We developed a quaterphenyl ligand conjugated with SN38 (QP-SN) via a hydroxyl-radical-responsive linkage, which was introduced to Hf-DBP nMOF to form a novel Hf-DBP-QP-SN nMOF with high biocompatibility. Upon 10 Gy X-ray irradiation, Hf-DBP-QP-SN nMOF released 13-fold higher SN38 than a homogeneous prodrug.

With low-dose X-ray irradiation, Hf-DBP-QP-SN suppressed tumor growth by 93.5% in a colon cancer mouse model with no dark toxicity.

Acknowledgements

It's been a long way to make it possible.

After five years of difficult journey, I humbly acknowledge that graduate research is distinct from college coursework and pursuing a PhD degree has proven to be even more challenging than I initially envisioned when applying to chemistry PhD programs. Fortunately, I survived! At this moment, I'd like to acknowledge numerous individuals who have supported me along the way, both technically and emotionally.

First and foremost, I extend my deepest appreciation to my advisor, Professor Wenbin Lin. Prior to his offer, I was engaged in lithium battery and electrocatalysis research at Peking University. In 2017, I was provided the opportunity to conduct summer research in his lab through the PKU-Uchicago exchange program. During that summer, I had the privilege to delve into the world of MOFs from scratch and became captivated by molecular design of MOFs for biomedical applications. Upon accepting the PhD offer from Uchicago, Professor Lin once again welcomed me to undertake my graduate research projects in his lab. These two research experiences equipped me with fundamental knowledges and skills for MOF research, enabling me to embark on my own project. However, designing and executing a project from the scratch proved to be an intricate endeavor. In my first year, I encountered numerous experiment failures, prompting thoughts of "master-out". Then in my second year the pandemic hit the world, and everyone was required to quarantine at home. While I considered this an opportunity to pause research and recuperate, Professor Lin perceived it as an ideal period for me to explore computational tools undisturbed. He challenged me to learn Monte Carlo simulation to investigate photon-matter interactions in radiotherapy. Although I wasn't sure about how far I could go in the beginning, Professor Lin continuously encouraged me and engaged in detailed discussions with me until I finalized the

simulation models and obtained consistent results with experimental data. Until then, I discovered the joy of research and became more confident. Throughout the following years, he constantly "challenged" me while providing insightful suggestions for the experimental designs. Moreover, his unwavering dedication to the clinical translation of MOFs has inspired me to work on projects with direct clinical relevance and think out of the box. I am truly grateful for his guidance throughout my academic journey!

I am also deeply grateful to other faculty members in the chemistry department at the University of Chicago for their unwavering support. In particular, I would like to express my appreciation to Professor Bozhi Tian and Professor John Anderson for their engaging discussions on my research progress and for reviewing my dissertation. Furthermore, I extend my thanks to the members of my candidacy exam committee−Professor Chuan He, Professor Dmitri Talapin, and Professor Joseph Piccirilli−for their constructive feedbacks on my research.

Within the Lin lab, I am exceptionally fortunate to be surrounded by supportive colleagues and fellow researchers who are not only mentors and collaborators in research but also close friends whom I share enjoyable moments outside of research. First and foremost, I would like to thank Dr. Guangxu Lan for his hands-on mentorship in MOF synthesis and characterization which began during my undergraduate years, as well as his free rides to various cuisine venues in Chicago. I would also like to express my profound gratitude to my exceptional collaborators, Dr. Kaiyuan Ni, Dr. Wenyao Zhen and Taokun Luo, for their tireless efforts in validating the chemistry design in biological systems. Wenyao's remarkable photography skills have beautifully captured our off-campus activities while Taokun has consistently taken the lead in organizing our outings. I would like to extend my gratitude to Dr. Pengfei Ji, Dr. Yang Song, Dr. Xuanyu Feng, Dr. Yangjian Quan, and Dr. Haifeng Zheng for their insightful discussions, particularly in the realm of organic

synthesis. Additionally, I would like to thank Dr. Xiaomin Jiang for teaching me how to use HPLC and LC-MS and sharing his experience in designing SN38 prodrugs. Geoffrey Nash, my English "tutor", deserves special thanks for his help in refining my writing, honing my speaking skills, and engaging in discussions about ligand design and MOF synthesis. I also want to express my gratitude to many other lab members, including Dr. Nining Guo, Dr. Ruoyu Xu, Dr. Christina Chan, Dr. Wenbo Han, Dr. Theint Aung, Yingjie Fan, Youyou Li, Jianming Mao, Jianqiao Liu, Zitong Wang, for their constant support and friendship. Finally, I am grateful for the collaboration with Caroline McCleary, a diligent Uchicago undergraduate whose contribution has greatly expedited my research progress during the summers.

Outside the lab, I am fortunate to have reunited with several college friends here at Uchicago. I extend my gratitude to Tong Lan, Cheng Peng, Yu Jin, Qinzhe Liu, Shiqi Chen and Zhongyu Zou. Tong, my roommate for five years, has been my constant travel companion, meal partner, and emotional therapist. Cheng's culinary skills rival his expertise in organic synthesis. Despite frequently bothering him with questions about ligand synthesis, he graciously invited me to his house for delicious meals or outings for barbecue. Yu provided invaluable assistance in coding and taught me how to utilize the research computing center at Uchicago. Through badminton, I have also formed new friendships with Carol Fan, Lang Yu, Zhao Xu, Alice Liu, Jiayi Guo, Francis Xing, Xiaodong Chen, Jielu Yu, Mitsuyo Machida, Kailong Wen and many others. I deeply cherish the time we spent together, striving to win every game, and relieving ourselves from the pressure of graduate research.

Finally, I wish to express my utmost gratitude to my parents, Yingqian Xu and Weiying He, for their lifelong care and unconditional love. When I was hesitant about pursuing a PhD degree, my father encouraged me to take the leap and consistently sought to understand my

research while tirelessly spreading the reports about my publications. My mother, on the other hand, always worried about my well-being in the United States, whether I was getting enough sleep and eating well. The pandemic made it even more challenging to traverse half the planet, but love has always bound us together. They have served as a steadfast safety net beneath me, always willing to protect and support me no matter the heights I aim to reach.

Chapter 1. Introduction

1.1. Metal–organic frameworks

Porous materials contain a large portion of void space (pores) within their structures, which enable selective adsorption of guest molecules in the host systems and thus various potential applications ranging from gas separation, energy storage, to heterogeneous catalysis.[1] There are natural porous materials such as rocks, zeolites and bones, among which zeolites (crystalline aluminosilicates) have drawn tremendous attention since 1940s. Extensive research on the formation of crystalline inorganic zeolitic frameworks has allowed pore size control at 1 to 10 Å, making zeolites arguably the most important type of heterogeneous catalysts.[2]

Besides inorganic materials, organic components were introduced to form microporosity via covalent bonds, giving rise to covalent organic frameworks (COFs),[3] or via coordination bonds with metals, forming organic-inorganic hybrid porous coordination polymers (PCPs), more well known as metal–organic frameworks (MOFs).[4] In MOFs, metal ions or metal-oxo clusters are cross-linked by multidentate organic ligands via coordination bonds to form porous and crystalline structures, where the rigid metal-oxo clusters are also called secondary building units (SBUs).[5] Besides crystallinity and regularly-sized pores, MOFs are noted for their tunable compositions due to diverse selection of SBUs and organic linkers as well as topologies of the frameworks, resulting in over 90,000 MOFs reported to date and over 500,000 MOF structures predicted (**Figure 1-1**).[6-8] The sizes of pores and channels within MOFs range from several Angstroms to several nanometers (usually 0-3 nm, up to 9.8 nm), bridging the gap between microporous zeolites and mesoporous materials (with pore sizes ranging between 2 nm and 50 nm).[9] As a result, MOFs have drawn tremendous attention from researchers in many fields.

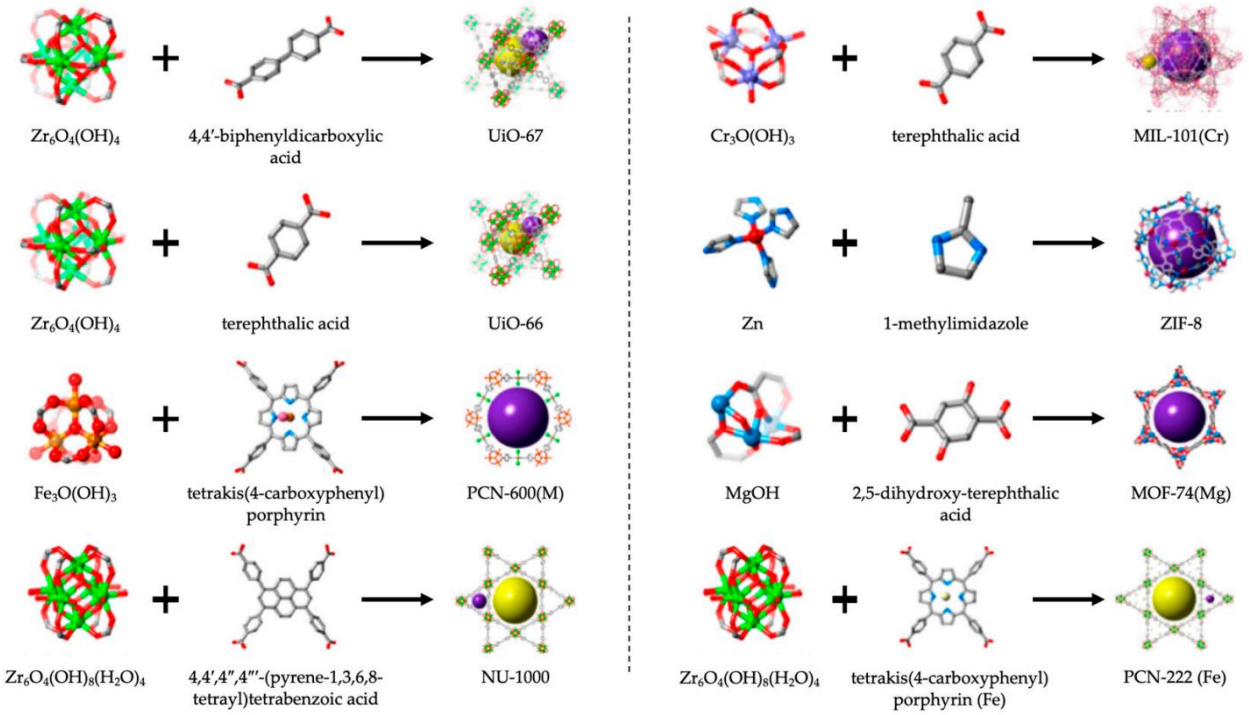

Figure 1-1. Examples of different metal–organic framework structures with their corresponding secondary building units and organic linkers. Adapted with permission from *Separations*, **2019,** *6* (4), 47. Copyright 2019 MDPI.

Besides molecular tunability, MOFs can incorporate multiple functionalities in a single framework and thus hold promise for a variety of applications such as gas storage and separation,[10-12] heterogenous catalysis,[13-15] chemical sensing,[16-17] and biomedicine.[18-20] To date, MOFs are the most porous materials known and can have experimental Brunauer–Emmett–Teller (BET) surface areas as high as 7140 m^2/g in NU-110E.[21] MOFs are excellent candidates for gas storage, especially in methane, H_2, and CO_2 storage for energy and environmental purposes.[22-24] Besides, the pores can be engineered to desired sizes, enabling selective adsorption and separation of gasses from a mixture,[25-26] as well as metal ions[27] or organic molecules[28] from wastewater.

In heterogenous catalysis, the periodic structures of MOFs allow uniform dispersion of active sites to avoid degradation, while ensuring their accessibility and transport of substrates and products through the open channels.[29] Moreover, the hybrid structure and the ease of surface

functionalization on MOFs allow the construction of heterogeneous catalysts for tandem reactions,[13, 30] where multiple catalysts could be engineered in different moieties of MOFs in close proximity to each other.

In the past two decades, extensive efforts have been devoted to exploring potential applications of MOFs in biological systems, as biosensors[31-32] or drug delivery systems.[33-34] These applications require good biocompatibility and cellular uptake of MOFs, leading to the development of various nanoscale metal–organic frameworks (nMOFs) of good stability in biological systems.[35] While the nanoscale size could facilitate internalization of nMOFs via endocytosis,[36] the stability of MOFs is a more complex issue to address since both thermodynamic and kinetic factors need to be taken into consideration.

Thermodynamic factors are mainly related to the metal-ligand coordination bond strength, which could be predicted by Pearson's hard and soft acid and base (HSAB) theory.[37] Therefore, robust frameworks can be formed either by assembly of soft bases (e.g. imidazolate, pyrazolate ligands) with low-valent metal ions (e.g. Zn(II), Cu(II), *etc.*), or by assembly of hard bases (e.g. carboxylate ligands) with high-valent metal ions (e.g. Zr(IV), Ti(IV), *etc.*).[38] In addition, high-valent metals can form various metal-oxo clusters to further improve the stability of MOFs.[39] Therefore, Zr-based UiO-type MOFs composed of $Zr_6(\mu_3\text{-}O)_4(\mu_3\text{-}OH)_4$ SBUs and linear dicarboxylate ligands in an *fcu* topology are extensively explored due to their stability in aqueous environment.[40] For MOFs with the same metal cluster and framework topology, kinetic factors such as rigidity of the linker, coordination number, and ligand hydrophobicity could significantly affect the stability. In general, rigid and highly connected frameworks are more stable due to high tolerance toward defects, especially in the case of nMOF with missing linker "defects".[41] In terms

of hydrophobicity, the water molecules can be repelled by the hydrophobic organic ligands and thus cannot enter the metal center to cause MOF degradation by formation of metal oxides.[42]

With all these factors in mind, UiO-type and M_{12}-type (M=Zr(IV), Hf(IV)) nMOFs[43-44] are often selected to explore their biomedical applications. The M_{12}-type MOFs are composed of $M_{12}(\mu_3\text{-}O)_8(\mu_3\text{-}OH)_8(\mu_2\text{-}OH)_6$ SBUs and linear dicarboxylate ligands in an *hcp* topology, in which the M_{12} SBU is formed by 2 $M_6(\mu_3\text{-}O)_4(\mu_3\text{-}OH)_4$ SBUs connected by 6 hydroxyl groups in a face-to-face manner. The difference in crystal structures also leads to different morphology, especially in nMOFs. UiO-nMOFs usually display nano-octahedron morphology, while M_{12}-nMOFs tend to form nanoplates, likely due to different growth rates along the lateral and perpendicular directions of M_{12}-nMOFs (**Figure 1-2**).[45]

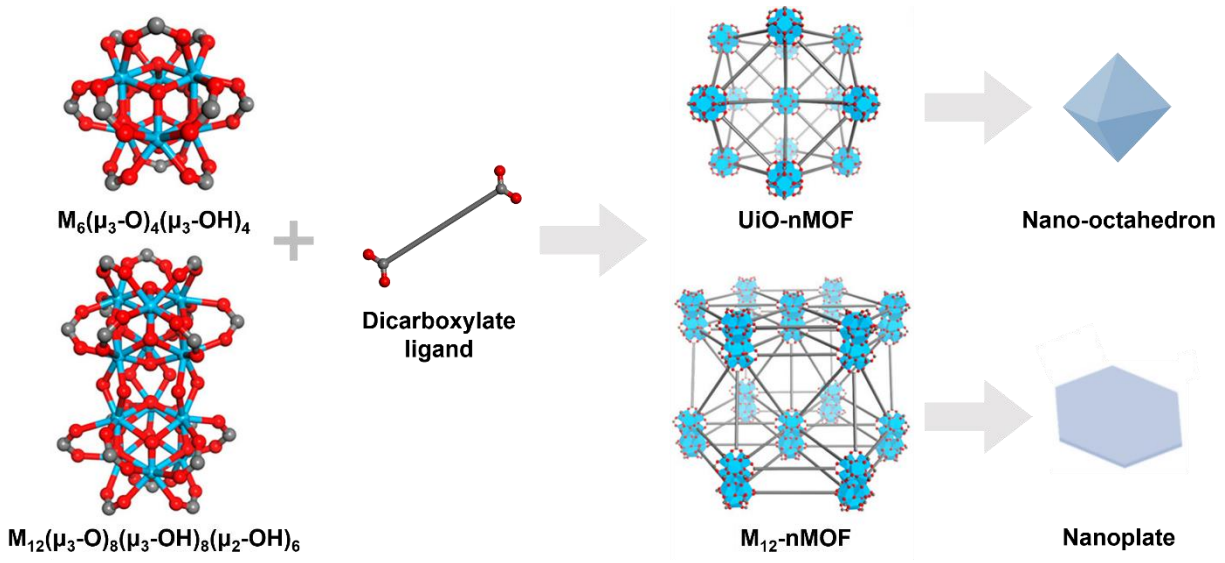

Figure 1-2. Crystal structures and morphologies of UiO-nMOF and M_{12}-nMOF. Blue: metal; red: oxygen; grey: carbon.

1.2. Heavy metal-based nMOFs for radiotherapy and radiodynamic therapy

Radiotherapy (RT) is a cancer treatment that employs ionizing radiations such as X-ray and γ-ray to kill cancer cells and shrink tumors, which is used in more than half of cancer patients.[46] The high-energy photons can either directly damage DNA or indirectly generate reactive oxygen

species (ROS) such as hydroxyl radical to decompose biomolecules and break the redox balance.[47] However, the efficacy of RT is limited by the dose tolerable by neighboring healthy tissues as they suffer from the radiation damage as well.

To enhance the cytotoxic effect of radiations to tumors while potentially reducing the side effects to normal tissues, radiosensitizers (also called radioenhancers) with high X-ray attenuation coefficients are developed to increase the energy deposition in tumors. As X-ray attenuation coefficient is proportional to the density and the 4th power of the atomic number,[48] heavy metal-based nanomaterials are extensively studied as radiosensitizers. In particular, they can interact with ionizing radiation to produce photoelectrons/Auger electrons, thereby generating reactive radicals to destruct cancer cells. Besides traditional nonporous nanoparticles such as gold nanoparticles[49-50] or HfO_2 nanoparticles,[51-53] nanoscale metal–organic frameworks (nMOFs) with heavy metal-based secondary building units (SBUs) have recently emerged as a novel class of radiosensitizers.[54-55] Compared with nonporous nanoparticles, nMOFs have larger surface areas for interaction with X-ray while retaining proper sizes for cell uptake. In addition, nMOFs are biodegradable while heavy metal-based nanoparticles would exhibit long-term body retention with possible long-term toxicity.[56]

In 2018, our group reported the rational design of two hafnium-based nMOFs, Hf_6-DBA and Hf_{12}-DBA (DBA = 2,5-di(p-benzoato)aniline), as radiosensitizers for radiotherapy.[57] Both nMOFs outperformed HfO_2, a clinically investigated radiosensitizer, in hydroxyl radical generation in test tube, as well as in anticancer efficacy *in vitro* and *in vivo*. Hf_{12}-DBA was better than Hf_6-DBA. The authors speculated that the increased X-ray absorption with larger Hf-SBUs and more facile ROS diffusion enabled by thin nanoplate structures are the key factors for the enhanced radioenhancement. To further enhance radiosensitization, another high-Z component,

Wells-Dawson-type W-based polyoxometalates ($[P_2W_{18}O_{62}]^{6-}$ POMs), were incorporated into the pores of a cationic Hf_{12}-DBB-Ir nMOF built from Hf_{12} SBUs and $[Ir(bpy)_2(ppy)]^+$-derived dicarboxylate ligands (DBB-Ir, bpy = 2,2′-bipyridine, and ppy = 2-phenylpyridine), giving rise to W_{18}@Hf_{12}-DBB-Ir.[58] Upon X-ray irradiation, multiple ROSs were generated: hydroxyl radical from Hf_{12} SBUs, singlet oxygen from DBB-Ir ligands, and superoxide from W_{18} POMs, contributing to the overall superior anticancer efficacy with >98% tumor regression at a low X-ray dose of 1 Gy for 5 fractions.

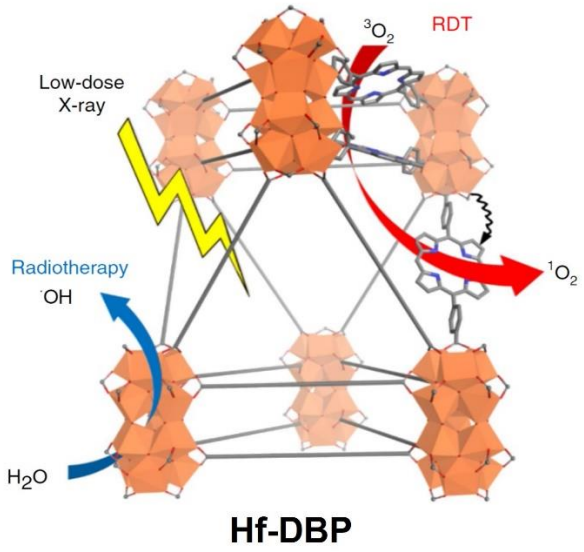

Figure 1-3. Synergistic radiotherapy–radiodynamic therapy achieved by Hf-DBP upon X-ray irradiation. Reprinted with permission from *Nat. Biomed. Eng.* **2018,** *2* (8), 600-610. Copyright 2018 Nature Portfolio.

To further exploit the potential of heavy-metal-based nMOFs for radiotherapy, photosensitizing ligands could be incorporated to achieve radiodynamic therapy (RDT), in which X-ray excited heavy-metal SBUs can transfer energy to neighboring photosensitizing ligands to generate singlet oxygen (**Figure 1-3**).[59] The synergistic RT–RDT technology was first demonstrated in Hf-DBP and Hf-TBP nMOFs, with Hf_{12}/Hf_6 SBUs and photosensitizing 5,15-di(p-benzoato)porphyrin (DBP)/5,10,15,20-tetra(p-benzoato)porphyrin (TBP) ligands,

respectively.[44] Benefited from efficient production of ·OH and $^1O_2$, the nMOFs efficiently eradicate 4 different tumor models with the use of extremely low doses of X-rays *in vivo*.

Besides porphyrin-type ligands,[56] transition metal-based photosensitizing ligands were also utilized for RDT.[58, 60] As cationic Ru-based photosensitizers have been reported to accumulate in mitochondria,[61] nMOFs with such photosensitizing ligands can achieve organelle-specific accumulation and ROS generation to further enhance the anticancer efficacy of RT–RDT. Hf-DBB-Ru nMOF with bis(2,2'-bipyridine)(5,5'-di(4-benzoato)-2,2'-bipyridine)ruthenium(II) chloride (DBB-Ru) and Hf_6 SBUs were constructed as a mitochondria-targeted nMOF for RT–RDT. The generation of ROS in and around mitochondria was shown to cause membrane damage and elicit efficient apoptosis. The *in vivo* anticancer efficacy of mitochondria-targeted RT with low-dose X-rays was further demonstrated on CT26 and MC38 colorectal tumor models.

As hypoxia in tumors could cause RT resistance and hamper the RDT effect with limited $^3O_2$ for conversion to $^1O_2$.[62] Catalase-like agents were integrated into nMOFs to catalyze the decomposition of H_2O_2 to generate O_2. Biomimetic porphyrin-$Fe^{III}Cl$ was introduced to Hf-DBP nMOF via postsynthetic metalation of DBP ligands, decomposing H_2O_2 in hypoxia tumors to generate both O_2 and ·OH.[63] The generated O_2 alleviated hypoxia and sensitized tumor cells to RT–RDT, giving rise to a tumor growth inhibition index of 98.3% in MC38 colorectal tumor-bearing mice. Manganese ions was also incorporated to fabricate catalase-like nMOFs to enhance radiotherapy in hypoxic cancer and prevent cancer recurrence.[64] Hypoxia-regulatory pathways can also be targeted to overcome hypoxic TMEs.[65] D-arginine (D-Arg), a metabolically inert enantiomer of L-arginine, was loaded into MIL-100(Fe) to form HA@MOF/D-Arg (HA = hyaluronic acid), which produces nitric oxide and downregulates hypoxia-inducible factor-1alpha (HIF-1α) to alleviate tumor hypoxia.[66] The Fe(III) ion in the SBUs also reacted with intracellular

H_2O_2 to generate ·OH and O_2. *In vivo* results showed that D-arginine-loaded MIL-100(Fe) NPs sensitized tumor cells to RT and 4 Gy X-ray irradiation improved mice survival and prevented lung metastasis in mice with osteosarcoma.

As the properties of materials are not only dependent on their compositions, but also affected by their structures and sizes.[67] In particular, dimensional reduction from three dimensional (3D) materials to two dimensional (2D) materials can significantly change their chemical reactivity.[68] Our group further postulated that the radiosensitizing properties of nMOFs could be further enhanced if one dimension of the nMOFs could be reduced to a monolayer thickness. As a 2D version of nMOFs, nanoscale metal-organic layers (nMOLs) retain the crystalline arrangement of heavy metal clusters and photosensitizing ligands to enable RT–RDT while facilitating ROS generation, leading to strong antitumor activity upon X-ray irradiation. In 2017, two Hf-based nMOLs, Hf_6-BPY-Ir and Hf_6-BPY-Ru, was reported for enhanced RT–RDT.[69] These nMOLs were obtained via postsynthetic metalation of Hf_6-BPY nMOL comprising Hf_6 SBUs and 4',6'-dibenzoato-[2,2'-bipyridine]-4-carboxylate (BPY) bridging ligands. The monolayer thickness was confirmed by atomic force microscopy, which contributes to the ROS diffusion and the complete eradication of both CT26 and MC38 tumors in mice models in MOL plus X-ray groups. Another version of nMOL based on electron-dense Hf_{12} SBUs, Hf_{12}-DBB-Ir, was developed for RT–RDT in 2018.[70] The flat monolayer morphology was very different from the wrinkled-sheet morphology observed in Hf_6-BPY-Ir nMOLs, which is believed to originate from the dual linkage between adjacent Hf_{12} SBUs. Hf_{12}-DBB-Ir nMOL exhibited more efficient RDT effects than Hf_6-BPY-Ir as more $^1O_2$ could be detected upon X-ray irradiation, leading to a 2-fold lower IC_{50} value upon 2 Gy X-ray irradiation *in vitro* and a 3-fold better tumor inhibition on MC38 model upon 2.5 Gy X-

ray irradiation *in vivo*. Hf-DBP MOL with similar monolayer topology was also developed to synergize with checkpoint blockade immunotherapy (CBI).[71]

In the past few years, Hf-based nMOFs and nMOLs have been successfully developed for RT and RDT. However, explorations on other heavy metal-based nMOFs are limited. In addition, mechanistic studies on how the compositions and crystal structures of nMOFs could affect their radiosensitizing properties are needed to guide the design of optimal nMOF-based radiosensitizers.

1.3. MOFs as drug carriers for chemotherapy

Chemotherapy is a type of cancer treatment that uses drugs to kill fast proliferating cancer cells. In particular, chemotherapeutic drugs prevent cancer cells from growing, dividing and making more cells.[72] Based on the mechanism of action, chemotherapeutic drugs can be divided into different types, including alkylating agents such as cisplatin to damage DNA directly,[73] antimetabolites such as 5-Fluorauracil to be mis-incorporated into RNA or DNA,[74] and topoisomerase inhibitors such as irinotecan to inhibit DNA replication by preventing topoisomerase I from separating the strands of DNA.[75]

Most chemotherapeutic drugs require intravenous injection to travel through the bloodstream and reach all parts of the body. However, non-selective distribution of drugs in the body will not only diminish the therapeutic efficacy due to insufficient accumulation of drugs in tumors, but also inevitably cause significant side effects to normal organs.[76] Numerous drug delivery systems are developed with the goals achieving selective distribution and controlled release of drugs in tumors.

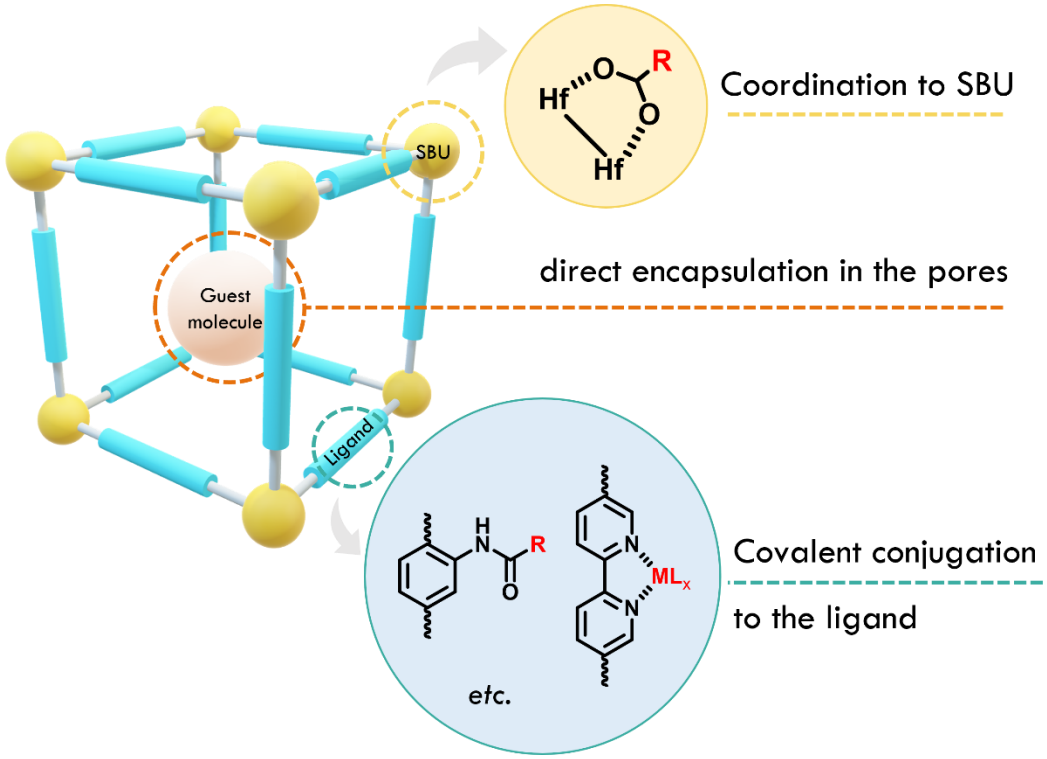

Figure 1-4. Different drug loading methods in MOFs.

Benefited from their porous structures and molecular tunability, nMOFs have been researched as drug delivery systems, where drugs are loaded via encapsulation in the pores, coordination to metal SBUs, or covalent conjugation to the ligands (**Figure 1-4**). In 2014, Our group reported the first use of an nMOF for the co-delivery of cisplatin and pooled small interfering RNAs (siRNAs) to enhance therapeutic efficacy by silencing multiple drug resistance (MDR) genes and re-sensitizing resistant ovarian cancer cells to cisplatin treatment.[77] A cisplatin prodrug and siRNAs were loaded to a Zr_{12}-based nMOF subsequently via encapsulation in the pores and surface coordination to metal sites, respectively. The endocytosis of the nMOF by cisplatin-resistant ovarian cells enhanced the cellular uptake of siRNAs, promoted their escape from endosomes to silence MDR genes, and protected them from nuclease degradation, resulting in an order-of-magnitude enhancement in chemotherapeutic efficacy of cisplatin *in vitro*. In a similar manner, co-delivery of a small-molecule toll-like receptor 7 agonist, imiquimod (IMD), and a

macromolecule, anti-CD47 antibody (αCD47), was achieved in Hf-DBP nMOF via encapsulation and coordination to metal SBUs, respectively.[78] For better modification efficiency, the acetate groups on Hf_{12} SBUs were first replaced with weakly coordinating trifluoroacetate (TFA), and then readily replaced by carboxylate groups in CD47.

In terms of covalent conjugation methods, click chemistry has been used to modify an azide-functionalized Zr-based UiO-66-N_3 MOF with dibenzylcyclooctyne (DBCO) functionalized oligonucleotides.[79] However, only the surfaces of MOF are modified due to small pore sizes. Enhanced stability and cellular uptake of MOF was observed *in vitro*, while no detailed release profiles were provided. Covalent linkage is more stable than Van der Waals force and coordination bond used in encapsulation and coordination methods, but requires an appropriate trigger or stimulus for controlled and on-demand release of drugs from the ligands.

For general prodrug designs, internal triggers such as pH,[80] glutathione[81] and esterase[82] and external triggers such as ultrasound[83] and photons[84] have been used to convert the prodrugs to their active forms after entering cells. In terms of photo-activatable prodrug design, the use of ionizing radiations such as X-rays could greatly expand the scope of prodrug application, as X-ray not only has deep penetration depth for prodrug activation in deep-seated tumors,[85] but also enables image-guided precise dosing.[86] Moreover, the radiotherapeutic effects of X-ray contribute to the overall anticancer efficacy.[62] In terms of detailed mechanism of X-ray triggered prodrug activation, ROS are often involved.[87] A masking group, 3,5-dihydroxybenzyl carbamate (DHBC), was reported to react with hydroxyl radicals produced by radiation to afford hydroxylation and subsequent 1,4- or 1,6-elimination to release the client molecule.[88] Radiation-generated hydroxyl radicals were also employed in proteolysis targeting chimera (PROTAC) strategy to precisely and spatiotemporally control protein degradation. An X-ray triggerable phenyl azide-cage, (4-azido-2,3,5,6-

tetrafluorophenyl)methanol, was incorporated into a bromodomain (BRD)-targeting PROTAC to afford RT-PROTAC, which can be activated by X-ray radiation *in vitro* and *in vivo* to degrade BRD4 and BRD2 and synergizes with radiotherapy to suppress tumor growth in a MCF-7 xenograft model.[89]

As heavy metal-based SBUs in nMOFs could enhance RT by promoting the generation of ROS, especially hydroxyl radical,[57] heavy metal-nMOFs with covalently conjugated X-ray triggerable prodrugs should be able to release drugs upon irradiation for synergistic radiotherapy and chemotherapy. However, there is no reported example, likely due to the difficulty of ligand design and synthesis. More efforts are needed in this area to explore the potential of nMOFs in multi-modality cancer treatment via covalent conjugation of X-ray triggerable prodrugs to the ligands.

1.4. The scope of this dissertation

Built on the significant achievements in RT–RDT with heavy metal-based nMOFs and drug delivery with MOFs, my PhD research focused on advancing the field of cancer therapy through the rational design of nMOFs with suitable SBUs and functional ligands. Divided into three parts, this dissertation aimed to elucidate the mechanism of nMOF-mediated radiotherapy, develop novel nMOFs with enhanced radiosensitization, and design functional ligands as X-ray triggerable prodrugs for synergistic chemotherapy and radiotherapy.

The first part, including Chapter 2, focuses on the mechanistic study of photon-matter interactions and energy deposition in radiosensitizer-mediated radiotherapy using Monte Carlo simulation. The simulations utilized lattice models representing nMOFs composed of nanoscale SBUs and demonstrated the superiority of lattice structures in promoting energy deposition through enhanced electron scattering. This chapter emphasized the importance of utilizing heavier

metals, optimizing SBU sizes, and inter-SBU distances to achieve optimal dose enhancement in nMOFs.

The second part, consisting of Chapter 3 and 4, center on the rational design of nMOFs based on bismuth (Bi) and thorium (Th) for improved radiosensitization over Hf-based nMOFs. Chapter 3 presents the design of Bi-DBP nMOF, composed of $Bi_{10}O_8$ clusters and photosensitizing DBP linkers. Bi-DBP exhibited strong RT–RDT effects, reversing immunosuppressive tumor microenvironments by reducing intratumoral TGF-β levels and enhancing the therapeutic effects of checkpoint blockade immunotherapy. Chapter 4 describes Th-DBP nMOF, composed of $Th_6O_4(OH)_4$ SBUs and DBP ligands, for increased energy deposition, reactive oxygen species (ROS) generation, and cytotoxicity to cancer cells over Hf-DBP.

The third part, comprising Chapter 5 and 6, focused on the design of functional ligands as X-ray triggerable prodrugs for synergistic chemotherapy in combination with RT or RT–RDT. In Chapter 5, Hf-TP-SN nMOF was developed, incorporating terphenyl ligands covalently conjugated with an X-ray triggerable SN38 prodrug. Upon X-ray irradiation, the electron-dense Hf_{12} SBUs served as radiosensitizers, enhancing hydroxyl radical generation for the triggered release of SN38. Hf-TP-SN demonstrated significant cytotoxicity to cancer cells *in vitro* and efficient tumor growth inhibition in a murine colon carcinoma model. Chapter 6 introduced the integration of a quaterphenyl ligand conjugated with SN38, QP-SN, into Hf-DBP, resulting in a mixed-ligand Hf-DBP-QP-SN nMOF for synergistic RT–RDT and chemotherapy. Hf-DBP-QP-SN nMOF exhibited enhanced radiation damage to tumors and generated high levels of ROS upon irradiation. In a colon cancer mouse model, Hf-DBP-QP-SN, in combination with X-ray irradiation, effectively suppressed tumor growth without obvious dark toxicity.

In summary, this dissertation describes our contributions to the field of cancer therapy by leveraging the molecular tunability of nMOFs for improved treatment efficacy and exploring the potential of multi-modality cancer treatments. The design principles uncovered in this thesis can be extended to design other molecular nanomaterials for biomedical applications.

1.5. References

(1) Bennett, T. D.; Coudert, F.-X.; James, S. L.; Cooper, A. I., The changing state of porous materials. *Nat. Mater.* **2021,** *20* (9), 1179-1187.

(2) Hendriks, F. C.; Valencia, D.; Bruijnincx, P. C. A.; Weckhuysen, B. M., Zeolite molecular accessibility and host–guest interactions studied by adsorption of organic probes of tunable size. *PCCP* **2017,** *19* (3), 1857-1867.

(3) Côté, A. P.; Benin, A. I.; Ockwig, N. W.; O'Keeffe, M.; Matzger, A. J.; Yaghi, O. M., Porous, Crystalline, Covalent Organic Frameworks. *Science* **2005,** *310* (5751), 1166-1170.

(4) Li, H.; Eddaoudi, M.; O'Keeffe, M.; Yaghi, O. M., Design and synthesis of an exceptionally stable and highly porous metal–organic framework. *Nature* **1999,** *402* (6759), 276-279.

(5) Kalmutzki, M. J.; Hanikel, N.; Yaghi, O. M., Secondary building units as the turning point in the development of the reticular chemistry of MOFs. *Sci. Adv. 4* (10), eaat9180.

(6) Moosavi, S. M.; Nandy, A.; Jablonka, K. M.; Ongari, D.; Janet, J. P.; Boyd, P. G.; Lee, Y.; Smit, B.; Kulik, H. J., Understanding the diversity of the metal–organic framework ecosystem. *Nat. Commun.* **2020,** *11* (1), 4068.

(7) Gutiérrez-Serpa, A.; Pacheco-Fernández, I.; Pasán, J.; Pino, V., Metal–Organic Frameworks as Key Materials for Solid-Phase Microextraction Devices—A Review. *Separations* **2019,** *6* (4), 47.

(8) Howarth, A. J.; Peters, A. W.; Vermeulen, N. A.; Wang, T. C.; Hupp, J. T.; Farha, O. K., Best Practices for the Synthesis, Activation, and Characterization of Metal–Organic Frameworks. *Chem. Mater.* **2017,** *29* (1), 26-39.

(9) Jiao, L.; Wang, Y.; Jiang, H.-L.; Xu, Q., Metal–Organic Frameworks as Platforms for Catalytic Applications. *Adv. Mater.* **2018,** *30* (37), 1703663.

(10) Fan, W.; Zhang, X.; Kang, Z.; Liu, X.; Sun, D., Isoreticular chemistry within metal–organic frameworks for gas storage and separation. *Coord. Chem. Rev.* **2021,** *443*, 213968.

(11) Li, H.; Wang, K.; Sun, Y.; Lollar, C. T.; Li, J.; Zhou, H.-C., Recent advances in gas storage and separation using metal–organic frameworks. *Mater. Today* **2018,** *21* (2), 108-121.

(12) Li, B.; Wen, H.-M.; Zhou, W.; Chen, B., Porous Metal–Organic Frameworks for Gas Storage and Separation: What, How, and Why? *J. Phys. Chem. Lett* **2014,** *5* (20), 3468-3479.

(13) Huang, Y.-B.; Liang, J.; Wang, X.-S.; Cao, R., Multifunctional metal–organic framework catalysts: synergistic catalysis and tandem reactions. *Chem. Soc. Rev.* **2017,** *46* (1), 126-157.

(14) Lee, J.; Farha, O. K.; Roberts, J.; Scheidt, K. A.; Nguyen, S. T.; Hupp, J. T., Metal–organic framework materials as catalysts. *Chem. Soc. Rev.* **2009,** *38* (5), 1450-1459.

(15) Dhakshinamoorthy, A.; Asiri, A. M.; Garcia, H., Metal–organic frameworks catalyzed C–C and C–heteroatom coupling reactions. *Chem. Soc. Rev.* **2015,** *44* (7), 1922-1947.

(16) Kreno, L. E.; Leong, K.; Farha, O. K.; Allendorf, M.; Van Duyne, R. P.; Hupp, J. T., Metal–Organic Framework Materials as Chemical Sensors. *Chem. Rev.* **2012,** *112* (2), 1105-1125.

(17) Koo, W.-T.; Jang, J.-S.; Kim, I.-D., Metal–organic frameworks for Chemiresistive Sensors. *Chem* **2019,** *5* (8), 1938-1963.

(18) Horcajada, P.; Gref, R.; Baati, T.; Allan, P. K.; Maurin, G.; Couvreur, P.; Férey, G.; Morris, R. E.; Serre, C., Metal–Organic Frameworks in Biomedicine. *Chem. Rev.* **2012,** *112* (2), 1232-1268.

(19) Mendes, R. F.; Figueira, F.; Leite, J. P.; Gales, L.; Almeida Paz, F. A., Metal–organic frameworks: a future toolbox for biomedicine? *Chem. Soc. Rev.* **2020,** *49* (24), 9121-9153.

(20) Simon-Yarza, T.; Mielcarek, A.; Couvreur, P.; Serre, C., Nanoparticles of Metal–organic frameworks: On the Road to In Vivo Efficacy in Biomedicine. *Adv. Mater.* **2018,** *30* (37), 1707365.

(21) Farha, O. K.; Eryazici, I.; Jeong, N. C.; Hauser, B. G.; Wilmer, C. E.; Sarjeant, A. A.; Snurr, R. Q.; Nguyen, S. T.; Yazaydın, A. Ö.; Hupp, J. T., Metal–Organic Framework Materials with Ultrahigh Surface Areas: Is the Sky the Limit? *J. Am. Chem. Soc.* **2012,** *134* (36), 15016-15021.

(22) Millward, A. R.; Yaghi, O. M., Metal−Organic Frameworks with Exceptionally High Capacity for Storage of Carbon Dioxide at Room Temperature. *J. Am. Chem. Soc.* **2005,** *127* (51), 17998-17999.

(23) He, Y.; Zhou, W.; Qian, G.; Chen, B., Methane storage in metal–organic frameworks. *Chem. Soc. Rev.* **2014,** *43* (16), 5657-5678.

(24) Murray, L. J.; Dincă, M.; Long, J. R., Hydrogen storage in metal–organic frameworks. *Chem. Soc. Rev.* **2009,** *38* (5), 1294-1314.

(25) Lin, R.-B.; Xiang, S.; Xing, H.; Zhou, W.; Chen, B., Exploration of porous metal–organic frameworks for gas separation and purification. *Coord. Chem. Rev.* **2019,** *378*, 87-103.

(26) Li, J.-R.; Kuppler, R. J.; Zhou, H.-C., Selective gas adsorption and separation in metal–organic frameworks. *Chem. Soc. Rev.* **2009,** *38* (5), 1477-1504.

(27) Yang, G.-S.; Lang, Z.-L.; Zang, H.-Y.; Lan, Y.-Q.; He, W.-W.; Zhao, X.-L.; Yan, L.-K.; Wang, X.-L.; Su, Z.-M., Control of interpenetration in S-containing metal–organic frameworks for selective separation of transition metal ions. *Chem. Commun.* **2013,** *49* (11), 1088-1090.

(28) Zhao, Y.; Wang, L.; Fan, N.-N.; Han, M.-L.; Yang, G.-P.; Ma, L.-F., Porous Zn(II)-Based Metal–Organic Frameworks Decorated with Carboxylate Groups Exhibiting High Gas Adsorption and Separation of Organic Dyes. *Cryst. Growth Des.* **2018,** *18* (11), 7114-7121.

(29) Zhao, M.; Yuan, K.; Wang, Y.; Li, G.; Guo, J.; Gu, L.; Hu, W.; Zhao, H.; Tang, Z., Metal–organic frameworks as selectivity regulators for hydrogenation reactions. *Nature* **2016,** *539* (7627), 76-80.

(30) Yin, Z.; Wan, S.; Yang, J.; Kurmoo, M.; Zeng, M.-H., Recent advances in post-synthetic modification of metal–organic frameworks: New types and tandem reactions. *Coord. Chem. Rev.* **2019,** *378*, 500-512.

(31) Zhao, Y.; Zeng, H.; Zhu, X.-W.; Lu, W.; Li, D., Metal–organic frameworks as photoluminescent biosensing platforms: mechanisms and applications. *Chem. Soc. Rev.* **2021,** *50* (7), 4484-4513.

(32) Wang, H.-S., Metal–organic frameworks for biosensing and bioimaging applications. *Coord. Chem. Rev.* **2017,** *349*, 139-155.

(33) Horcajada, P.; Chalati, T.; Serre, C.; Gillet, B.; Sebrie, C.; Baati, T.; Eubank, J. F.; Heurtaux, D.; Clayette, P.; Kreuz, C.; Chang, J.-S.; Hwang, Y. K.; Marsaud, V.; Bories, P.-N.; Cynober, L.; Gil, S.; Férey, G.; Couvreur, P.; Gref, R., Porous metal–organic-framework nanoscale carriers as a potential platform for drug delivery and imaging. *Nat. Mater.* **2010,** *9* (2), 172-178.

(34) Della Rocca, J.; Liu, D.; Lin, W., Nanoscale Metal–Organic Frameworks for Biomedical Imaging and Drug Delivery. *Acc. Chem. Res.* **2011,** *44* (10), 957-968.

(35) Lu, K.; Aung, T.; Guo, N.; Weichselbaum, R.; Lin, W., Nanoscale Metal–Organic Frameworks for Therapeutic, Imaging, and Sensing Applications. *Adv. Mater.* **2018,** *30* (37), 1707634.

(36) Rennick, J. J.; Johnston, A. P. R.; Parton, R. G., Key principles and methods for studying the endocytosis of biological and nanoparticle therapeutics. *Nat. Nanotechnol.* **2021,** *16* (3), 266-276.

(37) Pearson, R. G., Hard and soft acids and bases. *J. Am. Chem. Soc.* **1963,** *85* (22), 3533-3539.

(38) Bunzen, H., Chemical Stability of Metal–organic frameworks for Applications in Drug Delivery. *ChemNanoMat* **2021,** *7* (9), 998-1007.

(39) Wang, C.; Yan, J.; Chen, S.; Liu, Y., High-Valence Metal–organic framework Materials Constructed from Metal-Oxo Clusters: Opportunities and Challenges. *ChemPlusChem* **2023,** *88* (3), e202200462.

(40) Cavka, J. H.; Jakobsen, S.; Olsbye, U.; Guillou, N.; Lamberti, C.; Bordiga, S.; Lillerud, K. P., A New Zirconium Inorganic Building Brick Forming Metal Organic Frameworks with Exceptional Stability. *J. Am. Chem. Soc.* **2008,** *130* (42), 13850-13851.

(41) He, T.; Kong, X.-J.; Li, J.-R., Chemically Stable Metal–Organic Frameworks: Rational Construction and Application Expansion. *Acc. Chem. Res.* **2021,** *54* (15), 3083-3094.

(42) Nguyen, J. G.; Cohen, S. M., Moisture-Resistant and Superhydrophobic Metal−Organic Frameworks Obtained via Postsynthetic Modification. *J. Am. Chem. Soc.* **2010,** *132* (13), 4560-4561.

(43) Dai, R.; Peng, F.; Ji, P.; Lu, K.; Wang, C.; Sun, J.; Lin, W., Electron Crystallography Reveals Atomic Structures of Metal–Organic Nanoplates with M12(μ3-O)8(μ3-OH)8(μ2-OH)6 (M = Zr, Hf) Secondary Building Units. *Inorg. Chem.* **2017,** *56* (14), 8128-8134.

(44) Lu, K.; He, C.; Guo, N.; Chan, C.; Ni, K.; Lan, G.; Tang, H.; Pelizzari, C.; Fu, Y.-X.; Spiotto, M. T.; Weichselbaum, R. R.; Lin, W., Low-dose X-ray radiotherapy–radiodynamic therapy via nanoscale metal–organic frameworks enhances checkpoint blockade immunotherapy. *Nat. Biomed. Eng.* **2018,** *2* (8), 600-610.

(45) Chen, P.; Tang, Z.; Zeng, Z.; Hu, X.; Xiao, L.; Liu, Y.; Qian, X.; Deng, C.; Huang, R.; Zhang, J.; Bi, Y.; Lin, R.; Zhou, Y.; Liao, H.; Zhou, D.; Wang, C.; Lin, W., Machine-Learning-Guided Morphology Engineering of Nanoscale Metal–organic frameworks. *Matter* **2020,** *2* (6), 1651-1666.

(46) Atun, R.; Jaffray, D. A.; Barton, M. B.; Bray, F.; Baumann, M.; Vikram, B.; Hanna, T. P.; Knaul, F. M.; Lievens, Y.; Lui, T. Y. M.; Milosevic, M.; O'Sullivan, B.; Rodin, D. L.; Rosenblatt, E.; Van Dyk, J.; Yap, M. L.; Zubizarreta, E.; Gospodarowicz, M., Expanding global access to radiotherapy. *Lancet Oncol.* **2015,** *16* (10), 1153-1186.

(47) Hubenak, J. R.; Zhang, Q.; Branch, C. D.; Kronowitz, S. J., Mechanisms of injury to normal tissue after radiotherapy: a review. *Plast. Reconstr. Surg.* **2014,** *133* (1), 49e-56e.

(48) Jackson, D. F.; Hawkes, D. J., X-ray attenuation coefficients of elements and mixtures. *Physics Reports* **1981,** *70* (3), 169-233.

(49) James, F. H.; Daniel, N. S.; Henry, M. S., The use of gold nanoparticles to enhance radiotherapy in mice. *Phys. Med. Biol.* **2004,** *49* (18), N309.

(50) Ma, N.; Wu, F.-G.; Zhang, X.; Jiang, Y.-W.; Jia, H.-R.; Wang, H.-Y.; Li, Y.-H.; Liu, P.; Gu, N.; Chen, Z., Shape-Dependent Radiosensitization Effect of Gold Nanostructures in Cancer Radiotherapy: Comparison of Gold Nanoparticles, Nanospikes, and Nanorods. *ACS Appl. Mater. Interfaces* **2017,** *9* (15), 13037-13048.

(51) Zhang, P.; Marill, J.; Darmon, A.; Anesary, N. M.; Lu, B.; Paris, S., NBTXR3 radiotherapy-activated functionalized Hafnium Oxide nanoparticles show efficient antitumor effects across a large panel of human cancer models. *Int. J. Nanomedicine* **2021,** *16*, 2761.

(52) Bonvalot, S.; Rutkowski, P. L.; Thariat, J.; Carrère, S.; Ducassou, A.; Sunyach, M.-P.; Agoston, P.; Hong, A.; Mervoyer, A.; Rastrelli, M., NBTXR3, a first-in-class radioenhancer hafnium oxide nanoparticle, plus radiotherapy versus radiotherapy alone in patients with

locally advanced soft-tissue sarcoma (Act. In. Sarc): a multicentre, phase 2–3, randomised, controlled trial. *Lancet Oncol.* **2019,** *20* (8), 1148-1159.

(53) Bonvalot, S.; Le Pechoux, C.; De Baere, T.; Kantor, G.; Buy, X.; Stoeckle, E.; Terrier, P.; Sargos, P.; Coindre, J. M.; Lassau, N.; Ait Sarkouh, R.; Dimitriu, M.; Borghi, E.; Levy, L.; Deutsch, E.; Soria, J.-C., First-in-Human Study Testing a New Radioenhancer Using Nanoparticles (NBTXR3) Activated by Radiation Therapy in Patients with Locally Advanced Soft Tissue Sarcomas. *Clin. Cancer Res.* **2017,** *23* (4), 908-917.

(54) Ni, K.; Lan, G.; Lin, W., Nanoscale Metal–Organic Frameworks Generate Reactive Oxygen Species for Cancer Therapy. *ACS Cent. Sci.* **2020,** *6* (6), 861-868.

(55) Mao, J.; Xu, Z.; Lin, W., Nanoscale metal–organic frameworks for photodynamic therapy and radiotherapy. *Curr. Opin. Chem. Eng.* **2022,** *38*, 100871.

(56) Liu, J.; Yang, Y.; Zhu, W.; Yi, X.; Dong, Z.; Xu, X.; Chen, M.; Yang, K.; Lu, G.; Jiang, L.; Liu, Z., Nanoscale metal−organic frameworks for combined photodynamic & radiation therapy in cancer treatment. *Biomaterials* **2016,** *97*, 1-9.

(57) Ni, K.; Lan, G.; Chan, C.; Quigley, B.; Lu, K.; Aung, T.; Guo, N.; La Riviere, P.; Weichselbaum, R. R.; Lin, W., Nanoscale metal–organic frameworks enhance radiotherapy to potentiate checkpoint blockade immunotherapy. *Nat. Commun.* **2018,** *9* (1), 2351.

(58) Lan, G.; Ni, K.; Veroneau, S. S.; Luo, T.; You, E.; Lin, W., Nanoscale Metal–Organic Framework Hierarchically Combines High-Z Components for Multifarious Radio-Enhancement. *J. Am. Chem. Soc.* **2019,** *141* (17), 6859-6863.

(59) Lin, W.; He, C.; Kuangda, L., Nanoparticles for photodynamic therapy, X-ray induced photodynamic therapy, radiotherapy, chemotherapy, immunotherapy, and any combination thereof. Google Patents: 2019.

(60) Ni, K.; Lan, G.; Veroneau, S. S.; Duan, X.; Song, Y.; Lin, W., Nanoscale metal–organic frameworks for mitochondria-targeted radiotherapy–radiodynamic therapy. *Nat. Commun.* **2018,** *9* (1), 4321.

(61) Poynton, F. E.; Bright, S. A.; Blasco, S.; Williams, D. C.; Kelly, J. M.; Gunnlaugsson, T., The development of ruthenium(ii) polypyridyl complexes and conjugates for in vitro cellular and in vivo applications. *Chem. Soc. Rev.* **2017,** *46* (24), 7706-7756.

(62) Barker, H. E.; Paget, J. T. E.; Khan, A. A.; Harrington, K. J., The tumour microenvironment after radiotherapy: mechanisms of resistance and recurrence. *Nat. Rev. Cancer* **2015,** *15* (7), 409-425.

(63) Ni, K.; Lan, G.; Song, Y.; Hao, Z.; Lin, W., Biomimetic nanoscale metal–organic framework harnesses hypoxia for effective cancer radiotherapy and immunotherapy. *Chem. Sci.* **2020,** *11* (29), 7641-7653.

(64) Chen, Y.; Zhong, H.; Wang, J.; Wan, X.; Li, Y.; Pan, W.; Li, N.; Tang, B., Catalase-like metal–organic framework nanoparticles to enhance radiotherapy in hypoxic cancer and prevent cancer recurrence. *Chem. Sci.* **2019,** *10* (22), 5773-5778.

(65) Patiar, S.; Harris, A. L., Role of hypoxia-inducible factor-1α as a cancer therapy target. *Endocr. Relat. Cancer* **2006,** *13* (Supplement_1), S61-S75.

(66) Du, C.; Zhou, M.; Jia, F.; Ruan, L.; Lu, H.; Zhang, J.; Zhu, B.; Liu, X.; Chen, J.; Chai, Z.; Hu, Y., D-arginine-loaded metal–organic frameworks nanoparticles sensitize osteosarcoma to radiotherapy. *Biomaterials* **2021,** *269*, 120642.

(67) Arzt, E., Size effects in materials due to microstructural and dimensional constraints: a comparative review. *Acta Mater.* **1998,** *46* (16), 5611-5626.

(68) Akinwande, D.; Brennan, C. J.; Bunch, J. S.; Egberts, P.; Felts, J. R.; Gao, H.; Huang, R.; Kim, J.-S.; Li, T.; Li, Y.; Liechti, K. M.; Lu, N.; Park, H. S.; Reed, E. J.; Wang, P.; Yakobson, B. I.; Zhang, T.; Zhang, Y.-W.; Zhou, Y.; Zhu, Y., A review on mechanics and mechanical properties of 2D materials—Graphene and beyond. *Extreme Mech. Lett.* **2017,** *13*, 42-77.

(69) Lan, G.; Ni, K.; Xu, R.; Lu, K.; Lin, Z.; Chan, C.; Lin, W., Nanoscale Metal–Organic Layers for Deeply Penetrating X-ray-Induced Photodynamic Therapy. *Angew. Chem. Int. Ed.* **2017,** *56* (40), 12102-12106.

(70) Lan, G.; Ni, K.; Veroneau, S. S.; Song, Y.; Lin, W., Nanoscale Metal–Organic Layers for Radiotherapy–Radiodynamic Therapy. *J. Am. Chem. Soc.* **2018,** *140* (49), 16971-16975.

(71) Ni, K.; Lan, G.; Chan, C.; Duan, X.; Guo, N.; Veroneau, S. S.; Weichselbaum, R. R.; Lin, W., Ultrathin Metal-Organic-Layer Mediated Radiotherapy–radiodynamic Therapy. *Matter* **2019,** *1* (5), 1331-1353.

(72) Chabner, B. A.; Roberts, T. G., Chemotherapy and the war on cancer. *Nat. Rev. Cancer* **2005,** *5* (1), 65-72.

(73) Pujol, J. L.; Carestia; Daurès, J. P., Is there a case for cisplatin in the treatment of small-cell lung cancer? A meta-analysis of randomized trials of a cisplatin-containing regimen versus a regimen without this alkylating agent. *Br. J. Cancer* **2000,** *83* (1), 8-15.

(74) Benz, C.; Cadman, E., Modulation of 5-Fluorouracil Metabolism and Cytotoxicity by Antimetabolite Pretreatment in Human Colorectal Adenocarcinoma HCT-81. *Cancer Res.* **1981,** *41* (3), 994-999.

(75) Vanhoefer, U.; Harstrick, A.; Achterrath, W.; Cao, S.; Seeber, S.; Rustum, Y. M., Irinotecan in the Treatment of Colorectal Cancer: Clinical Overview. *J. Clin. Oncol.* **2001,** *19* (5), 1501-1518.

(76) Saha, R. N.; Vasanthakumar, S.; Bende, G.; Snehalatha, M., Nanoparticulate drug delivery systems for cancer chemotherapy. *Mol. Membr. Biol.* **2010,** *27* (7), 215-231.

(77) He, C.; Lu, K.; Liu, D.; Lin, W., Nanoscale Metal–Organic Frameworks for the Co-Delivery of Cisplatin and Pooled siRNAs to Enhance Therapeutic Efficacy in Drug-Resistant Ovarian Cancer Cells. *J. Am. Chem. Soc.* **2014,** *136* (14), 5181-5184.

(78) Ni, K.; Luo, T.; Culbert, A.; Kaufmann, M.; Jiang, X.; Lin, W., Nanoscale Metal–Organic Framework Co-delivers TLR-7 Agonists and Anti-CD47 Antibodies to Modulate Macrophages and Orchestrate Cancer Immunotherapy. *J. Am. Chem. Soc*. **2020,** *142* (29), 12579-12584.

(79) Morris, W.; Briley, W. E.; Auyeung, E.; Cabezas, M. D.; Mirkin, C. A., Nucleic Acid–Metal Organic Framework (MOF) Nanoparticle Conjugates. *J. Am. Chem. Soc.* **2014,** *136* (20), 7261-7264.

(80) Quader, S.; Liu, X.; Toh, K.; Su, Y.-L.; Maity, A. R.; Tao, A.; Paraiso, W. K. D.; Mochida, Y.; Kinoh, H.; Cabral, H.; Kataoka, K., Supramolecularly enabled pH- triggered drug action at tumor microenvironment potentiates nanomedicine efficacy against glioblastoma. *Biomaterials* **2021,** *267*, 120463.

(81) Liu, G.; Jiang, Z.; Lovell, J. F.; Zhang, L.; Zhang, Y., Design of a Thiol-Responsive, Traceless Prodrug with Rapid Self-Immolation for Cancer Chemotherapy. *ACS Appl. Bio Mater.* **2021,** *4* (6), 4982-4989.

(82) Zheng, Y.; Yu, B.; Li, Z.; Yuan, Z.; Organ, C. L.; Trivedi, R. K.; Wang, S.; Lefer, D. J.; Wang, B., An Esterase-Sensitive Prodrug Approach for Controllable Delivery of Persulfide Species. *Angew. Chem. Int. Ed.* **2017,** *56* (39), 11749-11753.

(83) Li, Y.; Teng, X.; Yang, C.; Wang, Y.; Wang, L.; Dai, Y.; Sun, H.; Li, J., Ultrasound Controlled Anti-Inflammatory Polarization of Platelet Decorated Microglia for Targeted Ischemic Stroke Therapy. *Angew. Chem. Int. Ed.* **2021,** *60* (10), 5083-5090.

(84) Obaid, G.; Bano, S.; Thomsen, H.; Callaghan, S.; Shah, N.; Swain, J. W. R.; Jin, W.; Ding, X.; Cameron, C. G.; McFarland, S. A.; Wu, J.; Vangel, M.; Stoilova-McPhie, S.; Zhao, J.; Mino-Kenudson, M.; Lin, C.; Hasan, T., Remediating Desmoplasia with EGFR-Targeted Photoactivable Multi-Inhibitor Liposomes Doubles Overall Survival in Pancreatic Cancer. *Adv. Sci.* **2022,** *9* (24), 2104594.

(85) Liu, J.; Saw, R. E.; Kiang, Y. H., Calculation of Effective Penetration Depth in X-Ray Diffraction for Pharmaceutical Solids. *J. Pharm. Sci.* **2010,** *99* (9), 3807-3814.

(86) Dawson, L. A.; Sharpe, M. B., Image-guided radiotherapy: rationale, benefits, and limitations. *Lancet Oncol.* **2006,** *7* (10), 848-858.

(87) Geng, J.; Zhang, Y.; Gao, Q.; Neumann, K.; Dong, H.; Porter, H.; Potter, M.; Ren, H.; Argyle, D.; Bradley, M., Switching on prodrugs using radiotherapy. *Nat. Chem.* **2021,** *13* (8), 805-810.

(88) Fu, Q.; Li, H.; Duan, D.; Wang, C.; Shen, S.; Ma, H.; Liu, Z., External-Radiation-Induced Local Hydroxylation Enables Remote Release of Functional Molecules in Tumors. *Angew. Chem. Int. Ed.* **2020,** *59* (48), 21546-21552.

(89) Yang, C.; Yang, Y.; Li, Y.; Ni, Q.; Li, J., Radiotherapy-Triggered Proteolysis Targeting Chimera Prodrug Activation in Tumors. *J. Am. Chem. Soc.* **2023,** *145* (1), 385-391.

Chapter 2. Monte Carlo Simulations Reveal New Design Principles for Efficient Nanoradiosensitizers Based on Nanoscale Metal–Organic Frameworks

2.1. Introduction

As a major method for cancer treatment, radiotherapy (RT) is currently used in 50-60% of cancer patients.[1] RT uses ionizing radiations such as X-ray and γ-ray to kill cancer cells and shrink tumors *via* either directly damaging DNA or indirectly generating reactive oxygen species (ROS) through radiolysis, which oxidize proteins and lipids and induce DNA damage.[2] However, ionizing radiations can damage healthy tissues along the radiation track, which sets a limit on the maximum radiation dose that can be given to a tumor mass and thus compromises the efficacy of RT.[3] To increase treatment efficacy while minimizing side effects, radiosensitizers have been explored for their ability to preferentially sensitize tumors to ionizing radiation.[4-5]

In 1984, Matsudaira *et al.* first demonstrated enhanced cytotoxic effects of radiation in the presence of iodine,[6] sparking intense interest in high-Z element-based radiosensitizers. As indicated by equation 1-1, the attenuation coefficient (μ) is proportional to the density (ρ) and the forth power of the atomic number (Z) of materials.[7]

$$\mu = A\frac{\rho Z^4}{E^3} \qquad (1\text{-}1)$$

During photon-matter interactions, the photoelectric process is more likely to occur on high-Z elements where photoelectrons are ejected following photon absorption. Auger electrons are then generated after the holes are filled by higher-orbital electrons. In addition, inorganic nanoparticles (NPs) usually have higher densities than organic molecules, leading to further enhancement of energy deposition per unit space. As a result, various studies have explored the potential of high-Z element-based nanoradiosensitizers, such as gold (Au) NPs and hafnium oxide

(HfO_2) NPs, to amplify the generation of photoelectrons and Auger electrons.[8-31] Hainfeld *et al.* reported improved survival of EMT-6 mammary carcinoma-bearing mice by one year after treatment with Au NPs and X-rays.[32] Notably, NBTXR3, a 50 nm HfO_2 NP developed by Nanobiotix, received European market approval (CE Mark) as a medical device for the treatment of locally advanced soft tissue sarcoma in 2019.[33-34]

The sizes of NPs can significantly impact their radiosensitizing effects.[35] In a study of Au NPs with various sizes, Misawa *et al.* found that smaller Au NPs exhibited greater yields of reactive oxygen species (ROS), including hydroxyl radical and superoxide,[36] indicating the positive effects of high surface areas on NP radiosensitization. Nevertheless, the interplay between a nanoradiosensitizer and a biological system is much more complex. First, NPs of sizes ranging from 10 to 200 nm can preferentially accumulate in tumor tissues via the enhanced permeability and retention (EPR) effect.[37] NPs smaller than 10 nm can be easily cleared through renal filtration without significant accumulation in tumors.[38] Second, the sizes of NPs can also affect their cellular uptake.[39] Chithrani *et al. investigated the size-dependent uptake of Au NPs in mammalian cells and observed that 50 nm Au NPs showed higher cellular uptake than 14 and 70 nm Au NPs.*[40] *Likewise, NBTXR3 was engineered to have a size of 50 nm to enhance cancer cell uptake.*[41] *Overall, the sizes of NPs can impact their radiosensitizing effects by influencing ROS generation and cellular uptake.*

We recently reported the design of nanoscale metal–organic frameworks (nMOFs) comprising Hf-oxo cluster secondary building units (SBUs) and dicarboxylate bridging ligands, and examined their potential use as a novel class of nanoradiosensitizers.[42-45] We hypothesized that highly porous nMOFs could afford unprecedentedly high radiosensitization with a suitable

combination of ultrasmall Hf-oxo secondary building units (SBUs) for efficient ROS generation and an appropriate particle size (~100 nm) for enhanced cellular uptake.

In this chapter, we validated this hypothesis through Monte Carlo (MC) simulations and *in vitro* radiosensitization studies. Through systematic comparisons of physical dose enhancements from nMOFs and solid NPs under different radiation and geometry settings we have identified new design principles for nanoradiosensitizers to enhance RT.

2.2. Results and discussion

2.2.1. *In vitro* comparison of dose enhancement from lattices and NPs

To verify the superior radiosensitization properties of nMOFs over NPs, we synthesized Hf_6-BDC (H_2BDC = terephthalic acid), the simplest hexagonal Hf-oxo nMOF, for *in vitro* assays and compared it against commercially available HfO_2 NPs. Hf_6-BDC was synthesized via a solvothermal reaction between $HfCl_4$ and H_2BDC in *N*,*N*-dimethylformamide (DMF)[46] and displayed a morphology similar to HfO_2 with a diameter of approximately 50 nm, as observed by transmission electron microscopy (TEM, **Figure 2-1**). The Z-average sizes of Hf_6-BDC and HfO_2 in ethanol were measured to be 90 ± 1 nm and 211 ± 3 nm, respectively, by dynamic light scattering (DLS, **Figure 2-2**).

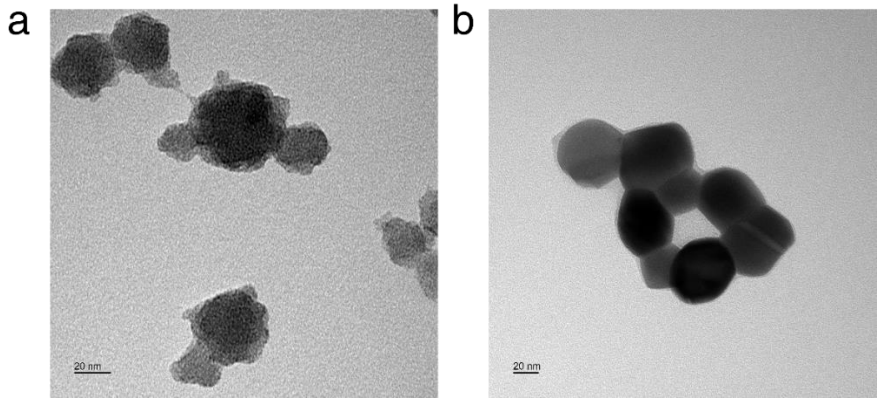

Figure 2-1. TEM images of (a) Hf_6-BDC nMOFs and (b) HfO_2 NPs.

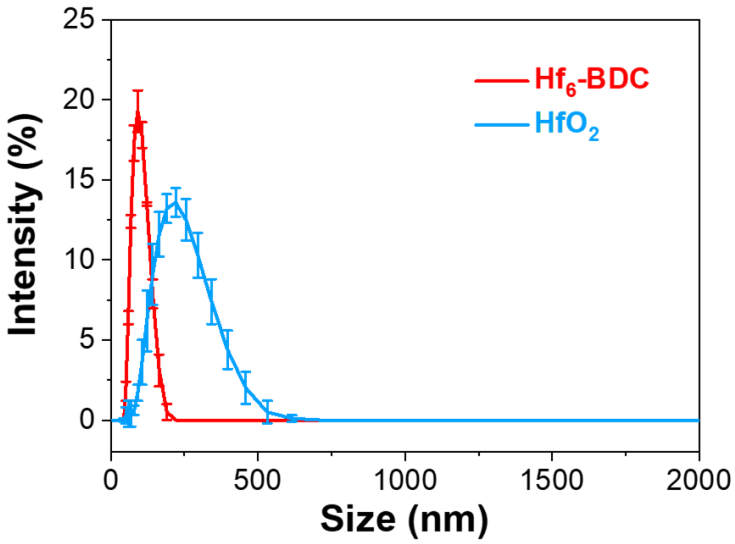

Figure 2-2. Size distributions of Hf_6-BDC nMOFs and HfO_2 NPs by DLS.

To evaluate the radiosensitizing effects of Hf_6-BDC and HfO_2, their cellular uptake by CT26 murine colorectal cancer cell was first tested. After 4 hours of incubation, they reached a similarly high intracellular level (**Figure 2-3**).

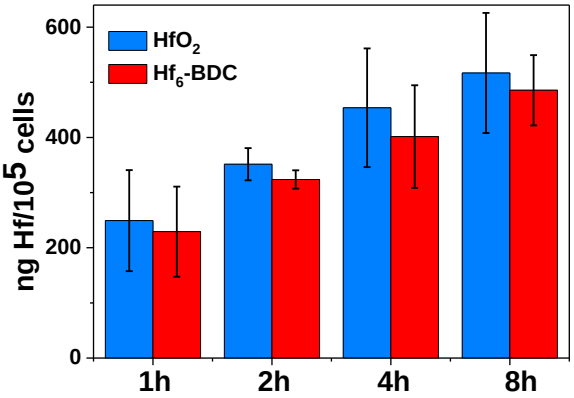

Figure 2-3. Cellular uptake of HfO_2 and Hf_6-BDC after 1, 2, 4 or 8 h incubation with equivalent Hf concentrations of 40 μM (n = 3). The Hf concentrations were determined by ICP-MS.

Next, clonogenic assays were performed to evaluate radiosensitization with different energy sources. The cells were pre-incubated with either Hf_6-BDC or HfO_2 at the same Hf concentration

of 40 μM, and followed by irradiation. The treated cells were trypsinized and re-seeded into a culture dish for colony formation. The survival results were fitted with equation 1-2.

$$SF(D) = \exp(-\alpha D - \beta D^2) \quad (1\text{-}2)$$

Where SF is survival fraction, D is X-ray dose, α and β are fitting parameters. Within the fitting curve, dose modifying ratio at 10% survival ($DMR_{10\%}$) was calculated according to equation 1-3:

$$DMR_{10\%} = D_{ctrl}/D_{NP} \quad (1\text{-}3)$$

Where D_{ctrl} is the X-ray dose at which the control group (PBS) reaches 10% survival, and D_{NP} is the X-ray dose at which the nanoparticle group reaches 10% survival.

Upon irradiation with either 225 kVp orthovoltage X-ray or ^{60}Co γ-ray, Hf_6-BDC elicited a higher dose enhancement compared to HfO_2, with $DMR_{10\%}$ values of 1.18 and 1.18 upon X-ray or γ-ray, respectively, which were significantly higher than those of HfO_2 at 1.08 and 1.06, respectively (**Figure 2-4**).

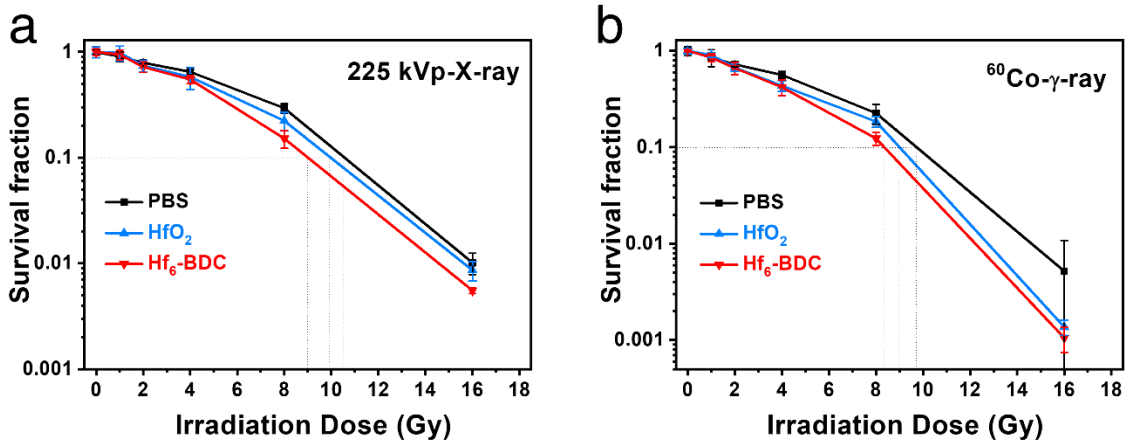

Figure 2-4. Clonogenic assays to evaluate radioenhancement of HfO_2 and Hf_6-BDC on CT26 cells upon irradiation with (a) 225 kVp-X-ray or (b) ^{60}Co-γ-ray, n=6.

To further investigate *in vitro* radiosensitization mechanisms, total ROS and DNA double-strand breaks (DSBs) were probed. Total ROS was detected using 2',7'-dichlorodihydrofluorescein diacetate (DCFH-DA) as a cell-permeant dye, which converts from nonfluorescent DCFH-DA to highly fluorescent 2',7'-dichlorofluorescein (DCF) after reaction with ROS. Both confocal laser scanning microscope (CLSM) imaging and flow cytometric analysis showed higher ROS generation by Hf_6-BDC upon irradiation (**Figure 2-5**). Specifically, the quantification of CLSM images revealed that the ROS fluorescence intensities were 31.2 ± 10.5, 54.0 ± 12.1, or 71.8 ± 15.1, respectively, for cells treated with PBS, HfO_2 or Hf_6-BDC and X-ray, and 30.3 ± 12.3, 64.8 ± 19.3, or 88.4 ± 16.9, respectively for cells treated with PBS, HfO_2 or Hf_6-BDC and γ-ray (**Figure 2-6**). Meanwhile, flow cytometric analysis gave intracellular ROS mean fluorescence intensities (MFIs) of 3688 ± 599, 5001 ± 233, or 8853 ± 850, respectively, for cells treated with PBS, HfO_2 or Hf_6-BDC and X-ray, and 7387 ± 503, 9090 ± 503, or 11277 ± 224, respectively, for cells treated with PBS, HfO_2 or Hf_6-BDC and γ-ray (**Figure 2-7**).

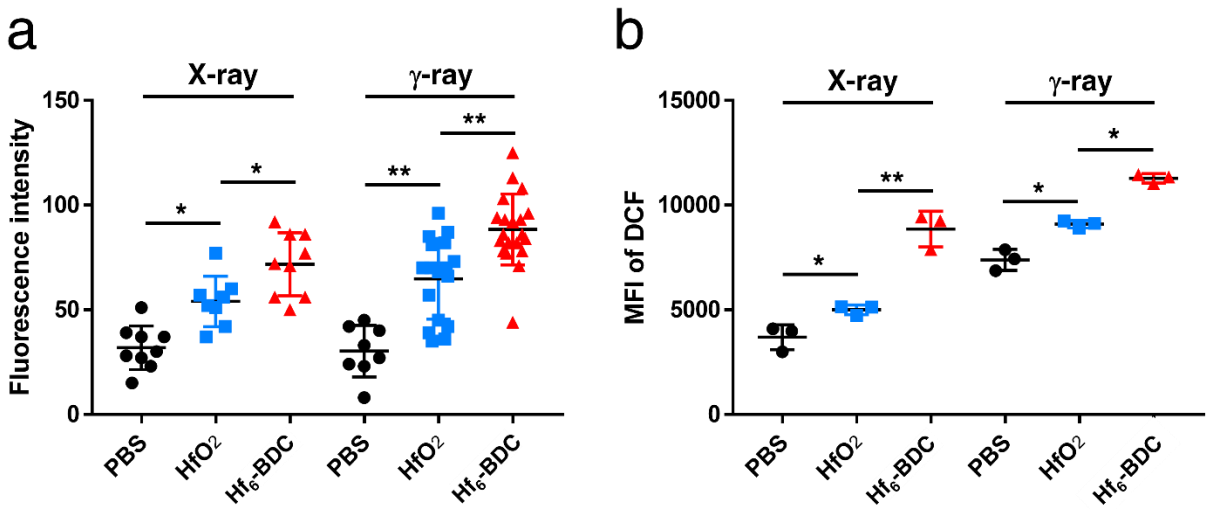

Figure 2-5. DCFH-DA assay showing total ROS inside cells treated with PBS, HfO_2 or Hf_6-BDC upon irradiation with 225 kVp X-ray or ^{60}Co γ-ray as quantified by (a) confocal imaging or (b) flow cytometry.

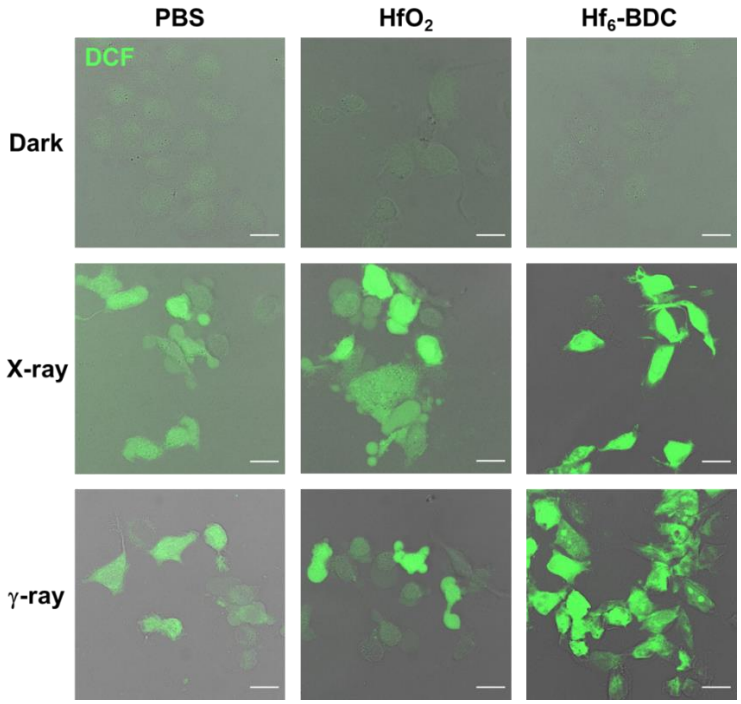

Figure 2-6. Confocal imaging of DCFH-DA assay showing total ROS detection in CT26 cells treated with PBS, HfO_2 or Hf_6-BDC and irradiated with X-ray or γ-ray at a dose of 4 Gy.

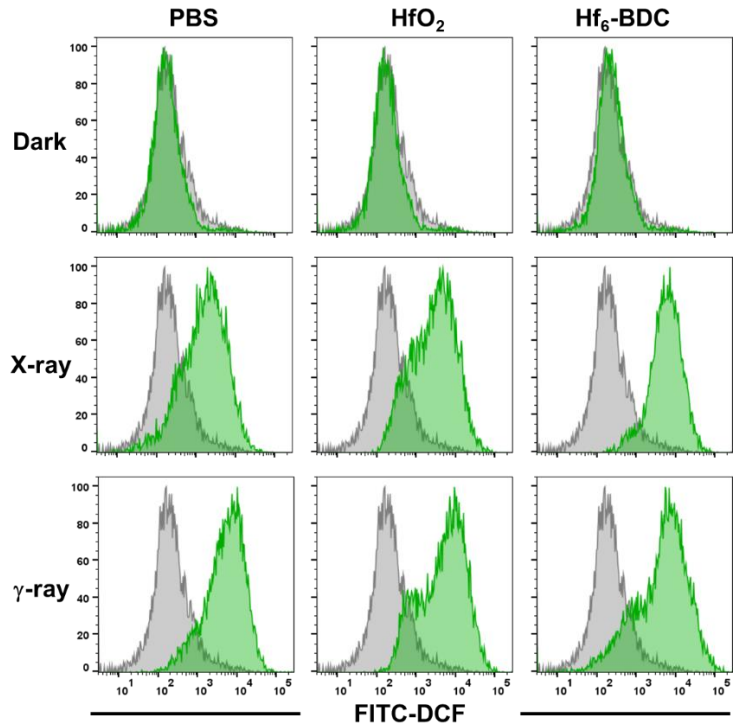

Figure 2-7. Flow cytometric analysis of DCFH-DA assay showing total ROS detection in CT26 cells treated with PBS, HfO_2 or Hf_6-BDC and irradiated with X-ray or γ-ray at a dose of 4 Gy. Grey histogram (control) and green histogram show the difference of DCF fluorescence in the cells. From left to right: PBS, HfO_2, and Hf_6-BDC.

DNA DSBs caused by direct ionization or ROS oxidation were then probed with phosphorylated H2A histone family member X (γ-H2AX), which plays a key role in DNA DSB repair. The results showed cells treated with Hf_6-BDC had significantly more fluorescence intensity and γ-H2AX foci per cell, as determined by CLSM and flow cytometry, respectively (**Figure 2-8**). For cells treated with PBS, HfO_2 or Hf_6-BDC and X-ray, the numbers of γ-H2AX foci per cell were 4.4 ± 1.1, 31.0 ± 8.0, or 41.0 ± 3.5, respectively, while for cells treated with PBS, HfO_2 or Hf_6-BDC and γ-ray, the numbers were 1.1 ± 1.0, 22.0 ± 4.4, or 39.6 ± 6.1, respectively (**Figure 2-9**). Flow cytometric analysis showed that γ-H2AX mean fluorescence intensity (MFI) was 587 ± 93, 3168 ± 455, or 10126 ± 765for cells treated with PBS, HfO_2 or Hf_6-BDC and X-ray, respectively, and 713 ± 15, 2655 ± 937, or 7770 ± 1156for cells treated with PBS, HfO_2 or Hf_6-BDC and γ-ray, respectively (**Figure 2-10**). These results indicate that Hf_6-DBC-mediated radiosensitization induces stronger DNA damage than HfO_2.

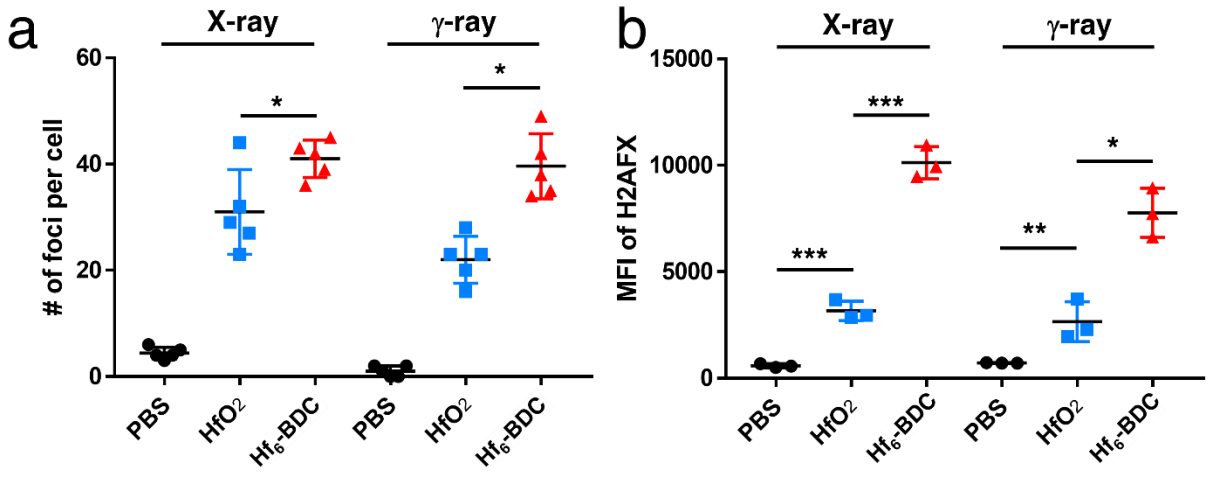

Figure 2-8. γ-H2AX assay showing DNA DSBs inside cells after treated with PBS, HfO_2 or Hf_6-BDC upon irradiation with 225 kVp X-ray or ^{60}Co γ-ray as quantified by (a) confocal imaging or (b) flow cytometry. MFI: mean fluorescence intensity.

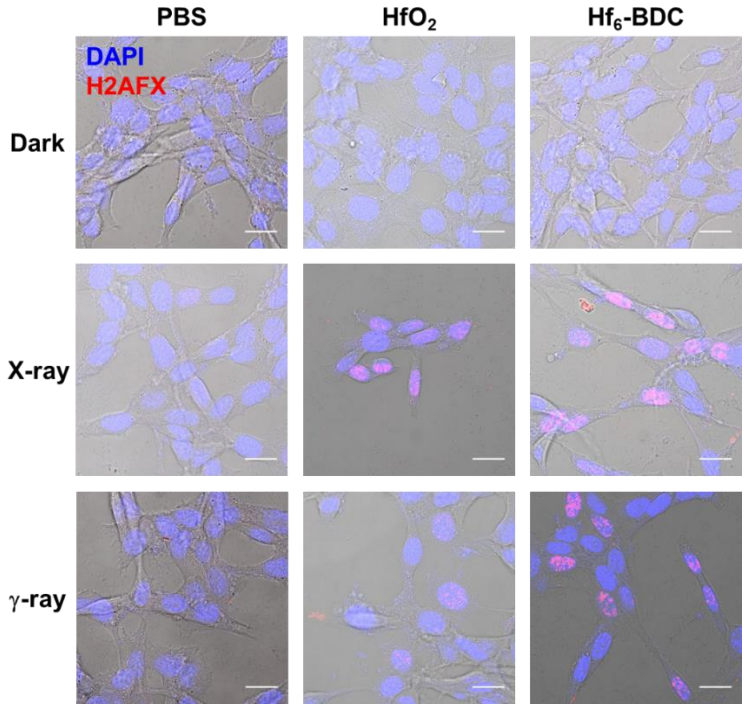

Figure 2-9. Confocal imaging of γ-H2AX expressions showing the DNA DSBs in CT26 cells treated with PBS, HfO_2 or Hf_6-BDC and irradiated with X-ray or γ-ray at a dose of 4 Gy. Blue and red fluorescence signals show DAPI-stained nucleus and antibody-labeled γ-H2AX in the cells, respectively. Scale bar = 10 μm.

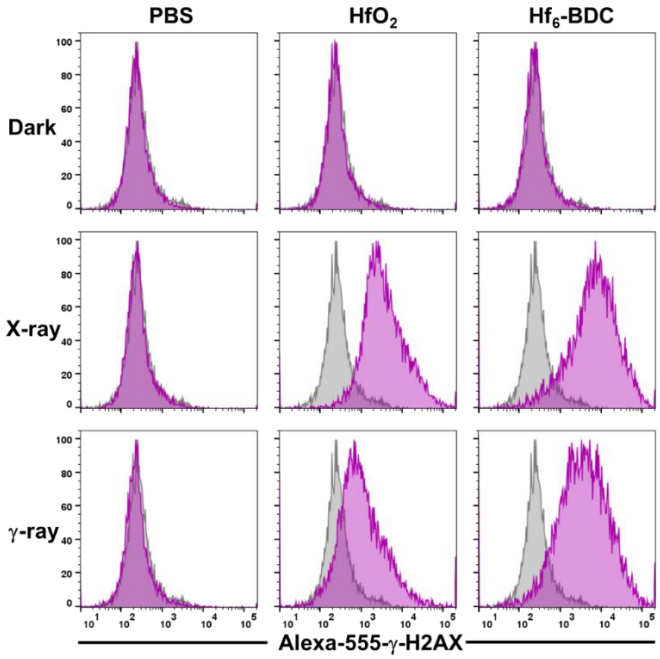

Figure 2-10. Flow cytometric analysis of γ-H2AX expressions showing the DNA DSBs in CT26 cells treated with PBS, HfO_2 or Hf_6-BDC and irradiated with X-ray or γ-ray at a dose of 4 Gy. Grey histogram (control) and magenta histogram show the difference of γ-H2AX levels in the cells. From left to right: PBS, HfO_2, and Hf_6-BDC.

2.2.2. Dependence of dose enhancement factors (DEFs) on radiation sources

We next carried out Monte Carlo (MC) simulations to compare the physical dose enhancements by nMOFs and HfO_2 NPs using EGSnrc, a code system that simulates coupled transport of electrons and photons in matters.[47] Geant4 simulation was also implemented to validate the major results from the EGSnrc simulation.[48-50] To improve computational efficiency while realistically representing the transport pathways of photons and electrons, MC simulations were performed in 2 steps following the reported procedures (**Figure 2-11**).[51] In the first step, a macroscopic simulation was conducted in a 20×20×20 cm^3 water phantom. Here, a parallel incident beam, with a cross-section of 20×20 cm^2, was introduced into the water phantom and transported to a macroscopic depth *d* in water. The phase space inside a central 10×10 cm^2 square, which contained numbers, energies and directions of motions of all particle types, was collected. In the second step, a microscopic simulation was performed in a 10×10×10 μm^3 water phantom. The as-generated phase space in the previous step was condensed with a cross-section of 4×4 μm^2 and used as a microscopic beam that had the same angular and energy distributions as the macroscopic one. A lattice or a NP was placed in the center of the phantom to interact with the microscopic beam transporting through the phantom. Here the lattice is a 3D hexagonal array of spheric SBUs, acting as a simplified model for nMOFs. The dose enhancement factor (DEF), defined as the energy deposited within a water shell around a lattice or a NP divided by the energy deposited in the same water shell around water, was used to compare their radiosensitizing properties.

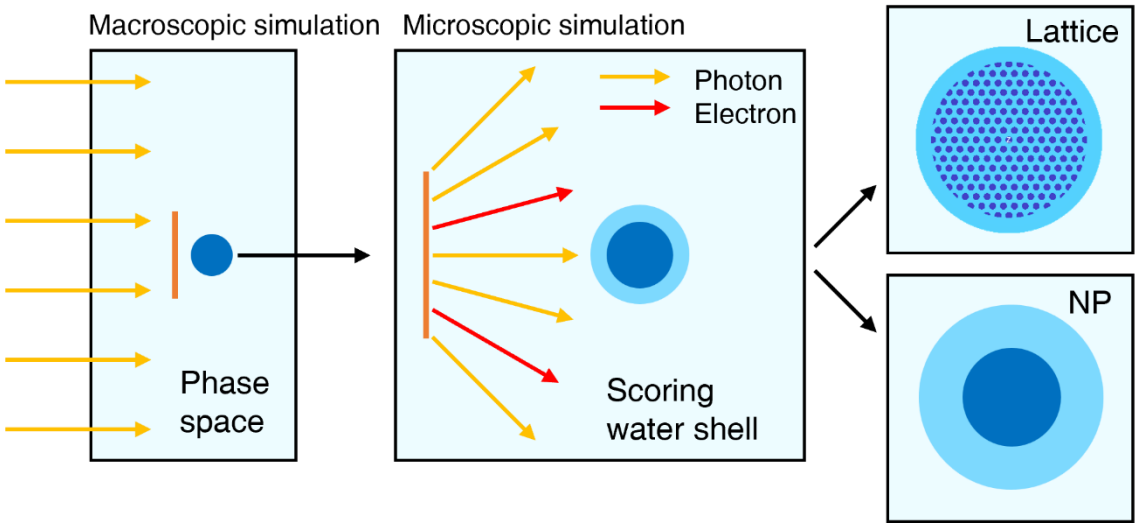

Figure 2-11. Schematic diagram of the macroscopic and microscopic simulation geometries for a lattice and a NP.

To ensure applicability of MC simulation results on nanoradiosensitizers, the geometry settings of lattices and NPs were based on Hf-based nMOFs[45] and HfO_2 nanoparticles,[33] respectively. Metal-oxo SBUs in nMOFs can be viewed as ultrasmall NPs that are connected by organic linkers to form lattices of different geometries.

The lattice was generated using the modified egs_lattice module[52] following the geometry of a hexagonal Hf_6-BDC nMOF with $Hf_6O_4(OH)_4$ SBUs and BDC linkers. Hf_6-BDC was modeled as a 3D spherical lattice with a diameter of 94 nm that was formed by linking spherical HfO_2 (r=0.44 nm) SBUs in a hexagonal manner. A single HfO_2 NP with a diameter of 50 nm was used for comparison. For megavoltage beams, the radii of the lattice and the NP were increased to 500 and 267 nm, respectively, to lower the uncertainty to less than 10% due to the small absorption cross-section of the NP. As there are the same number of Hf atoms in the lattice and the NP, the different doses deposited in water around the lattice or the NP must come from their physical (geometry) difference.

Since the dose enhancement effect comes from the photon-matter interactions, which are dependent on photon energy, we first investigated the dependence of DEFs on different radiation sources including monoenergetic 100 kV, orthovoltage 225 kVp (**Figure 2-12a**, generated by Spektr[53]), 6 MVp linear accelerator (LINAC, **Figure 2-12b**), and ^{60}Co γ-ray. For kilovoltage beams, we selected a macroscopic depth (*d*) of 1cm, whereas for megavoltage beams, which are primarily employed for treating deep-seated tumors in the clinic, we chose a macroscopic depth of 3 cm.

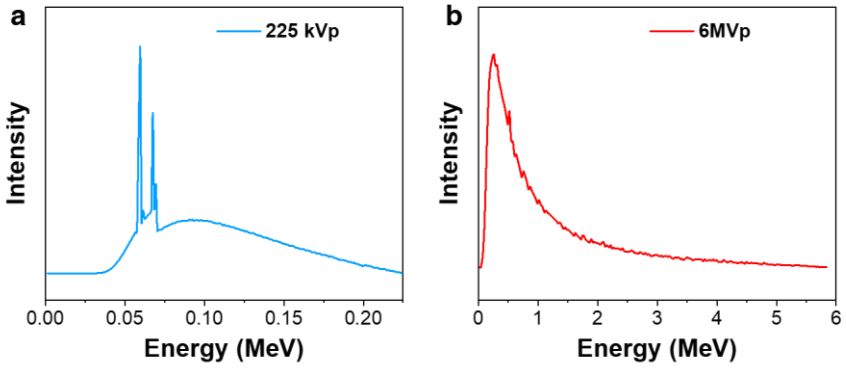

Figure 2-12. Spectrums of (a) 225 kVp and (b) 6 MVp photon source.

Irrespective of the radiation source employed, the DEF curves for lattices consistently exhibit higher values than those of NPs, showing that lattices outperform NPs in increasing the dose deposited in the surrounding water as far as 200 nm for 100 kV and 225 kVp X-rays, and 2.5 μm for 6MVp and ^{60}Co γ-rays (**Figure 2-13**). Specifically, in the case of 100 kV, the lattice exhibits a DEF of 6.75, while the NP demonstrates a DEF of 3.43 when the water shell radius is 47 nm, giving an enhancement of 1.97 for the lattice over the NP. Similarly, the dose enhancement of the lattice over the NP is 2.03 for 225 kVp. In contrast, for megavoltage beams, the dose enhancement from the NP is quite limited, with DEFs of 1.05 for 6 MVp LINAC and 1.20 for ^{60}Co γ-ray, while

the lattice significantly higher DEFs of 2.45 and 2.40, respectively, at a water radius of 500 nm, demonstrating the substantial dose deposited within the lattice.

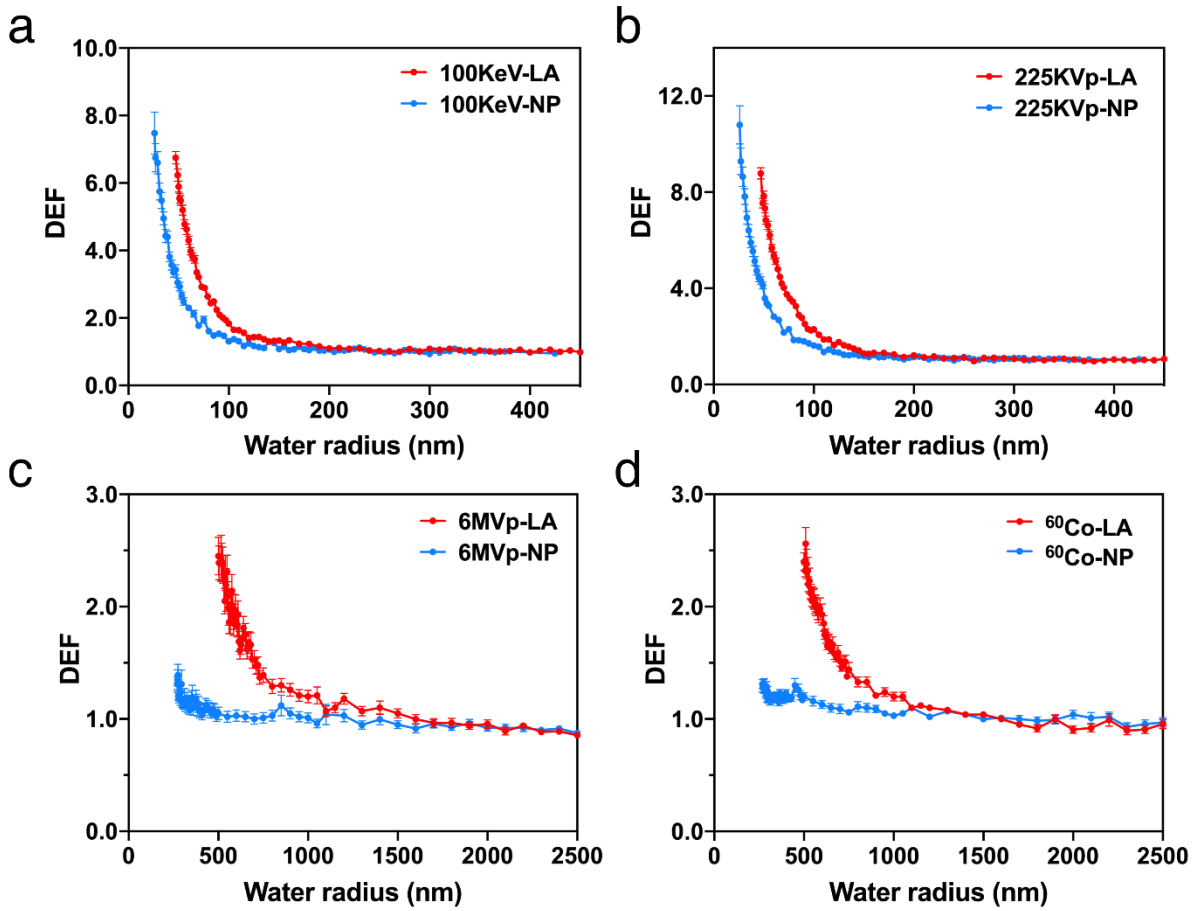

Figure 2-13. Dose enhancement factor (DEF) as a function of water shell radius for different phase space files as radiation sources. Phase space files were collected at depth of 1cm for (a) 100 kV, (b) 225 kVp while the radii of the LA and the NP were 47 and 25 nm, respectively. Phase space files were collected at depth of 3 cm for (c) 6MVp and (d) ^{60}Co while the radii of the lattice and the NP were 500 and 267 nm, respectively.

The Geant4 toolkit, widely employed for Monte Carlo simulations, was used to validate the results derived from EGSnrc simulations. To ensure a comprehensive assessment, we employed the Geant4 toolkit to compare the DEFs of lattices and NPs using identical radiation sources and geometry settings. As anticipated, the simulated DEFs and dose curves from the Geant4 simulation confirmed that lattices outperform NPs. Notably, the DEF ratios of lattices over NPs are consistent

between the two code systems (**Figure 2-14**). The consistency further strengthened the validity of our findings.

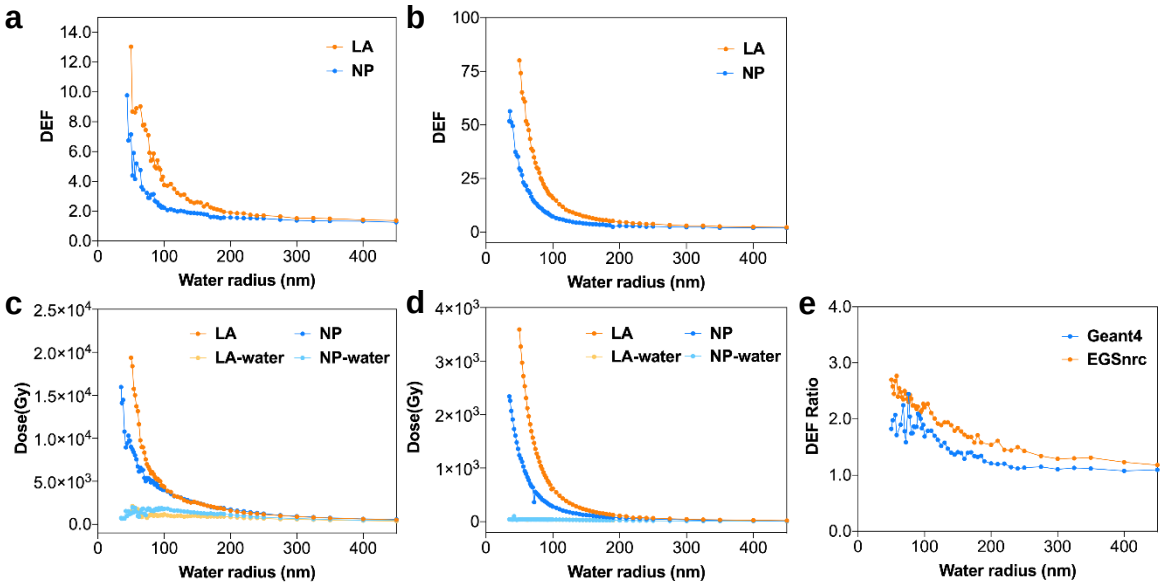

Figure 2-14. DEF curves of LAs and NPs obtained from (a) Geant4 and (b) EGSnrc codes. Dose curves of LA and NP obtained from (c) Geant4 and (d) EGSnrc codes. (e) Comparison of LA/NP DEF ratio. The lattice radius is 47 nm with an SBU radius of 2 nm and a lattice distance of 5.43 nm. The corresponding nanoparticle radius is 31 nm. The radiation source is phase space file of 225kVp source collected at 1 cm.

2.2.3. Dependence of DEFs on particle sizes

After entering a tumor cell, NPs are not as well dispersed as they are in cell media or buffers. In fact, they tend to form aggregates of microscopic sizes, e.g., by clustering in the endo/lysosomes (**Figure 2-15**).[41]

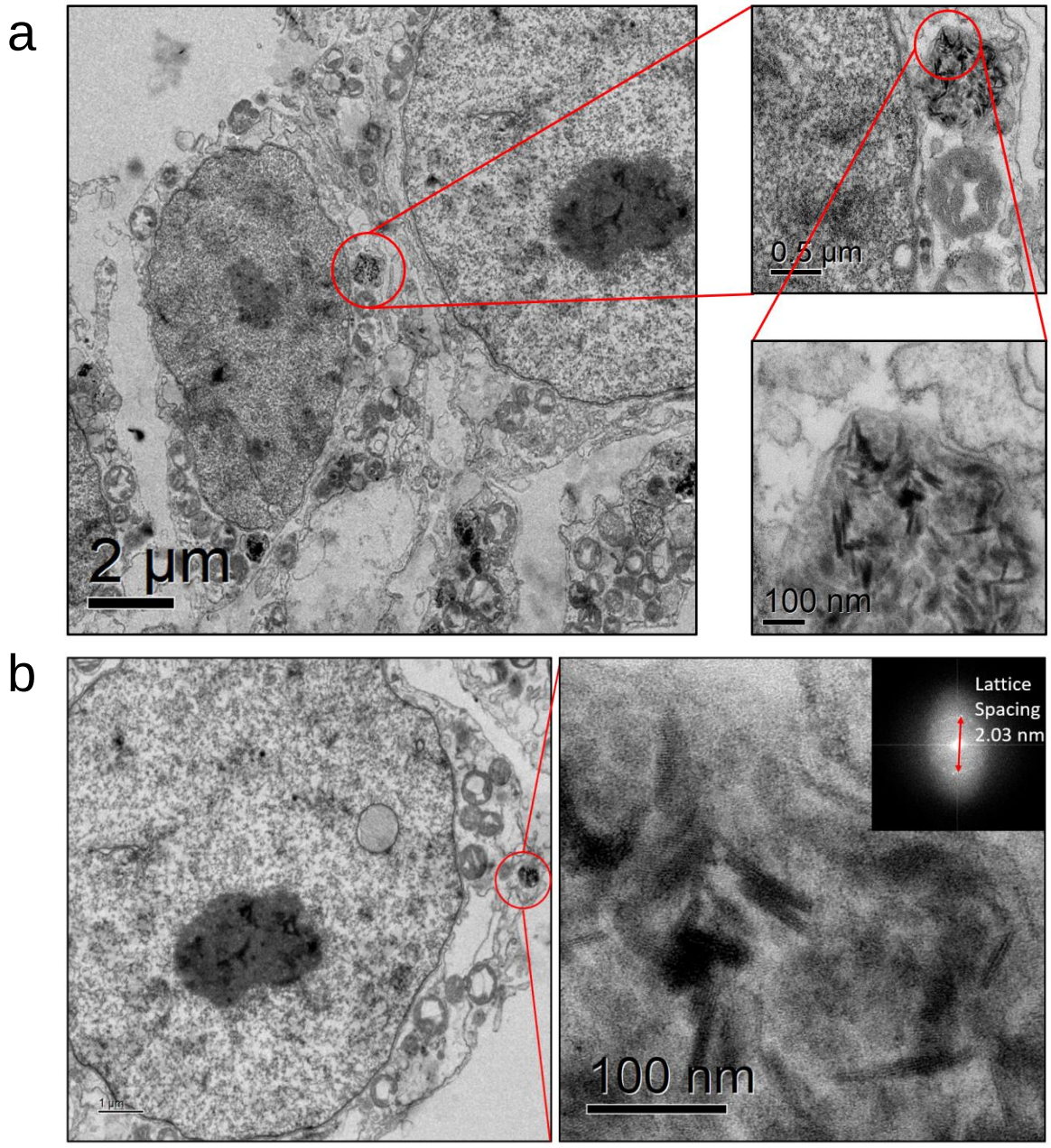

Figure 2-15. TEM images of Hf-DBP (H_2DBP= 5,15-di(p-benzoato)porphyrin) nMOFs in cells. (a) aggregated nMOFs, (b) crystalline nMOFs (inset: FFT of the image).

Assuming that the aggregate maintains the same density as the individual particle, we can then simplify the model by considering an aggregate as a lattice or a NP of a larger size. Therefore, we next investigated the impact of particle sizes on DEF for both lattices and NPs using 225 kVp

radiation (**Figure 2-16**). We obtained dose curves for various lattices or NPs and subsequently calculated corresponding DEFs (**Figure 2-17**).

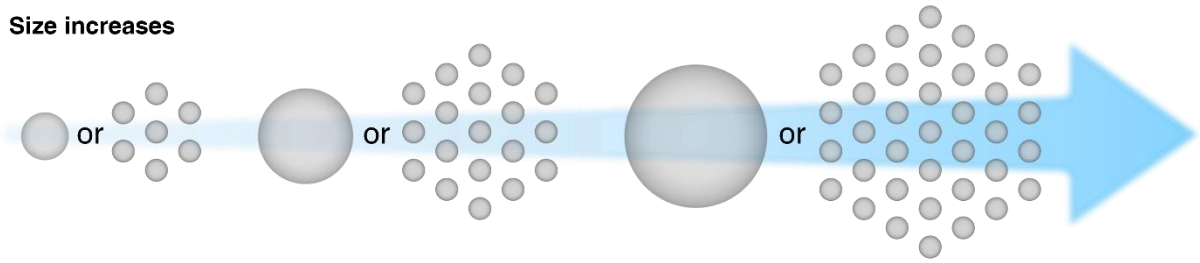

Figure 2-16. Schematic diagram of NPs and lattices of various sizes.

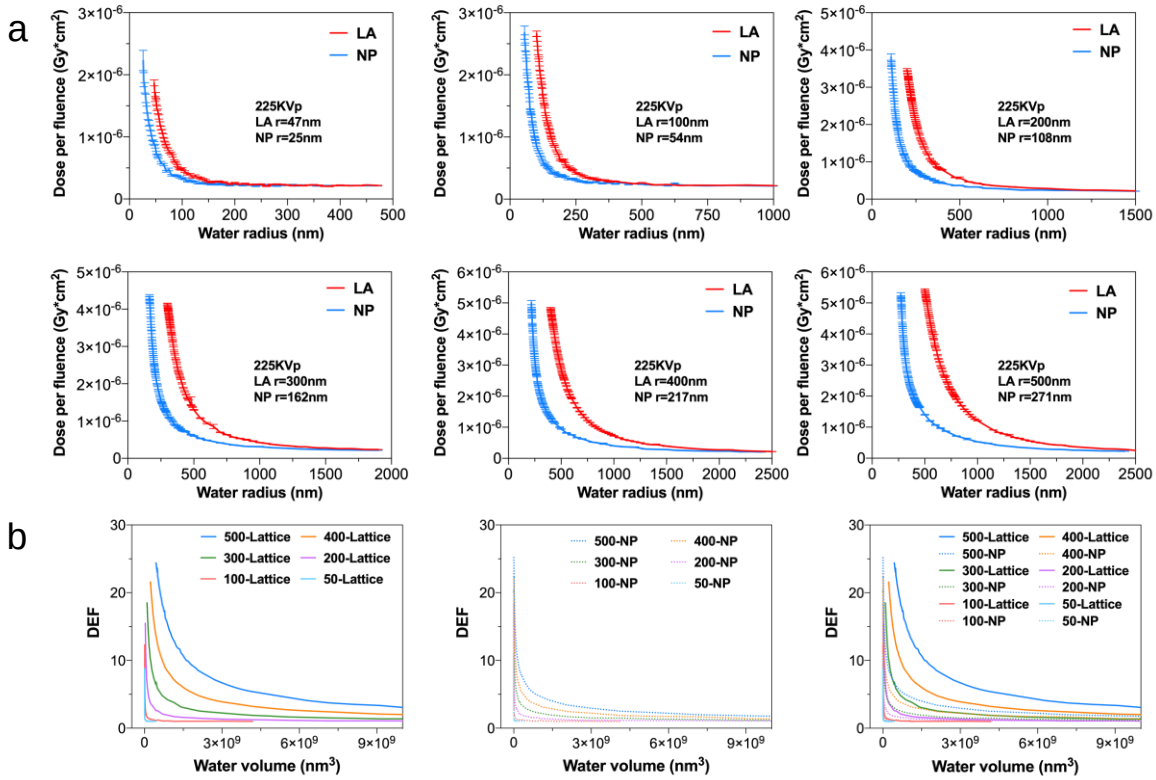

Figure 2-17. Dose curves of lattices and NPs of different sizes. (a) Dose curves of lattices or NPs of different radii. (b) Dose enhancement factor (DEF) as function of water volume with lattices (left) or NPs (middle) of different sizes and combined figure for comparison (right). 500-Lattice means a lattice with a radius of 500 nm while 500-NP means a NP with the same content of HfO_2 as the corresponding lattice.

Considering that the water volume within a sphere decreases as the particle size (HfO_2 volume) increases, we directly plotted the DEFs against the water volume included in the dose calculations (**Figure 2-18a**). The radiation source utilized here is a phase space file of a 225 kVp incident beam collected at a depth of 1cm. The term "500-Lattice" denotes a lattice with a radius of 500 nm, while "500-NP" denotes a nanoparticle with the same amount of HfO_2 as the 500nm-lattice. It is noteworthy that while both NPs and lattices exhibit increasing DEFs with particle size, the DEFs of lattices consistently exceed those of NPs irrespective of the size. To provide further insights, we plotted the DEFs in the same water volume of 4.44×10^8 nm^3 (equivalent to the entire water volume within the channels of a lattice with a radius of 500 nm) against the HfO_2 mass. Notably, the DEFs of both lattices and NPs increase linearly with HfO_2 mass while the slope for lattices is 3.17 times greater than that of NPs (**Figure 2-18b**). This finding demonstrates that particle clustering does not affect the advantage of lattices over NPs in terms of dose enhancement.

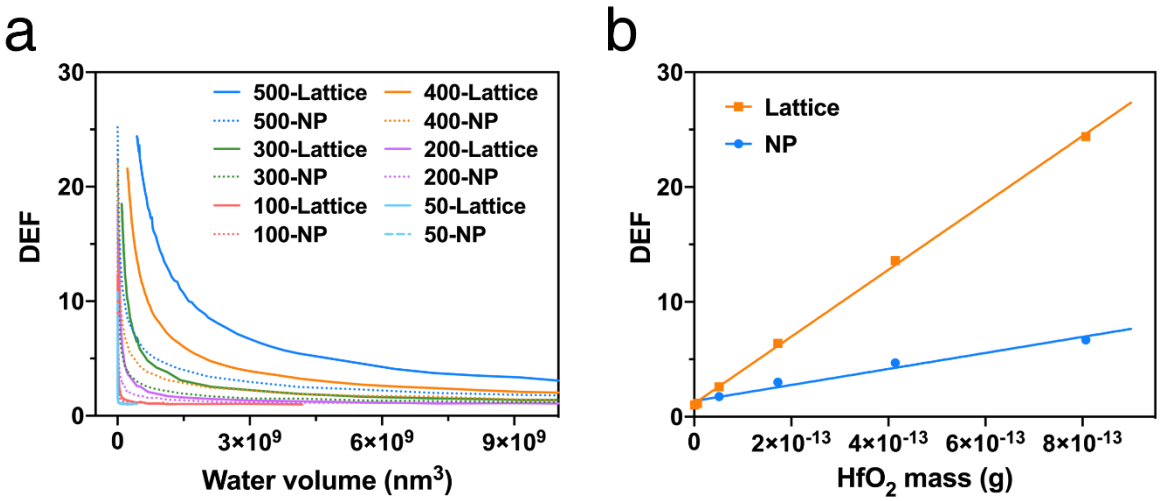

Figure 2-18. Dose dependence on size. (a) DEFs as a function of water volume for lattices (LAs) of different sizes. (b) DEFs as a function of HfO_2 mass in lattices and NPs.

2.2.4. Dependence of DEFs on heavy elements

To date, various heavy-metal NPs, including Au, Pt, Ag, Gd and Hf-based NPs, have been investigated as potential radiosensitizers.[54] In terms of photon-matter interactions, the mass attenuation coefficient (μ/ρ) is a crucial differentiating factor among these nanomaterials (**Figure 2-19**). Therefore, we studied the dependence of DEFs on the atomic number (*Z*) of heavy elements for both lattices and NPs using various radiation sources (100, 110, 120, 130, 150, 200 kV) and explored the relationship between DEFs and mass attenuation coefficients. For simplicity, Hf, Au, and Bi were chosen to examine the effects of heavy elements. The Hf lattice, with a diameter of 100 nm, was composed of 0.5 nm-sized Hf SBUs arranged at a lattice spacing of 1.5 nm, while Hf NP had a diameter of 56.5 nm. Similarly, the other lattice or NP geometries were constructed with an equal number of Au or Bi atoms (**Figure 2-20**). In addition, the number of heavy atoms in each SBU and the inter-SBU distance were kept the same for all lattices (**Table 2-1**).

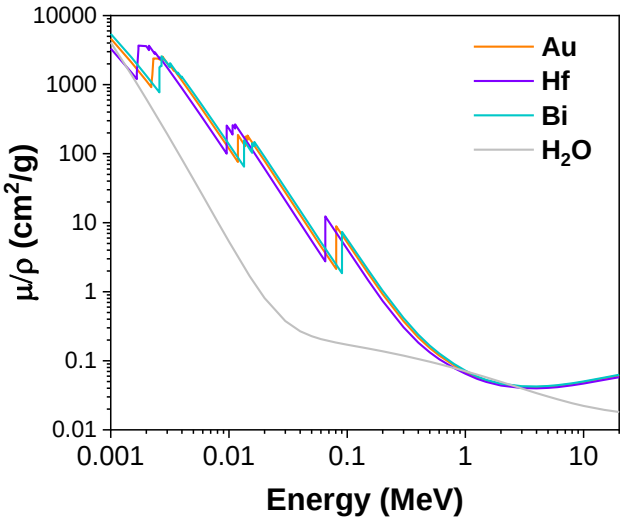

Figure 2-19. Mass attenuation coefficients of Hf, Au and Bi compared to water.[55]

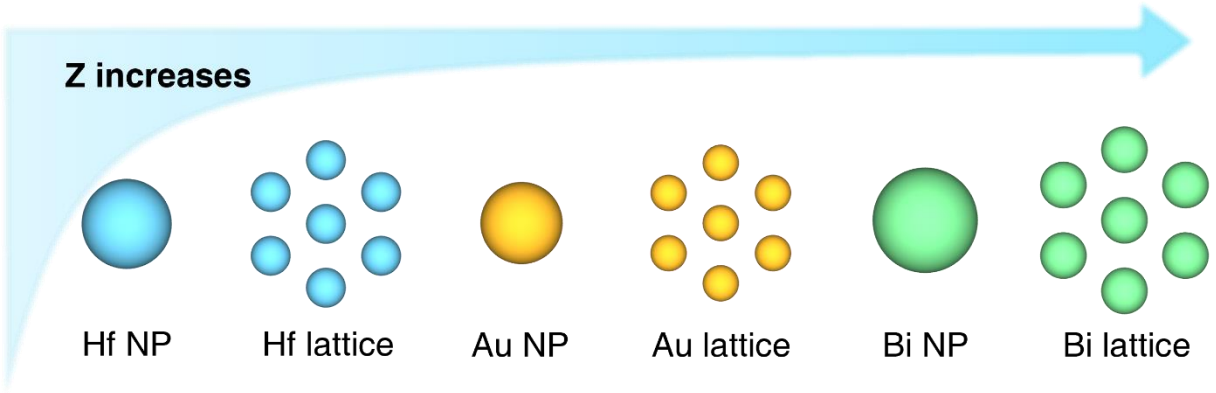

Figure 2-20. Schematic diagram of NPs and lattices of different materials.

Table 2-1: Geometry settings for lattices and nanoparticles of different materials.

	Parameters	**Hf**	**Au**	**Bi**
Lattice	SBU radius/nm	0.5	0.456	0.584
	Lattice distance/nm	1.6	1.512	1.768
	Lattice radius/nm	100	94.5	110.5
NP	NP Radius/nm	56.5	51.6	66.0
	Density/g·cm^{-3}	13.31	19.32	9.78
	K-edge (keV)	65.35	80.72	90.52

After obtaining dose curves for lattices and NPs composed of different materials (**Figure 2-21**), we proceeded to plot DEFs in the same water volume of 4.45×10^6 nm^3 against radiation energy (**Figure 2-22a**). Across all groups, DEF values consistently decrease as the energy increases. Notably, the DEFs for lattices consistently exceed those of corresponding NPs. In the case of NPs, the DEF value increases in the order of Hf, Au, and Bi, consistent with the increase in atomic number (*Z*). Furthermore, DEF value increases linearly as a function of mass attenuation coefficient. The relative slopes for Bi, Au, and Hf NPs are 1.255, 0.893 and 0.727, respectively,

while those for lattices are 2.695, 3.603 and 2.531, respectively (**Figure 2-22b**). These slopes for lattices are more than twice as large as those for corresponding NPs, demonstrating the advantages of lattices over NPs regardless of heavy elements.

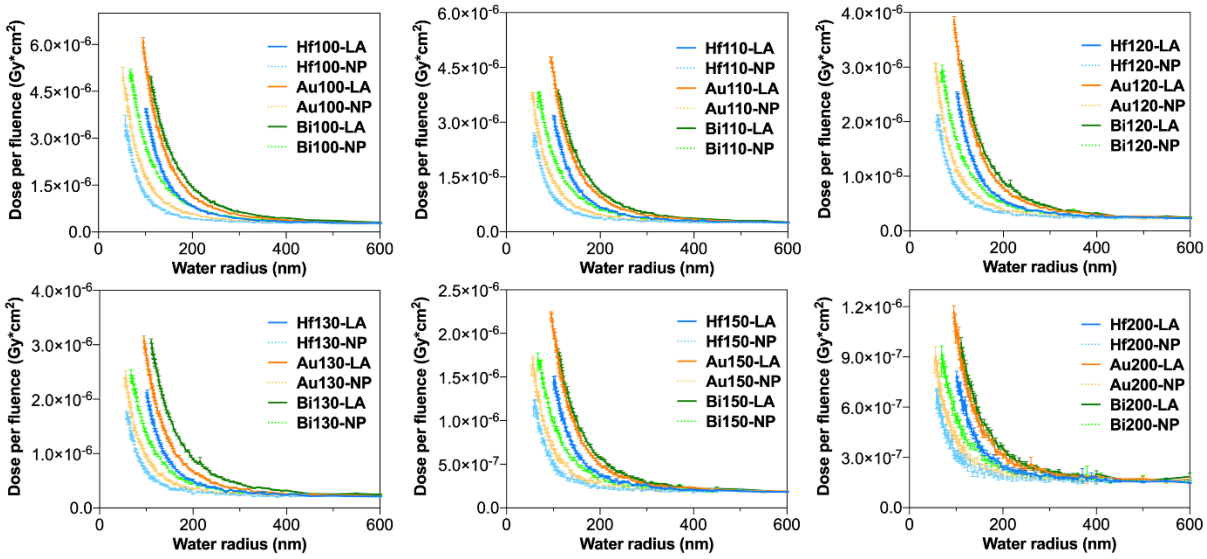

Figure 2-21. Dose curves of lattices or NPs of different particle materials.

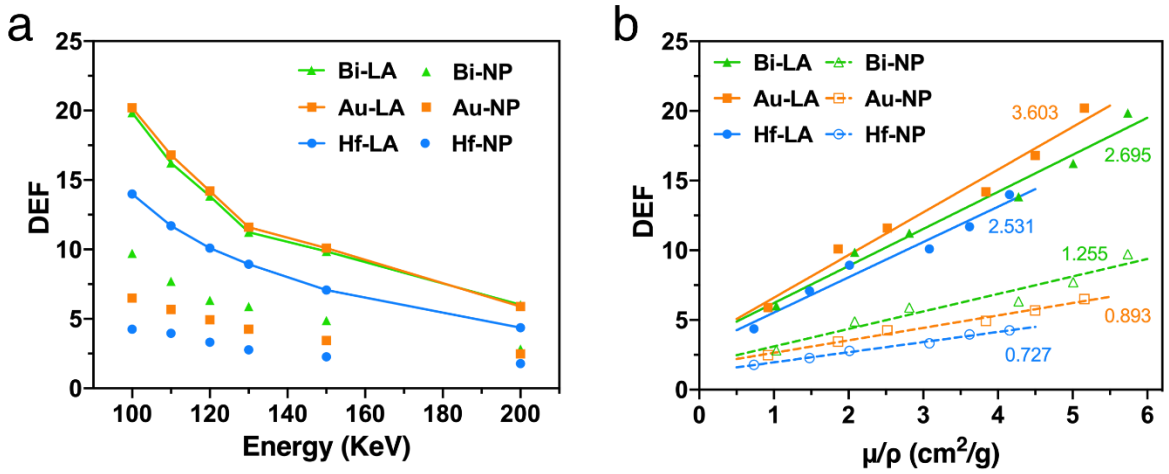

Figure 2-22. DEF dependence on beam energy and mass attenuation coefficient. DEFs as a function of (a) incident beam energy and (b) mass attenuation coefficient for lattices and NPs of Hf, Au and Bi. The numbers on the lines are the slopes.

2.2.5. Dependence of DEFs on lattice geometries

We then investigated the dependence of DEFs on lattice geometries, including SBU radii and inter-SBU distances (equivalent to ligand lengths in nMOFs) using 225 kVp radiation (**Figure 2-23**). Specifically, the radii of three SBUs are set to be 0.44, 0.56 and 1 nm, corresponding to $Hf_6O_4(OH)_4$, $Hf_{12}O_8(OH)_{14}$, and an imaginary large Hf-SBU, respectively, because several nMOFs based on $Hf_6O_4(OH)_4$ and $Hf_{12}O_8(OH)_{14}$ SBUs have been studied for their radiosensitizing properties.[42, 45] The inter-SBU distances are set to be 0.59, 1.02, 1.43, 1.85 nm, corresponding to four linear dicarboxylate ligands with phenyl (BDC), biphenyl (BPDC), terphenyl (TPDC), and quaterphenyl (QPDC) connectors, respectively. The as-constructed Hf-lattices were named based on their SBUs and linear dicarboxylate ligands, such as Hf_6-BDC and Hf_{1nm}-QPDC. As a base lattice, we utilized a HfO_2 lattice (R=500 nm) with 0.44 nm SBU and 0.59 nm inter-SBU distance. For all other lattices, we maintained the same number of Hf atoms (**Table 2-2**).

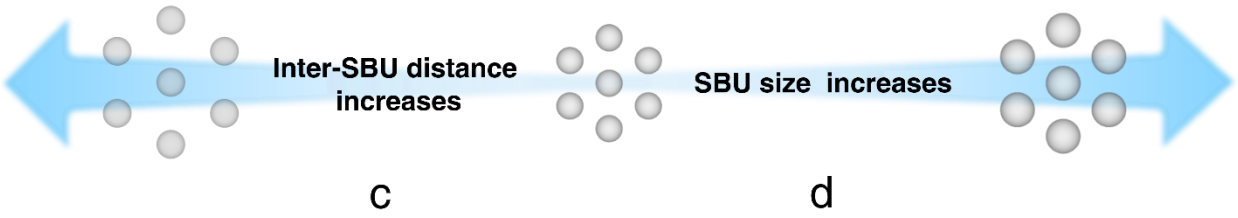

Figure 2-23. Schematic diagram of lattices with different inter-SBU distances (left) or SBU sizes (right).

Table 2-2: Geometry settings for lattices with different SBU radii and ligands.

Lattices	SBU radius [nm]	Lattice distance [nm]	Lattice radius [nm]
Hf_6-BDC	0.44	1.47	500
Hf_6-BPDC	0.44	1.90	646
Hf_6-TPDC	0.44	2.31	786
Hf_6-QPDC	0.44	2.73	929
Hf_{12}-QPDC	0.56	2.97	794
Hf_{1nm}-QPDC	1.00	3.85	577

First, we observed that all DEF curves for lattices consistently surpass those for NPs. Additionally, for the lattices with the same SBUs, shorter inter-SBU distance affords higher DEFs (**Figure 2-24**). We attribute this trend to dose contributions resulting from the bombardment of photons and electrons within the lattice. A shorter inter-SBU distance makes it harder for photons and electrons to escape from the lattice, thereby increasing their interactions with the SBUs and subsequent dose deposition.

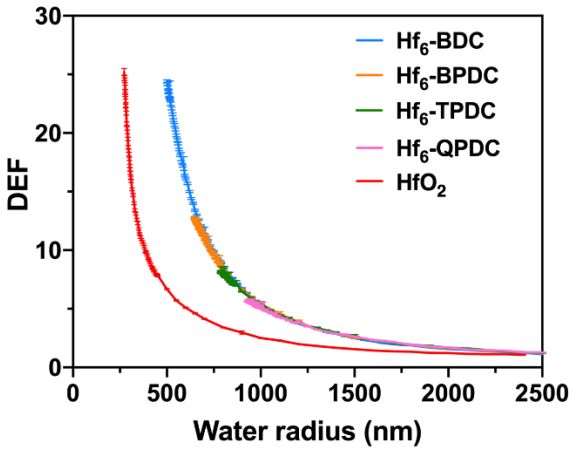

Figure 2-24. DEF dependence on inter-SBU distance. DEFs as a function of water shell radius with NPs or lattices (LAs) of different inter-SBU distances. The radiation source is a phase space file of 225 kVp incident beam collected at depth of 1cm. Hf_6, Hf_{12} and Hf_{1nm} represent $Hf_6O_4(OH)_4$ (r=0.44 nm), $Hf_{12}O_8(OH)_{14}$ (r=0.56 nm), and an imaginary Hf-SBU (r=1 nm), respectively. BDC, BPDC, TPDC, QPDC represent inter-SBU distances of 0.59 ,1.02, 1.43 and 1.85 nm, respectively.

To validate the simulation results, we synthesized Hf_6-BDC, Hf_6-BPDC and Hf_6-TPDC nMOFs with similar sizes to evaluate the influence of inter-SBU distance on the radiosensitizing effect (**Figure 2-25**). The Z-average sizes of Hf_6-BDC, Hf_6-BPDC and Hf_6-TPDC were determined by DLS to be 107± 1, 125± 1 and 173± 2 nm, respectively (**Figure 2-26**).

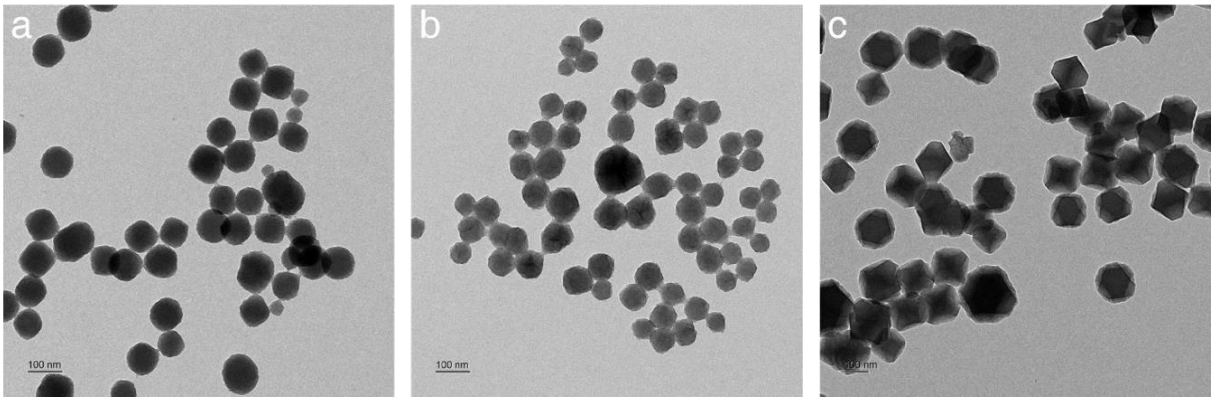

Figure 2-25. TEM images of (a) Hf_6-BDC, (b) Hf_6-BPDC and (c) Hf_6-TPDC nMOFs.

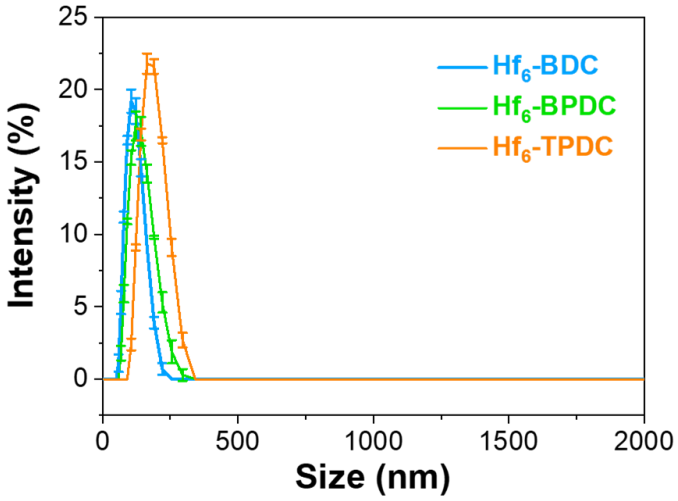

Figure 2-26. Size distributions of Hf_6-BDC, Hf_6-BPDC and Hf_6-TPDC nMOFs by dynamic light scattering, n=3.

The radioenhancement properties of nMOFs and NPs were first compared in solution via detection of total ROS using the DCFH-DA assay. HfO_2, Hf_6-BDC, Hf_6-BPDC, or Hf_6-TPDC

solution at an equivalent Hf concentration of 40 μM were mixed with 10 μM DCFH-DA separately and irradiated with 225 kVp-orthovoltage X-rays at doses of 0, 1, 2, 3, 5, or 10 Gy, followed by detection of DCF fluorescence. All experimental groups showed a linear increase of total ROS signal as a function of the X-ray dose. The relative enhancement of nMOFs or HfO_2 over H_2O was obtained by dividing the slope of each experimental group by that of the H_2O group. The enhancement factors were found to be 5.68, 32.5, 33.8 and 26.2 for HfO_2, Hf_6-BDC, Hf_6-BPDC and Hf_6-TPDC, respectively (**Figure 2-27**). These findings demonstrated the radiosensitization effect of Hf-nMOFs and HfO_2 as well as the advantage of Hf-nMOFs over HfO_2 in terms of ROS generation.

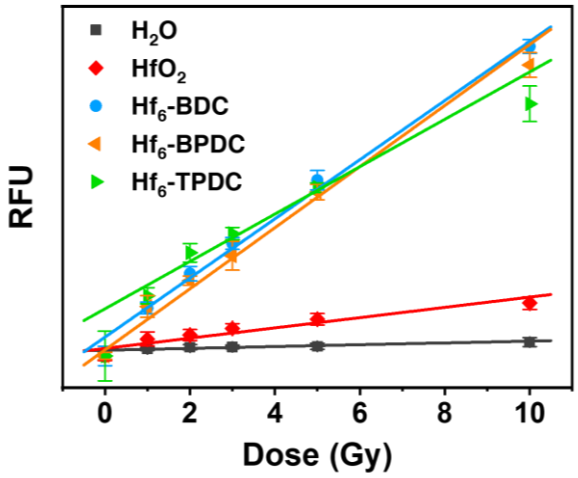

Figure 2-27. Enhanced DCF fluorescence of Hf-nMOFs over HfO_2 at equivalent Hf concentrations of 40 μM upon 225kVp X-ray irradiation, n=6.

The radioenhancement effect was further demonstrated *in vitro*. CT26 cells were firstly incubated with HfO_2, Hf_6-BDC, Hf_6-BPDC, or Hf_6-TPDC at an equivalent Hf concentration of 20 μM for 4 hours. The ells were then irradiated with 225 kVp-orthovoltage X-ray at different doses ranging from 0 to 8 Gy, followed by trypsinization, counting and re-seeding into culture dishes for colony assays. The $DMR_{10\%}$ values of Hf_6-BDC, Hf_6-BPDC, and Hf_6-TPDC were determined to

be 1.32, 1.31, 1.13, respectively, which showed a decreasing order with increasing lattice spacing (**Figure 2-28**). All three nMOFs displayed higher $DMR_{10\%}$ values than HfO_2 (1.03). However, the difference between three nMOFs was not as significant as observed in the simulated results, likely due to the complex biological effects involved, such as cellular uptake and particle aggregation.

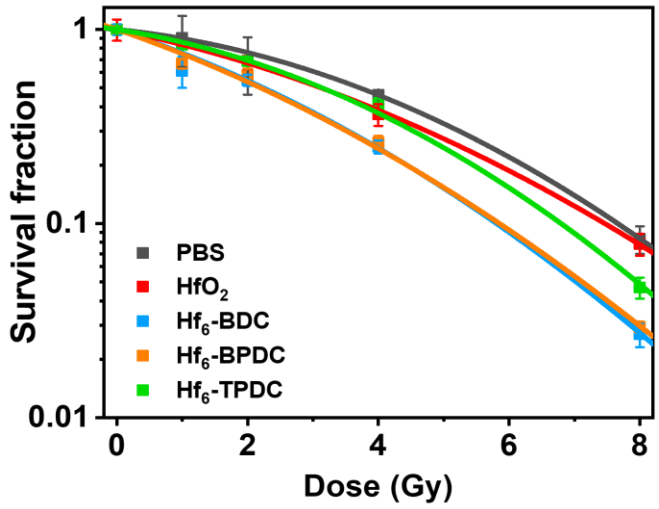

Figure 2-28. Survival curves of cells incubated with Hf-nMOFs, HfO_2, and PBS upon 225kVp X-ray irradiation.

For lattices with the same inter-SBU distance, we found that larger SBUs resulted in stronger dose enhancement from the comparison of 3 lattice geometries (**Figure 2-29**). This finding is consistent with the experimental data reported by Ni *et al.* which showed that Hf_{12}-based nMOFs are better radiosensitizers than Hf_6-based nMOFs.[45]

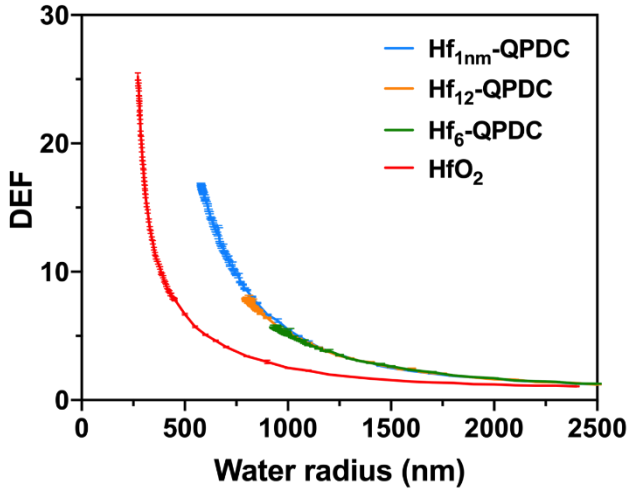

Figure 2-29. DEF dependence on SBU size. DEFs as a function of water shell radius with NPs or lattices (LAs) of different SBU sizes.

To gain further insights into the impacts of SBU size and inter-SBU distance on radiosensitization, we expanded the SBU radius up to 10 nm and calculated the DEFs at various water radii (**Table 2-3**).

Table 2-3: Geometry settings for lattices of different SBU radii.

SBU radius [nm]	Lattice distance [nm]	Lattice radius [nm]
0.44	1.47	500
0.56	1.71	457
0.70	1.99	426
0.85	2.29	403
1.00	2.59	388
1.50	3.59	358
2.00	4.59	344
3.50	7.59	325
5.00	10.59	317
7.50	15.59	311
10.0	20.59	308
Inter-SBU distance of 0.59 nm		

Table 2-3 continued

SBU radius [nm]	Lattice distance [nm]	Lattice radius [nm]
0.44	1.90	646
0.56	2.14	572
0.70	2.42	518
0.85	2.72	479
1.00	3.02	452
1.50	4.02	401
2.00	5.02	376
3.50	8.02	343
5.00	11.02	330
7.50	16.02	320
10.0	21.02	315
Inter-SBU distance of 1.02 nm		

SBU radius [nm]	Lattice distance [nm]	Lattice radius [nm]
0.44	2.31	786
0.56	2.55	682
0.70	2.83	605
0.85	3.13	551
1.00	3.43	513
1.50	4.43	442
2.00	5.43	406
3.50	8.43	361
5.00	11.43	342
7.50	16.43	328
10.0	21.43	321
Inter-SBU distance of 1.43 nm		

Table 2-3 continued

SBU radius [nm]	Lattice distance [nm]	Lattice radius [nm]
0.44	2.73	929
0.56	2.97	794
0.70	3.25	695
0.85	3.55	625
1.00	3.85	577
1.50	4.85	484
2.00	5.85	438
3.50	8.85	379
5.00	11.85	355
7.50	15.85	336
10.0	21.85	327
Inter-SBU distance of 1.85 nm		

When the SBU radius is 0.44 nm (as in Hf_6 SBU), the DEF within a 1000 nm water shell showed an inverse relationship with the inter-SBU distance (**Figure 2-30a & 2-31**). However, as the SBU radius increases to 0.70 nm, a peak in the DEF vs. inter-SBU distance curve emerges at an inter-SBU distance of 1.02 nm, suggesting an optimal inter-SBU distance that maximizes the dose enhancement for a given SBU size. For SBU radius larger than 0.85 nm, a positive correlation between DEF and inter-SBU distance becomes more apparent. The DEF vs inter-SBU distance curves exhibit a volcano shape, with the peak point shifting to higher inter-SBU distances as the SBU size increases. A similar volcano shape was observed in the DEF vs SBU radius curves, with the peak point shifting to larger SBU sizes as the inter-SBU distance increases (**Figure 2-30b & 2-32**).

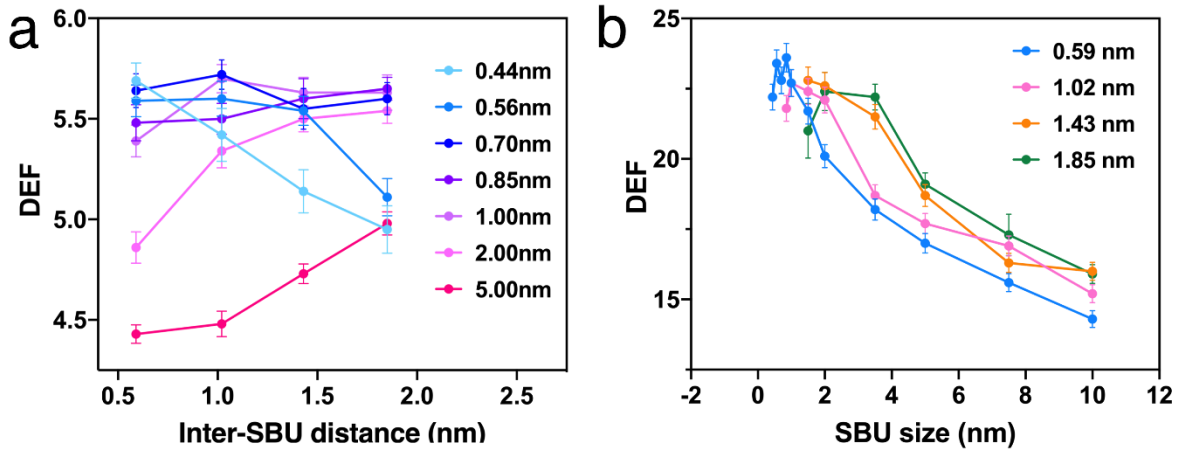

Figure 2-30. Volcano curve. DEFs as a function of (a) inter-SBU distance or (b) SBU radius. The water shell radii for DEF calculations are 1000 and 500 nm, respectively.

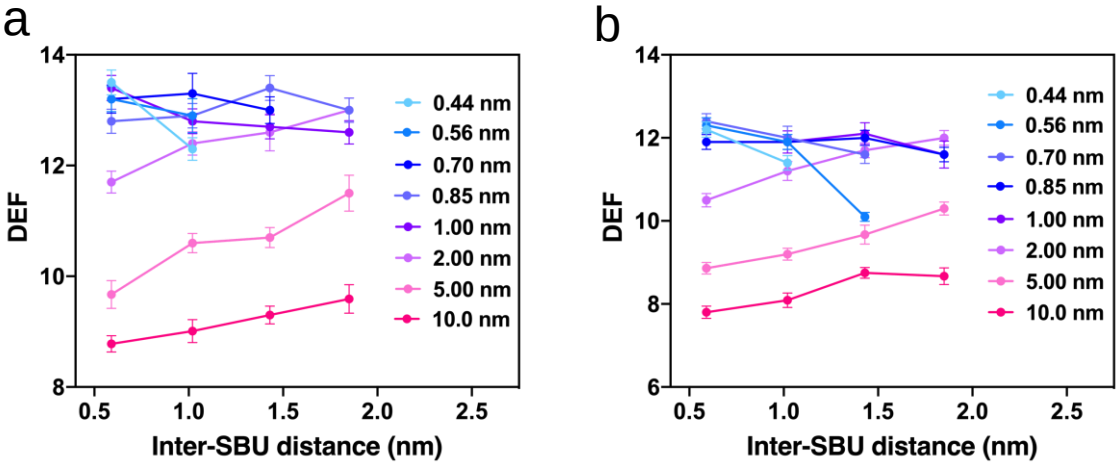

Figure 2-31. DEFs as a function of inter-SBU distances. The water shell radius is (a) 650 nm or (b) 682 nm.

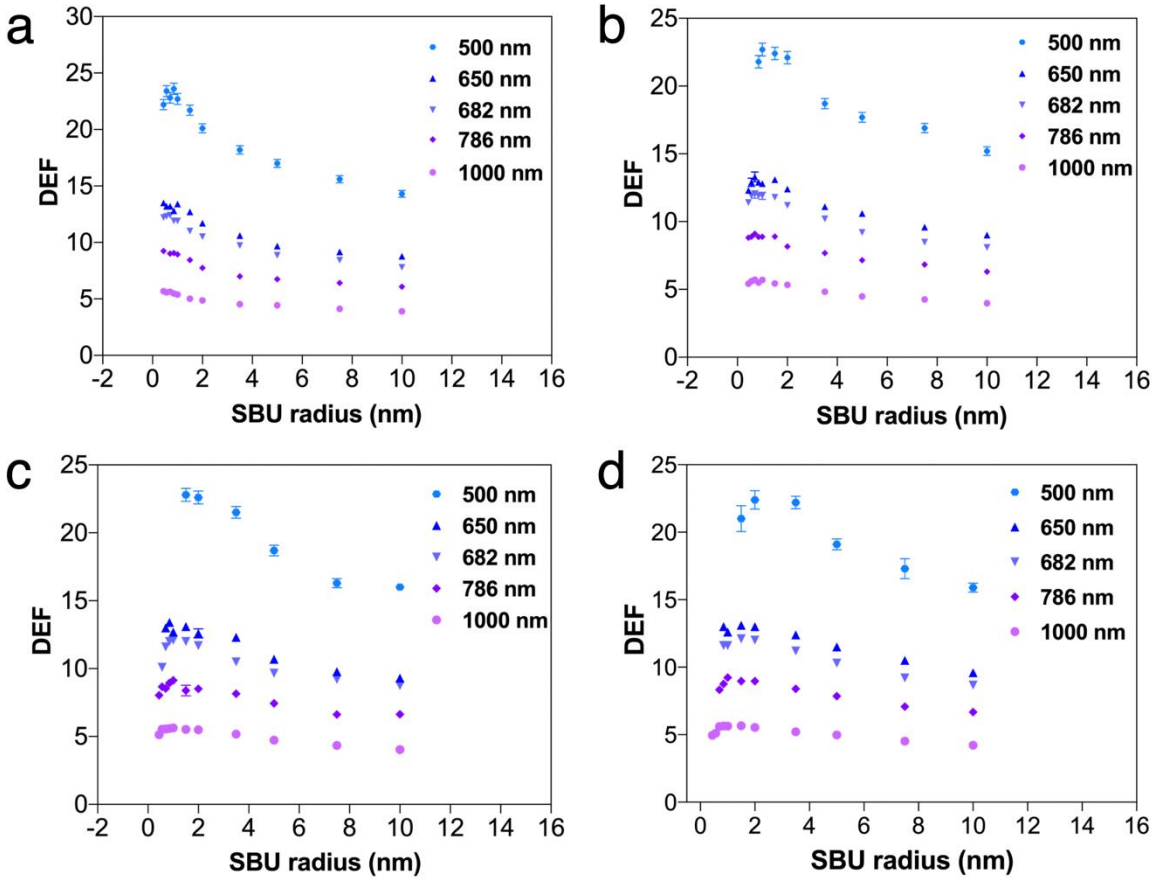

Figure 2-32. DEFs as a function of SBU radii at different water shell. The inter-SBU distance was set to be (a) 0.59 nm, (b) 1.02 nm, (c) 1.43 nm, (d) 1.85 nm.

2.2.6. Proposed mechanism for the radiosensitization enhancement of lattices over NPs

Based on the above results, we propose a two-step radiosensitization mechanism for lattices (**Figure 2-31**). First, each SBU within the lattice functions as a small NP to interact with incident photons and emits photons and electrons outward, which either deposit their energy directly in the surrounding water or in neighboring SBUs. In this step, with a fixed amount of radiosensitizing materials, the volume percentage of water over HfO_2 inside the lattice (F_{water}), which is presented by inter-SBU distance (D_{SBU}) and SBU radius (r), will determine the energy deposition in water as shown by equation 1-4. A small SBU radius and a large inter-SBU distance lead to an increase in the radiation dose.

$$F_{water} = \frac{V_{water}}{V_{HfO_2}} = 0.1688 \times (\frac{D_{SBU}}{r} + 2)^3 - 1 \qquad (1\text{-}4)$$

Second, some photons and electrons emitted from the central SBU are ejected to adjacent SBUs as secondary radiations. These photons and electrons bounce between neighboring SBUs before eventually losing all of their energy. This process greatly increases the dose deposited in the channels of the lattice.

The probability of neighboring SBUs capturing these secondary photons and electrons from the central SBU is proportional to the ratio of the occupied area by the neighboring SBUs (S_{SBU}) to the total surface area of a sphere (S_L) with a radius of lattice distance (L), sum of the inter-SBU distance (D_{SBU}) and twice the radius of the SBU (r). For UiO-type nMOFs, each SBU is surrounded by twelve SBUs.[56] The occupation ratio (R_{SBU}) can be described by equation 1-5.

$$R_{SBU} = \frac{S_{SBU}}{S_L} = \frac{12\pi r^2}{4\pi L^2} = \frac{3}{\left(2+\frac{D_{SBU}}{r}\right)^2} \qquad (1\text{-}5)$$

In this step, a larger SBU has a higher radiation dose as its large cross section enables it to capture more electron and photon from neighboring SBUs. Considering both steps, there would be an optimal SBU size for maximum interaction with both incident photons and secondary photons and electrons emitted from adjacent SBUs. In terms of inter-SBU distances, a larger distance is preferred in step 1 while a shorter one is preferred in step 2. As a result, a similar volcano curve is observed.

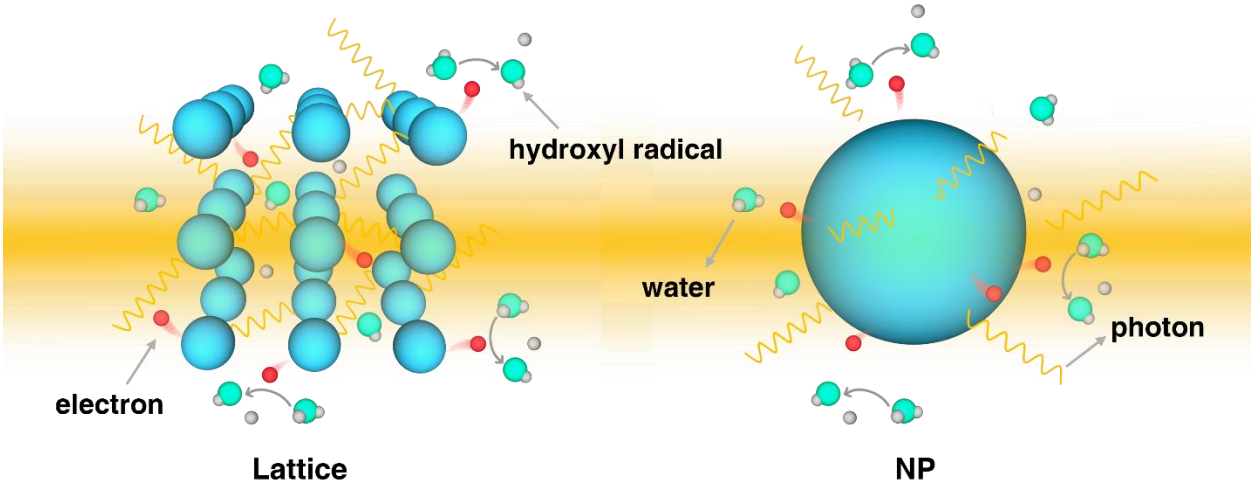

Figure 2-33. Radiation-induced reactions on a lattice (left) and a NP (right).

To gain a deeper insight into the proposed mechanism, the numbers of electron or photon collisions, which represent steps made by physical interactions, were scored using the Geant4 primitive scorers. While the numbers of photon collisions are comparable for lattices and NPs, lattices exhibit significantly higher numbers of electron collisions than NPs (**Figure 2-34**). Particularly, the ratio between the number of electron collisions in lattices over that in NPs shows the same trend as the corresponding DEF ratio. Therefore, the radiosensitization enhancement of lattices over NPs mainly comes from the enhanced electron collisions due to scattering and bouncing of electrons between SBUs.

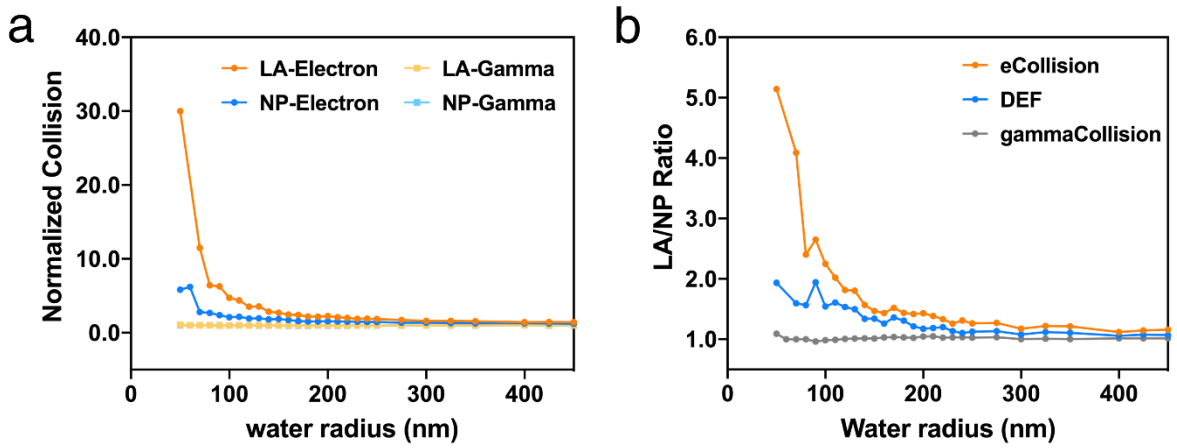

Figure 2-34. Electron and photon collisions. (a) Normalized collision of electrons and photons in a lattice or a NP and (b) their ratios in comparison with DEF ratios.

2.3 Conclusions

Our Monte Carlo simulation results revealed that lattices consisting of 3D arrays of SBUs are superior radiosensitizers over nonporous NPs in terms of physical dose enhancement regardless of radiation source and size. For both lattices and NPs, materials with larger mass attenuation coefficients exhibit stronger radiosensitizing effects. In terms of lattice geometry, the relationship between DEF and SBU size or inter-SBU distance follows a volcano-shaped curve. Since the lattices are built based on a simplified model of nMOFs, these simulation results confirm the advantages of nMOFs over NPs as radiosensitizers and reveal the general principle of designing optimal nMOFs for radiotherapy.

2.4. Methods

Monte Carlo Simulation Settings. MC simulations were performed in two steps following reported procedures using the EGSnrc code.[51] The egs_chamber module was used for dose calculation in the microscopic simulation, and the energy cuts for both photons and electrons were 1 keV to 50MeV, respectively. The egs_lattice module was modified and used to generate the

lattice geometry.[52] The vectors for populating subgeometries were modified as the following to simulate a hexagonal close-packed (hcp) lattice.

$$\overrightarrow{r_1}(i,j,k) = \quad i\,a\hat{x} \quad + \quad j\sqrt{3}\hat{y} \quad + \quad k\frac{2\sqrt{6}}{3}\hat{z}$$

$$\overrightarrow{r_2}(i,j,k) = \left(i+\frac{1}{2}\right)a\hat{x} \quad + \quad \left(j+\frac{1}{2}\right)\sqrt{3}\hat{y} \quad + \quad k\frac{2\sqrt{6}}{3}\hat{z}$$

$$\overrightarrow{r_3}(i,j,k) = \quad i\,a\hat{x} \quad + \quad \left(j+\frac{1}{3}\right)\sqrt{3}\hat{y} \quad + \quad (k+\frac{1}{2})\frac{2\sqrt{6}}{3}\hat{z}$$

$$\overrightarrow{r_4}(i,j,k) = \left(i+\frac{1}{2}\right)a\hat{x} \quad + \quad \left(j-\frac{1}{6}\right)\sqrt{3}\hat{y} \quad + \quad (k+\frac{1}{2})\frac{2\sqrt{6}}{3}\hat{z}$$

Geant4 simulations were implemented with the 10.7 version of the toolkit to validate the major results from the EGSnrc. The Geant4 standard electromagnetic physics package that describes electron and photon interactions between ~1 keV and 100 TeV was used in all simulations.[57] The energy cut was set according to the EGSnrc codes. The hexagonal lattice was generated with the same vectors. Since statistical uncertainty increases with the micro-beam size[1], the phase space was further condensed (200×200 nm^2) to reduce the uncertainty and used in both codes for comparison. For mechanistic studies, the numbers of electron and photon collisions, which represent steps made by physics interactions, were scored using the Geant4 primitive scorers.

Synthesis of Hf_6-BDC, Hf_6-BPDC and Hf_6-TPDC nMOFs. Smaller Hf-BDC nMOFs were synthesized following reported procedures.[46] For larger Hf-BDC nMOFs, 3.8 mg $HfCl_4$, 2 mg terephthalic acid (H_2BDC), 40 μL acetic acid and 1 mL DMF were mixed in a 1-dram vial and heated at 120 °C for 1 day. For Hf_6-BPDC nMOFs, 1 mg $HfCl_4$ and 0.8 mg [1,1'-biphenyl]-4,4'-dicarboxylic acid (H_2BPDC), 1 mL DMF and 1 μL trifluoroacetic acid (TFA) were mixed in a 1-dram vial and heated at 70 °C for 2 days. Hf_6-TPDC nMOFs were also synthesized based on reported procedures[45] except that 2,5-di(p-benzoato)aniline was replaced with [1,1':4',1"-

terphenyl]-4,4"- dicarboxylic acid of same mass. All nMOF were washed sequentially with DMF, 1% triethylamine in ethanol (v/v), and ethanol before finally being suspended in ethanol.

Cellular uptake. The cellular uptake of HfO_2 and UiO-66 was evaluated on CT26 cells. Murine colon adenocarcinoma cell, CT26 was purchased from the American Type Culture Collection (ATCC, USA). CT26 cells were cultured in Roswell Park Memorial Institute (RPMI) 1640 medium (GE Healthcare, USA) supplemented with 10% fetal bovine serum (FBS, VWR, USA). Mycoplasma was tested before use by MycoAlert detection kit (Lonza Nottingham, Ltd.). Cells were seeded on 6-well plate at 1.5×10^6/well and further cultured overnight. Particles were added to the cells at an Hf concentration of 40 μM. After incubation of 1, 2, 4 or 8 hours, the cells were collected, and the cell numbers were counted by a hemocytometer. Cells were digested with 1% hydrofluoric acid and concentrated nitric acid in a microwave reactor (CEM, USA) and the Hf concentrations were determined by ICP-MS (Agilent, USA). Results were expressed as the amount of Hf (ng) per 10^5 cells.

Clonogenic assay. CT26 cells were cultured in a 6-well plate overnight and incubated with particles at a Hf concentration of 40 μM for 4 h followed by X-ray or γ-ray irradiation with 0, 1, 2, 4, 8 and 16 Gy. The irradiated cells were trypsinized and counted immediately. 200-2000 cells were seeded in a 6-well plate and cultured with 2 mL medium for 12 days to form visible colonies, which were counted to determine the survival fraction. Once colony formation was observed, the culture medium was discarded. The plates were rinsed twice with PBS, then stained with 500 μL of 0.5% w/v crystal violet in 50% methanol/H_2O. The wells were rinsed with water three times and the colonies were counted manually. The radiation enhancement factor at 10% survival dose ($DMR_{10\%}$) was calculated as the ratio of equivalent irradiation doses needed to give 10% survival rate for the PBS control group over that for the experimental group.

Total ROS detection. Total ROS was detected by DCFH-DA assay. CT26 cells were cultured in a 6-well plate at 5×10^5/well overnight and incubated with PBS or nanoradiosensitizers at an equivalent concentration of 40 μM followed by irradiation at 0 and 4 Gy. Cells were then stained 2 h after irradiation with DCFH-DA (Thermo Fisher, USA) at a concentration of 10 μM for CLSM imaging and flow cytometric analysis.

DNA double strand breaks. The DNA double strand breaks were detected by probing phosphorylated γ-H2AX. CT26 cells were cultured in a 6-well plate at 5×10^5/well overnight and incubated with PBS or nanoradiosensitizers at an equivalent concentration of 40 μM followed by irradiation at 0 and 4 Gy. Cells were stained 2 h after irradiation with the HCS DNA damage kit (Life Technology, USA) with 1:500 dilution for confocal laser scanning microscope (CLSM, FV1000, Olympus, Japan) imaging and LSRFortessa 4-15 flow cytometric analysis (BD, USA).

Spectra simulation of 225 kVp photon source. The spectra of X-ray at 225 kVp with a 0.3 mm Cu filter was simulated using reported tungsten anode spectral model using interpolating cubic splines (TASMICS).[53]

Cell EM. CT26 cells were treated with Hf-DBP (H_2DBP= 5,15-di(p-benzoato)porphyrin)[58] nMOFs at a dose of 40 μM Hf for 24 h. Cells were then collected and fixed with OsO_4 staining solution for observation under Tecnai Spirit TEM.

Derivation of Equation 1-4. The total volume of a hexagonal close packed (hcp) lattice unit cell is defined as

$$V = \sqrt{2} \times (2r + D_{SBU})^3$$

where r is the SBU radius and D_{SBU} is the inter-SBU distance. One hcp lattice unit cell has two SBUs and thus the volumes of SBU and adjacent water are

$$V_{SBU} = 2 \times \frac{4}{3}\pi \times r^3 = \frac{8}{3}\pi r^3$$

$$V_{water} = V - V_{SBU}$$

Finally, the ratio of water volume inside the lattice to SBU volume is presented as the following

$$F_{water} = \frac{V_{water}}{V_{SBU}} = 0.1688 \times (\frac{D_{SBU}}{r} + 2)^3 - 1$$

Derivation of Equation 1-5. The probability for neighboring SBUs to capture secondary photons and electrons from the central SBU is proportional to the ratio of occupied area by neighboring SBUs (S_{SBU}) out of the total surface area of a sphere (S_L) with a radius of lattice distance (L), sum of the inter-SBU distance (D_{SBU}) and the radius of SBU (r).

In a hcp lattice, each SBU is surrounded by twelve SBUs. Thus, the intersected area by the neighboring SBUs can be approximated as the sum of areas of circles with radii of r

$$S_{SBU} = 12\pi r^2$$

The total surface area with a radius of lattice distance ($L = D_{SBU} + 2r$) is

$$S_L = 4\pi \times (2r + D_{SBU})^2$$

Finally, by integrating the two equations, the occupation ratio (R_{SBU}) can be derived as

$$R_{SBU} = \frac{S_{SBU}}{S_L} = \frac{12r^2}{4(2r + D_{SBU})^2} = \frac{3}{(2 + \frac{D_{SBU}}{r})^2}$$

2.5. References

(1) Delaney, G. P.; Barton, M. B., Evidence-based estimates of the demand for radiotherapy. *Clin. Oncol.* **2015,** *27* (2), 70-76.

(2) Borrego-Soto, G.; Ortiz-López, R.; Rojas-Martínez, A., Ionizing radiation-induced DNA injury and damage detection in patients with breast cancer. *Genet. Mol. Biol.* **2015,** *38* (4), 420-432.

(3) Thariat, J.; Hannoun-Levi, J.-M.; Sun Myint, A.; Vuong, T.; Gérard, J.-P., Past, present, and future of radiotherapy for the benefit of patients. *Nat. Rev. Clin. Oncol.* **2013,** *10* (1), 52-60.

(4) Wardman, P., Chemical Radiosensitizers for Use in Radiotherapy. *Clin. Oncol.* **2007,** *19* (6), 397-417.

(5) Babaye Abdollahi, B.; Malekzadeh, R.; Pournaghi Azar, F.; Salehnia, F.; Naseri, A. R.; Ghorbani, M.; Hamishehkar, H.; Farajollahi, A. R., Main Approaches to Enhance Radiosensitization in Cancer Cells by Nanoparticles: A Systematic Review. *Adv. Pharm. Bull.* **2021,** *11* (2), 212-223.

(6) Matsudaira, H.; Ueno, A. M.; Furuno, I., Iodine contrast medium sensitizes cultured mammalian cells to X rays but not to γ rays. *Radiat. Res.* **1980,** *84* (1), 144-148.

(7) Lusic, H.; Grinstaff, M. W., X-ray-computed tomography contrast agents. *Chem. Rev.* **2013,** *113* (3), 1641-1666.

(8) Kobayashi, K.; Usami, N.; Porcel, E.; Lacombe, S.; Le Sech, C., Enhancement of radiation effect by heavy elements. *Mutat. Res. Rev. Mutat. Res.* **2010,** *704* (1-3), 123-131.

(9) Hossain, M.; Su, M., Nanoparticle location and material-dependent dose enhancement in X-ray radiation therapy. *J. Phys. Chem. C* **2012,** *116* (43), 23047-23052.

(10) Sun, Y.; Xia, Y., Shape-Controlled Synthesis of Gold and Silver Nanoparticles. *Science* **2002,** *298* (5601), 2176.

(11) Sun, T.; Zhang, Y. S.; Pang, B.; Hyun, D. C.; Yang, M.; Xia, Y., Engineered Nanoparticles for Drug Delivery in Cancer Therapy. *Angew. Chem. Int. Ed.* **2014,** *53* (46), 12320-12364.

(12) Cho, E. C.; Zhang, Q.; Xia, Y., The effect of sedimentation and diffusion on cellular uptake of gold nanoparticles. *Nat. Nanotechnol.* **2011,** *6* (6), 385-391.

(13) Chen, J.; Wiley, B.; Li, Z.-Y.; Campbell, D.; Saeki, F.; Cang, H.; Au, L.; Lee, J.; Li, X.; Xia, Y., Gold Nanocages: Engineering Their Structure for Biomedical Applications. *Adv. Mater.* **2005,** *17* (18), 2255-2261.

(14) Zhang, L.; Gu, F. X.; Chan, J. M.; Wang, A. Z.; Langer, R. S.; Farokhzad, O. C., Nanoparticles in medicine: therapeutic applications and developments. *Clin. Pharmacol. Ther.* **2008,** *83* (5), 761-9.

(15) Sun, B.; Hagan, C. T. t.; Caster, J.; Wang, A. Z., Nanotechnology in Radiation Oncology. *Hematol. Oncol. Clin. North Am.* **2019,** *33* (6), 1071-1093.

(16) Mi, Y.; Smith, C. C.; Yang, F.; Qi, Y.; Roche, K. C.; Serody, J. S.; Vincent, B. G.; Wang, A. Z., A Dual Immunotherapy Nanoparticle Improves T-Cell Activation and Cancer Immunotherapy. *Adv. Mater.* **2018,** *30* (25), e1706098.

(17) Min, Y.; Roche, K. C.; Tian, S.; Eblan, M. J.; McKinnon, K. P.; Caster, J. M.; Chai, S.; Herring, L. E.; Zhang, L.; Zhang, T.; DeSimone, J. M.; Tepper, J. E.; Vincent, B. G.; Serody, J. S.; Wang, A. Z., Antigen-capturing nanoparticles improve the abscopal effect and cancer immunotherapy. *Nat. Nanotechnol.* **2017,** *12* (9), 877-882.

(18) Doughty, A. C. V.; Hoover, A. R.; Layton, E.; Murray, C. K.; Howard, E. W.; Chen, W. R., Nanomaterial Applications in Photothermal Therapy for Cancer. *Materials* **2019,** *12* (5), 779.

(19) Zhou, B.; Song, J.; Wang, M.; Wang, X.; Wang, J.; Howard, E. W.; Zhou, F.; Qu, J.; Chen, W. R., BSA-bioinspired gold nanorods loaded with immunoadjuvant for the treatment of melanoma by combined photothermal therapy and immunotherapy. *Nanoscale* **2018,** *10* (46), 21640-21647.

(20) Li, Y.; Li, X.; Zhou, F.; Doughty, A.; Hoover, A. R.; Nordquist, R. E.; Chen, W. R., Nanotechnology-based photoimmunological therapies for cancer. *Cancer Lett.* **2019,** *442*, 429-438.

(21) Wang, L.; Wang, M.; Zhou, B.; Zhou, F.; Murray, C.; Towner, R. A.; Smith, N.; Saunders, D.; Xie, G.; Chen, W. R., PEGylated reduced-graphene oxide hybridized with Fe3O4 nanoparticles for cancer photothermal-immunotherapy. *J. Mater. Chem. B* **2019,** *7* (46), 7406-7414.

(22) Xie, J.; Lee, S.; Chen, X., Nanoparticle-based theranostic agents. *Adv. Drug Deliv. Rev.* **2010,** *62* (11), 1064-1079.

(23) Xie, J.; Xu, C.; Kohler, N.; Hou, Y.; Sun, S., Controlled PEGylation of Monodisperse Fe3O4 Nanoparticles for Reduced Non-Specific Uptake by Macrophage Cells. *Adv. Mater.* **2007,** *19* (20), 3163-3166.

(24) Chen, H.; Zhang, W.; Zhu, G.; Xie, J.; Chen, X., Rethinking cancer nanotheranostics. *Nat. Rev. Mater.* **2017,** *2* (7), 17024.

(25) Chen, H.; Wang, G. D.; Chuang, Y.-J.; Zhen, Z.; Chen, X.; Biddinger, P.; Hao, Z.; Liu, F.; Shen, B.; Pan, Z.; Xie, J., Nanoscintillator-Mediated X-ray Inducible Photodynamic Therapy for In Vivo Cancer Treatment. *Nano Lett.* **2015,** *15* (4), 2249-2256.

(26) Bai, L.; Jiang, F.; Wang, R.; Lee, C.; Wang, H.; Zhang, W.; Jiang, W.; Li, D.; Ji, B.; Li, Z.; Gao, S.; Xie, J.; Ma, Q., Ultrathin gold nanowires to enhance radiation therapy. *J. Nanobiotechnology* **2020,** *18* (1), 131.

(27) Wang, G. D.; Nguyen, H. T.; Chen, H.; Cox, P. B.; Wang, L.; Nagata, K.; Hao, Z.; Wang, A.; Li, Z.; Xie, J., X-Ray Induced Photodynamic Therapy: A Combination of Radiotherapy and Photodynamic Therapy. *Theranostics* **2016,** *6* (13), 2295-2305.

(28) Cline, B.; Delahunty, I.; Xie, J., Nanoparticles to mediate X-ray-induced photodynamic therapy and Cherenkov radiation photodynamic therapy. *Wiley Interdiscip. Rev. Nanomed. Nanobiotechnol.* **2019,** *11* (2), e1541.

(29) Fan, W.; Tang, W.; Lau, J.; Shen, Z.; Xie, J.; Shi, J.; Chen, X., Breaking the Depth Dependence by Nanotechnology-Enhanced X-Ray-Excited Deep Cancer Theranostics. *Adv. Mater.* **2019,** *31* (12), 1806381.

(30) Yang, S.; Zhou, C.; Liu, J.; Yu, M.; Zheng, J., One-Step Interfacial Synthesis and Assembly of Ultrathin Luminescent AuNPs/Silica Membranes. *Adv. Mater.* **2012,** *24* (24), 3218-3222.

(31) Zhou, C.; Hao, G.; Thomas, P.; Liu, J.; Yu, M.; Sun, S.; Öz, O. K.; Sun, X.; Zheng, J., Near-Infrared Emitting Radioactive Gold Nanoparticles with Molecular Pharmacokinetics. *Angew. Chem. Int. Ed.* **2012,** *51* (40), 10118-10122.

(32) Hainfeld, J. F.; Slatkin, D. N.; Smilowitz, H. M., The use of gold nanoparticles to enhance radiotherapy in mice. *Phys. Med. Biol.* **2004,** *49* (18), N309.

(33) Bonvalot, S.; Le Pechoux, C.; De Baere, T.; Kantor, G.; Buy, X.; Stoeckle, E.; Terrier, P.; Sargos, P.; Coindre, J. M.; Lassau, N.; Ait Sarkouh, R.; Dimitriu, M.; Borghi, E.; Levy, L.; Deutsch, E.; Soria, J.-C., First-in-Human Study Testing a New Radioenhancer Using Nanoparticles (NBTXR3) Activated by Radiation Therapy in Patients with Locally Advanced Soft Tissue Sarcomas. *Clin. Cancer Res.* **2017,** *23* (4), 908-917.

(34) Bonvalot, S.; Rutkowski, P. L.; Thariat, J.; Carrère, S.; Ducassou, A.; Sunyach, M.-P.; Agoston, P.; Hong, A.; Mervoyer, A.; Rastrelli, M., NBTXR3, a first-in-class radioenhancer hafnium oxide nanoparticle, plus radiotherapy versus radiotherapy alone in patients with locally advanced soft-tissue sarcoma (Act. In. Sarc): a multicentre, phase 2–3, randomised, controlled trial. *Lancet Oncol.* **2019,** *20* (8), 1148-1159.

(35) Zheng, J.; Zhou, C.; Yu, M.; Liu, J., Different sized luminescent gold nanoparticles. *Nanoscale* **2012,** *4* (14), 4073-4083.

(36) Misawa, M.; Takahashi, J., Generation of reactive oxygen species induced by gold nanoparticles under x-ray and UV Irradiations. *Nanomed. Nanotechnol. Biol. Med.* **2011,** *7* (5), 604-614.

(37) Maeda, H., The enhanced permeability and retention (EPR) effect in tumor vasculature: the key role of tumor-selective macromolecular drug targeting. *Adv. Enzyme Regul.* **2001**.

(38) Choi, H. S.; Liu, W.; Misra, P.; Tanaka, E.; Zimmer, J. P.; Ipe, B. I.; Bawendi, M. G.; Frangioni, J. V., Renal clearance of nanoparticles. *Nat. Biotechnol.* **2007,** *25* (10), 1165.

(39) Liu, J.; Yu, M.; Zhou, C.; Yang, S.; Ning, X.; Zheng, J., Passive Tumor Targeting of Renal-Clearable Luminescent Gold Nanoparticles: Long Tumor Retention and Fast Normal Tissue Clearance. *J. Am. Chem. Soc.* **2013,** *135* (13), 4978-4981.

(40) Chithrani, B. D.; Ghazani, A. A.; Chan, W. C., Determining the size and shape dependence of gold nanoparticle uptake into mammalian cells. *Nano Lett.* **2006,** *6* (4), 662-668.

(41) Maggiorella, L.; Barouch, G.; Devaux, C.; Pottier, A.; Deutsch, E.; Bourhis, J.; Borghi, E.; Levy, L., Nanoscale radiotherapy with hafnium oxide nanoparticles. *Future Oncol.* **2012,** *8* (9), 1167-1181.

(42) Lu, K.; He, C.; Guo, N.; Chan, C.; Ni, K.; Lan, G.; Tang, H.; Pelizzari, C.; Fu, Y.-X.; Spiotto, M. T.; Weichselbaum, R. R.; Lin, W., Low-dose X-ray radiotherapy–radiodynamic therapy via nanoscale metal–organic frameworks enhances checkpoint blockade immunotherapy. *Nat. Biomed. Eng.* **2018,** *2* (8), 600-610.

(43) Lan, G.; Ni, K.; Veroneau, S. S.; Song, Y.; Lin, W., Nanoscale metal–organic layers for radiotherapy–radiodynamic therapy. *J. Am. Chem. Soc.* **2018,** *140* (49), 16971-16975.

(44) Ni, K.; Lan, G.; Veroneau, S. S.; Duan, X.; Song, Y.; Lin, W., Nanoscale metal-organic frameworks for mitochondria-targeted radiotherapy–radiodynamic therapy. *Nat. Commun.* **2018,** *9* (1), 1-13.

(45) Ni, K.; Lan, G.; Chan, C.; Quigley, B.; Lu, K.; Aung, T.; Guo, N.; La Riviere, P.; Weichselbaum, R. R.; Lin, W., Nanoscale metal-organic frameworks enhance radiotherapy to potentiate checkpoint blockade immunotherapy. *Nat. Commun.* **2018,** *9* (1), 1-12.

(46) He, T.; Xu, X.; Ni, B.; Wang, H.; Long, Y.; Hu, W.; Wang, X., Fast and scalable synthesis of uniform zirconium-, hafnium-based metal–organic framework nanocrystals. *Nanoscale* **2017,** *9* (48), 19209-19215.

(47) Kawrakow, I.; Rogers, D. W. O.; Mainegra-Hing, E.; Tessier, F.; Walters, B. R. B. *The EGSnrc Code System: Monte Carlo Simulation of Electron and Photon Transport*; NRC: Ottawa, 2000.

(48) Agostinelli, S.; Allison, J.; Amako, K. a.; Apostolakis, J.; Araujo, H.; Arce, P.; Asai, M.; Axen, D.; Banerjee, S.; Barrand, G., GEANT4—a simulation toolkit. *Nucl. Instrum. Methods. Phys. Res. B NUCL INSTRUM METH A* **2003,** *506* (3), 250-303.

(49) Allison, J.; Amako, K.; Apostolakis, J.; Araujo, H.; Dubois, P. A.; Asai, M.; Barrand, G.; Capra, R.; Chauvie, S.; Chytracek, R., Geant4 developments and applications. *IEEE Trans. Nucl. Sci.* **2006,** *53* (1), 270-278.

(50) Allison, J.; Amako, K.; Apostolakis, J.; Arce, P.; Asai, M.; Aso, T.; Bagli, E.; Bagulya, A.; Banerjee, S.; Barrand, G., Recent developments in Geant4. *Nucl. Instrum. Methods. Phys. Res. B NUCL INSTRUM METH A* **2016,** *835*, 186-225.

(51) Zygmanski, P.; Liu, B.; Tsiamas, P.; Cifter, F.; Petersheim, M.; Hesser, J.; Sajo, E., Dependence of Monte Carlo microdosimetric computations on the simulation geometry of gold nanoparticles. *Phys. Med. Biol.* **2013,** *58* (22), 7961.

(52) Martinov, M. P.; Thomson, R. M., Taking EGSnrc to new lows: Development of egs++ lattice geometry and testing with microscopic geometries. *Med. Phys.* **2020**.

(53) Hernandez, A. M.; Boone, J. M., Tungsten anode spectral model using interpolating cubic splines: unfiltered x-ray spectra from 20 kV to 640 kV. *Med. Phys.* **2014,** *41* (4), 042101.

(54) Liu, Y.; Zhang, P.; Li, F.; Jin, X.; Li, J.; Chen, W.; Li, Q., Metal-based nanoenhancers for future radiotherapy: radiosensitizing and synergistic effects on tumor cells. *Theranostics* **2018,** *8* (7), 1824.

(55) Hubbell, J. H.; Seltzer, S. M. Tables of X-Ray Mass Attenuation Coefficients and Mass Energy-Absorption Coefficients (version 1.4). http://physics.nist.gov/xaamdi (accessed May, 2021).

(56) Cavka, J. H.; Jakobsen, S.; Olsbye, U.; Guillou, N.; Lamberti, C.; Bordiga, S.; Lillerud, K. P., A New Zirconium Inorganic Building Brick Forming Metal Organic Frameworks with Exceptional Stability. *J. Am. Chem. Soc.* **2008,** *130* (42), 13850-13851.

(57) Casssola, V. F.; Hoff, G. In *Comparison between Geant4 and EGSnrc of dosimetric quantities and spectra simulation for electrons beam*, 2011 IEEE Nuclear Science Symposium Conference Record, Institute Of Electrical And Electronics Engineers Inc., 23-29 Oct. 2011; Institute Of Electrical And Electronics Engineers Inc., 2011; pp 1398-1400.

(58) Lu, K.; He, C.; Lin, W., Nanoscale Metal–Organic Framework for Highly Effective Photodynamic Therapy of Resistant Head and Neck Cancer. *J. Am. Chem. Soc.* **2014,** *136* (48), 16712-16715.

Chapter 3. Synergistic Checkpoint-Blockade and Radiotherapy–Radiodynamic Therapy via an Immunomodulatory Bismuth-Based MOF

3.1. Introduction

Cancer immunotherapy harnesses the host immune system to elicit systemic antitumor responses and long-term immunosurveillance.[1] One promising approach is checkpoint blockade immunotherapy (CBI), which targets T lymphocyte immunosuppressive pathways and has shown favorable response rates and low side effects in certain cancers.[2] However, its effectiveness in poorly immunogenic tumors such as prostate and pancreatic cancers remained limited.[3-4] To overcome this challenge, immunostimulatory adjuvant therapies such as photodynamic therapy (PDT)[5] and radiation therapy (RT)[6] have been combined with checkpoint inhibitors to achieve durable tumor control in a wider population of cancer patients. PDT is highly immunogenic by killing tumor cells with cytotoxic singlet oxygen ($^1O_2$), while its clinical application is severely hindered by the limited tissue penetration depth of light.[7-8] RT employs highly tissue-penetrating X-rays to generate hydroxyl radicals ($^{\bullet}OH$) for tumor destruction, but it is less immunogenic than PDT and associated with certain side effects.[9-10] Therefore, there is a need for new clinically applicable immunogenic treatment modalities as immunostimulatory adjuvants to enhance the efficacy of CBI.[11-14]

We have recently reported a novel immunogenic treatment modality termed radiotherapy–radiodynamic therapy (RT–RDT), which utilizes Hf-based nanoscale metal–organic frameworks (nMOFs) to enhance the radiotherapeutic effects of ionizing radiation, such as X-rays. This approach serves as a potent adjuvant therapy to synergize with cancer immunotherapy.[15-16] nMOFs are a class of crystalline, porous nanomaterials composed of metal-cluster secondary building units (SBUs) and organic linkers,[17-20] with unique attributes of structural tunability, synthetic modularity,

permanent porosity, and multifunctionality for various biomedical applications.[21-23] In RT–RDT, the heavy-element SBUs (such as Hf-oxo clusters) efficiently absorb radiation to generate •OH while simultaneously transferring energy to neighboring photosensitizing linkers *via* inelastic scattering of photoelectrons from radioexcited "hotspots" to produce $^1O_2$.[15, 24] Consequently, RT–RDT induces immunogenic cell death (ICD) and local inflammation to facilitate tumor antigen presentation, and, when combined with checkpoint blockade immunotherapy (CBI), promotes T cell expansion and infiltration to elicit systemic antitumor immunity.[25-26]

As X-ray absorption cross sections are positively correlated to the atomic number of heavy metals, we hypothesized that nMOFs constructed from heavier metals would exhibit stronger X-ray adsorption to enhance RD-RDT effects. Bismuth (Bi), the heaviest of all naturally occurring, non-radioactive elements, emerged as an ideal metal for constructing nanoradiosensitizers. Its higher K edge energy (90 keV) compared to Hf (65 keV) makes Bi-nMOFs particularly suitable for enhancing the cytotoxic effects of megavoltage photons produced by linear particle accelerators (LINACs) in clinic settings. Furthermore, Bi is known for its biocompatibility, rendering Bi-nMOFs promising candidates for clinical applications.[27] The enhanced RT–RDT effects achieved by Bi-nMOFs have the potential to induce robust local immune activation, thereby synergizing with CBI to promote systemic tumor regression.

In this chapter, we present the design of a novel Bi-nMOF that enhances local RT–RDT efficacy, while simultaneously activating innate immunity and modulating the biomechanics of poorly immunogenic tumors. Assembled from $Bi_{10}O_8$ clusters and photosensitizing 5,15-di(*p*-benzoato)-porphyrin (DBP) linkers, Bi-DBP nMOF demonstrated significantly higher radiosensitization than previously reported Hf-DBP nMOF. The higher absorption cross section of $Bi_{10}O_8$ clusters, leads to an augmented Auger cascade of ionizing reactions at the focal point of

irradiation, amplifying the radiolysis and radiodynamic process even at low doses of X-ray or ^{60}Co-γ-ray. As a result, Bi-DBP induces stronger local antitumor efficacy and ICD compared to Hf-DBP in murine prostate TRAMP-C2 and pancreatic Panc02 tumor models. Notably, Bi-DBP-mediated RT–RDT treatment decreases the levels of transforming growth factor (TGF-β) both locally and systemically, reversing immunosuppression and reducing extracellular matrix stiffness, and removing the physical barrier for T lymphocyte infiltration. When combined with CBI, Bi-DBP mediated RT–RDT not only eradicates local tumors but also triggers regression of distant tumors in poorly immunogenic mouse models through systemic antitumor immunity, immune-modulation, and increased T cell infiltration in tumors. Our findings highlight the ability of the optimized nanoradiosensitizer to convert the treated primary tumor into an immunological hotbed, while simultaneously modulating tumor biomechanics and relieving local immunosuppression to elicit systemic antitumor immune activation and immune modulation.

3.2. Results and discussion

3.2.1. Synthesis and characterization of Bi-DBP

Bi-DBP was solvothermally synthesized from $Bi(NO_3)_3$ and H_2DBP in a mixed solvent of *N*,*N*-dimethylformamide (DMF) and ethanol with trifluoroacetic acid as modulator and displayed a nanorod morphology of ~20 nm in diameter and ~180 nm in length under transmission electron microscopy (TEM, **Figure 3-1a**). Hf-DBP was synthesized as comparison (**Figure 3-1b**).[15] The number-averaged size of Bi-DBP in ethanol was measured to be 109 ± 5 nm with a polydispersity index (PDI) of 0.16 by dynamic light scattering (DLS, **Figure 3-1c**).

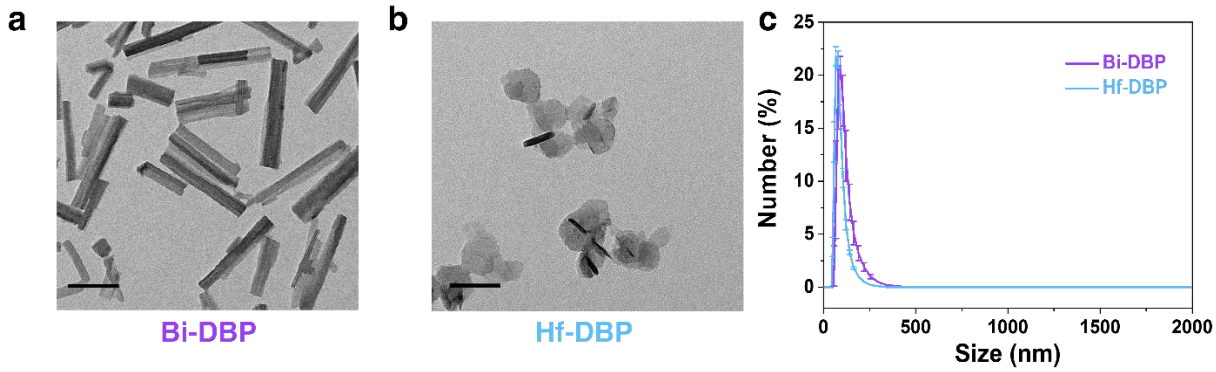

Figure 3-1. TEM images of (a) Bi-DBP and (b) Hf-DBP, and (c) their number-averaged sizes determined by dynamic light scattering.

Numerous attempts failed to obtain high-quality Bi-DBP crystals for single-crystal X-ray diffraction due to limited solubility of H_2DBP and rapid hydrolysis of Bi^{3+} precursor. Based on known carboxylate or hydroxyl-capped $Bi_{10}O_8$ clusters[28-29] and the presence of $Bi_{10}O_8$ SBUs in the Bi-BPDC crystal (BPDC = 4,4'-biphenyldicarboxylate, **Figure 3-2**, **Table 3-1**), the structure of Bi-DBP was modelled using $Bi_{10}O_8$ SBUs and DBP linkers in the *Cmcm* space group to give a formula of $Bi_{10}O_8(OH)_8(H_2O)_4(DBP)_3$ (**Figure 3-3**, **Table 3-2**).

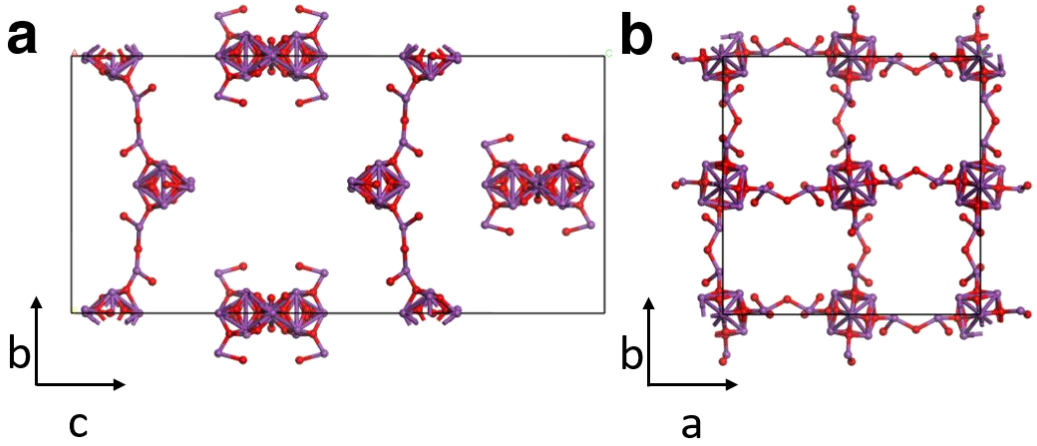

Figure 3-2. Views of $Bi_{10}O_8$ SBUs in Bi-BPDC along the crystallographic (a) a-axis or b-axis and (b) c-axis. Purple: bismuth; red: oxygen; blue: nitrogen; grey: carbon.

Table 3-1. Crystallographic information of Bi-BPDC single crystal.

Name	**Bi-BPDC**
Formula	Bi_5O_8
Fw	1172.892
Temperature (K)	100(2)
Wavelength (Å)	0.41328
Crystal system	Tetragonal
Space group	$I\bar{4}2d$
a (Å)	24.971(3)
b (Å)	24.971(3)
c (Å)	51.709(6)
α (°)	90
β (°)	90
γ (°)	90
V (Å^3)	32243(9)
Z	356
Density (calcd. g/cm^3)	4.620
Absorption coeff. (mm^{-1})	12.495
F(000)	37380.0
2θ range data collection	1.624-20.718
Limiting indices	-21 <= h <= 21 -21 <= k <= 21 -44 <= l <= 44
Reflection collected	73504
Independent reflection	5557
R (int)	0.1572
Data/restraints/parameters	5557/132/106
Goodness-of-fit on F^2	1.072
Final R indices [I>σ2(I)]	R1 = 0.0554, wR2 = 0.1533
R indices (all data)	R1 = 0.0569, wR2 = 0.1551

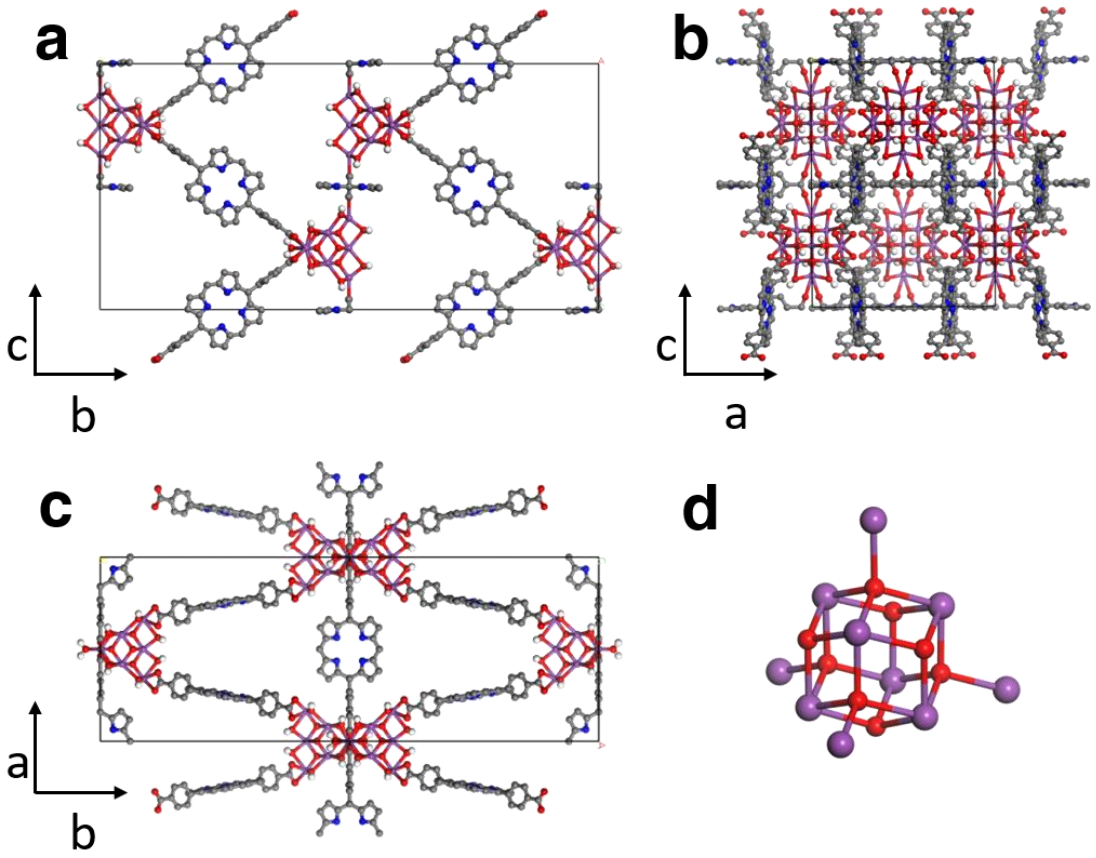

Figure 3-3. Modelled crystal structures of Bi-DBP projected along (a) the a-axis, (b) the b-axis, and (c) the c-axis and (d) $Bi_{10}O_8$ SBU. Purple: bismuth; red: oxygen; blue: nitrogen; grey: carbon.

Table 3-2. Crystallographic information of simulated Bi-DBP structure.

Name	**Bi-DBP**
Formula	$Bi_{10}O_8(OH)_8(H_2O)_4(DBP)_3$
Crystal system	Orthorhombic
Space group	*Cmcm*
***a* (Å)**	21.19
***b* (Å)**	57.38
***c* (Å)**	28.34
***α* (°)**	90
***β* (°)**	90
***γ* (°)**	90
***V* (Å³)**	34458

This structural model matches the experimental powder X-ray diffraction (PXRD) pattern of Bi-DBP (**Figure 3-4a**) with four main peaks at 2θ = 3.22, 4.34, 6.12, and 6.82°, as well as the

Bi/DBP ratio of 3.3 determined by inductively coupled plasma-mass spectrometry (ICP-MS) and UV-Vis absorption spectroscopy. The unchanged PXRD patterns of Bi-DBP in phosphate buffer solution (PBS) after different incubation time also confirmed the stability of Bi-DBP in biological environment (**Figure 3-4b**). The formula of Bi-DBP was further confirmed by thermogravimetric analysis (TGA), which revealed a weight loss of 43.9%, consistent with an expected weight loss of 41.8% for the decomposition of Bi-DBP to Bi_2O_3 (**Figure 3-4c**). The UV-Vis spectrum of Bi-DBP exhibited four Q bands characteristic of non-metalated DBP ligand (**Figure 3-2d**).

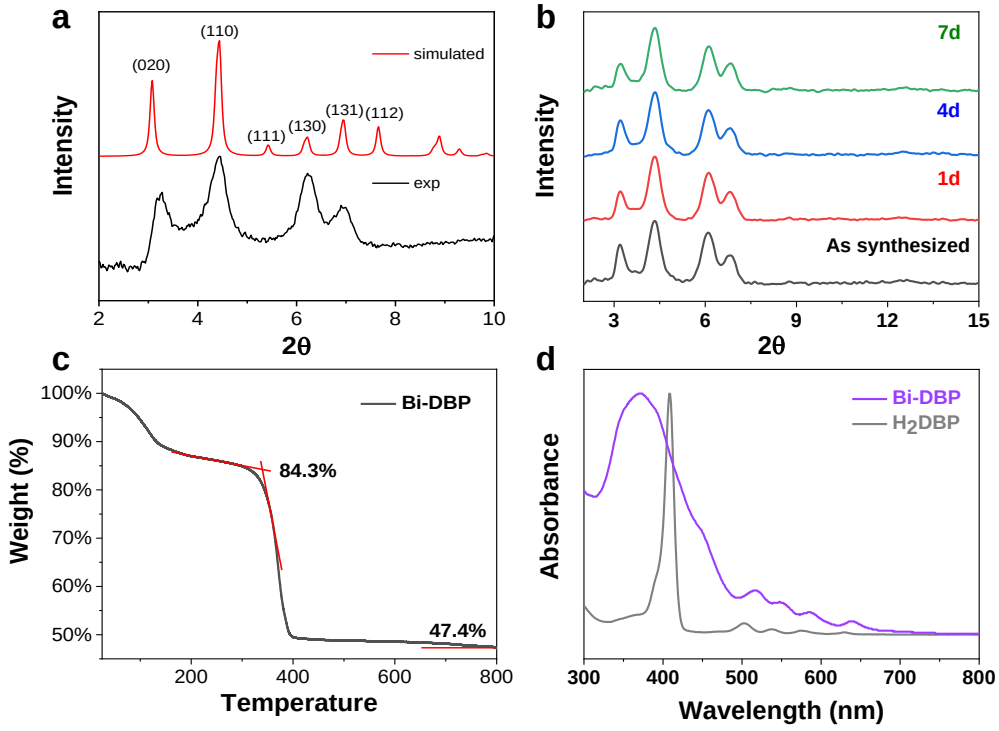

Figure 3-4. Characterization of Bi-DBP. (a) Comparison of the simulated PXRD pattern with experimental data. (b) Comparison of PXRD patterns to show stability of 1 mM Bi-DBP incubated in PBS for different lengths of time. (c) TGA of as-synthesized Bi-DBP. (d) UV-Vis spectra of Bi-DBP and H_2DBP in DMSO.

3.2.2. Enhanced radiosensitization with Bi-DBP

To evaluate the radiosensitization properties of Bi-DBP, radioluminescence and radiolysis assays were performed to probe X-ray absorption and $^{\bullet}$OH generation efficiencies, respectively.

Radioluminescent nMOFs, Hf-DBAn and Bi-DBAn, were assembled from luminescent 9,10-di(*p*-benzoato)anthracene (DBAn) linkers and shown to be isostructural to Hf-DBP and Bi-DBP, respectively (**Figure 3-5**). Radioluminescence signals emitted from DBAn linkers correlate with the X-ray absorption efficiencies of $Hf_{12}O_8$ SBUs in Hf-DBAn and $Bi_{10}O_8$ SBUs in Bi-DBAn. As anticipated, Bi-DBAn displayed 1.38-fold higher radioluminescence signal than Hf-DBAn (**Figure 3-6)**, indicating that $Bi_{10}O_8$ SBUs in Bi-DBAn exhibited higher X-ray absorption and energy transfer efficiency than $Hf_{12}O_8$ SBUs in Hf-DBAn.

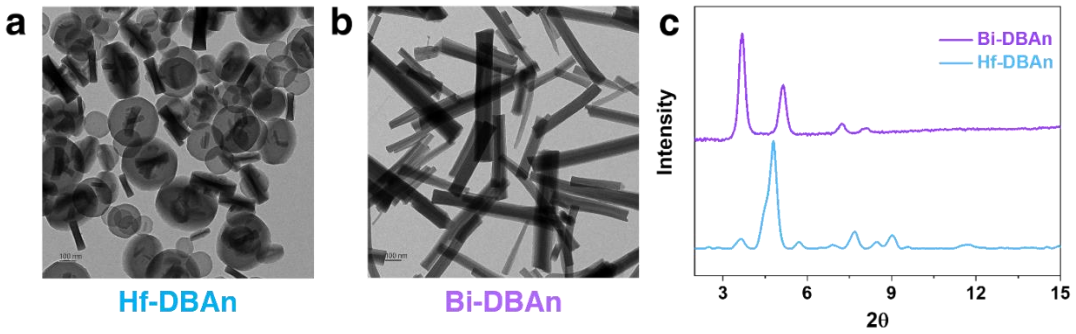

Figure 3-5. Representative TEM images of (a) Hf-DBAn and (b) Bi-DBAn. (c) PXRD of Hf-DBAn and Bi-DBAn.

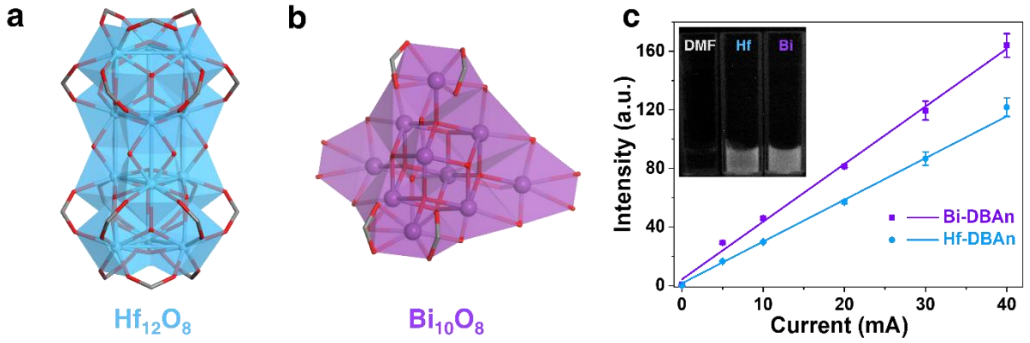

Figure 3-6. Structures of $Hf_{12}O_8$ SBUs in (a) Hf-DBP and (b) $Bi_{10}O_8$ SBUs in Bi-DBP. (c) Optical image (inset) and linear fitting of radioluminescence intensities with respect to X-ray tube current of Bi-DBP and Hf-DBP at equivalent concentrations of 1 mM after subtraction of the DMF background signal, n = 6.

Radiolysis enhancement by Bi-DBP was probed by aminophenyl fluorescein (APF) to detect $^{\bullet}OH$ generation after X-ray or γ-ray irradiation. Due to restricted access to LINAC, ^{60}Co

radiation was employed as an alternative γ-ray source. Both Bi-DBP and Hf-DBP showed a linear increase of •OH generation as a function of the irradiation dose. The relative enhancement of •OH generation over H_2O was obtained by dividing the slope of the experimental group by that of H_2O group. The X-ray enhancement factors are 2.08 for Bi-DBP and 1.86 for Hf-DBP (**Figure 3-7a**), respectively, whereas the γ-ray enhancement factors are 2.65 for Bi-DBP and 2.31 for Hf-DBP (**Figure 3-7b**). Radioluminescence and radiolysis enhancement results show that Bi-DBP is a more efficient nanoradiosensitizer than Hf-DBP with higher radiation energy deposition and •OH generation.

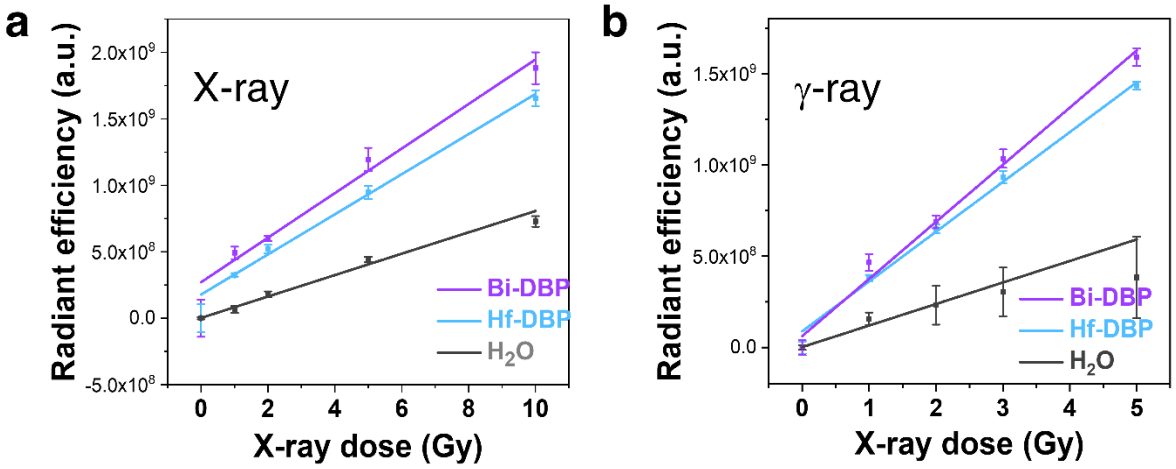

Figure 3-7. Enhanced APF fluorescence of Bi-DBP and Hf-DBP over H2O at equivalent concentrations of 20 μM upon (a) X-ray and (b) γ-ray irradiation, $n = 6$.

2.2.3. Enhanced RT–RDT induces robust immunogenic cell death

Efficient cellular internalization of both Hf-DBP and Bi-DBP was confirmed with murine prostate cancer cell line, TRAMP-C2, which reached a similar intracellular level 4 h post incubation (**Figure 3-8a**). The acute cytotoxicity caused by particles plus radiation was evaluated by the (3-(4,5-dimethylthiazol-2-yl)-5-(3-carboxymethoxyphenyl)-2-(4-sulfophenyl)-2H-tetrazolium) (MTS) assay. No cytotoxicity was observed in cells dosed with particles without irradiation on tumor cell line TRAMP-C2 (**Figure 3-8b**).

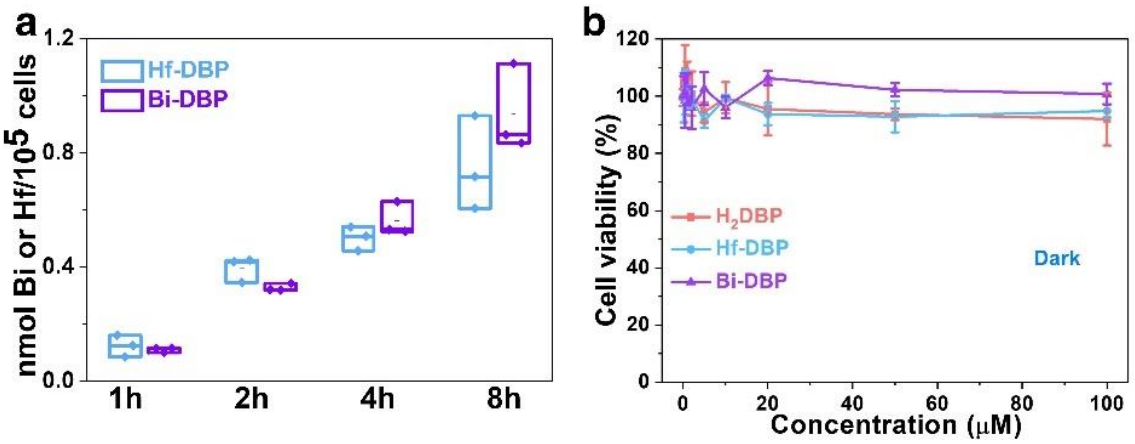

Figure 3-8. Cellular uptake and biosafety of Bi-DBP. (a) Cellular uptake of Hf-DBP and Bi-DBP after 1, 2, 4 or 8 h incubation with equivalent Hf or Bi concentrations of 20 μM, n=3. (b) Dark cytotoxicity of H_2DBP, Hf-DBP, and Bi-DBP against TRAMP-C2 cells at different concentrations.

Clonogenic assays were then conducted to assess the long-term anti-proliferative/cytotoxic effects of Bi-DBP and Hf-DBP upon X-ray or γ-ray irradiation. At the dose required for 10% survival, Bi-DBP gave radiation enhancement factors (REF_{10}) of 2.71 and 1.89 under X-ray (**Figure 3-9c**) and γ-ray (**Figure 3-9d**), respectively, which were substantially higher than those of Hf-DBP at 1.85 and 1.36 under X-ray (**Figure 3-9c**) and γ-ray (**Figure 3-9d**), respectively.

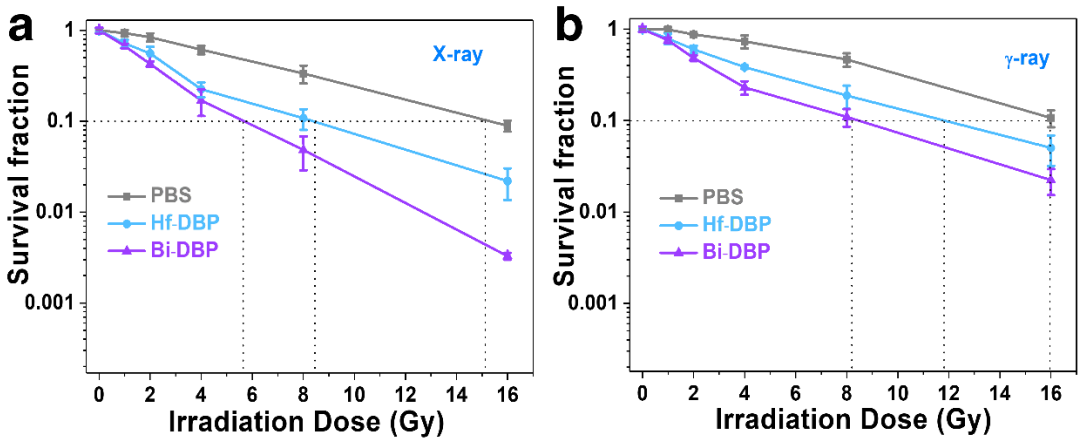

Figure 3-9. Clonogenic assays to evaluate radioenhancement of Hf-DBP and Bi-DBP on TRAMP-C2 cells upon 250 kVp (a) X-ray and (b) ^{60}Co γ-ray irradiation, n = 6.

Furthermore, Bi-DBP caused more extensive apoptosis and necrosis (29.6%) than Hf-DBP (19.2%) in TRAMP-C2 cells 24 h post treatment, supporting its superior radiosensitization

efficiency (**Figure 3-10**). Both X-ray and ^{60}Co γ-ray radiations are used in subsequent *in vitro* studies and we use (+) and (-) to denote with and without radiation, respectively.

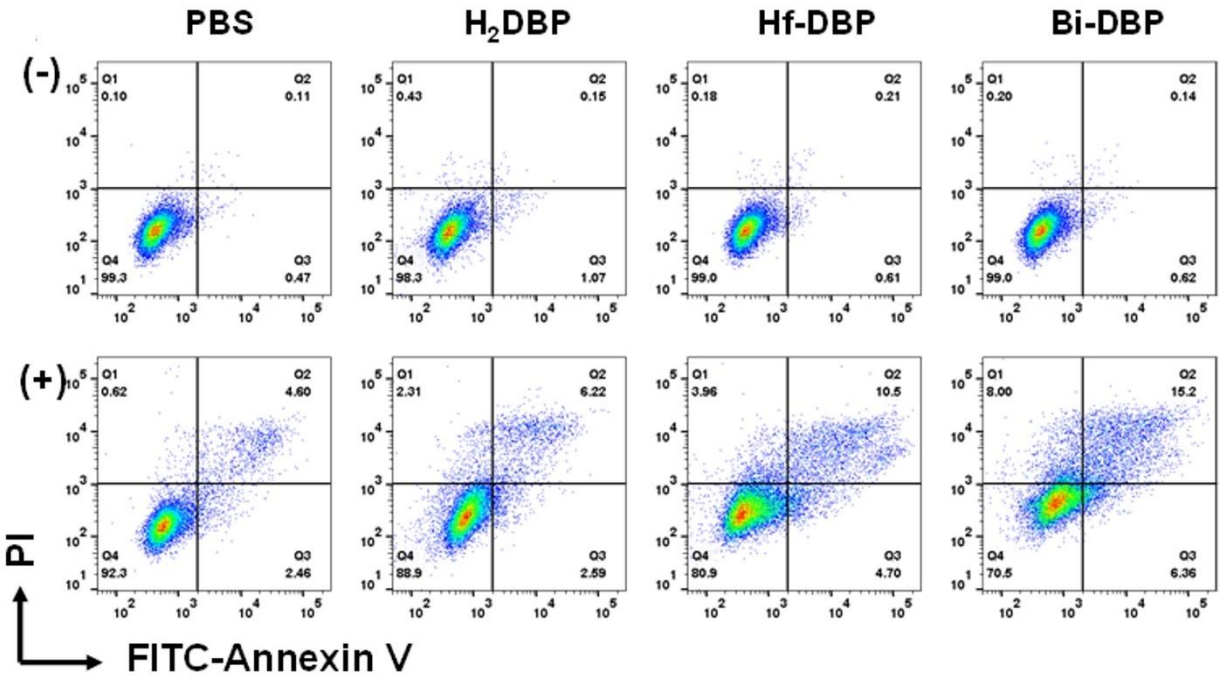

Figure 3-10. Flow cytometric analysis show apoptosis and necrosis of TRAMPC-2 cells treated with PBS, H_2DBP, Hf-DBP, or Bi-DBP upon X-ray irradiation at a dose of 0(-) or 2(+) Gy. The quadrants from lower left to upper left (counterclockwise) represent healthy, early apoptotic, late apoptotic, and necrotic cells, respectively. The percentage of cells in each quadrant is shown on the graphs.

We next determined the mechanism by which Bi-DBP elicited stronger cytotoxicity on TRAMP-C2 cells. The radiosensitization effect of Bi-DBP was probed *via* quantifying DNA double-strand breaks (DSBs) caused by •OH. When incubated with Bi-DBP or Hf-DBP and irradiated with 2 Gy of X-ray or γ-ray, significant γ-H2AX fluorescence indicating DSBs was observed in the cell nuclei, whereas no fluorescence was observed in cells treated with particles or radiation alone (**Figure 3-11**).

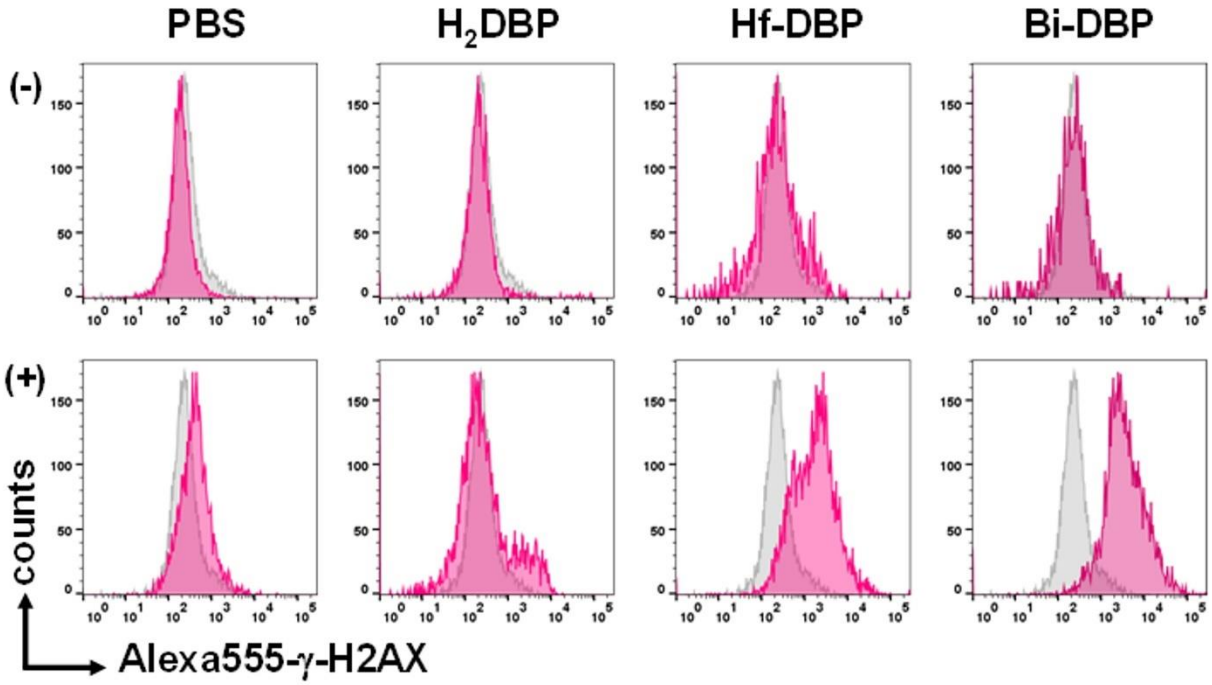

Figure 3-11. Flow cytometric analysis of γ-H2AX expressions showing the DNA double strain breaks (DSBs) in TRAMP-C2 cells treated with PBS, H_2DBP, Hf-DBP or Bi-DBP and irradiated with X-ray at a dose of 0(-) or 2(+) Gy. Grey histogram (control) and pink histogram show the difference of γ-H2AX levels in the cells.

Singlet oxygen sensor green (SOSG) assay showed that Bi-DBP(+) generated $^1O_2$ more efficiently than Hf-DBP(+) (**Figure 3-12**). Taken together, clonogenic, γ-H2AX, and SOSG assays showed that Bi-DBP(+) outperformed Hf-DBP(+) by eliciting a stronger long-term anti-proliferative effect *via* $^{\bullet}$OH-mediated RT and greater acute cytotoxic effect *via* $^1O_2$-mediated RDT under either orthovoltage X-ray or ^{60}Co γ-ray radiation.

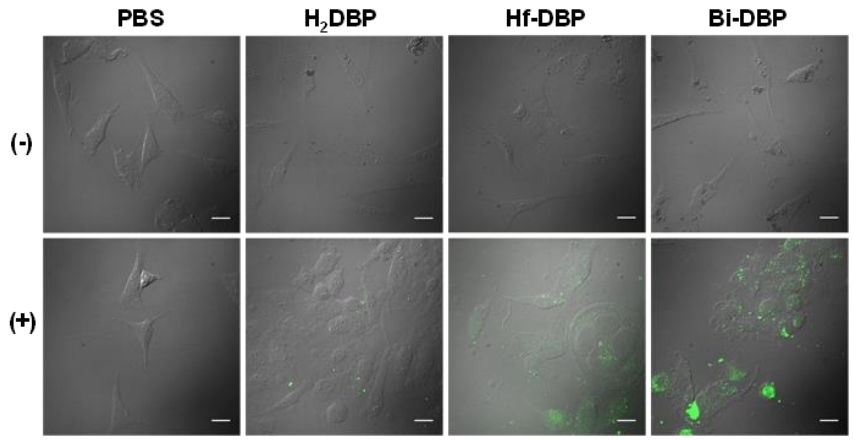

Figure 3-12. Confocal images of intracellular $^1O_2$ generation detected by SOSG. TRAMP-C2 cells were preloaded with SOSG, treated with PBS, H_2DBP, Hf-DBP, or Bi-DBP, irradiated upon X-ray irradiation at a dose of 0(-) or 2(+) Gy. Green fluorescence comes from SOSG that has reacted with $^1O_2$. Scale bar = 20 μm.

By efficiently causing intracellular oxidative stress, Bi-DBP-mediated RT–RDT afforded potent ICD to initiate the recognition of danger-associated molecular patterns (DAMPs), including calreticulin (CRT), high mobility group box-1 (HMGB-1) and adenosine triphosphate (ATP), by antigen presenting cells (APCs). CRT exposure serves as an "eat-me" signal to macrophages and dendritic cells (DCs) for phagocytosis.[30] HMGB-1 is a nucleosome-associated protein released from dead cells to interact with toll-like receptor-4 on DCs for tumor antigen presentation,[31] whereas ATP is a metabolite actively involved in caspase-dependent inflammasome activation for DC maturation.[32] We thus investigated Bi-DBP(+) induced ICD with either X-ray or γ-ray irradiation *via* detecting cell-surface exposure of CRT by flow cytometry and confocal laser scanning microscope (CLSM) as well as release of HMGB-1 and ATP by enzyme-linked immunosorbent assay (ELISA). Quantitative flow cytometric analysis and CLSM imaging showed that Bi-DBP(+) exhibited higher CRT mean fluorescence intensity (MFI) than Hf-DBP(+), suggesting that enhanced radiosensitization of Bi-DBP over Hf-DBP led to higher CRT exposure (MFI of 2471.6 ± 206.6 vs 1060.1 ± 331.4, **Figure 3-13a**). ELISA studies revealed that Bi-DBP(+)

treated cells showed higher HMGB-1 release and ATP secretion (71.6 ± 0.7 and 212.3 ± 5.6 nM, respectively) compared to Hf-DBP(+) treated cells (60.1 ± 5.1 and 153.1 ± 8.8 nM, respectively), providing further support for stronger ICD induced by Bi-DBP(+) (**Figure 3-13b&c**).

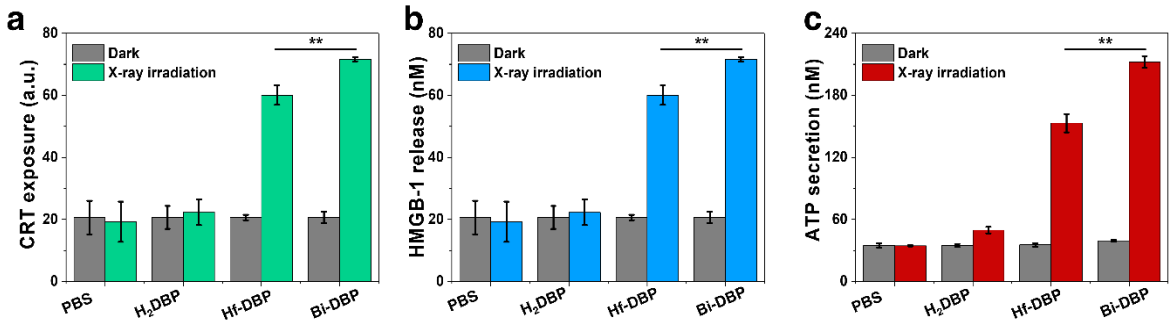

Figure 3-13. (a) CRT exposure, (b) HMGB-1 release and (c) ATP secretion from TRAMP-C2 cells treated with PBS, H_2DBP, Hf-DBP or Bi-DBP upon X-ray irradiation at a dose of 2 Gy quantified by flow cytometry or ELISA, n = 3.

3.2.4. *In vivo* anti-tumor efficacy

After demonstrating that Bi-DBP(+) exhibited stronger RT–RDT efficacy than Hf-DBP(+) for immunogenic cell death *in vitro*, we performed antitumor studies of Bi-DBP-mediated RT–RDT with X-ray *in vivo*. The biocompatibility of Bi-DBP was first demonstrated by steady body weights of C57BL/6 mice intravenously injected with 2 mol Bi-DBP every other day for a total of six doses (**Figure 3-14**).

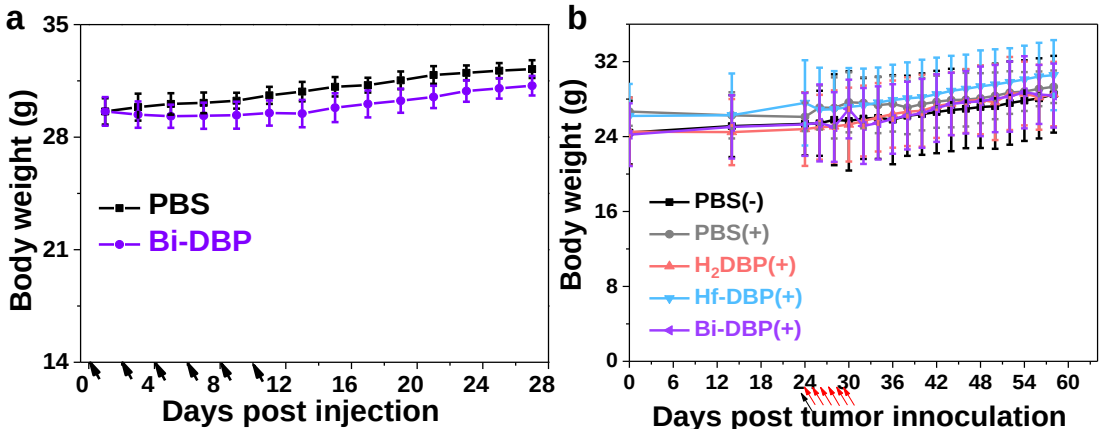

Figure 3-14. Body weights of C57BL/6 mice after intravenous injection of Bi-DBP.

The *in vivo* anti-tumor efficacy of Bi-DBP(+) was studied on immunosuppressive murine prostate tumor model TRAMP-C2 and murine pancreatic tumor model Panc02. In a single tumor model, tumors were established on the right flanks of C57BL/6 mice and treatments began on day 28 or day 14 post-inoculation when the tumors reached ~125 mm^3 or ~85 mm^3 in volume for TRAMP-C2 or Panc02, respectively. A single dose of PBS, H_2DBP, Bi-DBP, or Hf-DBP was intratumorally administered followed by six consecutive days of low X-ray doses at 1 Gy/fraction. For both models, X-ray radiation and H_2DBP(+) had no effect on tumor growth. While Hf-DBP(+) delayed tumor growth, Bi-DBP(+) showed rapid tumor regression, indicating more enhanced local radiosensitization compared to Hf-DBP(+) on both TRAMP-C2 and Panc02 models (**Figure 3-15**). Defined as (1 – (mean volume of treated tumors)/(mean volume of control tumors)) × 100%, the tumor growth inhibition indices (TGIs) of Bi-DBP(+) in TRAMP-C2 and Panc02 models were calculated to be 96.6% and 92.9%, respectively, compared to the TGI values of 74.7% and 74.6%, respectively, for Hf-DBP(+).

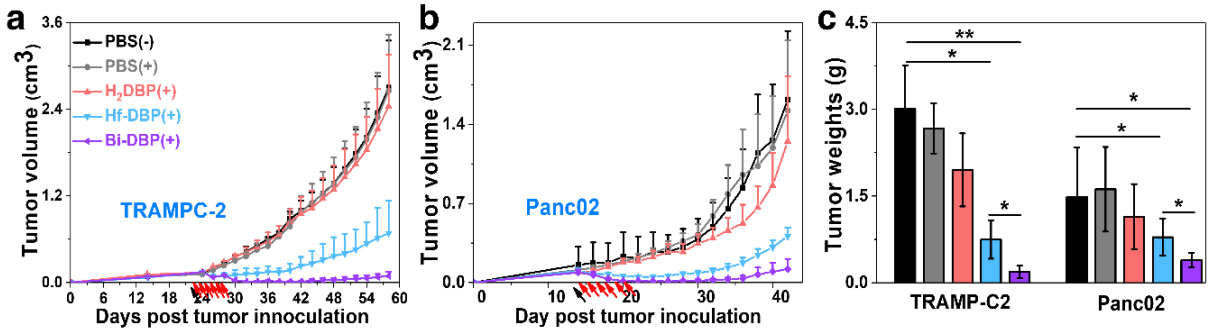

Figure 3-15. Anti-tumor efficacy of H_2DBP, Hf-DBP or Bi-TBP on (a) TRAMP-C2 or (b) Panc02 model, $n = 6$. Black and red arrows refer to intratumoral injections and X-ray irradiation, respectively. (c) Weights of excised tumors from as-treated mice bearing TRAMP-C2 or Panc02 tumors, $n = 6$.

3.2.5. Biomechanical analysis

The tumors were found to soften after nMOF-mediated RT–RDT treatment. We first measured stress relaxation of excised TRAMP-C2 tumors and found that Hf-DBP(+) and Bi-

DBP(+) treatment elicited significant changes of tumor elasticity. Tumors in PBS(+) group showed viscoelasticity, a typical mechanical response of a tissue with both viscous and elastic characteristics when undergoing deformation. In contrast, Hf-DBP(+) and Bi-DBP(+) treatments dramatically lowered tumor elasticity but increased viscosity, indicating change of tumor biomechanics (**Figure 3-16a**). Furthermore, Young's modulus, a mechanical parameter reflecting stiffness of a solid material, was determined for both TRAMP-C2 and Panc02 tumors (**Figure 3-16b**) by uniaxial compression. For TRAMP-C2 tumors, Bi-DBP(+), Hf-DBP(+), and PBS(-) treatments afforded Young's modulus values of 3.9, 7.8, and 24.9 kPa, respectively. For Panc02 tumors, Bi-DBP(+), Hf-DBP(+), and PBS(-) treatments afforded Young's modulus values of 4.6, 9.5, and 20.8 kPa, respectively. The observation of the lowest Young's modulus values in Bi-DBP(+) group showed that Bi-DBP-mediated RT–RDT notably decreased the stiffness of the tumor and modulated tumor biomechanics, which may reduce the physical barrier for T cell infiltration.

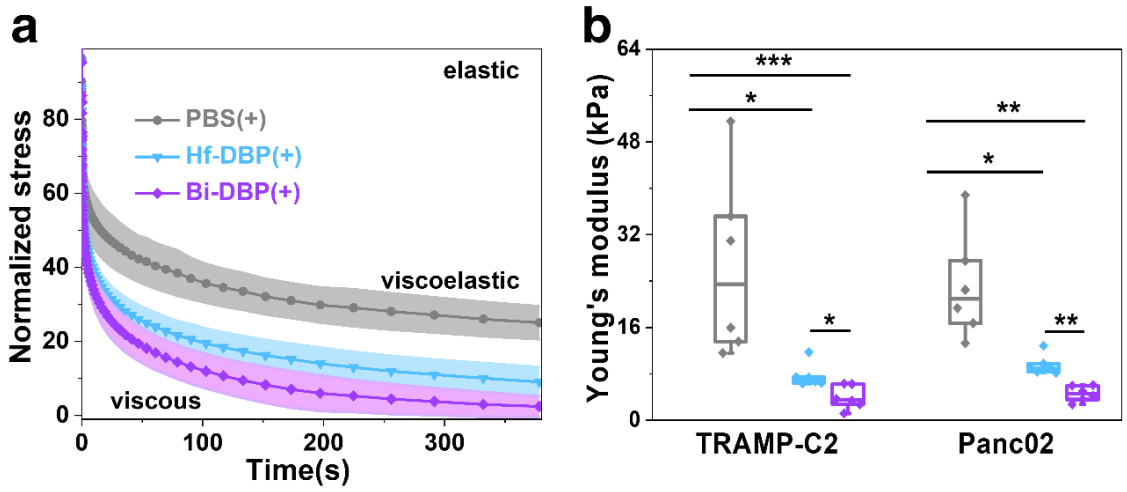

Figure 3-16. (a) Stress relaxation of TRAMP-C2 tumors intratumorally injected with PBS, Hf-DBP or Bi-DBP upon X-ray irradiation, $n = 6$ biological replicates. Shaded regions are s.d. of normalized stresses of different samples. **e**, Young's modulus of as-treated TRAMP-C2 or Panc02 tumors.

We next examined how Bi-DBP-mediated RT–RDT softened tumors. We posited that RT–RDT could break the cycle of desmoplasia and reduce tumor stiffness by alleviating TGF-β-induced immunosuppression. Intratumoral TGF-β expression was analyzed by quantitative polymerase chain reaction (qPCR) on TRAMP-C2 tumors. Bi-DBP(+) and Hf-DBP(+) reduced the TGF-β levels by 94.8% and 73.4%, respectively, relative to the PBS(-) control (**Figure 3-17a**). The intratumoral TGF-β levels thus showed a similar trend as tumor stiffness. Plasma TGF-β levels of TRAMP-C2 tumor- and Panc02 tumor-bearing mice were also quantitatively assayed with an ELISA kit. Consistent downregulation of plasma TGF-β in TRAMP-C2 tumor- and Panc02 tumor-bearing mice was observed in Bi-DBP(+) (74.4 ± 7.3 and 65.0 ± 5.6 ng/mL) or Hf-DBP(+) (114.7 ± 28.5 and 83.4 ± 20.5 ng/mL) groups when compared with the PBS(-) (147.2 ± 26.9 and 130.8 ± 21.8 ng/mL) groups, suggesting systemic decrease of TGF-β after local RT–RDT treatment (**Figure 3-17b**). Bi-DBP(+) reduced significantly more plasma TGF-β than Hf-DBP(+), indicating that better local radiosensitization led to stronger reversal of systemic immunosuppression.

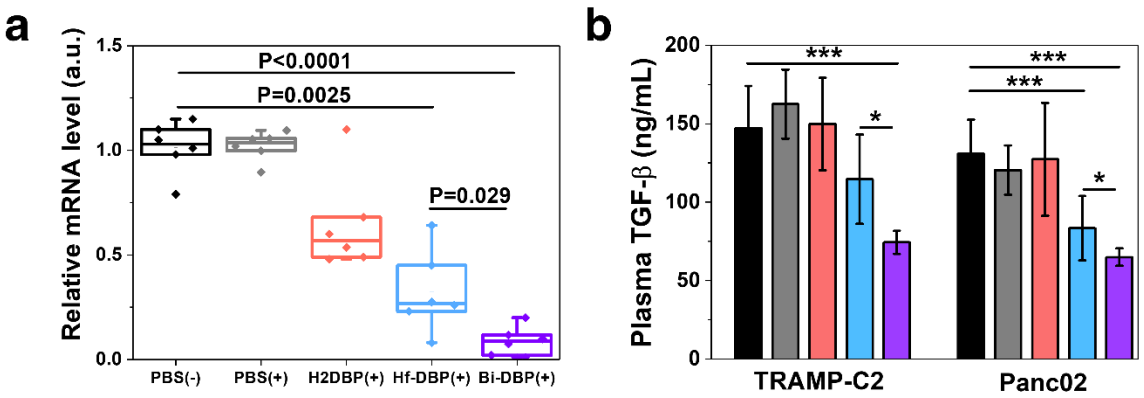

Figure 3-17. Reversal of systemic immunosuppression by TGF-β. (a) Intratumoral TGF-β RNA levels of tumors from TRAMP-C2 tumor-bearing mice, n = 6. (b) TGF-β concentration in plasma of as-treated mice bearing TRAMP-C2 or Panc02 tumors quantified by ELISA, n = 6.

3.2.6. Combination therapy with immune checkpoint blockade

We next investigated whether reversal of systemic immunosuppression and diminishment of physical barrier for T cell infiltration by Bi-DBP-mediated RT–RDT could benefit the therapeutic effect of checkpoint blockade immunotherapy. The combination of Bi-DBP(+) and an anti-PD-L1 antibody (αPD-L1) was evaluated in bilateral flank models of TRAMP-C2 and Panc02 tumors on C57BL/6 mice. Local Bi-DBP injection and intraperitoneal αPD-L1 injection followed by low dose X-ray irradiation led to regression or eradication of the treated primary tumors, and reduced volumes of the untreated distant tumors, suggesting that the treatment evoked an immune response in mouse models of prostate and pancreatic cancers (**Figure 3-18**). In comparison, PBS(+), αPD-L1(+), and Bi-DBP(-)+αPD-L1 treatments had no effect on the growth of both TRAMP-C2 and Panc02 tumors. Bi-DBP(+) slowed the growth of both primary and distant tumors on the TRAMP-C2 model but had no effect on the distant tumors of the Panc02 model. These results support the synergy between PD-L1 inhibition and Bi-DBP-mediated RT–RDT in eliciting systemic antitumor immunity. For TRAMP-C2 tumor-bearing mice, Bi-DBP(+)+αPD-L1 treatment led to complete response in 3 out of 6 mice and prolonged the median survival time to over 170 days from 71.5 days for the PBS(-) control (**Figure 3-18c** and **Table 3-3**). For Panc02 tumor-bearing mice, Bi-DBP(+)+αPD-L1 treatment led to complete response in 1 out of 6 mice and prolonged the median survival time to 112 days from 48 days for the PBS(-) control (**Figure 3-18f** and **Table 3-4**). The results demonstrate that Bi-TBP mediated RT–RDT elicit systemic antitumor response to improve the αPD-L1 checkpoint blockade immunotherapy, leading to the regression of both treated primary tumors and untreated distant tumors via abscopal effects.

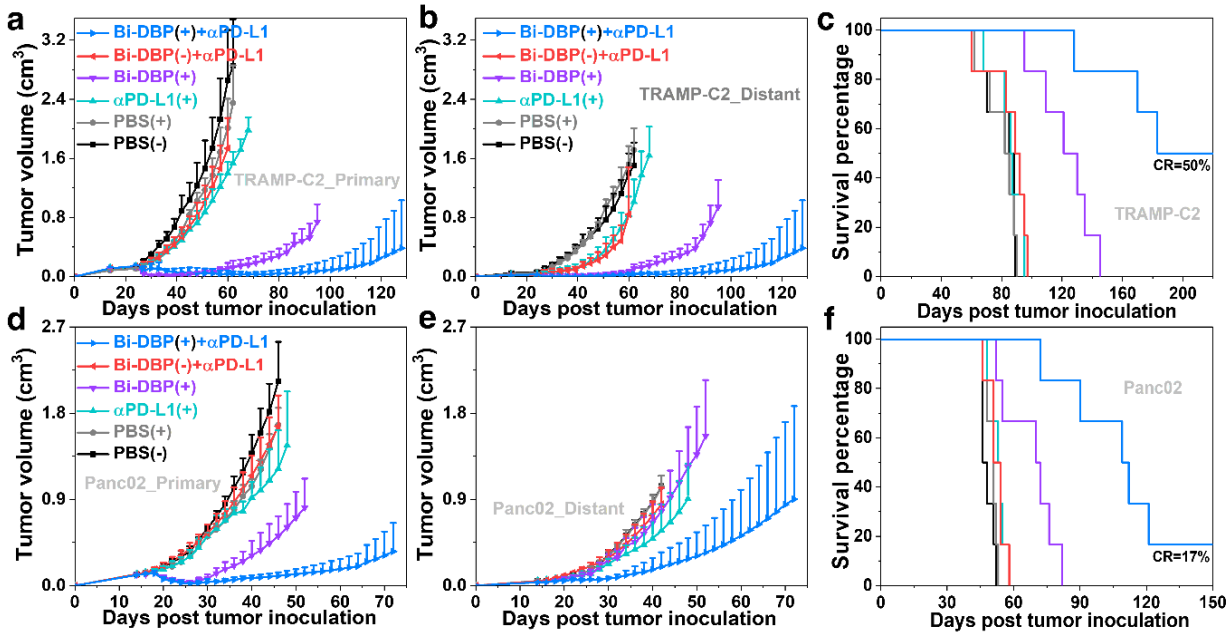

Figure 3-18. *In vivo* anticancer efficacy of combination therapy. Tumor growth curves of (**a**,**d**) primary and (**b**,**e**) distant tumors and (**c**,**f**) survival curves of TRAMP-C2 (**a**–**c**) or Panc02 (**d**–**f**) bilateral tumor-bearing mice treated with intratumorally injected Bi-DBP or PBS, intraperitoneally injected with αPD-L1 with (+) or without (–) X-ray irradiation, $n = 6$ biological replicates. CR, cure rate.

Table 3-3. Survival analysis of TRAMP-C2 tumor models with different treatments. P-values versus the Bi-DBP(+)+αPD-L1 group.

Group	TRAMP-C2		
	Median survival (d)	P-value	Cure rate (%)
PBS(-)	77.5	<0.001	0
PBS(+)	71.5	<0.001	0
αPD-L1(+)	74.5	<0.001	0
Bi-DBP(+)	113.5	<0.01	0
Bi-DBP(-)+αPD-L1	78.5	<0.001	0
Bi-DBP(+)+αPD-L1	170	-	50

Table 3-4. Survival analysis of Panc02 tumor models with different treatments. P-values versus the Bi-DBP(+)+αPD-L1 group.

Group	Panc02		
	Median survival (d)	P-value	Cure rate (%)
PBS(-)	47	<0.001	0
PBS(+)	51	<0.001	0
αPD-L1(+)	53.5	<0.001	0
Bi-DBP(+)	71	<0.001	0
Bi-DBP(-)+αPD-L1	52	<0.001	0
Bi-DBP(+)+αPD-L1	110.5	-	16.7

3.3 Conclusions

In this chapter, we showed that the radiosensitization capability of RT–RDT could be optimized by maximizing energy deposition with Bi, the heaviest naturally occurring non-radioactive and biocompatible element. $Bi_{10}O_8$ SBUs in Bi-DBP exhibit higher X-ray absorption and energy transfer efficiency than $Hf_{12}O_8$ SBUs in Hf-DBP to enhance ROS generation: $^{\bullet}OH$ from RT and $^1O_2$ from RDT. The intracellular oxidative stress caused by RT–RDT efficiently induces ICD as evidenced by CRT exposure, HMGB-1 release and ATP secretion. This nanoradiosensitizer effectively reverses immunosuppression in poorly immunogenic tumors and improves T cell infiltration. In conjunction with αPD-L1 checkpoint blockade, Bi-DBP-mediated RT–RDT reverses immunosuppression in both primary and distant tumors by systemically reducing TGF-β levels and the stiffness of solid tumors, promotes T cell infiltration and affords robust abscopal effect in immunosuppressive prostate and pancreatic tumor models (**Figure 3-19**). These findings highlight the potential of RT–RDT as a local tumor management approach and a promising immunoadjuvant treatment to enhance the therapeutic efficacy of cancer immunotherapy.

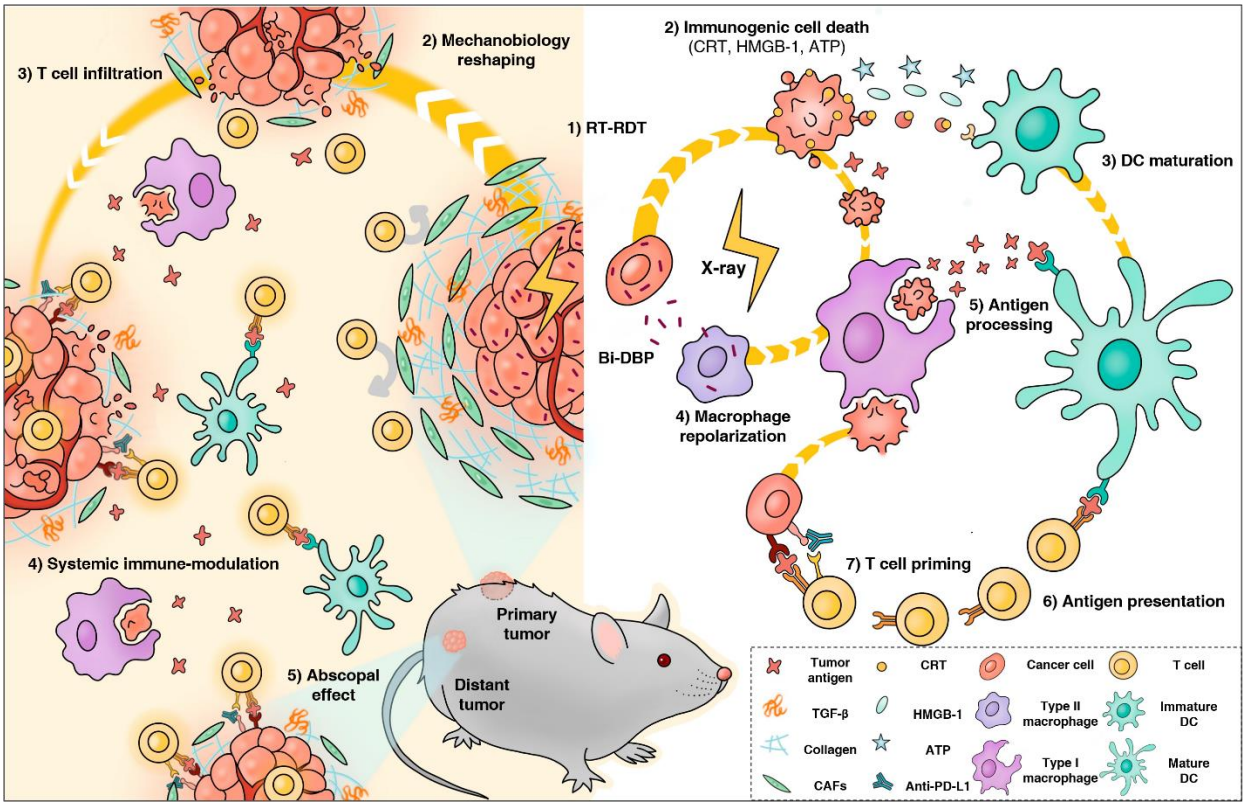

Figure 3-19. Proposed mechanism for biomechanic modulation by Bi-DBP-mediated RT–RDT.

3.4. Methods

Synthesis and characterizations of Bi-DBP. $Bi(NO_3)_3 \cdot 5H_2O$ and H_2DBP were separately dissolved in a mixed solvent of DMF and ethanol (EtOH) (3:1 v/v) at a concentration of 2 g/L. 2 μL trifluoroacetic acid (TFA, 99%), 65 μL deionised water, 700 μL $Bi(NO_3)_3$ solution and 300 μL H_2DBP solution were then mixed in a 1-dram vial and heated at 80 °C for 1 day. The resulting purple powder was washed sequentially with copious amounts of DMF, 1% triethylamine in ethanol (v/v), and ethanol before finally being suspended in ethanol. ICP-MS (7700x, Agilent, USA) was used to quantify the Bi content in Bi-DBP after digestion with a mixture of hydrofluoric acid and concentrated nitric acid (v/v=1:99). The sample was also digested with H_3PO_4/DMSO (85% H_3PO_4: DMSO = 5: 95 v/v) for UV-Vis detection of H_2DBP.

Synthesis of Hf-DBAn and Bi-DBAn. Hf-DBAn was synthesized through a solvothermal reaction between $HfCl_4$ and 4,4'-(9,10-anthracenediyl)dibenzoic acid (H_2DBAn) in DMF at 80 °C according to previous protocol.[33] Bi-DBAn was synthesized by heating a mixture of 1.8 mg $Bi(NO_3)_3 \cdot 5H_2O$ and 0.6 mg H_2DBAn in 1 mL of DMF, 2 μL TFA, and 5 μL H_2O at 80 °C for 12 hours. The white precipitate was collected by centrifugation and washed with DMF three times before being dispersed in DMF as a stock suspension.

Cellular uptake. The cellular uptake of Hf-DBP and Bi-DBP was evaluated on TRAMP-C2 cells. Cells were seeded on 6-well plate at 1.5×10^6/well and further cultured overnight. Particles were added to the cells at a Hf or Bi concentration of 20 μM. After incubation of 1, 2, 4 or 8 hours, the cells were collected, and the cell numbers were counted by a hemocytometer. Cells were digested with 1% hydrofluoric acid and concentrated nitric acid in a microwave reactor (CEM, USA) and the Hf concentrations were determined by ICP-MS (Agilent, USA). Results were expressed as the amount of Hf or Bi (ng) per 10^5 cells.

Irradiator settings. An RT250 orthovoltage X-ray machine model (Philips, USA) with fixed setting at 250 kVp, 15 mA and a built-in 1 mm Cu filter was used for *in vitro studies*. An X-RAD 225 image-guided biological irradiator (Precision X-ray Inc., USA) was used for both test tube and *in vivo* studies. The instrument was set at 225 kVp and 13 mA, with a 0.3 mm flat-board Cu filter installed before a 15 mm collimator. A γ-ray irradiator was used for APT assay and clonogenic assay. All three irradiators are maintained and calibrated for dosimetry routinely by the Department of Radiation Oncology, the University of Chicago, before all experiments.

Radioluminescence. Hf-DBAn and Bi-DBAn were suspended in ethanol at an equivalent concentration of 1 mM, degassed and filled with nitrogen gas. The solutions were transferred to 1 dram vials for X-ray irradiation with a maximum dose rate of 2.93 Gy/min. X-ray luminescence

measurements were acquired with a small animal irradiator (X-RAD 225Cx by Precision X-ray) through a 2 mm aluminum filter. The radioluminescence was detected using a cooled CoolSNAP HQ2 CCD camera (Photometrics, USA) equipped with a DX Micro-NIKKOR f/2.8 macro lens (Nikon, Japan). Samples were tested at a voltage of 70 kVp and current values ranging from 5, 10, 20, 30 to 40 mA for 30 s. Radioluminescence intensities were processed by ImageJ with background subtraction.

$^{\bullet}$OH generation with APF assay. Aminophenyl fluorescein (APF, ThermoFisher, USA) reacts with $^{\bullet}$OH to give bright green fluorescence (excitation/emission maxima 490/515 nm). Hf-DBP and Bi-DBP were suspended in water at an equivalent concentration of 20 mM in the presence of 5 μM APF. A water solution of 5 μM APF was used as blank control. 100 μL of each suspension was added to a 96-well plate and then irradiated with X-rays at 0, 1, 2, 5, or 10 Gy or γ-rays at 0, 1, 2, 3 or 5 Gy. The fluorescence signal was collected with an IVIS 200 imaging system (Xenogen, USA).

Cytotoxicity assay. 3-(4,5-dimethylthiazol-2-yl)-5-(3-carboxymethoxyphenyl)-2-(4-sulfo-phenyl)-2H-tetrazolium (MTS) assay (Promega, USA) was used to evaluate cytotoxicity with or without X-ray or γ-ray irradiation. TRAMP-C2 cells were seeded on 96-well plates at 1×10^4/well and further cultured for 12 h. PBS, H_2DBP, Hf-DBP, or Bi-DBP was added to the cells at an equivalent dose of 0, 1, 2, 5, 10, 20, 50 and 100 μM and incubated for 4 h. The cells were then irradiated at a dose of 2 Gy and further incubated for 72 h before determining the cell viability by MTS assay.

Clonogenic assay. TRAMP-C2 cells were cultured in a 6-well plate overnight and incubated with particles at a Hf or Bi concentration of 20 μM for 4 h followed by X-ray or γ-ray irradiation with 0, 1, 2, 4, 8 Gy. The irradiated cells were trypsinised and counted immediately. 200-2000 cells

were seeded in a 6-well plate and cultured with 2 mL medium for 14 days to form visible colonies, which were counted to determine the survival fraction. Once colony formation was observed, the culture medium was discarded. The plates were rinsed twice with PBS, then stained with 500 μL of 0.5% w/v crystal violet in 50% methanol/H_2O. The wells were rinsed with water three times and the colonies were counted manually. The radiation enhancement factor at 10% survival dose (REF_{10}) was calculated as the ratio of equivalent irradiation doses needed to give 10% survival rate for the PBS control group over that for the experimental group.

Apoptosis/necrosis assay. The cell death analysis was performed with an apoptotic cell death kit. TRAMP-C2 cells were cultured in a 6-well plate at 5×10^5/well overnight and incubated with H_2DBP, Hf-DBP, or Bi-DBP at an equivalent concentration of 20 μM followed by irradiation at 0 or 2 Gy. Cells incubated with PBS served as a control. 24 h later, the cells were stained with the AlexaFluor 488 Annexin V/dead cell apoptosis kit (Life technology, USA), imaged under confocal laser scanning microscope (CLSM, FV1000, Olympus, Japan) and quantified by LSRFortessa 4-15 flow cytometer (BD, USA).

SOSG assay. Singlet oxygen sensor green (SOSG) reagent (Life Technologies, USA) was employed for the detection of singlet oxygen. TRAMP-C2 cells were cultured in a 6-well plate at 5×10^5/well overnight, preloaded with SOSG and incubated with H_2DBP, Hf-DBP, or Bi-DBP at an equivalent concentration of 20 μM followed by irradiation at 0 or 2 Gy. Cells incubated with PBS served as a control. The slides were then immediately washed with PBS and observed under CLSM (FV1000, Olympus, Japan).

COX-2 upregulation. The cell membrane damage caused by RDT upon X-ray irradiation was investigated by COX-2 assay (BD Bioscience, USA). TRAMP-C2 cells were cultured in a 6-well plate at 5×10^5/well overnight and incubated with H_2DBP, Hf-DBP, or Bi-DBP at an equivalent

concentration of 20 μM followed by irradiation at 0 or 2 Gy. Cells incubated with PBS served as a control. Cells were fixed with 4% paraformaldehyde 24 h after X-ray irradiation. Biotin-conjugated anti-COX-2 antibody (PerkinElmer, USA) with a concentration of 10 μg/mL was incubated with cells at 4 °C overnight then followed by incubation with Cy5-conjugated streptavidin. The nuclei were stained with DAPI and the red fluorescence indicated the up-regulated expression of COX-2 stained with Cy3-labeled antibody. The cells were imaged with CLSM.

DNA double strand breaks. The DNA double strand breaks were detected by probing phosphorylated γ-H2AX. TRAMP-C2 cells were cultured in a 6-well plate at 5×10^5/well overnight and incubated with PBS, H_2DBP, Hf-DBP, or Bi-DBP at an equivalent concentration of 20 μM followed by irradiation at 0 and 2 Gy. Cells were stained 2 h after irradiation with the HCS DNA damage kit (Life Technology, USA) with 1:500 dilution for confocal laser scanning microscope (CLSM, FV1000, Olympus, Japan) imaging and LSRFortessa 4-15 flow cytometric analysis (BD, USA).

Immunogenic cell death. The immunogenic cell death was examined by calreticulin (CRT) exposure, HMGB-1 secretion and ATP release. TRAMP-C2 cells were cultured in a 6-well plate at 5×10^5/well overnight and incubated with PBS, H_2DBP, Hf-DBP, or Bi-DBP at an equivalent concentration of 20 μM followed by irradiation at 0 and 2 Gy. The supernatant was harvested for extracellular HMGB-1 and ATP secretion assayed by HMGB-1 ELISA kit (Invitrogen, USA) and Chemiluminescence ATP Determination kit (Thermo Fisher, USA), respectively. The cells were then washed with PBS gently and stained with AlexaFluor 488-CRT antibody (Enzo Life Sciences, USA) with 1: 100 dilution, imaged under CLSM and quantified by flow cytometric analysis.

***In vivo* anticancer efficacy.** *In vivo* anticancer efficacy of Bi-DBP and Hf-DBP on subcutaneous prostate (TRAMP-C2) and pancreatic (Panc02) mouse models. 5×10^6 TRAMP-C2 or 2×10^6 Panc02 cells were subcutaneously inoculated into the right flanks of C57BL/6 mice. When the tumors reached 100-150 mm^3 in volume for TRAMP-C2 or 75-100 mm^3 for Panc02, mice were injected intratumorally with H_2DBP, Hf-DBP or Bi-DBP at an equivalent dose of 0.2 μmol or PBS. 12 h after injection, mice were anaesthetized with 2% (v/v) isoflurane and the primary tumors were irradiated with 1 Gy X-ray/fraction for a total of 6 daily fractions. When the size of the tumors in the control group reached 2 cm^3, all of the mice were euthanized and tumors were exercised, weighed, and sectioned for immunofluorescence staining.

Mechanical analysis. Uniaxial compression and stress relaxation tests were conducted for mechanical analysis of tumors on a strain-controlled dynamic mechanical analyser (RSA-G2, TA instruments, USA). Tumors of 50-500 mm^3 in sizes were loaded between 1.5 cm diameter stainless steel parallel plates with an excess of buffer to maintain adequate hydration during the course of the experiment. All tests were performed at ambient temperature (20 ℃). For uniaxial test to quantify tumor Young's moduli, tumor samples were pre-loaded with compression force of 0.05 N and subjected to a compressive strain with a 50 % per minute constant compression rate. The average Young's moduli for the control and treated tumors were obtained from analysis of the stress-strain curves in the linear viscoelastic regions, below 5% compression. For stress relaxation to determine tumor viscoelasticity, tumor samples were pre-loaded with a compression force of 0.05 N and subjected to a uniaxial compressive step strain (2%). The generated compressive stress was monitored for 400 s.

Abscopal effect. Synergistic bilateral tumor models, TRAMP-C2 and Panc02 were established to evaluate the *in vivo* anti-cancer efficacy of combination of Bi-DBP-mediated RT–RDT and αPD-

L1 CBI. For TRAMP-C2, 5×10^6 and 1×10^6 TRAMP-C2 cells were subcutaneously inoculated onto the right and left flanks of C57BL/6 mice for respective primary and distant tumors. For Panc02, 2×10^6 and 1×10^6 Panc02 cells were subcutaneously inoculated onto the right and left flanks ofC57BL/6 mice for respective primary and distant tumors. When the primary tumors reached 100-150 mm^3 in volume, mice were injected intratumorally with Bi-DBP at a dose of 0.2 μmol Bi or PBS. 12 h after injection, mice were anesthetized with 2% (v/v) isoflurane and the primary tumors were irradiated with 1 Gy X-ray/fraction for a total of 6 daily fractions. Antibodies were given every three days by intraperitoneal injection at a dose of 75 μg/mouse. The tumor sizes were measured daily with a caliper where tumor volume equals $(width^2 \times length)/2$. Statistical analysis was performed using the log-rank Kaplan-Meier estimation.

Statistical analysis. Group sizes ($n \geq 5$) were chosen to ensure proper statistical ANOVA analysis for efficacy studies. Student's t-tests were used to determine if the variance between groups is similar. Statistical analysis was performed using OriginPro (OriginLab Corp.). Statistical significance was calculated using two-tailed Student's t-tests and defined as * $P < 0.05$, ** $P < 0.01$, *** $P < 0.001$. Animal experiments were not performed in a blinded fashion and are represented as mean $\pm$ SD. The immune analysis was performed in a blinded fashion and are represented as median $\pm$ SD.

3.5. References

(1) Blankenstein, T.; Coulie, P. G.; Gilboa, E.; Jaffee, E. M., The determinants of tumour immunogenicity. *Nat Rev Cancer* **2012,** *12* (4), 307-13.

(2) Hodi, F. S.; O'Day, S. J.; McDermott, D. F.; Weber, R. W.; Sosman, J. A.; Haanen, J. B.; Gonzalez, R.; Robert, C.; Schadendorf, D.; Hassel, J. C.; Akerley, W.; van den Eertwegh, A. J. M.; Lutzky, J.; Lorigan, P.; Vaubel, J. M.; Linette, G. P.; Hogg, D.; Ottensmeier, C. H.; Lebbé, C.; Peschel, C.; Quirt, I.; Clark, J. I.; Wolchok, J. D.; Weber, J. S.; Tian, J.; Yellin, M. J.; Nichol, G. M.; Hoos, A.; Urba, W. J., Improved Survival with Ipilimumab in Patients with Metastatic Melanoma. *New England Journal of Medicine* **2010,** *363* (8), 711-723.

(3) Beer, T. M.; Kwon, E. D.; Drake, C. G.; Fizazi, K.; Logothetis, C.; Gravis, G.; Ganju, V.; Polikoff, J.; Saad, F.; Humanski, P.; Piulats, J. M.; Gonzalez Mella, P.; Ng, S. S.; Jaeger, D.; Parnis, F. X.; Franke, F. A.; Puente, J.; Carvajal, R.; Sengelov, L.; McHenry, M. B.; Varma, A.; van den Eertwegh, A. J.; Gerritsen, W., Randomized, Double-Blind, Phase III Trial of Ipilimumab Versus Placebo in Asymptomatic or Minimally Symptomatic Patients With Metastatic Chemotherapy-Naive Castration-Resistant Prostate Cancer. *J Clin Oncol* **2017,** *35* (1), 40-47.

(4) Martinez-Bosch, N.; Vinaixa, J.; Navarro, P., Immune Evasion in Pancreatic Cancer: From Mechanisms to Therapy. *Cancers* **2018,** *10* (1), 6.

(5) Castano, A. P.; Mroz, P.; Hamblin, M. R., Photodynamic therapy and anti-tumour immunity. *Nat Rev Cancer* **2006,** *6* (7), 535-45.

(6) Weichselbaum, R. R.; Liang, H.; Deng, L.; Fu, Y.-X., Radiotherapy and immunotherapy: a beneficial liaison? *Nature Reviews Clinical Oncology* **2017**.

(7) Zheng, G.; Chen, J.; Stefflova, K.; Jarvi, M.; Li, H.; Wilson, B. C., Photodynamic molecular beacon as an activatable photosensitizer based on protease-controlled singlet oxygen quenching and activation. *Proceedings of the National Academy of Sciences* **2007,** *104* (21), 8989-8994.

(8) Zhou, Z.; Song, J.; Nie, L.; Chen, X., Reactive oxygen species generating systems meeting challenges of photodynamic cancer therapy. *Chemical society reviews* **2016,** *45* (23), 6597-6626.

(9) Siva, S.; MacManus, M. P.; Martin, R. F.; Martin, O. A., Abscopal effects of radiation therapy: a clinical review for the radiobiologist. *Cancer Lett* **2015,** *356* (1), 82-90.

(10) Wan, C.; Sun, Y.; Tian, Y.; Lu, L.; Dai, X.; Meng, J.; Huang, J.; He, Q.; Wu, B.; Zhang, Z.; Jiang, K.; Hu, D.; Wu, G.; Lovell Jonathan, F.; Jin, H.; Yang, K., Irradiated tumor cell–derived microparticles mediate tumor eradication via cell killing and immune reprogramming. *Sci. Adv.* **2020,** *6* (13), eaay9789.

(11) Nam, J.; Son, S.; Park, K. S.; Zou, W.; Shea, L. D.; Moon, J. J., Cancer nanomedicine for combination cancer immunotherapy. *Nature Reviews Materials* **2019,** *4* (6), 398-414.

(12) Chen, H.; Wang, G. D.; Chuang, Y.-J.; Zhen, Z.; Chen, X.; Biddinger, P.; Hao, Z.; Liu, F.; Shen, B.; Pan, Z., Nanoscintillator-mediated X-ray inducible photodynamic therapy for in vivo cancer treatment. *Nano letters* **2015,** *15* (4), 2249-2256.

(13) Sang, W.; Zhang, Z.; Dai, Y.; Chen, X., Recent advances in nanomaterial-based synergistic combination cancer immunotherapy. *Chemical Society Reviews* **2019,** *48* (14), 3771-3810.

(14) Luo, M.; Wang, H.; Wang, Z.; Cai, H.; Lu, Z.; Li, Y.; Du, M.; Huang, G.; Wang, C.; Chen, X., A STING-activating nanovaccine for cancer immunotherapy. *Nature nanotechnology* **2017,** *12* (7), 648.

(15) Lu, K.; He, C.; Guo, N.; Chan, C.; Ni, K.; Lan, G.; Tang, H.; Pelizzari, C.; Fu, Y.-X.; Spiotto, M. T.; Weichselbaum, R. R.; Lin, W., Low-dose X-ray radiotherapy–radiodynamic therapy via nanoscale metal–organic frameworks enhances checkpoint blockade immunotherapy. *Nat. Biomed. Eng.* **2018,** *2* (8), 600-610.

(16) Lin, W.; He, C.; Kuangda, L., Nanoparticles for photodynamic therapy, x-ray induced photodynamic therapy, radiotherapy, chemotherapy, immunotherapy, and any combination thereof. Google Patents: 2014.

(17) Furukawa, H.; Cordova, K. E.; O'Keeffe, M.; Yaghi, O. M., The chemistry and applications of metal-organic frameworks. *Science* **2013,** *341* (6149), 1230444.

(18) Cui, Y.; Yue, Y.; Qian, G.; Chen, B., Luminescent functional metal–organic frameworks. *Chemical reviews* **2012,** *112* (2), 1126-1162.

(19) Zhou, H.-C.; Long, J. R.; Yaghi, O. M., Introduction to metal–organic frameworks. ACS Publications: 2012.

(20) Rabone, J.; Yue, Y.-F.; Chong, S.; Stylianou, K.; Bacsa, J.; Bradshaw, D.; Darling, G.; Berry, N.; Khimyak, Y.; Ganin, A., An adaptable peptide-based porous material. *Science* **2010,** *329* (5995), 1053-1057.

(21) He, C.; Liu, D.; Lin, W., Nanomedicine applications of hybrid nanomaterials built from metal–ligand coordination bonds: nanoscale metal–organic frameworks and nanoscale coordination polymers. *Chemical reviews* **2015,** *115* (19), 11079-11108.

(22) Morris, W.; Briley, W. E.; Auyeung, E.; Cabezas, M. D.; Mirkin, C. A., Nucleic acid–metal organic framework (MOF) nanoparticle conjugates. *Journal of the American Chemical Society* **2014,** *136* (20), 7261-7264.

(23) Wang, S.; McGuirk, C. M.; d'Aquino, A.; Mason, J. A.; Mirkin, C. A., Metal–organic framework nanoparticles. *Advanced Materials* **2018,** *30* (37), 1800202.

(24) Wang, C.; Volotskova, O.; Lu, K.; Ahmad, M.; Sun, C.; Xing, L.; Lin, W., Synergistic Assembly of Heavy Metal Clusters and Luminescent Organic Bridging Ligands in Metal–Organic Frameworks for Highly Efficient X-ray Scintillation. *Journal of the American Chemical Society* **2014,** *136* (17), 6171-6174.

(25) Dougherty, T. J.; Gomer, C. J.; Henderson, B. W.; Jori, G.; Kessel, D.; Korbelik, M.; Moan, J.; Peng, Q., Photodynamic Therapy. *JNCI: Journal of the National Cancer Institute* **1998,** *90* (12), 889-905.

(26) Garg, A. D.; Nowis, D.; Golab, J.; Agostinis, P., Photodynamic therapy: illuminating the road from cell death towards anti-tumour immunity. *Apoptosis* **2010,** *15* (9), 1050-71.

(27) Rabin, O.; Perez, J. M.; Grimm, J.; Wojtkiewicz, G.; Weissleder, R., An X-ray computed tomography imaging agent based on long-circulating bismuth sulphide nanoparticles. *Nature materials* **2006,** *5* (2), 118-122.

(28) Mendoza-Espinosa, D., Synthesis and characterization of a Bi 10 O 8 (OAr) 16 oxo-cluster supported by p-tert-butylcalix [5] arene ligands. *Dalton Transactions* **2016,** *45* (34), 13399-13405.

(29) Andrews, P. C.; Deacon, G. B.; Junk, P. C.; Kumar, I.; MacLellan, J. G., Synthesis, ethanolysis, and hydrolysis of bismuth (III) ortho-nitrobenzoate complexes en route to a pearl necklace-like polymer of Bi10 oxo-clusters. *Organometallics* **2009,** *28* (14), 3999-4008.

(30) Obeid, M.; Panaretakis, T.; Joza, N.; Tufi, R.; Tesniere, A.; Van Endert, P.; Zitvogel, L.; Kroemer, G., Calreticulin exposure is required for the immunogenicity of γ-irradiation and UVC light-induced apoptosis. *Cell Death & Differentiation* **2007,** *14* (10), 1848-1850.

(31) Sims, G. P.; Rowe, D. C.; Rietdijk, S. T.; Herbst, R.; Coyle, A. J., HMGB1 and RAGE in Inflammation and Cancer. *Annual Review of Immunology* **2010,** *28* (1), 367-388.

(32) Aymeric, L.; Apetoh, L.; Ghiringhelli, F.; Tesniere, A.; Martins, I.; Kroemer, G.; Smyth, M. J.; Zitvogel, L., Tumor Cell Death and ATP Release Prime Dendritic Cells and Efficient Anticancer Immunity. *Cancer Research* **2010,** *70* (3), 855-858.

(33) Ni, K.; Lan, G.; Chan, C.; Quigley, B.; Lu, K.; Aung, T.; Guo, N.; La Riviere, P.; Weichselbaum, R. R.; Lin, W., Nanoscale metal-organic frameworks enhance radiotherapy to potentiate checkpoint blockade immunotherapy. *Nat. Commun.* **2018,** *9* (1), 2351.

Chapter 4. Monte Carlo Simulation-Guided Design of a Thorium-based MOF for Efficient Radiotherapy–Radiodynamic Therapy

4.1. Introduction

As the second leading cause of death globally, cancer accounted for nearly 10 million deaths in 2020.[1] Several treatment strategies, including surgery,[2] radiotherapy (RT),[3-6] chemotherapy,[7] and immunotherapy, [8-10] have been developed to reduce cancer deaths. Among them, RT provides important curative and palliative treatments to more than half of all cancer patients.[11] RT utilizes ionizing radiation such as X-rays and γ-rays to kill cancer cells by directly inducing DNA damage or indirectly generating reactive oxygen species (ROS) to decompose biomolecules and break the redox balance.[12-13] However, high doses of radiation required for tumor eradication by RT often cause debilitating side effects to healthy tissues. As a result, radiosensitizers have been explored to enhance the cytotoxic effect of radiation on tumor cells and reduce side effects on normal tissues.[12, 14-15] In particular, heavy metal-based radiosensitizers such as gold[16-20] and hafnium oxide[21-22] nanoparticles (NPs) have attracted significant attention because the X-ray attenuation coefficient is proportional to the density and the 4th power of the atomic number of the materials.[23-26]

We have recently discovered nanoscale metal–organic frameworks (nMOFs) with heavy metal secondary building units (SBUs) and photosensitizing ligands as a novel class of radiosensitizers via a unique radiotherapy–radiodynamic therapy (RT–RDT) mode of action.[27-30] With three dimensional (3D) arrays of ultrasmall heavy metal SBUs, nMOFs afford superior radiosensitization over nonporous NPs by more efficiently scattering secondary photons and electrons.[31] It was further revealed that nMOFs with larger mass attenuation coefficients exhibit stronger dose enhancement effects.[31-34]

We posited that, as the heaviest naturally occurring element with low radioactivity (Z = 90 and half-life of the major isotope ^{232}Th = 14 billion years), Th could serve as an ideal element for constructing nMOF radiosensitizers. In particular, the higher K-edge energy of Th (110 keV) over that of Hf (65 keV) makes Th more suitable for clinically relevant megavoltage beams from linear particle accelerators and ^{60}Co sources.[35-36]

In this chapter, we report Monte Carlo simulation-guided design of a Th-DBP nMOF based on $Th_6O_4(OH)_4$ SBUs and photosensitizing DBP ligands (DBP = 5,15-di(p-benzoato)porphyrin) for efficient RT–RDT. Under X-ray or γ-ray irradiation, the electron-dense Th_6 SBUs effectively interact with photons and generate hydroxyl radicals while exciting the photosensitizing DBP ligands to generate $^1O_2$. The produced ROS efficiently kill cancer cells and regress colon and pancreatic cancers in mouse models.

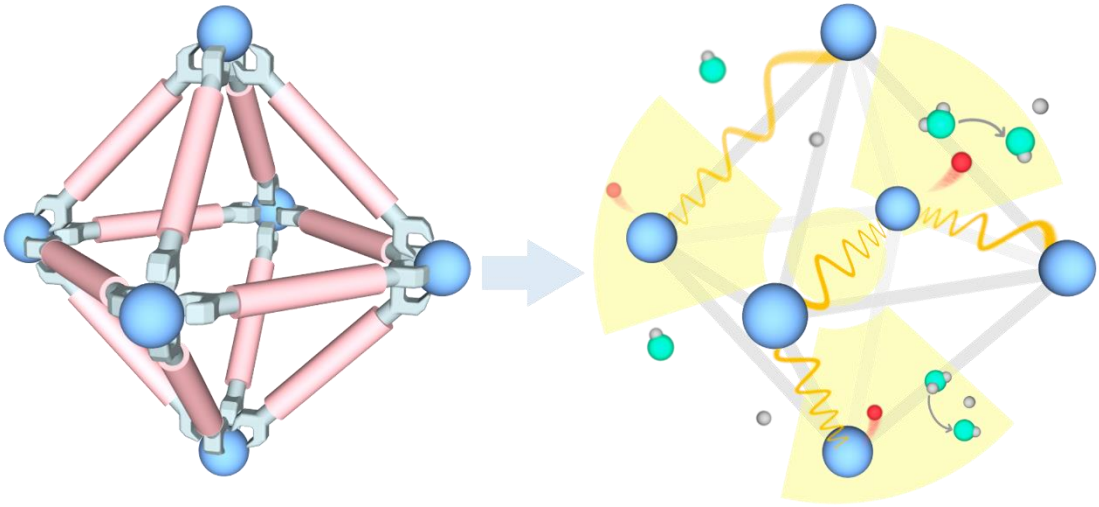

Figure 4-1. Schematic showing radioenhancement by a Th lattice.

4.2. Results and discussion

4.2.1. Monte Carlo simulation

We first performed Monte Carlo (MC) simulations with the EGSnrc toolkit[37-38] to compare physical dose enhancements of Th-nMOF and Hf-nMOF using a lattice model of nMOFs consisting of 3D hexagonal arrays of nanoscale SBUs (**Figure 4-1**). The lattice parameters were carefully selected to ensure the same lattice structure, inter-SBU distance, and atom number in each SBU for the Hf and Th lattices. MC simulations were performed via simulating phase space at a macroscopic depth in water and microscopically simulating energy deposition within a water shell around a lattice with condensed phase space as the incident beam. Dose enhancement factor (DEF), defined as the ratio of deposited energy in surrounding water by a metal lattice over that by water, was used to compare the radiosensitizing efficiencies between Th and Hf. The radii of the Hf and Th lattices for MC simulation were larger for ^{60}Co γ-ray, to lower the uncertainty to less than 10% due to the small absorption cross-section of lattices at megavoltage energy range. As expected, DEFs of the Th-lattice were higher than those of the Hf-lattice under both 120 keV monoenergetic X-ray and ^{60}Co γ-ray (**Figure 4-2, Table 4-1**), with maximum DEF(Th) over DEF(Hf) ratios of 1.77 and 1.22, respectively. Thus, MC simulations supported the enhanced radiosensitizing efficiency of Th-nMOFs over Hf-nMOFs.

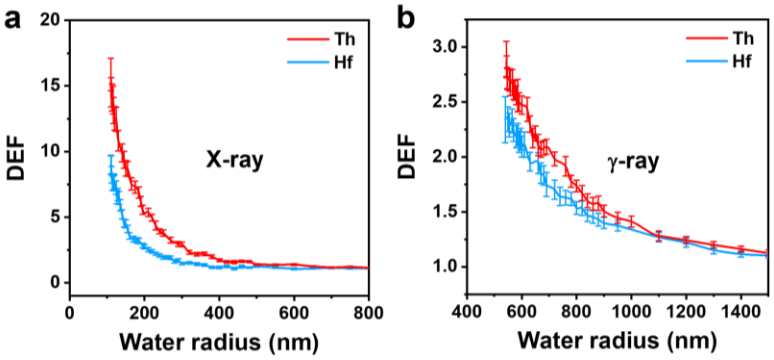

Figure 4-2. Comparisons of DEF curves of Th and Hf lattices under (a) X-ray or (b) γ-ray irradiation.

Table 4-1. Geometry settings for Th and Hf lattices and physical properties of Th and Hf.

Parameters	Hf	Th
SBU radius/nm	0.5	0.569
Lattice distance/nm	1.6	1.738
Lattice radius/nm (X-ray)	100	108.6
Lattice radius/nm (γ-ray)	500	543
Molar mass/ g·mol^{-1}	178.49	232.04
Density/g·cm^{-3}	13.31	11.72
K-edge (keV)	65.35	109.65

4.2.2. Synthesis and Characterization

We then rationally designed a Th-based nMOF with DBP photosensitizing ligands for enhanced RT–RDT. Th-DBP nMOF was synthesized via a solvothermal reaction between $Th_6O_4(OH)_4(HCOO)_{12}$ clusters, H_2DBP, formic acid, and water in *N*, *N*-dimethylformamide at 120 °C for 3 days (**Figure 4-3**).

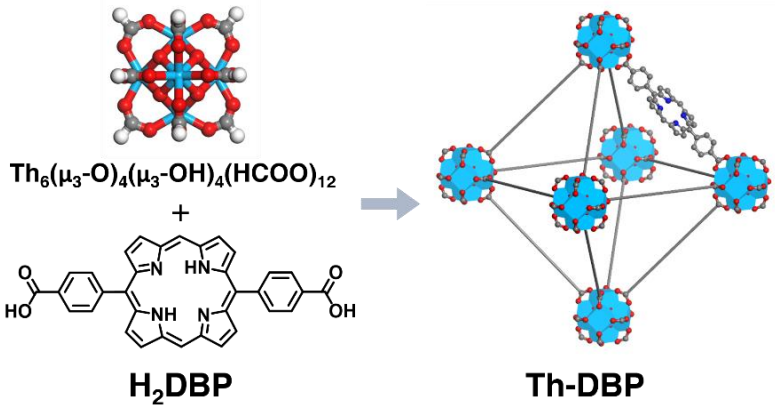

Figure 4-3. Synthesis of Th-DBP from Th_6 cluster and H_2DBP ligand.

Th-DBP displayed a nano-octahedron morphology with a diameter of ~80 nm under transmission electron microscopy (TEM) and scanning electron microscopy (SEM) (**Figure 4-4a&b**). The octahedron morphology is commonly observed for UiO-type MOFs with hexa-nuclear SBUs, suggesting successful linking of Th_6 clusters by linear DBP ligands. Th-DBP was coated

with phosphate-functionalized methoxy polyethylene glycol (mPEG-PO_3H_2) to ensure dispersibility and stability in biologically relevant media. Th-DBP@PEG was synthesized by stirring Th-DBP and mPEG-PO_3H_2 in ethanol for 24 hours and showed a similar but less regular octahedron morphology than Th-DBP (**Figure 4-5c**).[39]

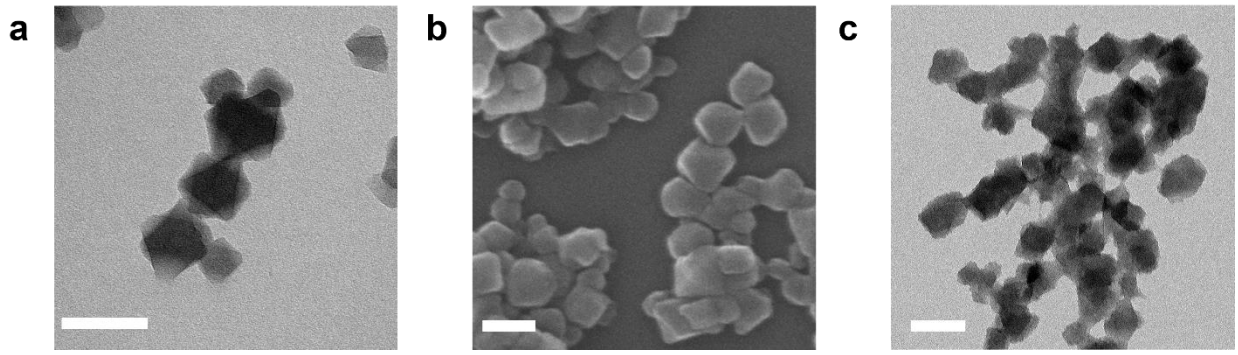

Figure 4-4. Morphology characterization. (a) TEM and (b) SEM images of Th-DBP. (c) TEM image of Th-DBP@PEG (Scale bars = 100 nm).

Th-DBP and Th-DBP@PEG showed number-averaged sizes of 127 ± 5 nm and 122 ± 6 nm, respectively, and ζ -potentials of −29 ± 2 mV and −32.6 ± 0.4 mV, respectively, by dynamic light scattering (DLS, **Figure 4-5**), suggesting that Th-DBP maintained the nanoscale size and surface charge after PEGylation.

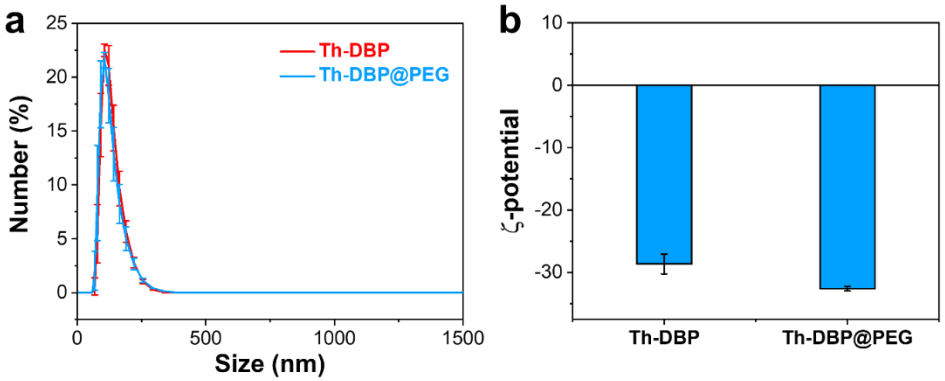

Figure 4-5. Size and charge characterization. (a) Number-averaged sizes of Th-DBP, Th-DBP@PEG, and Hf-DBP. (b) ζ -potentials of Th-DBP and Th-DBP@PEG in H_2O.

Powder X-ray diffraction (PXRD) patterns showed that Th-DBP adopted the same *fcu* topology as the previously reported UiO-69[40-41] with a slightly smaller 2θ value (3.94°) than UiO-

69 (2θ =3.96°) for the (111) reflection. This result is consistent with the larger lattice parameters of Th-nMOF over Zr-nMOF (**Figure 4-6a**). Based on the UiO-69 structure, Th-DBP has an idealized formula of $Th_6(\mu_3\text{-}O)_4(\mu_3\text{-}OH)_4(DBP)_6$. However, inductively coupled plasma-mass spectrometry (ICP-MS), UV-Vis spectroscopy, and ^1H NMR spectroscopy analyses of Th-DBP gave an empirical formula of $Th_6(\mu_3\text{-}O)_4(\mu_3\text{-}OH)_4(DBP)_{4.37}(HCOO)_{1.22}(OH)_{2.04}$ (**Figure 4-7**), likely due to a highly defected structure with missing DBP ligands. PXRD studies showed that Th-DBP@PEG retained crystallinity after incubation in 1 mM PBS for 3 days, ensuring its stability for biological applications (**Figure 4-6b**). Hf-DBP nMOF and Hf-DBP@PEG with a similar size to Th-DBP were synthesized[27] and used for radiosensitization comparisons.[42-43]

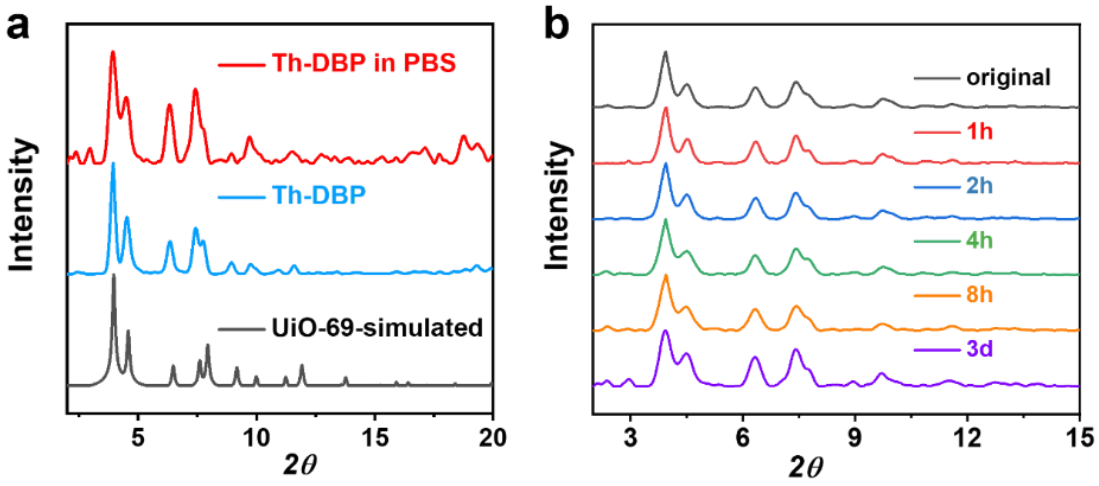

Figure 4-6. PXRD patterns of (a) Th-DBP (as synthesized and after incubation in PBS for 3 days) along with the simulated pattern for UiO-69. (b) PXRD patterns of Th-DBP@PEG after incubation in PBS for various time.

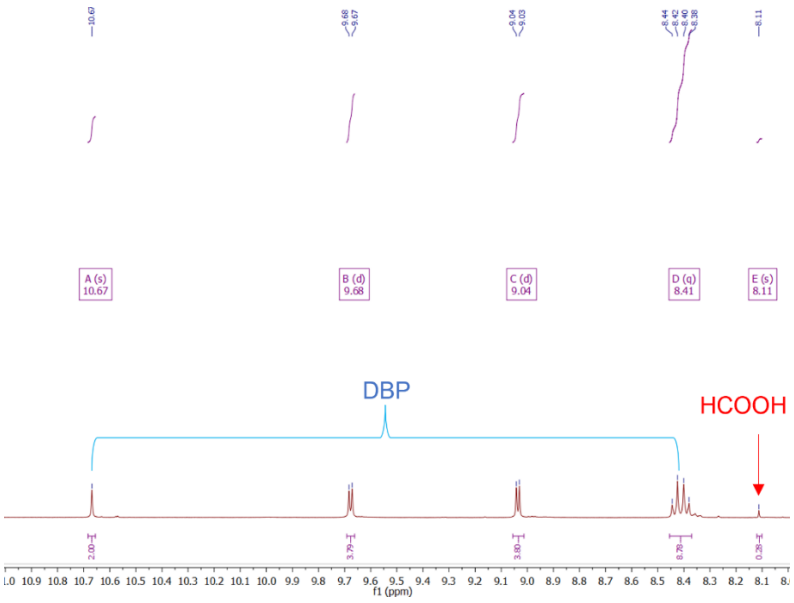

Figure 4-7. [1]H NMR spectrum of digested Th-DBP.

4.2.3. ROS detection

The ROS generation efficiency of Th-DBP and Hf-DBP was determined by the 2',7'-dichlorodihydrofluorescein (DCFH) assay in test tubes.[44] The ROS signals of both groups increased linearly with X-ray and γ-ray doses. The relative ROS enhancements of Th-DBP and Hf-DBP over PBS were 99% and 30%, respectively, under X-ray irradiation (**Figure 4-8a**), and 70% and 21%, respectively, under γ-ray irradiation (**Figure 4-8b**).

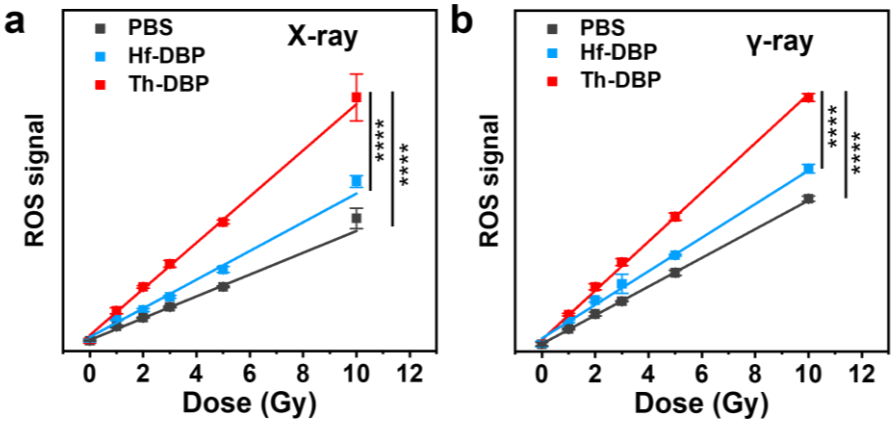

Figure 4-8. Total ROS signals of PBS, Hf-DBP, and Th-DBP after different doses of (a) X-ray or (b) γ-ray radiation, $n = 6$.

To compare the ROS generation by Th-based nMOF and Hf-based nMOF in RT, we synthesized isostructural Th_6-DBA and Hf_{12}-DBA (DBA = 2,5-di(p-benzoato)aniline) nMOFs via similar solvothermal reactions. Th_6-DBA and Hf_{12}-DBA nMOFs showed only 35% and 22% more ROS generation over PBS, respectively, which supports the contribution of the radiodynamic effect from DBP ligand and the better radiosensitizing ability of Th over Hf (**Figure 4-9**).

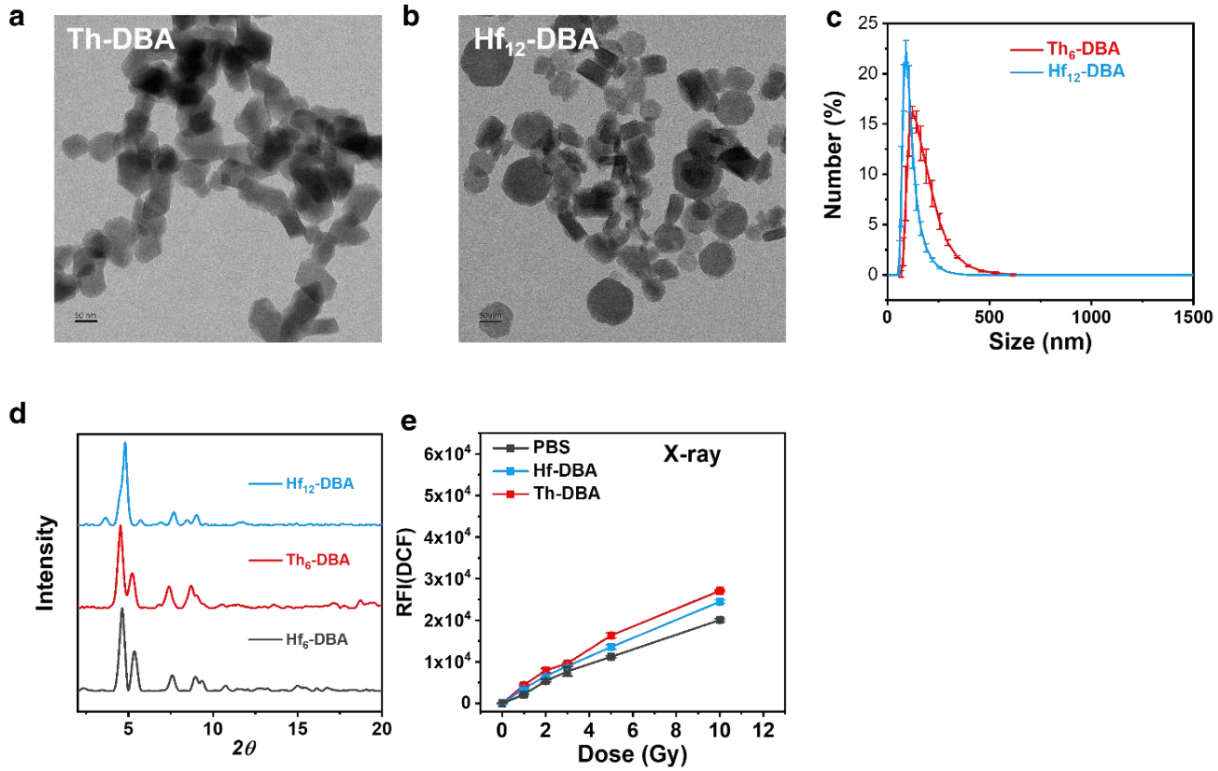

Figure 4-9. Characterization of Th_6-DBA and Hf_{12}-DBA. TEM images of (a) Th_6-DBA and (b) Hf_{12}-DBA and (c) their number-averaged sizes. (d) PXRD patterns of Hf_{12}-DBA and Th_6-DBA compared with Hf_6-DBA. (e) Total ROS signals of PBS, Hf_{12}-DBA, and Th_6-DBA by DCFH assays after different doses of X-ray irradiation. n=6.

4.2.4. *In vitro* experiments

After PEGylation, Th-DBP showed a similar cellular uptake to Hf-DBP as determined by ICP-MS (**Figure 4-10a**) and flow cytometry (**Figure 4-10b**). Cell viability assays showed that

neither Hf-DBP nor Th-DBP was toxic to CT26 (**Figure 4-10c**) and Panc02 (**Figure 4-10d**) cells at a metal concentration up to 50 μM, suggesting the biocompatibility of the two nMOFs.

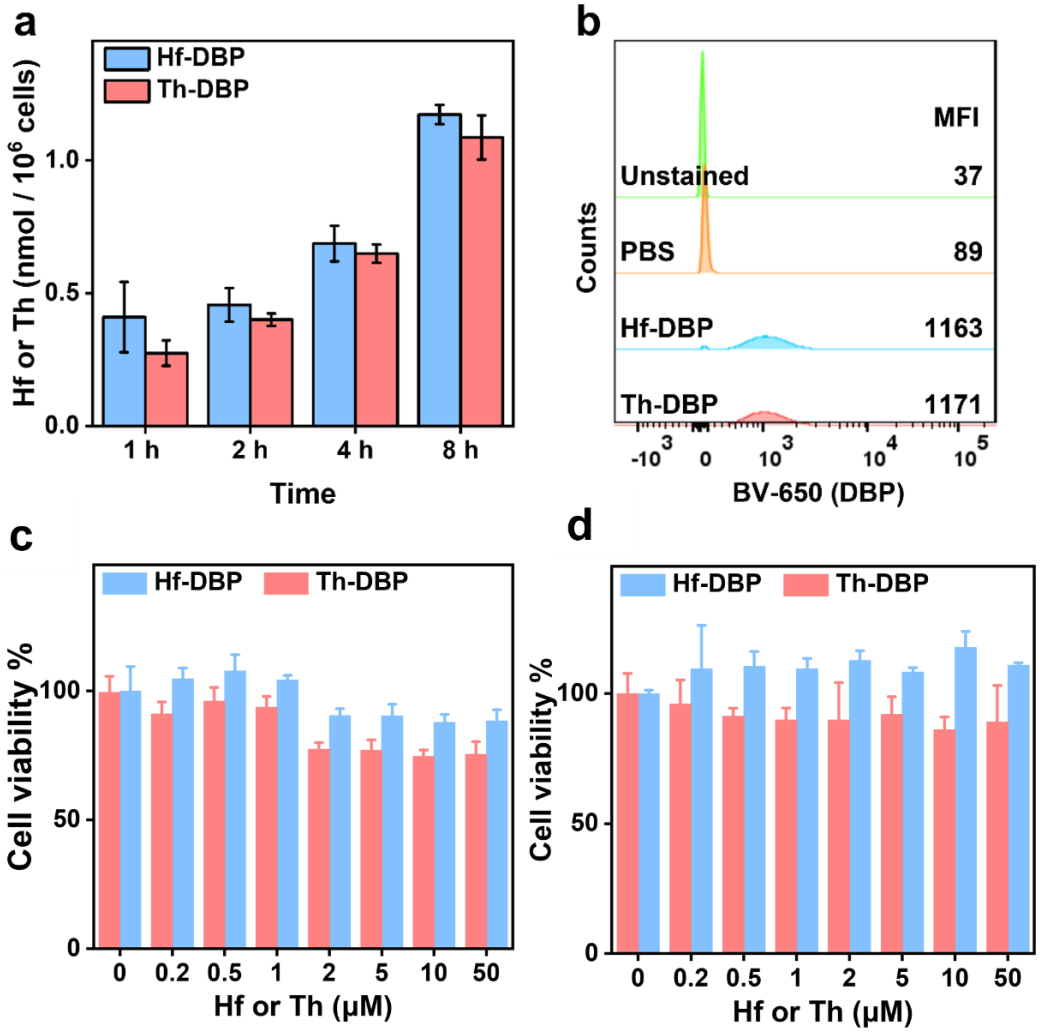

Figure 4-10. Cellular uptake and dark toxicity. (a) Time-dependent cellular uptake of Hf-DBP and Th-DBP quantified by ICP-MS (n = 3). (b) BV650 histograms showing mean fluorescence intensity (MFI) of DBP containing cells by flow cytometry. Cell viability curves of (a) CT26 and (b) Panc02 cells treated by Hf-DBP or Th-DBP without X-ray irradiation, respectively (n = 3).

In vitro 2',7'-dichlorodihydrofluorescein diacetate (DCFH-DA) assays showed that Th-DBP exhibited 1.16-fold and 1.08-fold higher ROS signals than Hf-DBP under X-ray and γ-ray irradiation, respectively (**Figure 4-11a**). In addition, Th-DBP showed 1.61-fold and 1.48-fold higher surface calreticulin (CRT) expressions than Hf-DBP under X-ray and γ-ray irradiation,

respectively (**Figure 4-11b**).[27, 45-47] Since CRT serves as an "eat-me" signal of dying cells for their recognition by phagocytes, more surface CRT expression indicates more cell apoptosis. Owing to the enhanced RT–RDT effect, Th-DBP gave 1.51-fold and 1.56-fold apoptotic cell death over Hf-DBP under X-ray (**Figure 4-11c**) and γ-ray (**Figure 4-11d**) irradiation, respectively.

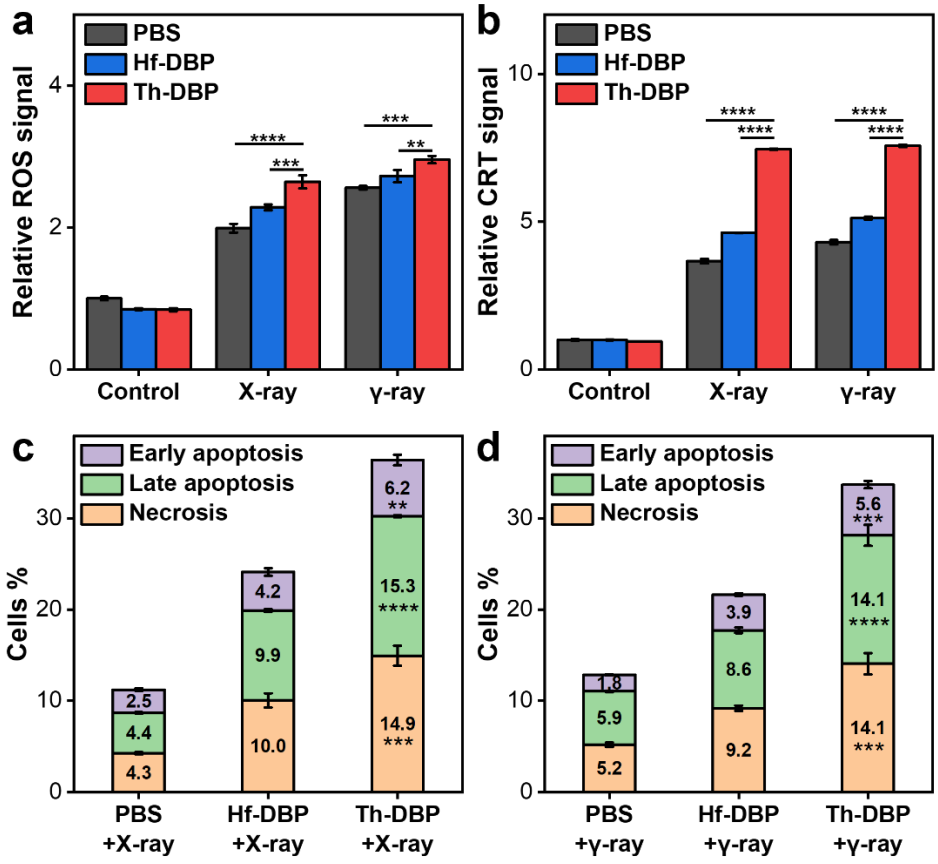

Figure 4-11. (a) Total ROS signals and (b) surface calreticulin expressions in CT26 cells after incubation with Hf-DBP or Th-DBP and irradiated with 2 Gy X-ray or 4 Gy γ-ray. Percentages of early apoptotic, late apoptotic, and necrotic CT26 cells after incubation with Hf-DBP or Th-DBP and irradiated with (a) 2 Gy X-ray or (b) 4 Gy γ-ray, n = 3. **, p<0.01, ***, p<0.001, and ****, p<0.0001.

The radiosensitizing effects of Th-DBP were evaluated by clonogenic assays, growth rate inhibition (GRI) assays, and DNA double-strand break (DSB) quantifications in CT26 and Panc02 cells. As the gold standard for radiotoxicity assessment, the clonogenic assay gave a dose modifying ratio at 10% surviving fraction ($DMR_{10\%}$) to evaluate radiation damage to proliferative

cells. For CT26 cells, the $DMR_{10\%}$ values were 1.72 and 1.20 for Th-DBP and Hf-DBP, respectively, under X-ray irradiation (**Figure 4-12a** and **Table 4-2**), and 2.25 and 1.44 for Th-DBP and Hf-DBP, respectively, under γ-ray irradiation (**Figure 4-12b** and **Table 4-3**). For Panc02 cells, the $DMR_{10\%}$ values were 1.32 and 1.22 for Th-DBP and Hf-DBP, respectively, under X-ray irradiation (**Figure 4-12c** and **Table 4-2**), and 1.52 and 1.17 for Th-DBP and Hf-DBP, respectively, under γ-ray irradiation (**Figure 4-12d** and **Table 4-3**).

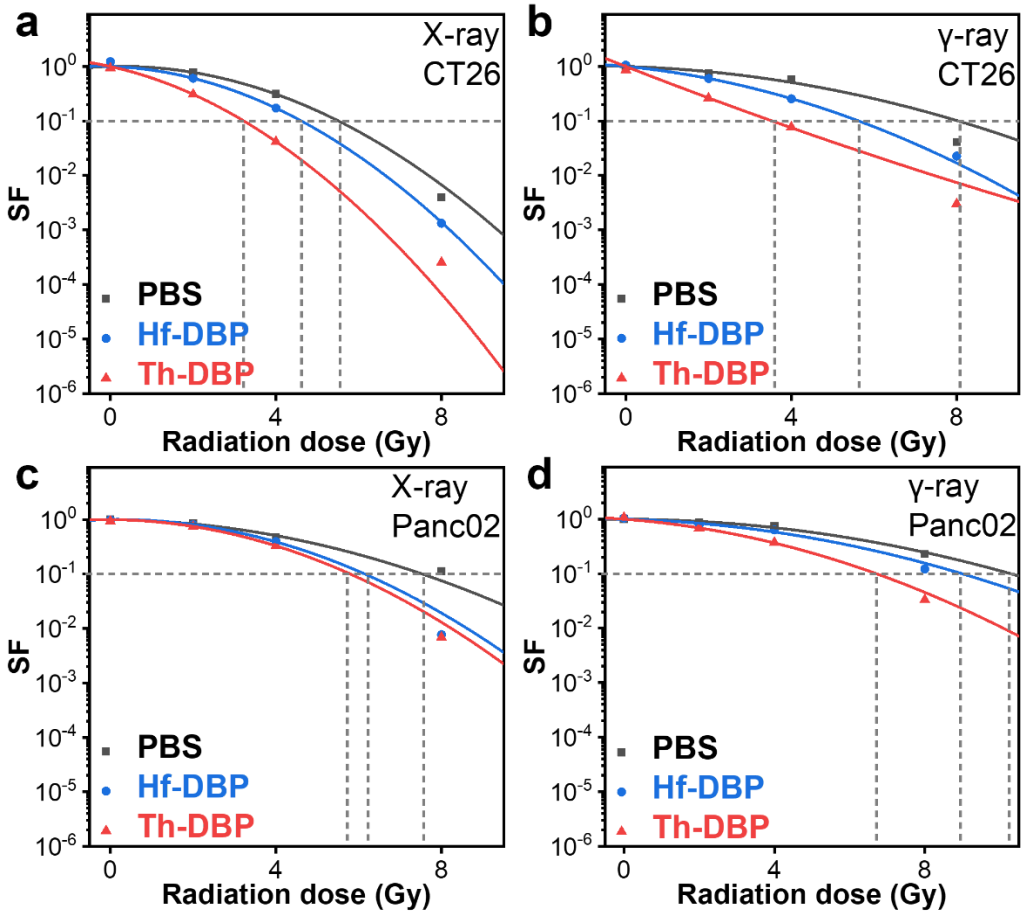

Figure 4-12. Clonogenic assays in CT26 cells. Linear-quadratic dose-fitting curves for surviving fractions (SF, log scale) of CT26 cells after (a) X-ray and (b) γ-ray irradiation and Panc02 cells after (c) X-ray and (d) γ-ray irradiation in clonogenic assays.

Table 4-2. SF, fitting parameters α and β, and $DMR_{10\%}$ of clonogenic assays with X-ray.

Cell Line		CT26			Panc02		
X-ray dose		PBS	Hf-DBP	Th-DBP	PBS	Hf-DBP	Th-DBP
SF	0 Gy	1.000	1.225	0.933	1.000	0.987	0.938
	2 Gy	0.778	0.608	0.308	0.858	0.806	0.746
	4 Gy	0.311	0.172	0.042	0.474	0.393	0.330
	8 Gy	0.004	0.001	0.0003	0.113	0.008	0.007
Fitting Parameters	α	-0.041	0.057	0.38	0.015	-0.022	0.013
	β	0.083	0.096	0.10	0.038	0.065	0.066
$DMR_{10\%}$		Hf-DBP	Th-DBP		Hf-DBP	Th-DBP	
		1.20	1.72		1.22	1.32	

Table 4-3. SF, fitting parameters α and β, and $DMR_{10\%}$ of clonogenic assays with γ-ray.

Cell Line		CT26			Panc02		
γ-ray dose		PBS	Hf-DBP	Th-DBP	PBS	Hf-DBP	Th-DBP
SF	0 Gy	1.000	1.055	0.865	1.000	1.047	1.076
	2 Gy	0.741	0.603	0.264	0.873	0.789	0.685
	4 Gy	0.583	0.255	0.078	0.737	0.636	0.374
	8 Gy	0.041	0.023	0.003	0.229	0.122	0.033
Fitting Parameters	α	0.051	0.168	0.681	0.004	0.039	0.117
	β	0.029	0.043	-0.008	0.021	0.024	0.034
$DMR_{10\%}$		Hf-DBP	Th-DBP		Hf-DBP	Th-DBP	
		1.44	2.25		1.17	1.52	

These observations were supported by unbiased live imaging-based growth rate inhibition assays, which provided a growth inhibition factor at 10% growth rate inhibition ($GIF_{10\%}$) to evaluate the real-time proliferation rate after treatment. Consistent with the clonogenic assay results, the $GIF_{10\%}$ values for CT26 cells were 1.38 and 1.12 for Th-DBP and Hf-DBP, respectively, under X-ray irradiation (**Figure 4-13a** and **Table 4-4**), and 2.65 and 1.28 for Th-DBP and Hf-DBP, respectively, under γ-ray irradiation (**Figure 4-13b** and **Table 4-5**). For Panc02 cells, the $GIF_{10\%}$ values were 1.16 and 1.08 for Th-DBP and Hf-DBP, respectively, under X-ray irradiation (**Figure**

4-13c and **Table 4-4**), and 1.43 and 1.17 for Th-DBP and Hf-DBP, respectively, under γ-ray irradiation (**Figure 4-13d** and **Table 4-5**).

Table 4-4. GRI, slopes, and $GIF_{10\%}$ of GR assays with X-ray.

Cell Line		CT26			Panc02		
X-ray dose		PBS	Hf-DBP	Th-DBP	PBS	Hf-DBP	Th-DBP
GRI	0 Gy	1.000	0.934	0.932	1.000	0.998	1.007
	2 Gy	0.929	0.698	0.489	0.869	0.788	0.745
	4 Gy	0.698	0.438	0.236	0.733	0.658	0.560
	8 Gy	0.153	0.132	0.069	0.326	0.228	0.159
	16 Gy	0.035	0.028	0.015	0.037	0.028	0.026
Fitting Parameters	Slope	-0.090	-0.098	-0.122	-0.084	-0.091	-0.097
$GIF_{10\%}$		Hf-DBP		Th-DBP	Hf-DBP		Th-DBP
		1.12		1.38	1.08		1.16

Table 4-5. GRI, slopes, and $GIF_{10\%}$ of GR assays with γ-ray.

Cell Line		CT26			Panc02		
γ-ray dose		PBS	Hf-DBP	Th-DBP	PBS	Hf-DBP	Th-DBP
GRI	0 Gy	1.000	1.039	0.949	1.000	0.923	0.891
	2 Gy	0.971	0.845	0.515	0.919	0.871	0.617
	4 Gy	0.771	0.646	0.319	0.755	0.713	0.469
	8 Gy	0.450	0.395	0.114	0.239	0.215	0.179
	16 Gy	0.235	0.157	0.050	0.080	0.049	0.027
Fitting Parameters	Slope	-0.039	-0.050	-0.091	-0.068	-0.080	-0.097
$GIF_{10\%}$		Hf-DBP		Th-DBP	Hf-DBP		Th-DBP
		1.28		2.65	1.17		1.43

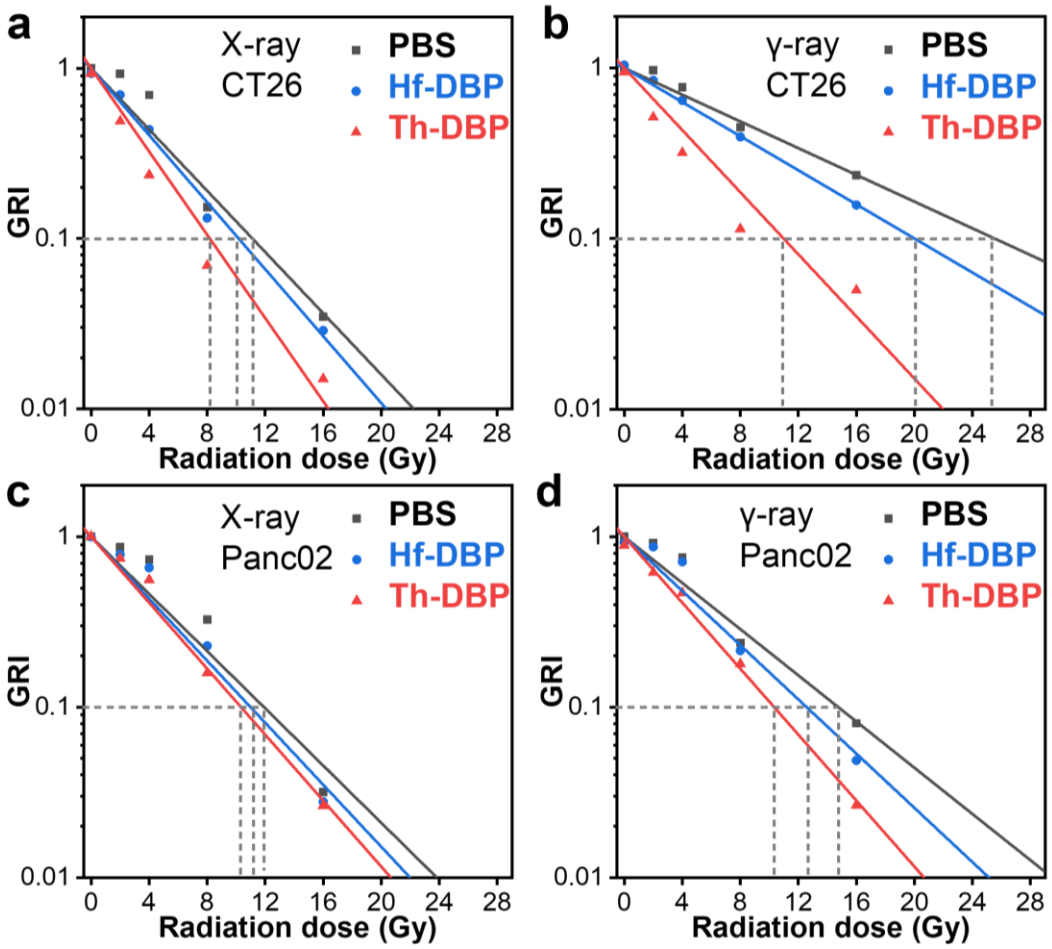

Figure 4-13. Growth rate inhibition assays in CT26 cells. Linear dose-fitting curves for growth rate inhibition indices (GRI log scale) of CT26 cells after (a) X-ray and (b) γ-ray irradiation and Panc02 cells after (a) X-ray and (b) γ-ray irradiation in growth rate inhibition assays.

Confocal laser scanning microscopy imaging and flow cytometry analysis after staining the phosphorylated histone H2A.X (γ-H2AX) of CT26 cells showed that Th-DBP gave 1.33-fold and 1.44-fold more DSBs than Hf-DBP 24 hours after X-ray or γ-ray irradiation, respectively (**Figure 4-15**). These results demonstrate that Th-DBP is a better radiosensitizer than Hf-DBP, particularly for clinically relevant γ-ray radiation.

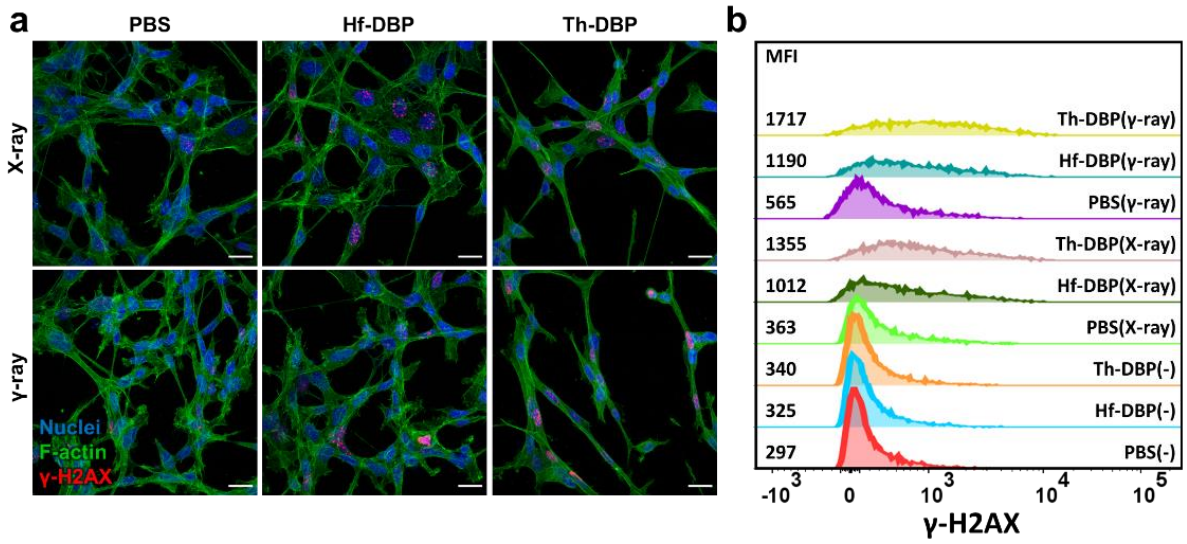

Figure 4-14. DNA DSBs in cells. (a) CLSM images and (b) flow cytometric histograms of CT26 cells showing DNA double stranded breaks (DSB) labeled by γ-H2AX 24 hours after 2 Gy X-ray or 4 Gy γ -ray irradiation, respectively (scale bar = 20 μm).

4.2.4. *In vivo* experiments

We then assessed the *in vivo* radiosensitizing effect of Th-DBP and Hf-DBP on subcutaneous tumors of CT26 murine colon carcinoma and Panc02 murine pancreatic adenocarcinoma (**Figure 4-15**). PBS, Hf-DBP, or Th-DBP was injected intratumorally before fractionated irradiation, after which tumor volumes were monitored to compare the anticancer efficacy of different treatments. Irradiation of CT26 tumors with 2 Gy X-ray by 3 fractions and Panc02 tumors with 4 Gy X-ray by 3 fractions moderately inhibited tumor growth with tumor growth inhibition indices (TGIs) of 0.460 and 0.632, respectively. Hf-DBP further inhibited tumor growth with TGIs of 0.806 and 0.865 for CT26 and Panc02 tumors, respectively. Th-DBP(+) outperformed Hf-DBP(+) with TGIs of 0.876 and 0.970 for CT26 and Panc02 tumors, respectively. Moreover, Th-DBP(+) treatment eradicated 3 out of 5 Panc02 tumors.

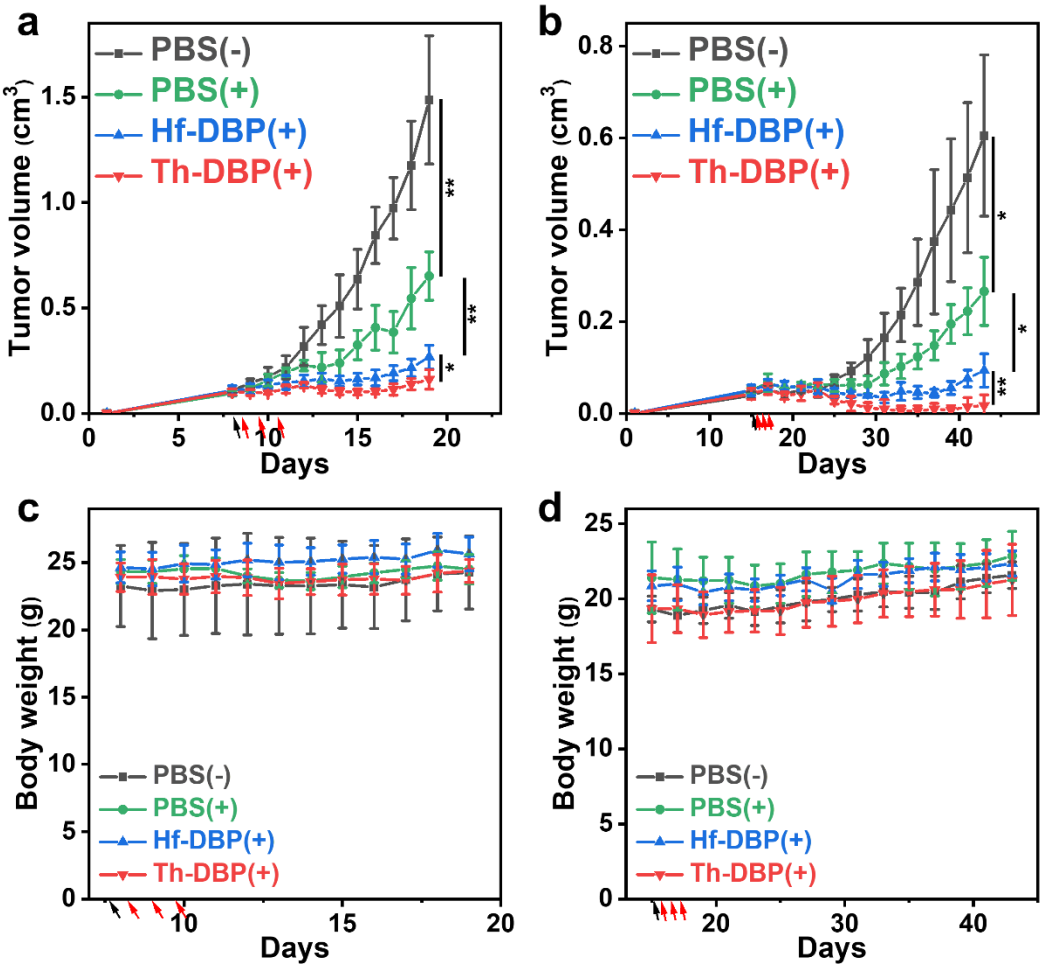

Figure 4-15. Growth curves of subcutaneous (a) CT26 tumors in BALB/c mice and (b) Panc02 tumors in C57BL/6 mice after treatment with Th-DBP or Hf-DBP followed by X-ray irradiation. Body weight curves of (c) CT26 tumor-bearing BALB/c mice and (d) Panc02 tumor-bearing C57BL/6 mice. *n* = 5. Black arrows indicate nMOF injection whereas red arrows indicate irradiation. The CT26 tumors were irradiated with 2 Gy X-ray/fraction in 3 consecutive days, and the Panc02 tumors were irradiated with 4 Gy X-ray/fraction in 3 consecutive days. (+) and (-) denote with and without irradiation, respectively.

Computerized tomography (CT) imaging showed that Hf-DBP and Th-DBP retained in the tumors for at least 7 days (**Figure 4-16**). Th-DBP showed a 3.7-fold higher CT contrast than Hf-DBP, suggesting that Th-DBP deposited more radiation energy in tumors than Hf-DBP. This result suggests that Th-DBP can be a promising candidate for image-guided radiotherapy for precise radiation dose to tumors.

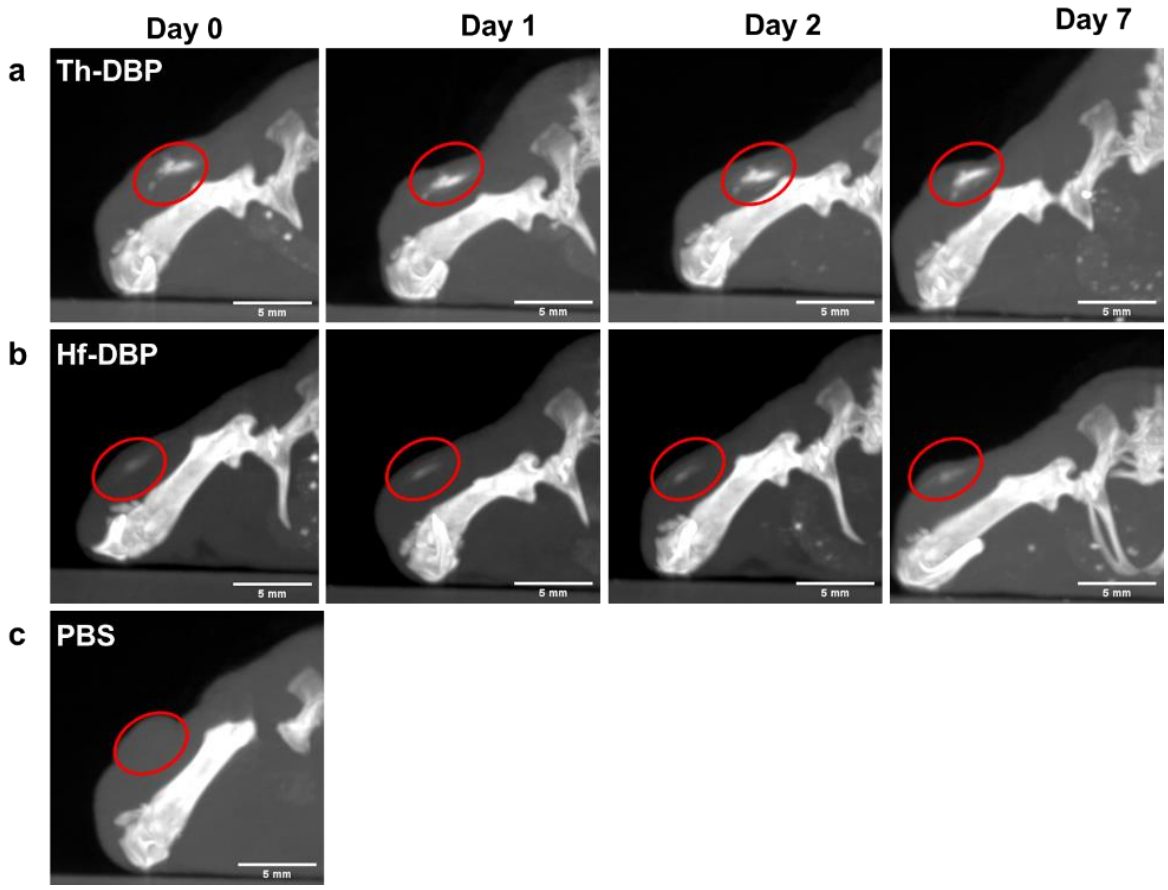

Figure 4-16. CT images showing tumoral contrast at different timepoints after injection of Th-DBP (a), Hf-DBP (b), and PBS (c) (scale bar = 5 mm).

Ki67 staining revealed that Th-DBP(+) induced a 1.35-fold stronger inhibition of tumor proliferation than Hf-DBP(+), whereas γ-H2AX staining indicated that Th-DBP(+) caused 1.89-fold more DSBs than Hf-DBP(+) (**Figures 4-17** and **4-18**).

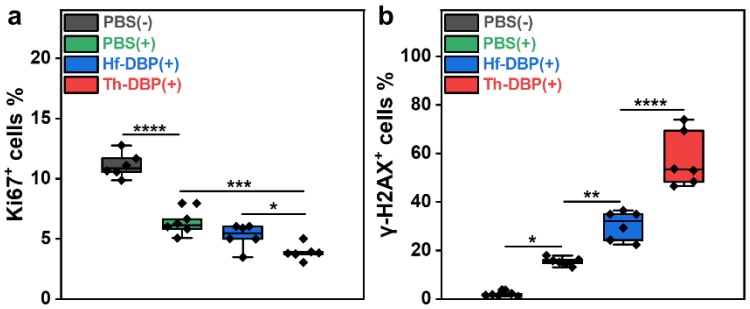

Figure 4-17. Ki67 γ-H2AX staining. Statistical analysis of positive rates of (a) Ki67 and (b) γ-H2AX staining in CT26 tumor slides ($n = 6$). *, $p<0.05$, **, $p<0.01$, ***, $p<0.001$, ****, $p<0.0001$.

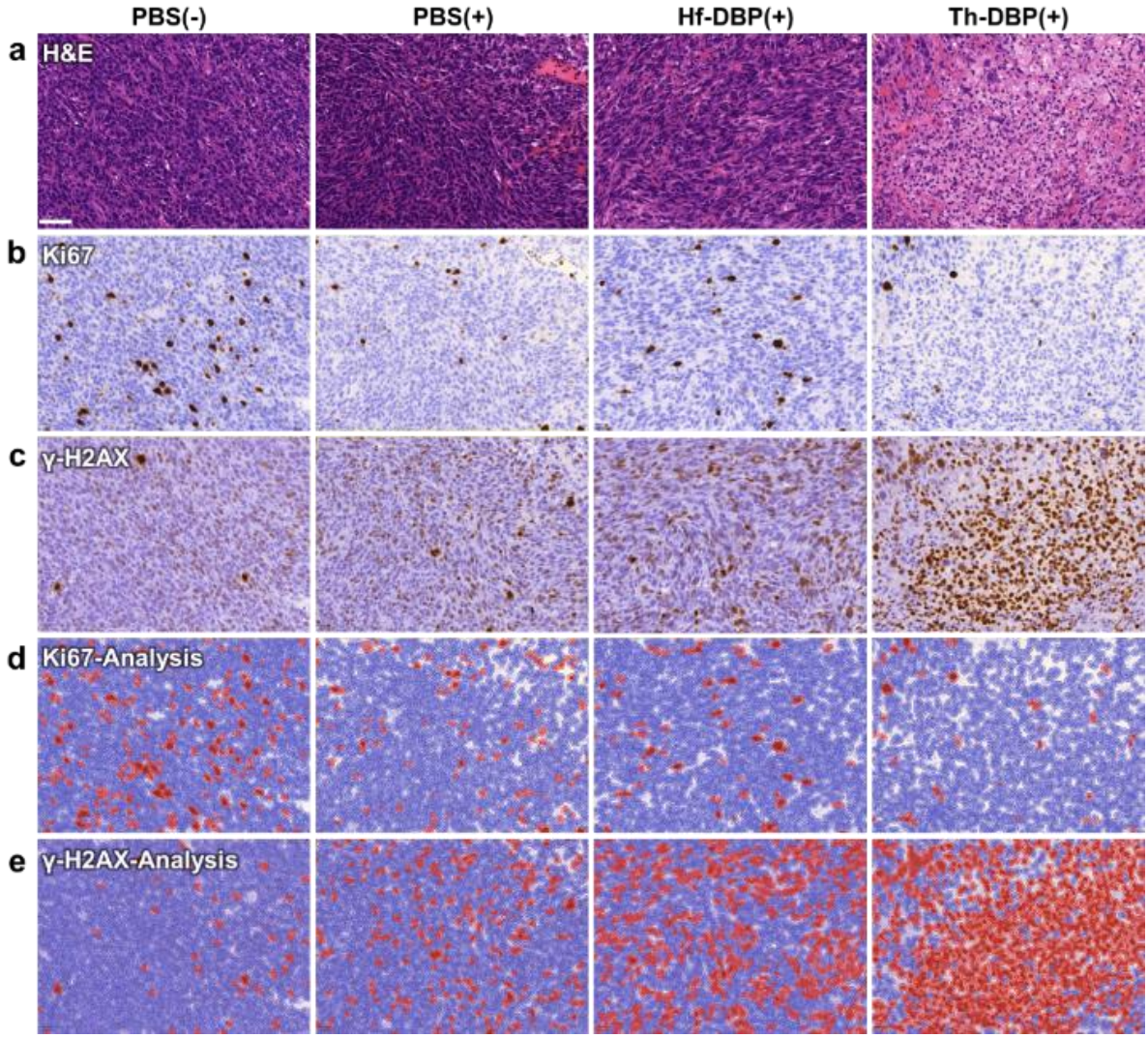

Figure 4-18. Representative original images for multiple staining of CT26 tumors and analysis of positive detection. Representative original images of (a) H&E, (b) Ki67, and (c) γ-H2AX staining of CT26 tumors treated by PBS(-), PBS(+), Hf-DBP(+), and Th-DBP(+), respectively. Representative analysis of positive detection in (d) Ki67 and (e) γ-H2AX slides (Scale bar = 50 μm; the DAB-positive cells were marked with red masks and the negative cells were marked with blue masks).

Th-DBP(+) treatment did not cause general toxicity to mice, as indicated by their steady bodyweights (**Figure 4-15c&d**) and lack of abnormality in the histology of major organs, hematological parameters, and liver enzymes (**Figure 4-19**). These results support the rational design of Th-DBP as a biocompatible and potent radiosensitizer for the effective treatment of preclinical colon and pancreatic tumor models.

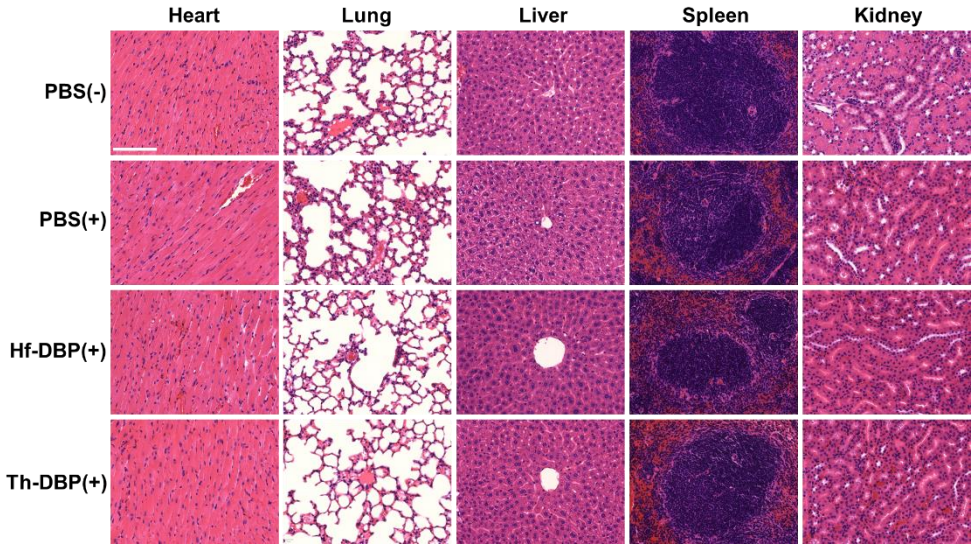

Figure 4-19. H&E staining of hearts, lungs, livers, spleens, and kidneys of CT26 tumor-bearing BALB/c mice in different treatment groups (the scale bar = 100 μm).

4.3 Conclusions

In this chapter, we have rationally developed Th-DBP as a potent nMOF radiosensitizer for RT–RDT. MC simulations demonstrated improved physical dose enhancement of the Th-lattice over the Hf-lattice under X-ray and γ-ray irradiation owing to a higher mass attenuation coefficient of Th over Hf. As a result, Th-DBP efficiently enhances hydroxyl radical and $^1O_2$ generation upon irradiation to kill cancer cells and regress colon and pancreatic cancers in mice models.

4.4. Methods

4.4.1. Monte Carlo Simulations

Monte Carlo simulations were performed with the EGSnrc toolkit in two steps as described previously. [31, 48] First, a macroscopic simulation in a 20 × 20 × 20 cm^3 water phantom with a parallel incident beam (cross-section: 20×20 cm^2) was conducted to obtain the phase space files containing numbers, energies, and momenta of all particles (photons, electrons, and positrons)

passing a central 10 × 10 cm^2 plane at a certain depth. For X-ray simulation, a 120 keV monoenergetic beam was used and the depth was 1 cm. For γ-ray simulation, a ^{60}Co beam was used and the depth was 3 cm. Second, a microscopic simulation using the condensed phase space as the incident beam was conducted. The cross-section of the condensed phase space was 4 × 4 μm^2 for X-ray simulation and 10 × 10 μm^2 for γ-ray simulation. A lattice model of nMOFs consisting of 3D hexagonal arrays of nanoscale SBUs was placed in the center of a microscopic water phantom (20 × 20 × 20 μm^3) to interact with the beam and deposit energy in the surrounding water. The lattice parameters are listed in Table S1, which ensured the lattice structure, inter-SBU distance, and atom number in each SBU were the same for Hf-lattice and Th-lattice. To reduce the uncertainty of the calculated dose, lattices used in γ-ray simulations were larger than those used in X-ray simulations. The egs_lattice module[49] was used to construct the lattice geometry while the egs_chamber module was used to calculate the dose deposited in the water around the lattice within a certain water radius. For the dose enhancement factor (DEF), water lattices were constructed by changing the material of a Hf-lattice or a Th-lattice to water and the resulting dose curves were denoted as Hf-water or Th-water, respectively. DEF was calculated as the ratio of deposited energy in surrounding water by a metal-lattice over that by water.

4.4.3. Synthesis and characterization

Synthesis of Th_6-DBA, Hf_{12}-DBA, Th-DBP and Hf-DBP nMOFs. First, $Th_6O_4(OH)_4(HCOO)_{12}$ clusters were synthesized following the reported procedure,[50] which were then dissolved in DMF at a concentration of 2 mg/mL. 4,4'-(Porphyrin-5,15-diyl)dibenzoic acid (H_2DBP) was synthesized as described previously[51] and dissolved in DMF at a concentration of 3.5 mg/mL. 500 μL $Th_6O_4(OH)_4(HCOO)_{12}$ solution and 500 μL H_2DBP solution were then combined in a 1-dram vial with the addition of 10 μL formic acid and 5 μL water as modulators. The mixture was heated in

an oven at 120 °C for 3 days, after which the purple precipitate was collected by centrifugation and washed with DMF, 1% triethylamine (TEA) in ethanol (EtOH) (v/v), and EtOH sequentially. Th_6-DBA was synthesized by combining 500 μL $Th_6O_4(OH)_4(HCOO)_{12}$ solution (2 mg/mL in DMF), 500 μL H_2DBA solution (DBA = 2,5-di(p-benzoato)aniline, 2 mg/mL in DMF), 15 μL formic acid and 5 μL water in a 1-dram vial and heating the mixture in an oven at 120 °C for 1 day. Hf_{12}-DBA and Hf-DBP nMOF were synthesized as described previously for comparison.[28, 51]

Synthesis of Th-DBP@PEG and Hf-DBP@PEG. Th-DBP nMOF (Th: 15 μmol) and 50 mg mPEG-PO_3 were mixed in 10 mL EtOH and stirred at room temperature for 24 hours, after which the precipitate was collected by centrifugation and washed with EtOH three times. The precipitate was dried under vacuum for further applications. Hf-DBP@PEG was prepared following a previously reported procedure.[27] The PEGylated samples were used for all *in vitro* and *in vivo* experiments.

Digestion of Th-DBP for UV-Vis spectroscopic measurement. 50 μL Th-DBP solution, 900 μL DMSO and 50 μL H_3PO_4 were mixed and sonicated for 1 hour, after which the mixture was diluted to a proper concentration for UV-Vis measurement. The absorption of H_2DBP at 408nm was used to calculate the concentration of H_2DBP in Th-DBP after comparison with the standard curve of H_2DBP in DMSO.[34]

Digestion of Th-DBP for ^{1}H NMR. Th-DBP was dried under vacuum overnight. 500 μL DMSO-d_6 and 50 μL D_3PO_4 were added to the resulting solid. The mixture was sonicated for 1 hour, followed by the addition of 50 μL D_2O for ^{1}H NMR analysis.

Stability test of Th-DBP@PEG in PBS. Th-DBP@PEG was dispersed in 1mL PBS (1mM) with a Th concentration of 5 mM. 200 μL suspension was taken out after incubation for 1, 2, 4, and 8 hours and 3 days and centrifuged for PXRD measurement.

Stability test of Th-DBP@PEG and Hf-DBP@PEG upon X-ray and γ-ray irradiation. Th-DBP@PEG and Hf-DBP@PEG were dispersed in 1mL H_2O seperately with a metal concentration of 5 mM. 500 μL of each suspension was subjected to 12 Gy X-ray or γ-ray irradiation. TEM, DLS and PXRD measurements were performed to evaluate the crystallinity and morphology of irradiated nMOFs.

4.4.3. *In Vitro* Experiments

Cellular uptake. The cellular uptake of Hf-DBP and Th-DBP was evaluated on CT26 cells. The cells were seeded in 6-well plates at a density of 5×10^5/well and cultured overnight. Hf-DBP and Th-DBP were added at an equivalent metal concentration of 20 μM into medium (n = 3). The cells were incubated in a 37 ℃ incubator for 1, 2, 4, and 8 hours. At each time point, the medium was aspirated, the cells were washed with PBS for three times, trypsinized, collected by centrifugation, and counted with a hemocytometer. The cell pellets were digested with a mixture of 99% (v/v) concentrated nitric acid and 1% (v/v) hydrofluoric acid for 48 hours and the Hf or Th concentration was determined by ICP-MS. The relative cellular uptake was also confirmed by flow cytometry after incubating CT26 cells with Hf-DBP and Th-DBP for 8 hours. The fluorescence intensity of DBP was monitored by BV650 channel (ex. 405 nm / em. 645 nm).

Dark toxicity. The cytotoxicity of Hf-DBP and Th-DBP on CT26 and Panc02 cells were determined by (3-(4,5-dimethylthiazol-2-yl)-5-(3-carboxymethoxyphenyl)-2-(4-sulfophenyl)-2H-tetrazolium) (MTS) assay. CT26 and Panc02 cells were seeded in 96-well plates at a density of

1500 cells/well. Different concentrations of Hf-DBP or Th-DBP were added and 48 hours later 10% (v/v) of MTS reagent was added to each well. 90 minutes later the absorbance of each well at 490 nm was read by a Synergy HTX plate reader to calculate cell viability.

ROS generation. To assess ROS generation, CT26 cells were seeded in 24-well plates at a density of 5×10^4/well and cultured overnight. Hf-DBP or Th-DBP was added at an equivalent metal concentration of 20 μM (n = 4) and further incubated in a 37℃ incubator for 4 hours. The cells were washed with PBS twice and 1 mL warm medium with 20 μM DCFH-DA was added and incubated at 37℃ for an additional hour. Then the cells were irradiated with X-ray or γ-ray, washed with PBS three times, and the fluorescence (em. 520/20 nm) was read immediately with a Synergy HTX plate reader with a fixed green light filter (ex. 485/20 nm). Afterwards the cells were scanned with an IncuCyte S3 live-cell analysis system with green fluorescence channel (ex. 441–481 nm, em. 503–544 nm) to obtain fluorescence images.

CRT expression. To quantify CRT expression, CT26 cells were seeded in 6-well plates at a density of 5×10^5/well and cultured overnight. Hf-DBP or Th-DBP was added at an equivalent metal concentration of 20 μM (n = 3) for 4 hours and irradiated with X-ray or γ-ray. 24 hours later, the cells were washed with PBS, trypsinized to afford single cell suspensions, washed with 0.5% BSA in PBS, and resuspended in Fluorescein isothiocyanate (FITC)-conjugated CRT antibody (1:100 in 0.5% BSA in PBS) on ice for 30 minutes. The cells were then washed with PBS and resuspended in 0.5% BSA in PBS for flow cytometric analysis (FITC channel).

Apoptotic cell death. To quantify the apoptotic status of cells after treatment, CT26 cells were seeded, treated, and trypsinized in the same way as the above CRT staining protocol to afford single cell suspensions (n = 3). The cells were stained with the dead cell apoptosis kit with annexin

V Alexa Fluor 488 & PI following the manufacturer's protocol and resuspended in the binding buffer for flow cytometric analysis (Annexin-V in FITC channel, PI in PE-dazzole594 channel).

Clonogenic assay. CT26 or Panc02 cells were first seeded in 6-well plates at a density of 2×10^5 cells/well and cultured overnight. The cells were incubated with PBS, Hf-DBP, or Th-DBP at an equivalent metal concentration of 20 μM for 4 hours, and then irradiated with 0, 2, 4, 8, or 16 Gy X-ray or γ-ray (n = 3). The cells were washed with PBS twice and then trypsinized to afford single cell suspensions. The cells were counted and diluted, then 200-2000 cells were seeded in each well of 6-well plates and cultured in 4 mL medium with extra 10 % FBS for up to 10 days. When an appropriate colony size was observed, the plates were rinsed once with PBS, fixed by 4% paraformaldehyde for 15 minutes at room temperature, and washed with PBS once. The 6-well plates were then scanned with IncuCyte S3 in the whole well mode with a 4× objective. The colonies were identified with IncuCyte 2021A software in a cellular resolution and the confluence was used as a parameter to calculate the plating efficiency (PE)and surviving fraction (SF):[52]

$$PE = \frac{Confluence\ (0\ Gy, PBS)}{Cell\#\ (0\ Gy, PBS)} \qquad SF(D, MOF) = \frac{Confluence\ (D, MOF)}{Cell\#\ (D, MOF) \times PE}$$

Where D was the radiation dose and $Cell\#\ (D, MOF)$ was the number of cells seeded for a certain radiation dose D and a certain treatment group. The SF was reported to fit in a linear-quadratic model:

$$SF(D) = e^{(-\alpha D - \beta D^2)}$$

Where α and β were fitting parameters. The dose modifying ratio at a 10% SF ($DMR_{10\%}$) was used as a parameter to assess radiosensitization effect and defined as the ratio of doses under reference conditions to produce a 10% SF:[53]

$$DMR_{10\%} = \frac{D_{PBS}}{D_{MOF}}$$

Growth rate inhibition assay. The growth rate inhibition assay is an improved and unbiased version of clonogenic assay to assess radioenhancement. CT26 or Panc02 cells were first seeded and treated in the same way as in the clonogenic assay. The cells were then counted, diluted to 1000~2000 cells/mL, and reseeded in 24-well plates. The plates were put in IncuCyte S3 and continuously observed by a 10× objective in phase contrast mode. The phase contrast images were collected and analyzed with IncuCyte 2021A software to obtain a time-dependent confluence in each well (25 tiles per well, triplicates for each treatment group). The first derivative was calculated based on time-dependent growth curve to give growth rate (k_t). The time point where the k of control group (PBS, 0 Gy) reached maximum (t_{max}) was selected as the time for the definition of growth rate inhibition index (GRI). The GRI in radiosensitization experiment was defined using the equation below[54]:

$$GRI(D, t_{max}) = 2^{k(D,t_{\max})/k(0)} - 1$$

Where D was the radiation dose and $k(0)$ was the growth rate of control group at t_{max}. GRI data could be fitted linearly with GRI in log scale:

$$\log\left[GRI(D)\right] = \alpha D + \beta$$

Where α was the slope and β was fixed as 0. Then the growth inhibition factor at $GRI = 10\%$ ($GIF_{10\%}$) was defined based on the fitting curve of $GRI(D)$ to quantify the radiosensitizing effect of Hf-DBP or Th-DBP:

$$GIF_{10\%} = \frac{D_{PBS}}{D_{MOF}}$$

DNA damage. For CLSM imaging, CT26 cells (2× 10^5 cells/well) were seeded in 6-well plates with a coverslip at the bottom of each well. The cells were treated in the same way as in the clonogenic assay. 24 hours after radiation, the cells were washed with PBS and fixed with 4% paraformaldehyde (pH = 7.2) at room temperature for 15 minutes. The cells were again rinsed with PBS, blocked and permeabilized with 5% FBS + 0.3% Triton-X in PBS at room temperature for 1 hour. After blocking, the cells were incubated with the γ-H2AX primary antibody (1:400) in 1% BSA + 0.3% Triton-X in PBS at 4 °C overnight. The cells were then washed with PBS and incubated with the Alexa Fluor 647 conjugated secondary antibody (1:1500) in 1% BSA + 0.3% Triton-X in PBS at room temperature for 1 hour. Afterwards, the cells were washed with PBS and further incubated with Acti-stain 488 (1:500) and Hoechst 33342 (1:3000) in PBS for 30 min to visualize cell skeletons and nuclei, respectively. Finally, the coverslips were mounted on glass slides with ProLong Glass antifade mountant, cured at room temperature overnight, sealed with nail polish and observed on a Leica Stellaris 8 confocal microscope.

For flow cytometry, CT26 cells (5× 10^5 cells/well) were seeded in 6-well plates and treated in the same way above. The cells were then trypsinized to afford a single cell suspension (100 μL), fixed and permeabilized with ice-cold methanol (100%, 900 μL) dropwise to reach a final concentration of 90% methanol and kept on ice for 10 minutes. The cells were washed twice with PBS to remove methanol, and resuspended in 100 μL of γ-H2AX primary antibody (1:200) in 0.5% BSA in PBS at room temperature for 1 hour. The cells were washed twice with PBS and stained by 100 μL of the Alexa Fluor 647 conjugated secondary antibody (1:2000) in 0.5% BSA in PBS at room temperature in dark for 30 minutes. The cells were then washed with PBS twice and resuspended in 500 μL 0.5% BSA in PBS for flow cytometric analysis (Allophycocyanin (APC) channel).

3.4.4. *In Vivo* Experiments

Anti-cancer efficacy and CT imaging. To evaluate the *in vivo* RT–RDT efficacy of Th-DBP, subcutaneous CT26 and Panc02 tumor models were established on BALB/c mice and C57BL/6 mice by inoculating 2×10^6 cells/mouse subcutaneously onto the right flanks at day 0, respectively. When CT26 tumors reached ~100 mm^3 and Panc02 tumors reached ~40 mm^3, the mice were randomized for irradiation treatment. PBS, Hf-DBP, or Th-DBP was injected intratumorally with an equivalent metal dose of 0.5 μmol in 20 μL saline (n = 5). 8 hours later, the mice were anaesthetized with 2.5% (v/v) isoflurane/O_2 and mounted onto the X-Rad 225 irradiator. The CT26 tumors were irradiated with 2 Gy X-ray/fraction for 3 consecutive days and the Panc02 tumors were irradiated with 4 Gy X-ray/fraction for 3 consecutive days. Tumor sizes were measured with an electronic caliper (tumor volume = length × $width^2/2$) and body weights were monitored with an electronic scale. At day 19 and day 43 for CT26 and Panc02 model, respectively, the mice were euthanized, and the tumors and major organs were sectioned for hematoxylin-eosin (H&E) staining to evaluate general toxicity. The tumor growth inhibition index (TGI) was defined as the equation below:

$$TGI = 1 - \frac{\frac{T_e}{T_s} \Big/ \frac{C_e}{C_s}}{1 - \frac{C_s}{C_e}} \times 100\%$$

where T_e, T_s, C_e, and C_s represent average tumor volumes of treated mice at endpoint, treated mice at starting-point, control mice at endpoint and control mice at starting-point, respectively.

For CT imaging, Panc02-bearing mice were established and injected with nMOFs in the same way as described above but not irradiated. The mice were then anesthetized, and the CT scans were collected immediately, 1 day, 2 days, and 7 days after injection with an X-Rad 225 irradiator with

a setting of a 2 mm aluminum filter, 60 kVp, and 10 mA. PBS was injected as a control and the tumor was imaged immediately post injection.

Immunohistochemistry analysis. To evaluate DNA damage and tumor proliferation after RT–RDT treatment, a group of CT26-bearing mice were established and treated in the same way as described above but euthanized one day after the last irradiation (day 11). The tumors were excised and fixed in 4% PFA for 1 day and 70% ethanol for 1 day. The tissues were embedded in paraffin, sectioned and stained for H&E, γ-H2AX, and Ki67 by Human Tissue Resource Center at the University of Chicago. Briefly, the slides were deparaffinized and rehydrated using xylenes and serial dilutions of ethanol to distilled water. Then the slides were treated with antigen retrieval buffer (Leica Biosystems, AR9640) and heated in a steamer over 97°C for 20 minutes). After washing with tris-buffered saline , the slides were incubated with primary γ-H2AX antibody (1:400) or primary Ki67 antibody (Thermo Fisher Scientific, Clone# SP6, 1:400) at room temperature for 1 hour in a wet chamber. The slides were washed with tris-buffered saline, then γ-H2AX and Ki67 slides were incubated with anti-rabbit-polymer (Bond Polymer Refine Detection, Leica Biosystems, DS9800) for 30 minutes at room temperature. The antigen-antibody binding was detected with the 3,3′-Diaminobenzidine (DAB) (DAKO, K3468) system. Tissue sections were then immersed in hematoxylin for counterstaining and covered with cover glasses. The slides were scanned on a CRi Pannoramic SCAN 40× whole slide scanner by Integrated Light Microscopy Core at the University of Chicago. The images were analysed with QuPath-0.2.3 software,[55] and the DAB-positive cells were marked red and the negative cells were marked blue. The detection parameters were set as: Setup parameters – Detection image – Optical density sum; Nucleus parameters – Requested pixel size – 0.1 μm; Background radius – 25 μm; Median Filter radius – 2 μm; Sigma – 1.5 μm; Minimum area – 8 mm^2; Maximum area – 400 mm^2; Intensity

parameters – Threshold – 0.1 for γ-H2AX, 0.03 for Ki67; Max background intensity 20; Split by shape – True; Exclude DAB – False; Cell expansion – Include cell nucleus – 3 μm; General parameters –Smooth boundaries – True; Make measurements – True; Intensity threshold parameters – Score compartment – Nucleus: DAB OD mean; Single Threshold – True; Threshold 1+ – 0.2 for γ-H2AX, 0.01 for Ki67.

Biodistribution, hematology, and biochemistry. To evaluate the biological safety of Th-DBP *in vivo*, we examined biodistribution of Th, hematological parameters, and blood chemistry after intratumoral injection of Th-DBP up to 72 hours. Th was barely detected in plasma and other major organs. The hematological parameters remained normal compared to healthy controls. The alanine transaminase activity and aspartate aminotransferase activity assays showed that Th-DBP had minimal impact on liver functions (SigmaAldrich, USA).

4.5. References

(1) Sung, H.; Ferlay, J.; Siegel, R. L.; Laversanne, M.; Soerjomataram, I.; Jemal, A.; Bray, F., Global Cancer Statistics 2020: GLOBOCAN Estimates of Incidence and Mortality Worldwide for 36 Cancers in 185 Countries. *CA Cancer J. Clin.* **2021,** *71* (3), 209-249.

(2) Sullivan, R.; Alatise, O. I.; Anderson, B. O.; Audisio, R.; Autier, P.; Aggarwal, A.; Balch, C.; Brennan, M. F.; Dare, A.; D'Cruz, A.; Eggermont, A. M. M.; Fleming, K.; Gueye, S. M.; Hagander, L.; Herrera, C. A.; Holmer, H.; Ilbawi, A. M.; Jarnheimer, A.; Ji, J.-f.; Kingham, T. P.; Liberman, J.; Leather, A. J. M.; Meara, J. G.; Mukhopadhyay, S.; Murthy, S. S.; Omar, S.; Parham, G. P.; Pramesh, C. S.; Riviello, R.; Rodin, D.; Santini, L.; Shrikhande, S. V.; Shrime, M.; Thomas, R.; Tsunoda, A. T.; van de Velde, C.; Veronesi, U.; Vijaykumar, D. K.; Watters, D.; Wang, S.; Wu, Y.-L.; Zeiton, M.; Purushotham, A., Global cancer surgery: delivering safe, affordable, and timely cancer surgery. *Lancet Oncol.* **2015,** *16* (11), 1193-1224.

(3) Schaue, D.; McBride, W. H., Opportunities and challenges of radiotherapy for treating cancer. *Nat. Rev. Clin. Oncol.* **2015,** *12* (9), 527-540.

(4) Wan, C.; Sun, Y.; Tian, Y.; Lu, L.; Dai, X.; Meng, J.; Huang, J.; He, Q.; Wu, B.; Zhang, Z.; Jiang, K.; Hu, D.; Wu, G.; Lovell Jonathan, F.; Jin, H.; Yang, K., Irradiated tumor cell–derived microparticles mediate tumor eradication via cell killing and immune reprogramming. *Sci. Adv.* **2020,** *6* (13), eaay9789.

(5) Ding, Z.; Guo, Z.; Zheng, Y.; Wang, Z.; Fu, Q.; Liu, Z., Radiotherapy Reduces N-Oxides for Prodrug Activation in Tumors. *J. Am. Chem. Soc.* **2022,** *144* (21), 9458-9464.

(6) Zhang, P.; Xu, M.; Ding, J.; Chen, J.; Zhang, T.; Huo, L.; Liu, Z., Fatty acid-conjugated radiopharmaceuticals for fibroblast activation protein-targeted radiotherapy. *Eur. J. Nucl. Med. Mol. Imaging* **2022,** *49* (6), 1985-1996.

(7) Chabner, B. A.; Roberts, T. G., Chemotherapy and the war on cancer. *Nat. Rev. Cancer* **2005,** *5* (1), 65-72.

(8) Mellman, I.; Coukos, G.; Dranoff, G., Cancer immunotherapy comes of age. *Nature* **2011,** *480* (7378), 480-489.

(9) Lou, J.; Zhang, L.; Zheng, G., Advancing Cancer Immunotherapies with Nanotechnology. *Adv. Ther.* **2019,** *2* (4), 1800128.

(10) Damasco, J. A.; Ohulchanskyy, T. Y.; Mahajan, S.; Chen, G.; Singh, A.; Kutscher, H. L.; Huang, H.; Turowski, S. G.; Spernyak, J. A.; Singh, A. K.; Lovell, J. F.; Seshadri, M.; Prasad, P. N., Excretable, ultrasmall hexagonal NaGdF4:Yb50% nanoparticles for bimodal imaging and radiosensitization. *Cancer Nanotechnol.* **2021,** *12* (1), 4.

(11) Delaney, G. P.; Barton, M. B., Evidence-based estimates of the demand for radiotherapy. *Clin. Oncol.* **2015,** *27* (2), 70-76.

(12) Gong, L.; Zhang, Y.; Liu, C.; Zhang, M.; Han, S., Application of Radiosensitizers in Cancer Radiotherapy. *Int. J. Nanomedicine* **2021,** *16*, 1083-1102.

(13) Kong, H.; Chandel, N. S., Regulation of redox balance in cancer and T cells. *J. Biol. Chem.* **2018,** *293* (20), 7499-7507.

(14) Wang, H.; Gao, H.; Jiang, X.; Zhao, P.; Ni, D.; Tang, Z.; Liu, Y.; Zheng, X.; Bu, W., Regulating water states by vacancies for cancer therapy. *Nano Today* **2021,** *37*, 101099.

(15) Wang, Y.; Zhang, H.; Liu, Y.; Younis, M. H.; Cai, W.; Bu, W., Catalytic radiosensitization: Insights from materials physicochemistry. *Mater. Today* **2022**.

(16) Haume, K.; Rosa, S.; Grellet, S.; Śmiałek, M. A.; Butterworth, K. T.; Solov'yov, A. V.; Prise, K. M.; Golding, J.; Mason, N. J., Gold nanoparticles for cancer radiotherapy: a review. *Cancer Nanotechnol.* **2016,** *7* (1), 8.

(17) Hainfeld, J. F.; Slatkin, D. N.; Smilowitz, H. M., The use of gold nanoparticles to enhance radiotherapy in mice. *Phys. Med. Biol.* **2004,** *49* (18), N309.

(18) Jiang, X.; Du, B.; Yu, M.; Jia, X.; Zheng, J., Surface-ligand effect on radiosensitization of ultrasmall luminescent gold nanoparticles. *J. Innov. Opt. Health Sci.* **2016,** *09* (04), 1642003.

(19) Zhou, C.; Hao, G.; Thomas, P.; Liu, J.; Yu, M.; Sun, S.; Öz, O. K.; Sun, X.; Zheng, J., Near-Infrared Emitting Radioactive Gold Nanoparticles with Molecular Pharmacokinetics. *Angew. Chem. Int. Ed.* **2012,** *51* (40), 10118-10122.

(20) Xu, J.; Yu, M.; Peng, C.; Carter, P.; Tian, J.; Ning, X.; Zhou, Q.; Tu, Q.; Zhang, G.; Dao, A.; Jiang, X.; Kapur, P.; Hsieh, J.-T.; Zhao, X.; Liu, P.; Zheng, J., Dose Dependencies and Biocompatibility of Renal Clearable Gold Nanoparticles: From Mice to Non-human Primates. *Angew. Chem. Int. Ed.* **2018,** *57* (1), 266-271.

(21) Bonvalot, S.; Le Pechoux, C.; De Baere, T.; Kantor, G.; Buy, X.; Stoeckle, E.; Terrier, P.; Sargos, P.; Coindre, J. M.; Lassau, N.; Ait Sarkouh, R.; Dimitriu, M.; Borghi, E.; Levy, L.; Deutsch, E.; Soria, J.-C., First-in-Human Study Testing a New Radioenhancer Using Nanoparticles (NBTXR3) Activated by Radiation Therapy in Patients with Locally Advanced Soft Tissue Sarcomas. *Clin. Cancer Res.* **2017,** *23* (4), 908-917.

(22) Bonvalot, S.; Rutkowski, P. L.; Thariat, J.; Carrère, S.; Ducassou, A.; Sunyach, M.-P.; Agoston, P.; Hong, A.; Mervoyer, A.; Rastrelli, M., NBTXR3, a first-in-class radioenhancer hafnium oxide nanoparticle, plus radiotherapy versus radiotherapy alone in patients with locally advanced soft-tissue sarcoma (Act. In. Sarc): a multicentre, phase 2–3, randomised, controlled trial. *Lancet Oncol.* **2019,** *20* (8), 1148-1159.

(23) Lusic, H.; Grinstaff, M. W., X-ray-computed tomography contrast agents. *Chem. Rev.* **2013,** *113* (3), 1641-1666.

(24) Wang, G. D.; Nguyen, H. T.; Chen, H.; Cox, P. B.; Wang, L.; Nagata, K.; Hao, Z.; Wang, A.; Li, Z.; Xie, J., X-Ray Induced Photodynamic Therapy: A Combination of Radiotherapy and Photodynamic Therapy. *Theranostics* **2016,** *6* (13), 2295-2305.

(25) Liu, J.; Zhang, W.; Kumar, A.; Rong, X.; Yang, W.; Chen, H.; Xie, J.; Wang, Y., Acridine Orange Encapsulated Mesoporous Manganese Dioxide Nanoparticles to Enhance Radiotherapy. *Bioconjugate Chem.* **2020,** *31* (1), 82-92.

(26) Ma, X.; Lee, C.; Zhang, T.; Cai, J.; Wang, H.; Jiang, F.; Wu, Z.; Xie, J.; Jiang, G.; Li, Z., Image-guided selection of Gd@C-dots as sensitizers to improve radiotherapy of non-small cell lung cancer. *J. Nanobiotechnology* **2021,** *19* (1), 284.

(27) Lu, K.; He, C.; Guo, N.; Chan, C.; Ni, K.; Lan, G.; Tang, H.; Pelizzari, C.; Fu, Y.-X.; Spiotto, M. T.; Weichselbaum, R. R.; Lin, W., Low-dose X-ray radiotherapy–radiodynamic therapy via nanoscale metal–organic frameworks enhances checkpoint blockade immunotherapy. *Nat. Biomed. Eng.* **2018,** *2* (8), 600-610.

(28) Ni, K.; Lan, G.; Chan, C.; Quigley, B.; Lu, K.; Aung, T.; Guo, N.; La Riviere, P.; Weichselbaum, R. R.; Lin, W., Nanoscale metal-organic frameworks enhance radiotherapy to potentiate checkpoint blockade immunotherapy. *Nat. Commun.* **2018,** *9* (1), 2351.

(29) Ni, K.; Lan, G.; Veroneau, S. S.; Duan, X.; Song, Y.; Lin, W., Nanoscale metal-organic frameworks for mitochondria-targeted radiotherapy–radiodynamic therapy. *Nat. Commun.* **2018,** *9* (1), 4321.

(30) Lan, G.; Ni, K.; Veroneau, S. S.; Song, Y.; Lin, W., Nanoscale metal–organic layers for radiotherapy–radiodynamic therapy. *J. Am. Chem. Soc.* **2018,** *140* (49), 16971-16975.

(31) Xu, Z.; Ni, K.; Mao, J.; Luo, T.; Lin, W., Monte Carlo Simulations Reveal New Design Principles for Efficient Nanoradiosensitizers Based on Nanoscale Metal–Organic Frameworks. *Adv. Mater.* **2021,** *33* (40), 2104249.

(32) Sherck, N. J.; Won, Y.-Y., Technical Note: A simulation study on the feasibility of radiotherapy dose enhancement with calcium tungstate and hafnium oxide nano- and microparticles. *Med. Phys.* **2017,** *44* (12), 6583-6588.

(33) Lan, G.; Ni, K.; Veroneau, S. S.; Luo, T.; You, E.; Lin, W., Nanoscale Metal–Organic Framework Hierarchically Combines High-Z Components for Multifarious Radio-Enhancement. *J. Am. Chem. Soc.* **2019,** *141* (17), 6859-6863.

(34) Ni, K.; Xu, Z.; Culbert, A.; Luo, T.; Guo, N.; Yang, K.; Pearson, E.; Preusser, B.; Wu, T.; La Riviere, P.; Weichselbaum, R. R.; Spiotto, M. T.; Lin, W., Synergistic checkpoint-blockade and radiotherapy–radiodynamic therapy via an immunomodulatory nanoscale metal–organic framework. *Nat. Biomed. Eng.* **2022,** *6* (2), 144-156.

(35) Suda, Y.; Hariu, M.; Yamauchi, R.; Miyasaka, R.; Myojoyama, A.; Chang, W.; Saitoh, H., Direct energy spectrum measurement of X-ray from a clinical linac. *J. Appl. Clin. Med. Phys.* **2021,** *22* (8), 255-264.

(36) Schreiner, L. J.; Joshi, C. P.; Darko, J.; Kerr, A.; Salomons, G.; Dhanesar, S., The role of Cobalt-60 in modern radiation therapy: Dose delivery and image guidance. *J Med Phys* **2009,** *34* (3), 133-136.

(37) Kawrakow, I.; Rogers, D. W. O.; Mainegra-Hing, E.; Tessier, F.; Walters, B. R. B. *The EGSnrc Code System: Monte Carlo Simulation of Electron and Photon Transport*; NRC: Ottawa, 2000.

(38) Martinov, M. P.; Thomson, R. M., Taking EGSnrc to new lows: Development of egs++ lattice geometry and testing with microscopic geometries. *Med. Phys.* **2020,** *47*, 3225-3232.

(39) Chen, X.; Zhuang, Y.; Rampal, N.; Hewitt, R.; Divitini, G.; O'Keefe, C. A.; Liu, X.; Whitaker, D. J.; Wills, J. W.; Jugdaohsingh, R.; Powell, J. J.; Yu, H.; Grey, C. P.; Scherman, O. A.; Fairen-Jimenez, D., Formulation of Metal–Organic Framework-Based Drug Carriers by Controlled Coordination of Methoxy PEG Phosphate: Boosting Colloidal Stability and Redispersibility. *J. Am. Chem. Soc.* **2021,** *143* (34), 13557-13572.

(40) Manna, K.; Ji, P.; Greene, F. X.; Lin, W., Metal–Organic Framework Nodes Support Single-Site Magnesium–Alkyl Catalysts for Hydroboration and Hydroamination Reactions. *J. Am. Chem. Soc.* **2016,** *138* (24), 7488-7491.

(41) Feng, L.; Yuan, S.; Qin, J.-S.; Wang, Y.; Kirchon, A.; Qiu, D.; Cheng, L.; Madrahimov, S. T.; Zhou, H.-C., Lattice Expansion and Contraction in Metal-Organic Frameworks by Sequential Linker Reinstallation. *Matter* **2019,** *1* (1), 156-167.

(42) Wang, C.; Volotskova, O.; Lu, K.; Ahmad, M.; Sun, C.; Xing, L.; Lin, W., Synergistic Assembly of Heavy Metal Clusters and Luminescent Organic Bridging Ligands in Metal–Organic Frameworks for Highly Efficient X-ray Scintillation. *J. Am. Chem. Soc.* **2014,** *136* (17), 6171-6174.

(43)Overchuk, M.; Cheng, M. H. Y.; Zheng, G., X-ray-Activatable Photodynamic Nanoconstructs. *ACS Cent. Sci.* **2020,** *6* (5), 613-615.

(44) Ju, E.; Dong, K.; Chen, Z.; Liu, Z.; Liu, C.; Huang, Y.; Wang, Z.; Pu, F.; Ren, J.; Qu, X., Copper(II)–Graphitic Carbon Nitride Triggered Synergy: Improved ROS Generation and Reduced Glutathione Levels for Enhanced Photodynamic Therapy. *Angew. Chem. Int. Ed.* **2016,** *55* (38), 11467-11471.

(45) Ni, K.; Lan, G.; Guo, N.; Culbert, A.; Luo, T.; Wu, T.; Weichselbaum Ralph, R.; Lin, W., Nanoscale metal-organic frameworks for x-ray activated in situ cancer vaccination. *Sci. Adv.* **2020,** *6* (40), eabb5223.

(46) Guo, N.; Ni, K.; Luo, T.; Lan, G.; Arina, A.; Xu, Z.; Mao, J.; Weichselbaum, R. R.; Spiotto, M.; Lin, W., Reprogramming of Neutrophils as Non-canonical Antigen Presenting Cells by Radiotherapy–Radiodynamic Therapy to Facilitate Immune-Mediated Tumor Regression. *ACS Nano* **2021,** *15* (11), 17515-17527.

(47) Sun, Y.; Feng, X.; Wan, C.; Lovell, J. F.; Jin, H.; Ding, J., Role of nanoparticle-mediated immunogenic cell death in cancer immunotherapy. *Asian J. Pharm. Sci.* **2021,** *16* (2), 129-132.

(48) Zygmanski, P.; Liu, B.; Tsiamas, P.; Cifter, F.; Petersheim, M.; Hesser, J.; Sajo, E., Dependence of Monte Carlo microdosimetric computations on the simulation geometry of gold nanoparticles. *Phys. Med. Biol.* **2013,** *58* (22), 7961.

(49) Martinov, M. P.; Thomson, R. M., Taking EGSnrc to new lows: Development of egs++ lattice geometry and testing with microscopic geometries. *Med. Phys.* **2020**.

(50) Knope, K. E.; Wilson, R. E.; Vasiliu, M.; Dixon, D. A.; Soderholm, L., Thorium(IV) Molecular Clusters with a Hexanuclear Th Core. *Inorg. Chem.* **2011,** *50* (19), 9696-9704.

(51) Lu, K.; He, C.; Lin, W., Nanoscale Metal–Organic Framework for Highly Effective Photodynamic Therapy of Resistant Head and Neck Cancer. *J. Am. Chem. Soc.* **2014,** *136* (48), 16712-16715.

(52) Franken, N. A. P.; Rodermond, H. M.; Stap, J.; Haveman, J.; van Bree, C., Clonogenic assay of cells in vitro. *Nat. Protoc.* **2006,** *1* (5), 2315-2319.

(53) Subiel, A.; Ashmore, R.; Schettino, G., Standards and Methodologies for Characterizing Radiobiological Impact of High-Z Nanoparticles. *Theranostics* **2016,** *6* (10), 1651-1671.

(54) Hafner, M.; Niepel, M.; Chung, M.; Sorger, P. K., Growth rate inhibition metrics correct for confounders in measuring sensitivity to cancer drugs. *Nat. Methods* **2016,** *13* (6), 521-527.

(55) Bankhead, P.; Loughrey, M. B.; Fernández, J. A.; Dombrowski, Y.; McArt, D. G.; Dunne, P. D.; McQuaid, S.; Gray, R. T.; Murray, L. J.; Coleman, H. G.; James, J. A.; Salto-Tellez, M.; Hamilton, P. W., QuPath: Open source software for digital pathology image analysis. *Sci. Rep.* **2017,** *7* (1), 16878.

Chapter 5. Nanoscale MOF with an X-ray Triggerable Prodrug for Synergistic Radiotherapy and Chemotherapy

5.1. Introduction

Metal–organic frameworks (MOFs) have recently been exploited for biomedical applications due to their tunable compositions, large porosity, ease of surface functionalization, and biodegradability.[1-4] In particular, MOFs have been widely used as drug carriers.[5-10] To date, three methods have been used to load drugs into MOFs: direct encapsulation of drugs in the pores,[11-12] coordination of drugs to metal-cluster secondary building units (SBUs),[13] and covalent conjugation of drugs to the ligands.[14] While the first two methods can have premature drug release due to weak interactions between MOFs and drug molecules,[15] the third method requires an actionable trigger to release the conjugated drug from the MOF.[16-17] Among many possible triggers,[18-27] X-ray stands out as a great external stimulus due to its deep tissue penetration,[28] image-guided precise dosing,[29-30] and radiotherapeutic effects through direct DNA damages or indirect cytotoxic effects via generating reactive oxygen species (ROS).[31-38]

Heavy metal-based nanoscale MOFs (nMOFs) have recently been reported as excellent radioenhancers by enhancing energy deposition and ROS generation.[39-41] We hypothesized that heavy metal-nMOFs with covalently conjugated drugs could be efficiently triggered by X-rays to release drugs via enhanced ROS generation and radiation-induced cleavage of drug molecules for synergistic radiotherapy and chemotherapy while significantly reducing the systemic exposure of chemotherapeutics.

In this chapter, we report the design of Hf-TP-SN nMOF with an X-ray triggerable 7-ethyl-10-hydroxycamptothecin (SN38) prodrug for synergistic radiotherapy and chemotherapy. As a topoisomerase I inhibitor, SN38 is the active metabolite of irinotecan that has been used in the

treatment of colorectal and pancreatic cancer.[42-43] Hf-TP-SN was synthesized via a combination of pre-functionalization of terphenyl ligands with 3,5-dimethylbenzyl alcohol and post-synthetic modification with SN38 via a carbonate bond. Here Hf_{12}-type nMOF with a nanoplate morphology was selected due to its high surface area for efficient post-synthetic modification. Upon X-ray irradiation, electron-dense Hf_{12}-SBUs served as radiosensitizers to enhance ·OH generation, leading to 5-fold higher release of SN38 from Hf-TP-SN than a homogeneous counterpart. Hf-TP-SN not only enhanced the radiotherapeutic efficacy but also achieved chemotherapeutic effect through on-demand release of SN38. Such a chemoradiotherapy strategy effectively reduces the radiation dose required for tumor regression and minimizes the side effects of chemotherapy via burst release of SN38 inside the cancer cells.

5.2. Results and discussion

5.2.1. Synthesis and characterization of Hf-TP-SN

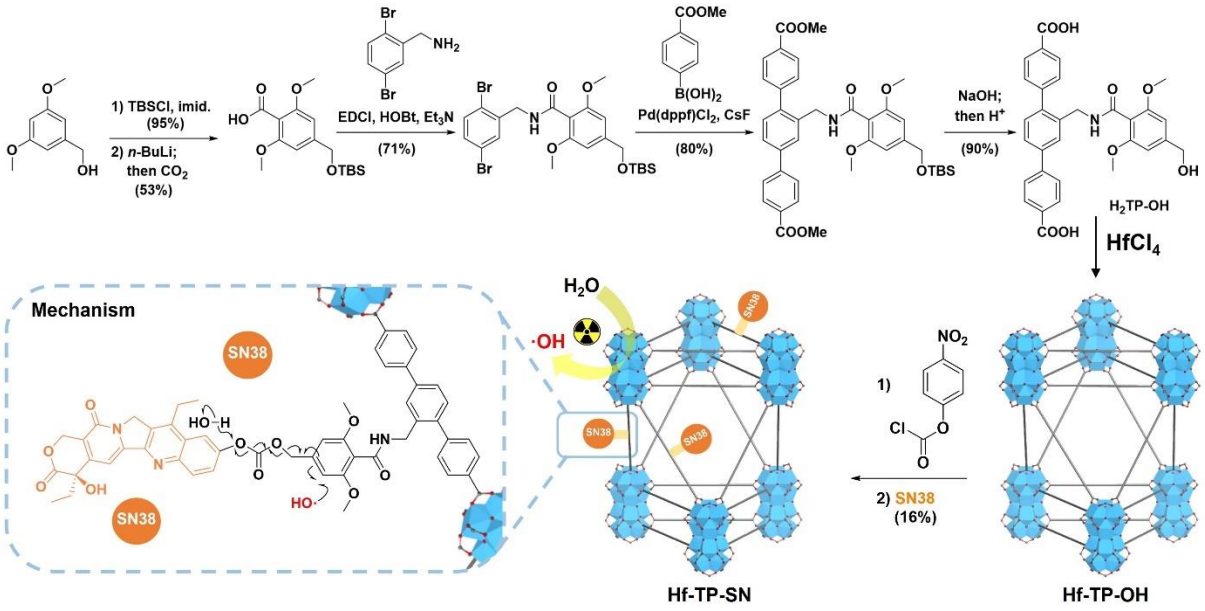

Figure 5-1. Synthesis of Hf-TP-OH nMOF and its post-synthetic modification with SN38 to afford Hf-TP-SN nMOF along with the proposed mechanism for X-ray triggered release of SN38 from Hf-TP-SN.

We conjugated SN38 to Hf-TP-OH nMOF via the 3,5-dimethoxylbenzyl carbonate linkage, which can be cleaved by hydroxyl radical (·OH).[38] Hf-TP-SN was synthesized via a combination of pre-functionalization and post-synthetic modification (**Figure 5-1**). The terphenyl dicarboxylate ligand was pre-functionalized with dimethoxybenzyl alcohol via an amide bond, incorporated into a Hf-nMOF, and then post-synthetically modified with SN38 via a carbonate bond.

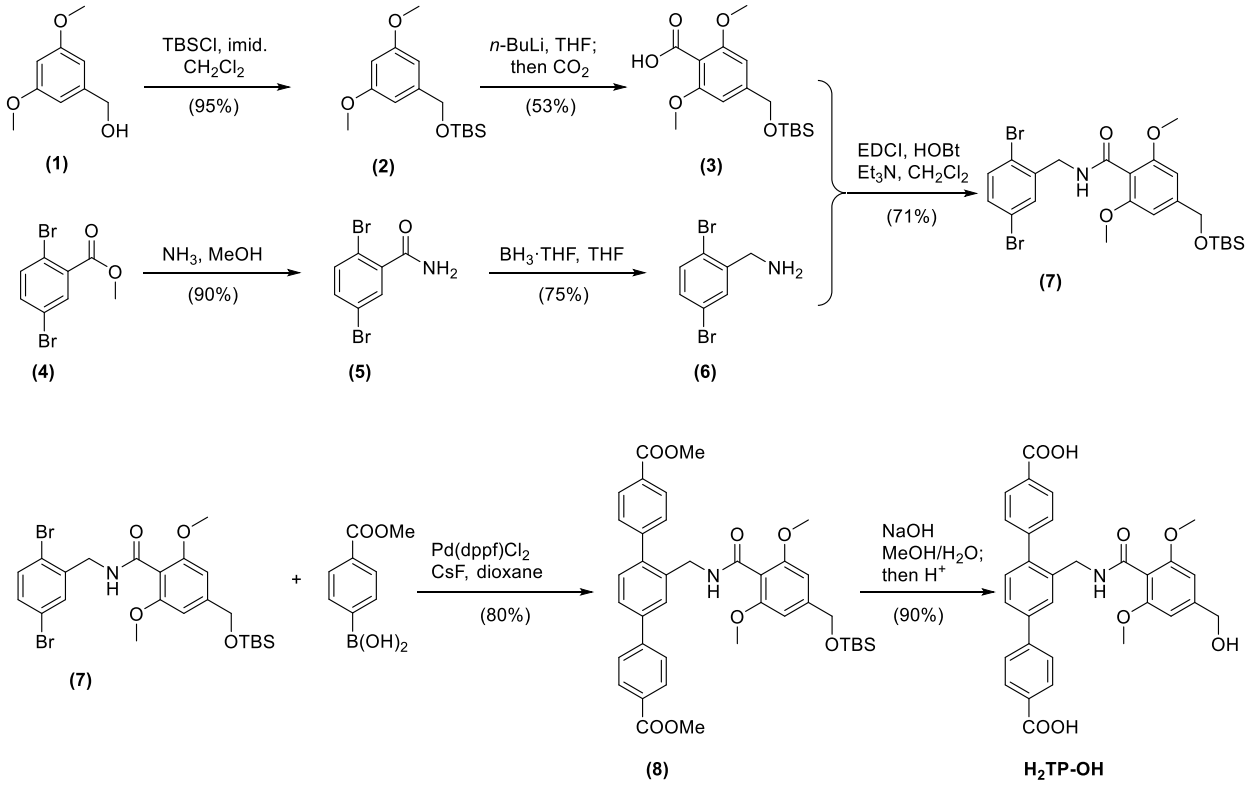

Scheme 5-1. Synthesis of H_2TP-OH.

First, the dicarboxylic acid H_2TP-OH was synthesized in five steps starting from 3,5-dimethoxylbenzyl alcohol (**1**) via protection with *tert*-butyldimethylsilyl group, lithiation and carboxyl group installation, coupling with 2,5-dibromobenzylamine via an amide bond, Suzuki coupling with (4-(methoxycarbonyl)phenyl)boronic acid, and base-catalyzed hydrolysis (**Scheme 5-1**). Next, Hf-TP-OH nMOF with Hf_{12} SBUs was synthesized via a solvothermal reaction between $HfCl_4$, H_2TP-OH, trifluoracetic acid, and water in *N*, *N*-dimethylformamide at 80 °C for

1 day. Finally, Hf-TP-OH was treated with 4-nitrophenyl chloroformate followed by SN38 to afford Hf-TP-SN.

Hf-TP-OH and Hf-TP-SN both displayed a nanoplate morphology with a diameter of ~70 nm and a thickness of ~10 nm by transmission electron microscopy (TEM). The high-resolution TEM (HRTEM) image and its fast Fourier transform (FFT) pattern of Hf-TP-OH demonstrated the crystallinity and 6-fold symmetry, consistent with the projection of Hf_{12}-TP (TP = terphenyldicarboxylate) structure along the vertical direction (**Figure 5-2**).

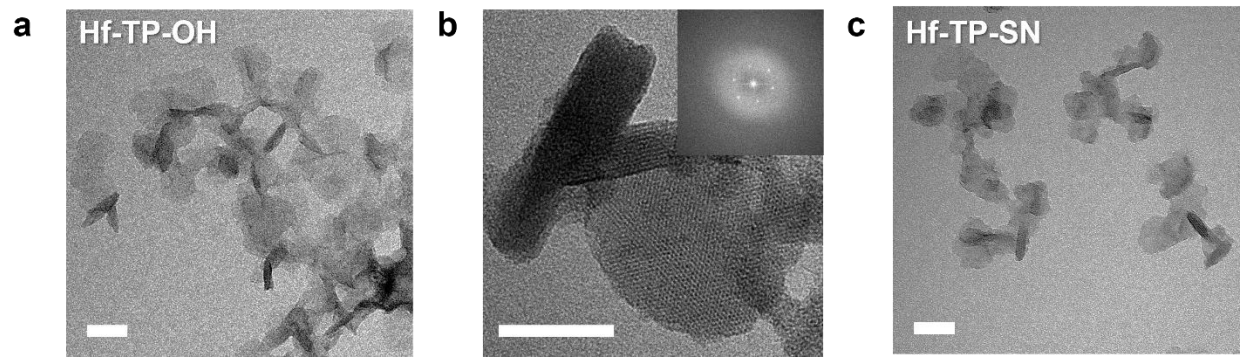

Figure 5-2. (a) TEM image and (b) HRTEM image and FFT pattern (inset) of Hf-TP-OH. (c) TEM image of Hf-TP-SN. Scale bar = 50 nm.

The number-averaged sizes of Hf-TP-OH and Hf-TP-SN were 125 ± 4 and 124 ± 2 nm (**Figure 5-3a**), respectively, while their ζ-potentials were -11.2 ± 1.2 and -10.3 ± 0.4 mV (**Figure 5-3b**), respectively, suggesting that Hf-TP-OH maintained the nanoscale size and surface charge after post-synthetic modification. Powder X-ray diffraction (PXRD) studies confirmed that Hf-TP-SN and Hf-TP-OH adopted the same structure as Hf_{12}-TP MOF consisting of $Hf_{12}(\mu_3\text{-}O)_8(\mu_3\text{-}OH)_8(\mu_2\text{-}OH)_6$ SBUs and TP ligand in a *hcp* topology (**Figure 5-3c**).[44] Moreover, Hf-TP-SN retained its crystallinity after incubation in PBS (1 mM, pH 7.4) for 24 hours (**Figure 5-4d**), ensuring its stability for biological applications.

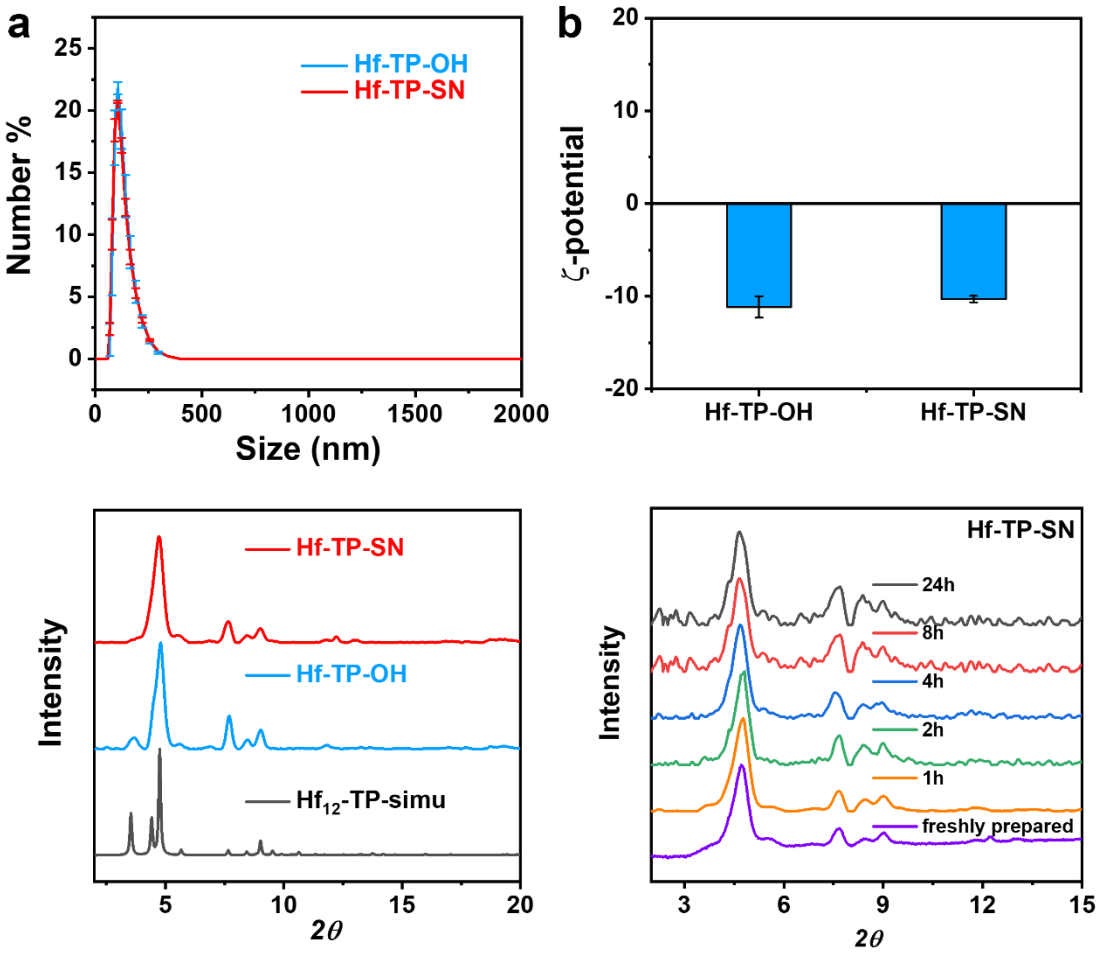

Figure 5-3. (a) Number-averaged sizes of Hf-TP-OH and Hf-TP-SN in ethanol. (b) ζ -potentials of Hf-TP-OH and Hf-TP-SN in H2O. (c) PXRD patterns of Hf-TP-OH, Hf-TP-SN, and the simulated pattern for Hf_{12}-TP MOF. (d) PXRD patterns of Hf-TP-SN freshly prepared and dispersed in PBS for 1, 2, 4, 8 and 24 hours.

UV-Vis spectroscopic analysis of digested Hf-TP-SN indicated ~16% of TP-OH ligands were conjugated with SN38 (**Figure 5-5**) after comparing the absorbance of TP-OH ligand and SN38 with their standard curves (**Figure 5-6**).

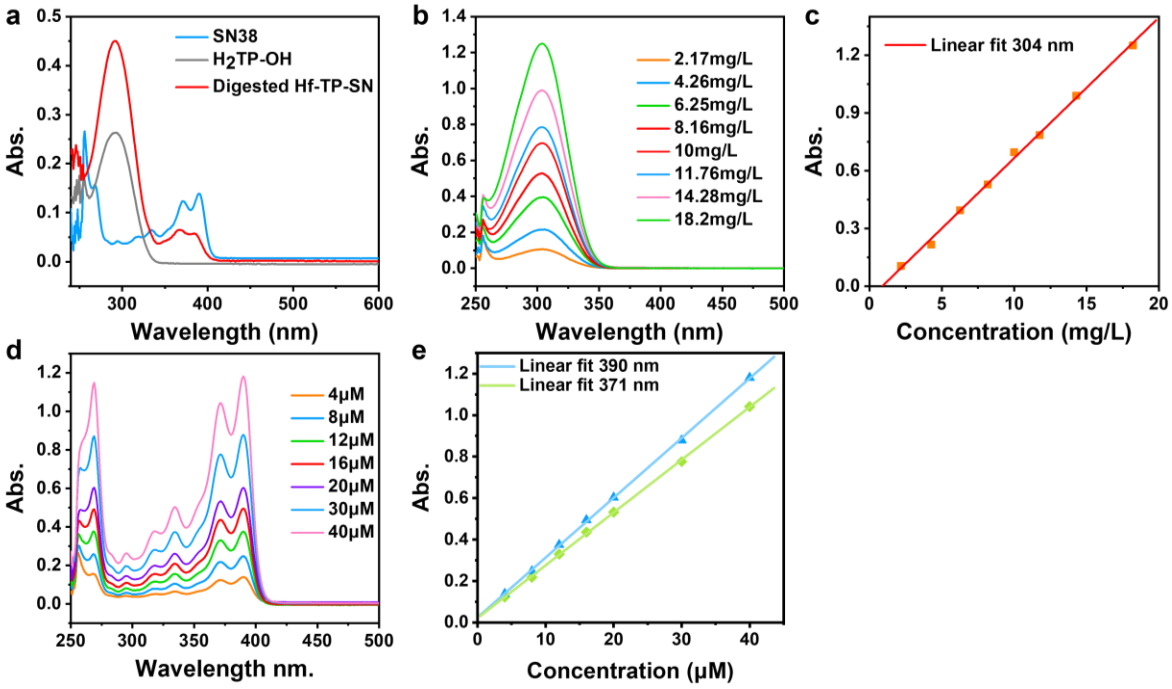

Figure 5-4. UV-Vis absorption spectra of (a) digested Hf-TP-SN, (b) H_2TP-OH and (d) SN38 and the fitted standard curves of (c) H_2TP-OH and (e) SN38 in DMSO.

Liquid chromatography-mass spectrometry (LC-MS) analysis indicated the trapping of 2.6% free SN38 (relative to total SN38) in the pores after digesting Hf-TP-SN using $NaHCO_3$[45] and extraction with ethyl acetate (**Figure 5-5**). After determining the Hf content by inductively coupled plasma mass spectrometry (ICP-MS), the formula of Hf-TP-SN was determined as $Hf_{12}(\mu_3\text{-}O)_8(\mu_3\text{-}OH)_8(\mu_2\text{-}OH)_6(TP\text{-}SN)_{1.08}(TP\text{-}OH)_{5.66}(OH)_{4.52}(H_2O)_{4.52}(SN38)_{0.03}$.

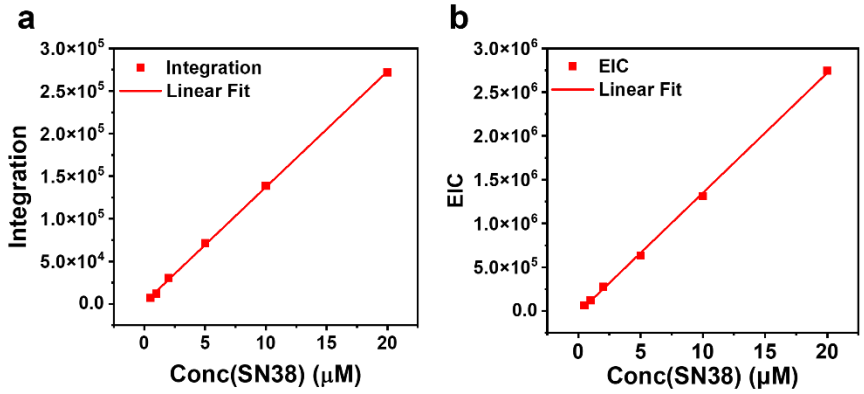

Figure 5-5. HPLC and LC-MS. The fitted standard curves of SN38 in EA by (a) HPLC or (b)LC-MS.

5.2.2. ROS generation and X-ray triggered release

A molecular counterpart, Me_2TP-SN, was synthesized from compound **8** to support the post-synthetic modification and to examine the cytotoxicity of the prodrug (**Schemes 5-2**). Because of low aqueous solubility of Me_2TP-SN, we synthesized MeO-SN from **1** and used it as a homogeneous control (**Scheme 5-3**).

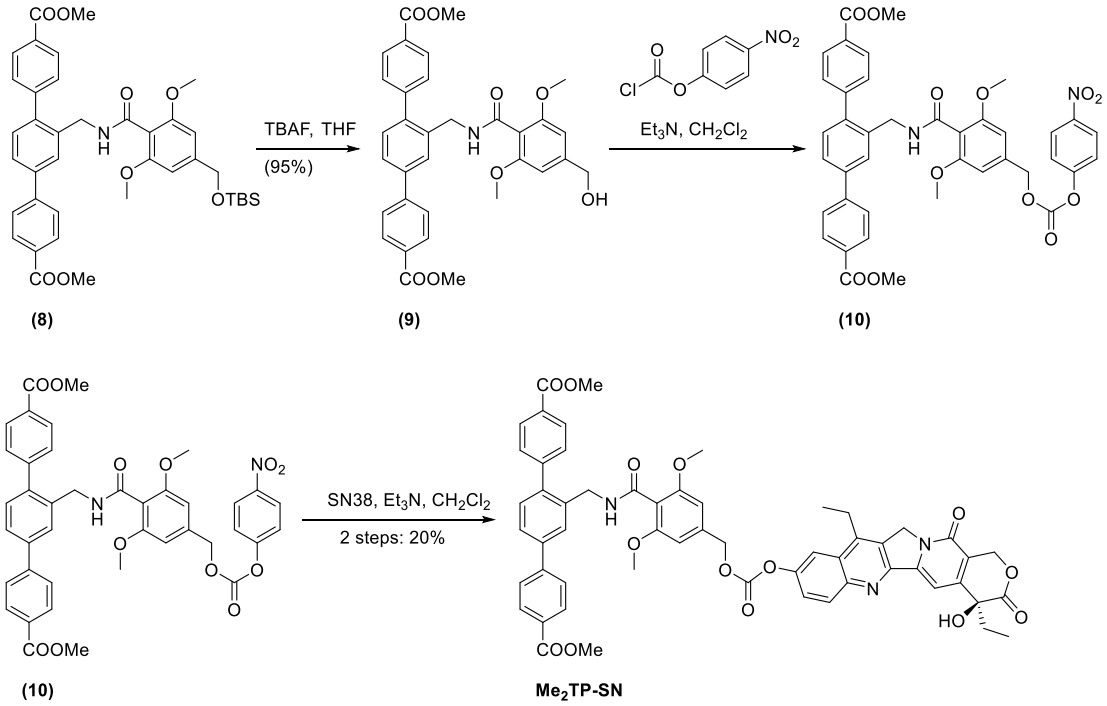

Scheme 5-2. Synthesis of Me_2TP-SN.

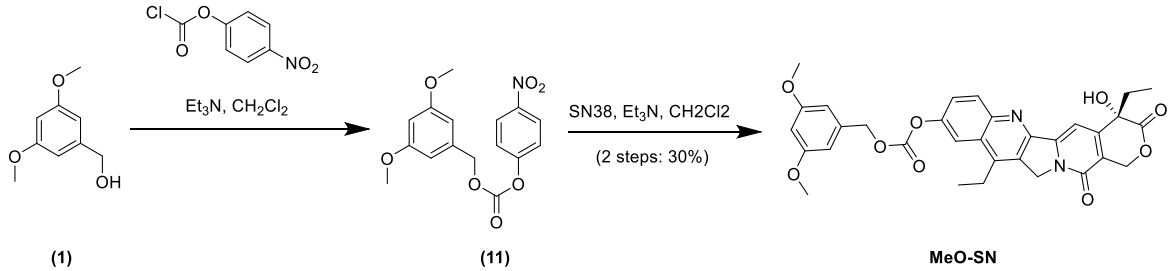

Scheme 5-3. Synthesis of MeO-SN.

We first evaluated ROS generation by 2',7'-dichlorodihydrofluorescein (DCFH) assay.[46] The total ROS signals in PBS, Hf-TP-OH, and Hf-TP-SN groups all increased linearly with X-ray doses. The relative enhancements of Hf-TP-OH and Hf-TP-SN over PBS were 47% and 19%,

respectively (**Figure 5-6a**). Aminophenyl fluorescein (APF) assay showed that Hf-TP-OH and Hf-TP-SN enhanced ·OH generation by 96% and 59%, respectively, over PBS (**Figure 5-6b**). The reduced ROS and hydroxyl radical signals from Hf-TP-SN are likely due to the consumption of ·OH by the 3,5-dimethoxylbenzyl carbonate linkage to release SN38.

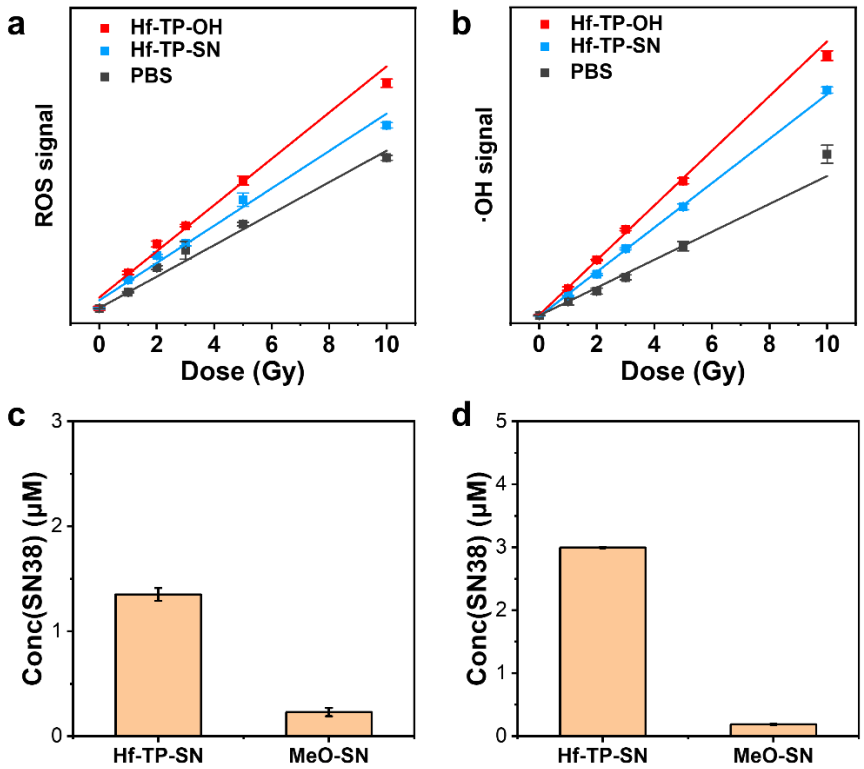

Figure 5-6. (a) Total ROS signals and (b) hydroxyl radical signals of PBS, Hf-TP-OH, and Hf-TP-SN by DCFH assay and APF assay, respectively, after different X-ray doses, *n* = 6. Hf concentration was 40 μM. SN38 released from MeO-SN or Hf-TP-SN (c) after 10 Gy X-ray irradiation or (d) after reacting with ·OH generated by the Fenton reaction. Starting MeO-SN or Hf-TP-SN concentration was 100 μM.

High performance-liquid chromatography analyses showed that Hf-TP-SN released ~1.35% of total SN38 after 10 Gy X-ray irradiation, which was 5-fold higher than SN38 released from MeO-SN under identical conditions (**Figure 5-6c**). The triggered release of SN38 was confirmed using ·OH generated by the Fenton reaction;[47] Hf-TP-SN showed 14.8-fold higher SN38 release than MeO-SN under this condition (**Figures 5-6d**). These results showed that upon X-ray irradiation, electron-dense Hf_{12} SBUs serve as radiosensitizers to enhance ·OH generation for the

triggered release of SN38 via hydroxylation of the 3,5-dimethoxylbenzyl carbonate followed by 1,4-elimination (**Figure 5-1**).

5.2.3. *In vitro* experiments

MTS assays revealed that H_2TP-OH ligand and Hf-TP-OH nMOF did not show obvious cytotoxicity to CT26 colon carcinoma cells at a TP concentration of 100 μM (**Figure 5-7a&b**), indicating their non-toxic nature without X-ray irradiation. On the other hand, clonogenic assay showed that Hf-TP-OH possessed strong radiosensitizing property with a dose modifying ratio at 10% survival fraction ($DMR_{10\%}$) of 1.255 (**Figure 5-7c**) due to enhanced ·OH generation via radiosensitization as probed by hydroxyphenyl fluorescein (HPF) assay (**Figure 5-7d**).

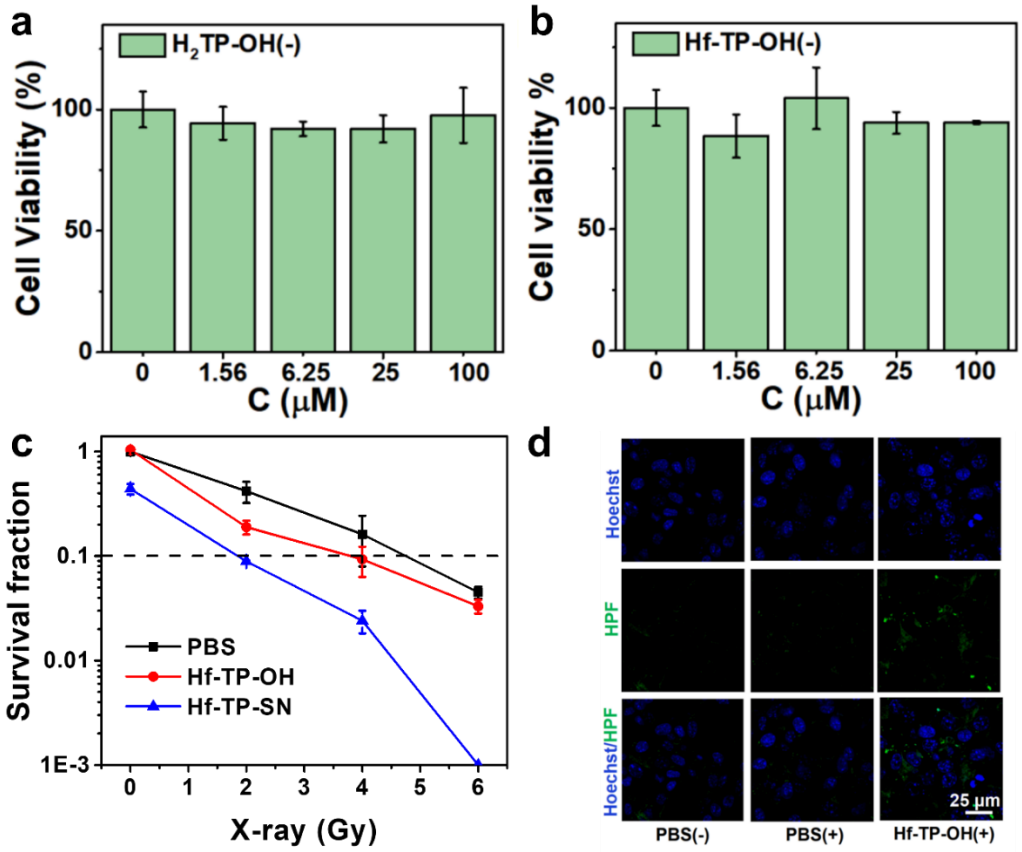

Figure 5-7. Toxicity of H_2TP-OH ligand and Hf-TP-OH nMOF. Cell viability of CT26 cells treated by (a) H_2TP-OH(-) or (b) Hf-TP-OH(-). (c) Survival fractions of CT26 cells after incubation with PBS, Hf-TP-OH, or Hf-TP-SN under different doses of X-ray irradiation. (d) CLSM images of CT26 cells stained by hydroxyphenyl fluorescein (HPF, green) and Hoechst 33342 (blue, cell nucleus) for detecting the generation of ·OH.

The cytotoxicity of SN38 and Me_2TP-SN was also evaluated. While SN38 showed a half-maximal inhibitory concentration (IC_{50}) of 0.584 μM (**Figure 5-8a**),[33] Me_2TP-SN had much lower cytotoxicity with an IC_{50} of 13.5 μM (**Figure 5-8b**), suggesting the successful construction of SN38 prodrug via the dimethoxybenzyl carbonate masking group.

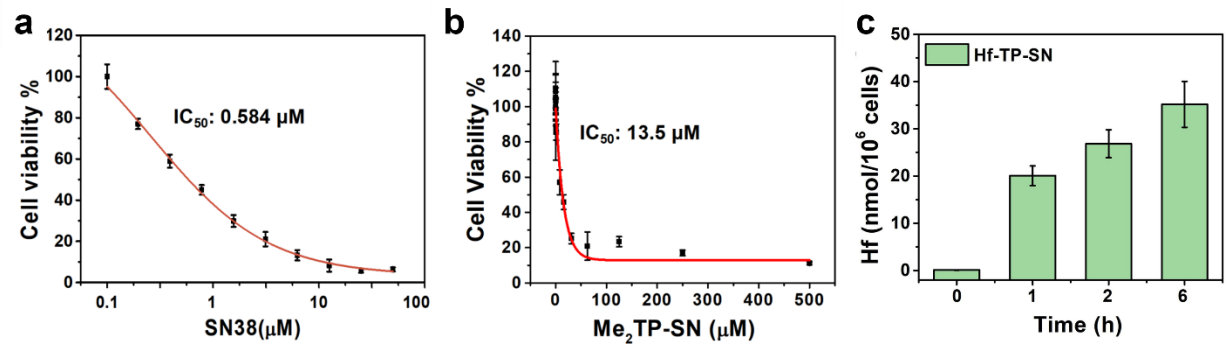

Figure 5-8. Cell viability curves of CT26 cells treated by (a) SN38(-) or (b) Me_2TP-SN(-). (c) Time-dependent cellular uptake of Hf-TP-SN quantified by ICP-MS (n = 3).

The cellular uptake of Hf-TP-SN was examined before investigation of its cytotoxicity. Hf-TP-SN showed efficient and time-dependent cellular uptake as quantified by ICP-MS (**Figure 5-8c**). To confirm X-ray triggered release of SN38, we detected the cytotoxicity of Hf-TP-SN on CT26 cells with varying doses of X-ray by clonogenic assay [denoted Hf-TP-SN(+)]. Hf-TP-SN showed a significantly increased $DMR_{10\%}$ of 2.566 over Hf-TP-OH (1.255), likely due to the combined chemo-radiotherapeutic effects of the released SN38 and X-ray irradiation (**Figure 5-7c**). Interestingly, confocal laser scanning microscopy (CLSM) and flow cytometry studies show that Hf-TP-OH(+) and Hf-TP-SN(+) exhibited 2.29- and 9.30-fold higher intracellular ROS signals than PBS(+), respectively, at an X-ray dose of 3 Gy (**Figures 5-9**). The stronger ROS signal in Hf-TP-SN(+) group likely resulted from the oxidative pressure of the released SN38 on the cells and the radiosensitizing effect of electron-dense Hf_{12} SBUs.[48]

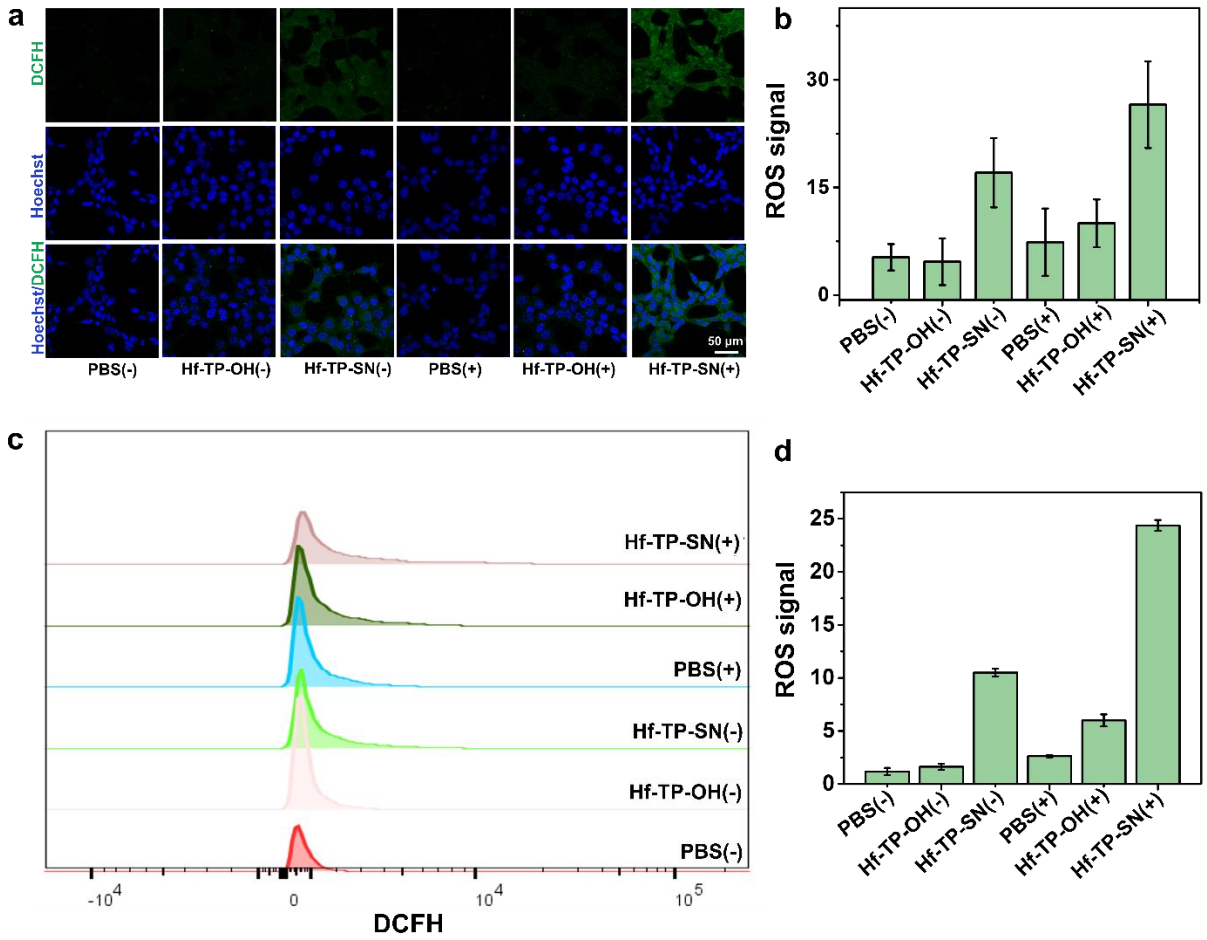

Figure 5-9. ROS generation *in vitro*. (a) CLSM images of CT26 cells stained by DCFH-DA (green) and Hoechst (blue) for detecting the generation of ROS. (b) Relative FL intensity analyzed by Image J. (c) Quantification of histograms of intracellular ROS signals by flow cytometry. (d) Percentage of DCF^{+} CT26 cells after Hf-TP-OH(+) or Hf-TP-SN(+) treatment. X-ray dose was 3 Gy.

We next investigated DNA double strand breaks (DSBs) in CT26 cells via detecting the expression of γ-H2AX, a phosphorylated protein biomarker for DSBs.[49] PBS(+) induced a small amount of red γ-H2AX fluorescence due to X-ray's ability to cause DNA damage.[50] More pronounced DSBs were observed in Hf-TP-OH(+) and Hf-TP-SN(+) groups, while no fluorescence was observed in Hf-TP-OH(-) group (**Figure 5-10**), which supports potent radiosensitization by Hf-nMOFs. Hf-TP-SN(-) also showed significantly enhanced γ-H2AX signal

over PBS control, likely due to the entrapped SN38 in the pores of Hf-TP-SN. Free SN38 inhibits the nuclear enzyme topoisomerase I during DNA replication, leading to DSBs.[42-43]

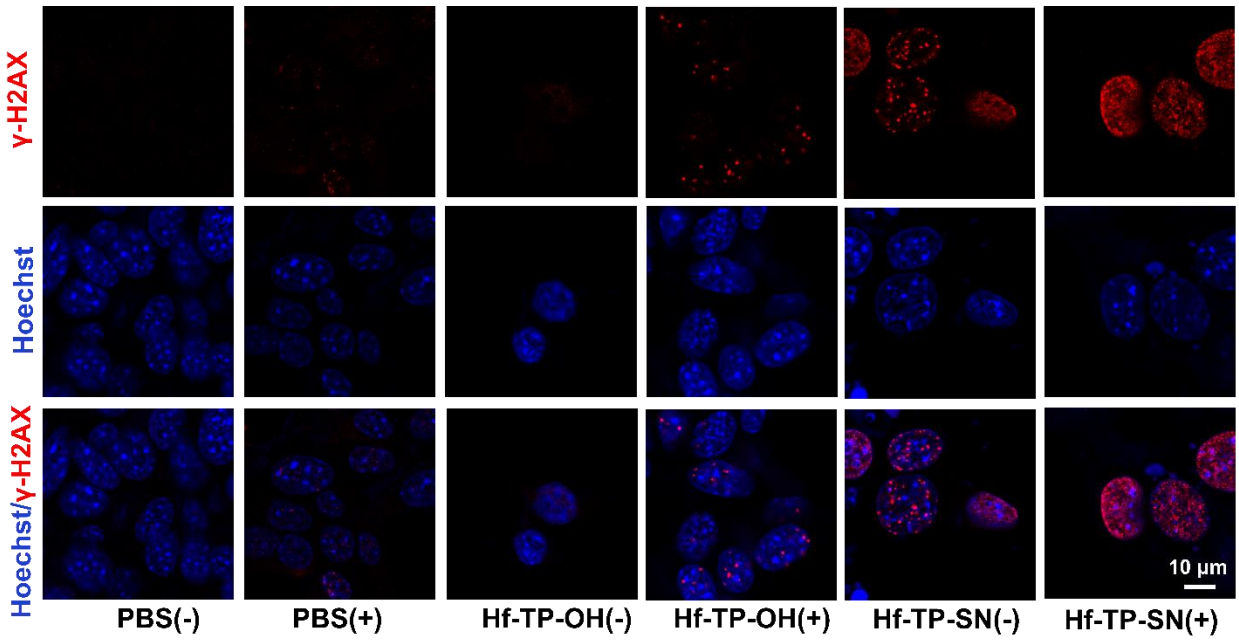

Figure 5-10. CLSM images of CT26 cells for γ-H2AX assay, (scale bar: 10 μm). X-ray dose: 3Gy.

Cell death pathways were evaluated with the annexin V Alexa fluor 488 and propidium iodide (PI) cell apoptosis kit. More than 85% cells remained healthy in Hf-TP-OH(-) group, confirming that Hf-TP-OH exhibited negligible cytotoxicity. While Hf-TP-OH(+) and Hf-TP-SN(-) groups showed 77.5% and 59.6% healthy cells, respectively, Hf-TP-SN(+) treatment significantly reduced the percentage of healthy cells to 46.3% (**Figure 5-11**). This result suggests synergistic therapeutic effects of Hf-TP-SN(+) due to the radiosensitizing effect of the nMOF and potent chemotherapeutic effect of the released SN38.

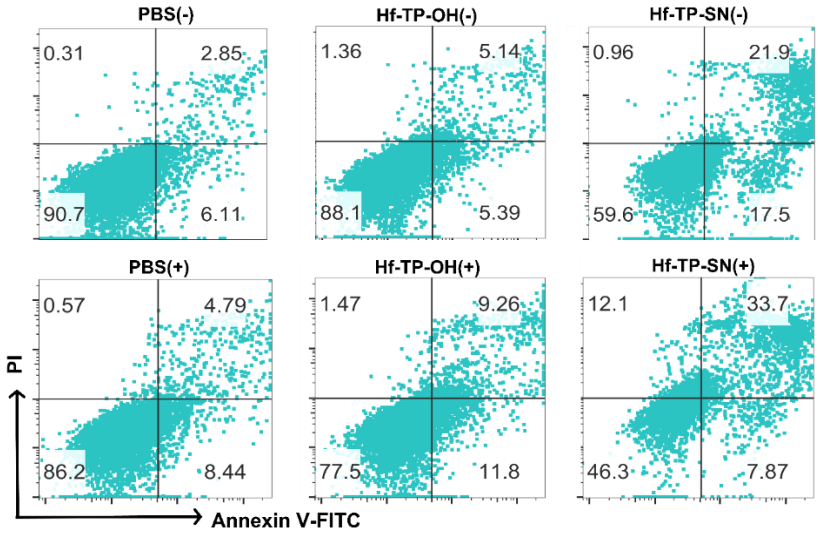

Figure 5-11. Immunogenic cell death. (e) Representative flow cytometry dot plots showing cell apoptosis/death stained by FITC-annexin-V and PI in different treatment groups.

5.2.4. *In vivo* experiments

We established a subcutaneous CT26 tumor model to assess the *in vivo* anticancer efficacy of Hf-TP-SN(+). CT26 tumor-bearing mice were intratumorally injected with PBS, irinotecan (a prodrug of SN38, 0.046 μmol),[34] Hf-TP-OH (0.5 μmol Hf), or Hf-TP-SN (0.5 μmol Hf and 0.046 μmol SN38). Six to eight hours later, the tumors were exposed to X-ray at the dose of 2 Gy. X-ray irradiation was repeated on two consecutive days (for a total of 6 Gy) (Figure S14). Tumor volumes and mouse body weights were monitored daily until the PBS(-) end point (**Figures 5-12**). While PBS(+) moderately inhibited tumor growth with a tumor growth inhibition index (TGI) of 0.468, irinotecan(+) and Hf-TP-OH(+) enhanced tumor growth inhibition with TGIs of 0.695 and 0.869, respectively. Hf-TP-SN(+) potently regressed tumors with a TGI value of 0.965 and completed tumor eradication in 40% mice. In contrast, Hf-TP-SN(-) treatment modestly inhibited tumor growth with a TGI of 0.362. The impressive *in vivo* therapeutic effects of Hf-TP-SN(+) resulted from synergistic actions of nMOF-mediated radiosensitization and X-ray triggered release of SN38

from Hf-TP-SN. The mice in all treatment groups showed steady body weights (**Figure 5-12d**), suggesting the lack of general toxicity.

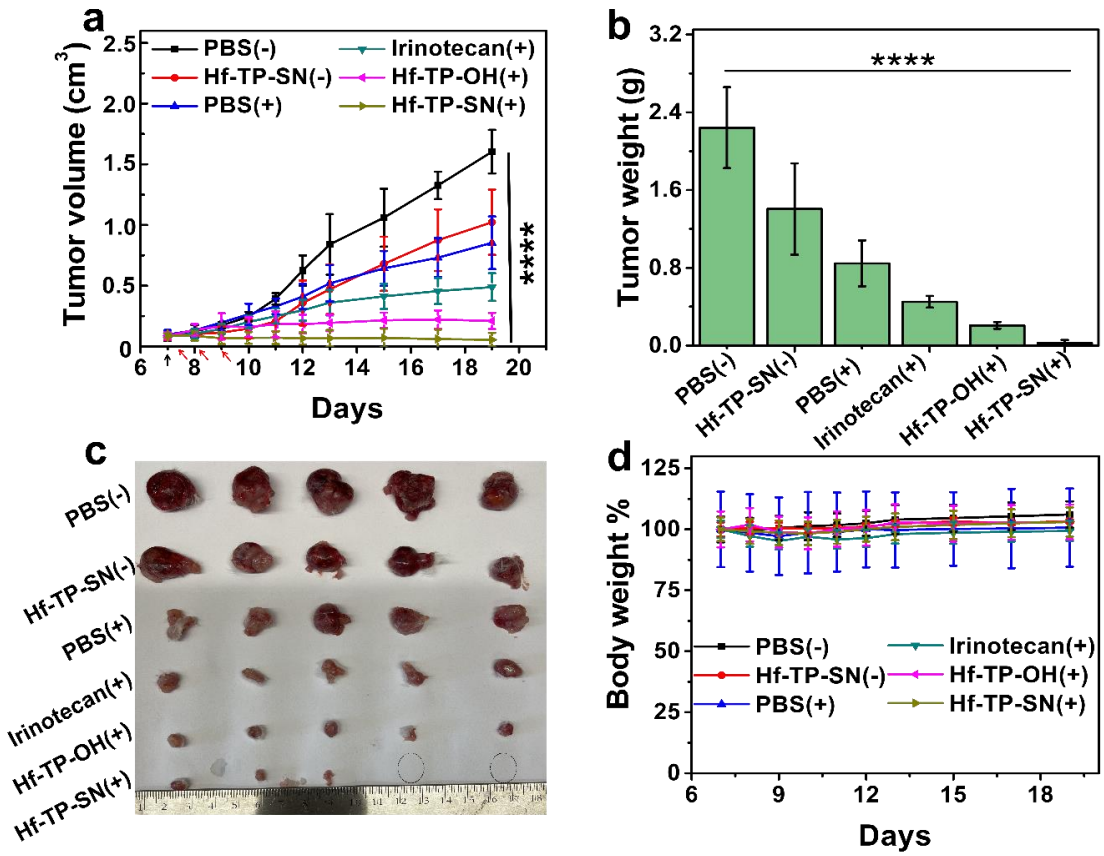

Figure 5-12. *In vivo* anticancer efficacy. (a) Growth curves of subcutaneous CT26 tumors in BALB/c mice after treatment with PBS, irinotecan, Hf-TP-OH, or Hf-TP-SN followed by X-ray irradiation, n = 5. Black arrows indicate nMOF injection whereas red arrows indicate irradiation. (b) Weights of the excised tumors at the endpoint (day 19). (c) Photograph of the excised tumors. (d) Relative body weights of CT26 bearing BLAB/c mice after different treatments.

One day after the last X-ray irradiation, tumor slices were processed to evaluate pathological changes via γ-H2AX, Ki67, terminal deoxynucleotidyl transferase mediated dUTP-biotin nick end labeling (TUNEL), and hematoxylin and eosin (H&E) staining. Hf-TP-SN(+) treatment increased the expression of γ-H2AX (**Figure 5-13a**), reduced cell proliferation with lower Ki67 signal (**Figure 5-13b)**, and increased cell apoptosis in TUNEL staining (**Figure 5-13c**). H&E staining showed distinctive cellular damage in the tumors treated with Hf-TP-OH(+) and Hf-

TP-SN(+); minimal cellular damage was observed in PBS(+) and irinotecan(+) groups (**Figure 5-13d**).

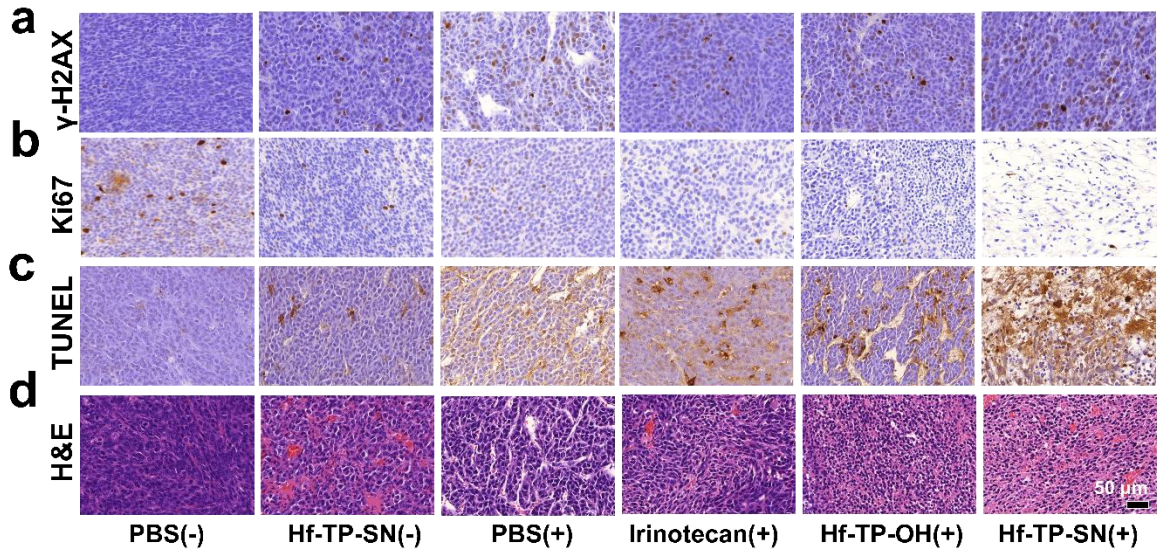

Figure 5-13. Pathological changes. (a) γ-H2AX, (b) Ki67, (c) TUNEL and (d) H&E staining of excised CT26 tumors (scale bar: 50 μm).

Furthermore, histology of the hearts, livers, spleens, lungs, and kidneys of treated mice did not show any abnormality (**Figure 5-14**), supporting the safety of Hf-TP-SN(+) treatment in mice.

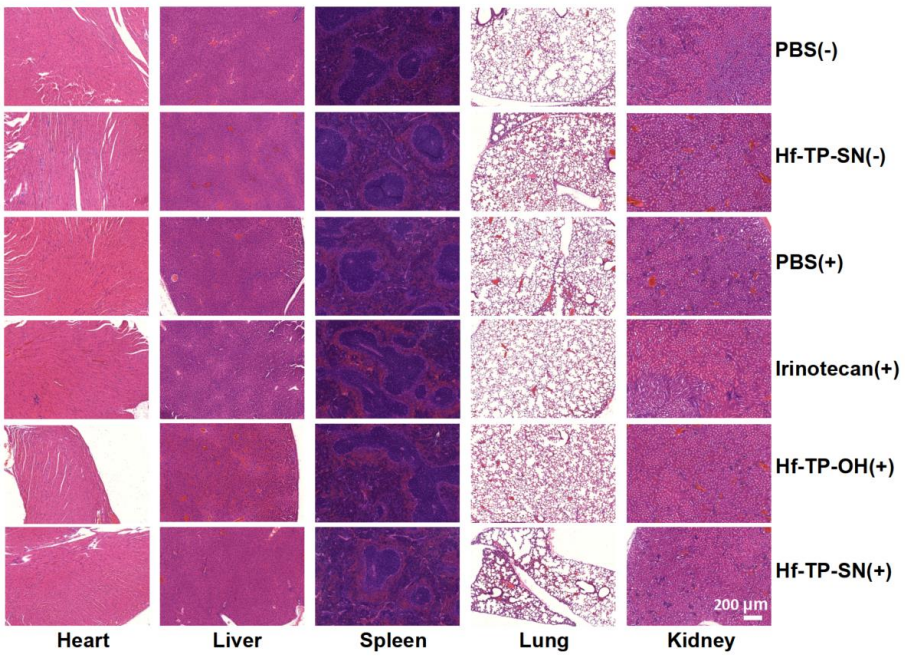

Figure 5-14. H&E staining of hearts, livers, spleens, lungs, and kidneys of CT26 tumor-bearing BALB/c mice in different treatment groups (scale bar: 200 μm).

5.3. Conclusions

In this chapter, we designed Hf-TP-SN nMOF with an X-ray triggerable SN38 prodrug for synergistic radiotherapy and chemotherapy. Hf-TP-SN was synthesized via a combination of pre-functionalization of terphenyl ligands with 3,5-dimethylbenzyl alcohol and post-synthetic modification with SN38 via a carbonate bond. Upon X-ray irradiation, electron-dense Hf_{12}-SBUs served as radiosensitizers to enhance ·OH generation, leading to 5-fold higher release of SN38 from Hf-TP-SN than a homogeneous counterpart. Hf-TP-SN not only enhanced the radiotherapeutic efficacy but also achieved chemotherapeutic effect through on-demand release of SN38. Such a chemoradiotherapy strategy effectively reduces the radiation dose required for tumor regression and minimizes the side effects of chemotherapy via burst release of SN38 inside cancer cells. As the post-synthetic modification step only requires a hydroxyl or amino group in a drug for nucleophilic substitution, a variety of therapeutic agents can be grafted onto the Hf-TP-OH to form novel Hf-TP-conjugated drugs for disease management. This work highlights the potential of nMOFs in multi-modality cancer treatment via on-demand, triggered release of therapeutic agents.

5.4. Methods

5.4.1 Synthesis of Organic Ligands and Molecular Prodrugs

4-(((*tert*-Butyldimethylsilyl)oxy)methyl)-2,6-dimethoxybenzoic acid (3). A solution of imidazole (6.08 g, 0.089 mol) and 3,5-dimethoxybenzyl alcohol (**1**, 5 g, 0.030 mol) in dry dichloromethane (DCM, 60 mL) was combined with *tert*-butyldimethylsilyl chloride (TBSCl, 6.74 g, 0.045 mol) and stirred at room temperature for 2 hours. Excess TBSCl was quenched by 2 mL methanol (MeOH); the resulting solution was condensed via rotary evaporation and then purified by flash silica gel column chromatography to give *tert*-butyl((3,5-

dimethoxybenzyl)oxy)dimethylsilane (**2**, 8 g, 0.028 mol, 95%). ^{1}H NMR (400 MHz, Chloroform-*d*) δ 6.52-6.47 (m, 2H), 6.34 (s, 1H), 4.69 (s, 2H), 3.79 (s, 6H), 0.95 (s, 9H), 0.10 (s, 6H); ^{13}C NMR (101 MHz, $CDCl_3$) δ 160.91, 144.23, 103.85, 99.05, 64.99, 55.42, 26.09, 18.57, -5.11. HR-MS (ESI, positive mode): *m/z* calc'd for $C_{15}H_{27}O_3Si$ $[M+H]^+$: 283.1729, found 283.1727.

Compound **2** (10 g, 0.035 mol) was dissolved in dry tetrahydrofuran (THF, 100 mL) and cooled to 0 °C under N_2, to which 1.6 M *n*-butyllithium in hexanes (22.2 mL, 0.035 mol) was added dropwise; the resulting mixture was then stirred at room temperature for 1 hour. Dry ice (10 g, 0.227 mol) was added afterwards, and the reaction mixture was allowed to stand at room temperature overnight. The resulting solution was condensed via rotary evaporation and water (50 mL) was added to the residue, which was extracted with ethyl acetate (EA, 20 mL) twice. The aqueous layer was carefully acidified with 1M hydrochloric acid (dropwise) until the pH reached about 3. The white precipitate was separated via filtration, washed with water, dried under vacuum, and purified by column chromatography to give compound **3** (6.1 g, 0.019 mol, 53%). ^{1}H NMR (400 MHz, Chloroform-*d*) δ 6.60 (s, 2H), 4.74 (s, 2H), 3.88 (s, 6H), 0.96 (s, 8H), 0.12 (s, 6H); ^{13}C NMR (101 MHz, $CDCl_3$) δ 168.75, 158.57, 146.94, 109.33, 101.59, 64.73, 56.35, 26.01, 18.51, -5.12. HR-MS (ESI, positive mode): *m/z* calc'd for $C_{16}H_{27}O_5Si$ $[M+H]^+$: 327.1628, found 327.1695.

2,5-Dibromobenzyl amine (6). 2,5-Dibromobenzyl amine (**6**) was prepared based on reported procedures with modification in the second step.[51] To a solution of 7M ammonia (NH_3) in MeOH (100 mL, 0.70 mol) was added methyl 2,5-dibromobenzoate (**4**, 10.0 g, 0.034 mol) at room temperature; the resulting dissolved solution was evenly separated into five 20-mL vials, sealed, and stirred for 3 days. The white precipitate formed was separated and collected via filtration, dispersed in hexanes (100 mL), recollected via filtration, and dried under vacuum to produce 2,5-dibromobenzamide (**5**, 8.58 g, 0.031 mol, 90%). ^{1}H NMR (400 MHz, Chloroform-*d*) δ 7.78 (d, *J*

= 2.4 Hz, 1H), 7.48 (d, *J* = 8.5 Hz, 1H), 7.42 (dd, *J* = 8.5, 2.4 Hz, 1H), 6.02 (d, *J* = 63.0 Hz, 2H); ^{13}C NMR (101 MHz, $CDCl_3$) δ 167.63, 138.29, 135.14, 134.84, 133.00, 121.79, 117.98. HR-MS (ESI, positive mode): *m/z* calc'd for $C_7H_6Br_2NO$ $[M+H]^+$: 279.8796, found 279.8790.

1M borane-tetrahydrofuran complex (BH_3 in THF) was added in excess (35 mL, 0.035 mol) to compound **5** (4.11 g, 0.0144 mol); the resulting mixture was stirred at reflux for 24 hours and then quenched with concentrated HCl (3.5 mL). The solution was then refluxed for 2 more hours and cooled to room temperature. The suspension was filtered to obtain the white solid, which was then dissolved in water and basified to pH~10 by addition of sat. sodium carbonate (Na_2CO_3) while the solution was stirring. The reaction mixture was extracted with EA (30 mL) 3 times. The combined organic phase was dried over sodium sulfate (Na_2SO_4), filtered, and evaporated to give compound **6** (2.91 g, 0.011 mol, 74.6%). ^{1}H NMR (400 MHz, Chloroform-*d*) δ 7.55 (d, *J* = 2.6 Hz, 1H), 7.39 (d, *J* = 8.5 Hz, 1H), 7.24 (dd, *J* = 8.4, 2.4 Hz, 1H), 3.88 (s, 2H); ^{13}C NMR (101 MHz, $CDCl_3$) δ 144.34, 134.22, 131.99, 131.45, 122.07, 121.76, 46.65. HR-MS (ESI, positive mode): *m/z* calc'd for $C_7H_8Br_2N$ $[M+H]^+$: 265.9003, found 265.8999.

4-(((*tert*-Butyldimethylsilyl)oxy)methyl)-*N*-(2,5-dibromobenzyl)-2,6-dimethoxybenzamide (7). Compound **6** (1 g, 3.77 mmol), **3** (1.23 g, 3.77 mmol), 1-(3-dimethylaminopropyl)-3-ethylcarbodiimide hydrochloride (EDCI, 1.536 g, 8.0 mmol), hydroxybenzotriazole (HOBt, 0.6486 g, 4.8 mmol), and triethylamine (TEA, 1.3675 mL) were combined in 75 mL dry DCM under Ar. The resulting mixture was stirred at room temperature for 12 hours before 10 mL H_2O was added and the mixture was extracted by DCM (3x20 mL); the combined organic phase was then dried over Na_2SO_4, filtered, evaporated, and separated via column chromatography to give **7** (1.534 g, 2.68 mmol, 71%). ^{1}H NMR (400 MHz, Chloroform-*d*) δ 7.83 (dd, *J* = 2.4, 0.9 Hz, 1H), 7.39 (dd, *J* = 8.4, 0.9 Hz, 1H), 7.24 (d, *J* = 2.4 Hz, 1H), 6.58 (d, *J* = 1.0 Hz, 2H), 6.17 (t, *J* = 6.5

Hz, 1H), 4.73 (d, *J* = 1.0 Hz, 2H), 4.68 (d, *J* = 6.4 Hz, 2H), 3.88 (d, *J* = 0.9 Hz, 6H), 0.96 (d, *J* = 0.9 Hz, 9H), 0.11 (d, *J* = 0.9 Hz, 6H); ^{13}C NMR (101 MHz, $CDCl_3$) δ 166.22, 157.58, 145.50, 139.87, 133.93, 131.86, 121.83, 121.53, 113.82, 101.42, 64.90, 56.04, 43.48, 26.03, 18.53, -5.09. HR-MS (ESI, positive mode): *m/z* calc'd for $C_{23}H_{32}Br_2NO_4Si$ $[M+H]^+$: 574.0447, found 574.0463.

Dimethyl 2'-((4-(((*tert*-butyldimethylsilyl)oxy)methyl)-2,6-dimethoxybenzamido)methyl)-[1,1':4',1''-terphenyl]-4,4''-dicarboxylate (8). To compound **7** (1 g, 0.0017 mol) was added (4-(methoxycarbonyl)phenyl)boronic acid (0.942 g, 0.0052 mol), CsF (1.591 g, 0.0105 mol), and [1,1′-bis(diphenylphosphino)ferrocene]dichloropalladium(II) [$Pd(dppf)Cl_2$, 0.128 g, 0.00017 mol]; the solids were collected in a Schlenk flask and put under vacuum. Degassed dioxane (45 mL) was added to the flask; the resulting solution was stirred at 90 °C for 3 days, after which the solution was allowed to cool to room temperature, filtered through celite, rid of dioxane via rotary evaporation, dried under vacuum and purified via column chromatography to yield **8** (0.95 g, 1.4 mmol, 80%). ^{1}H NMR (400 MHz, Chloroform-*d*) δ 8.15 – 8.10 (m, 4H), 7.99 (d, *J* = 1.9 Hz, 1H), 7.78 – 7.72 (m, 2H), 7.60 (dd, *J* = 7.9, 1.9 Hz, 1H), 7.51 – 7.45 (m, 2H), 7.36 (d, *J* = 7.9 Hz, 1H), 6.53 (s, 2H), 5.98 (t, *J* = 6.0 Hz, 1H), 4.70 (s, 2H), 4.68 (d, *J* = 6.0 Hz, 2H), 3.96 (d, *J* = 2.8 Hz, 6H), 3.71 (s, 6H), 0.94 (s, 9H), 0.10 (s, 6H); ^{13}C NMR (101 MHz, $CDCl_3$) δ 167.11, 167.01, 166.13, 157.55, 145.34, 145.30, 145.02, 140.23, 140.05, 136.57, 130.49, 130.24, 129.85, 129.48, 129.39, 129.27, 127.30, 127.20, 126.09, 114.05, 101.43, 64.88, 56.00, 52.37, 52.33, 41.48, 26.02, 18.52, -5.10. HR-MS (ESI, positive mode): *m/z* calc'd for $C_{39}H_{46}NO_8Si$ $[M+H]^+$: 684.2993, found 684.3101.

2'-((4-(Hydroxymethyl)-2,6-dimethoxybenzamido)methyl)-[1,1':4',1''-terphenyl]-4,4''-dicarboxylic acid (H_2TP-OH). To compound **8** (0.6911 g, 1.01 mmol) was added NaOH (4.04 g, 101 mmol, 50 eq. per ester group) and MeOH and H_2O in a 1:1 ratio (20 mL: 20 mL). The resulting

mixture was stirred at 40 °C for 1 day; it was then allowed to cool to room temperature before being acidified (while being stirred) to pH~1-2 by addition of concentrated HCl; the acidic solution was left to stir for 2 hours to ensure the completion of the acid-base reaction. The resulting solution was filtered, washed with H_2O and dried under vacuum to produce H_2TP-OH (**9**, 0.493 g, 0.91 mmol, 90%).^{1}H NMR (400 MHz, DMSO-d_6) δ 12.99 (s, 2H), 8.63 (t, J = 6.0 Hz, 1H), 8.11 – 8.03 (m, 4H), 7.97 (d, J = 2.0 Hz, 1H), 7.88 – 7.82 (m, 2H), 7.72 (dd, J = 8.0, 1.9 Hz, 1H), 7.63 – 7.56 (m, 2H), 7.40 (d, J = 8.0 Hz, 1H), 6.63 (s, 2H), 4.49 (s, 2H), 4.37 (d, J = 5.9 Hz, 2H), 3.63 (s, 6H) (**Figure 5-15)**. ^{13}C NMR (101 MHz, DMSO-d_6) δ 167.14, 167.12, 164.90, 156.53, 145.24, 144.26, 144.16, 139.30, 138.55, 137.25, 130.10, 130.01, 129.80, 129.70, 129.42, 129.38, 126.77, 126.34, 125.29, 114.89, 101.87, 62.90, 55.55, 25.81 (**Figure 5-16)**. HR-MS (ESI, positive mode): *m/z* calc'd for $C_{31}H_{28}NO_8$ $[M+H]^+$: 542.1815, found 542.1780.

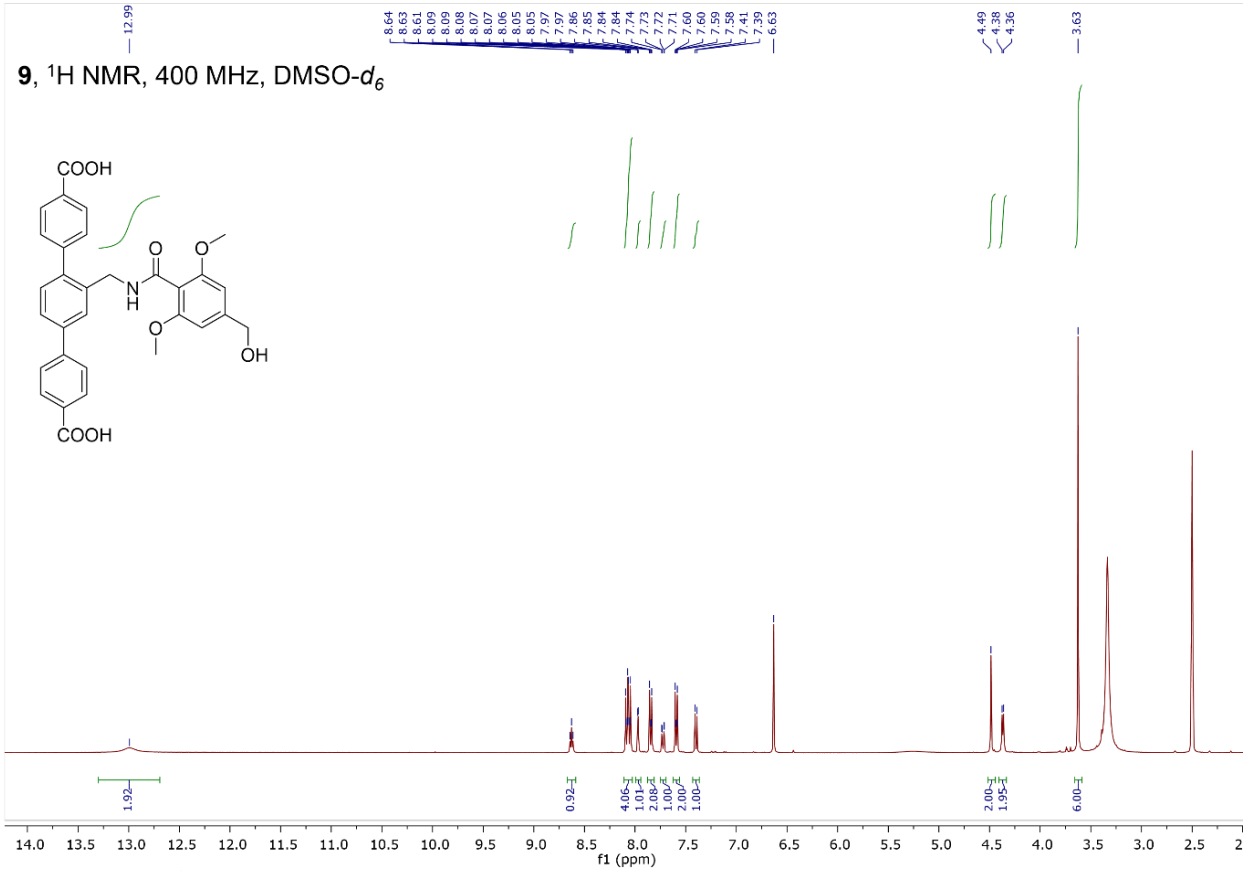

Figure 5-15. ^{1}H NMR spectrum of H_2TP-OH.

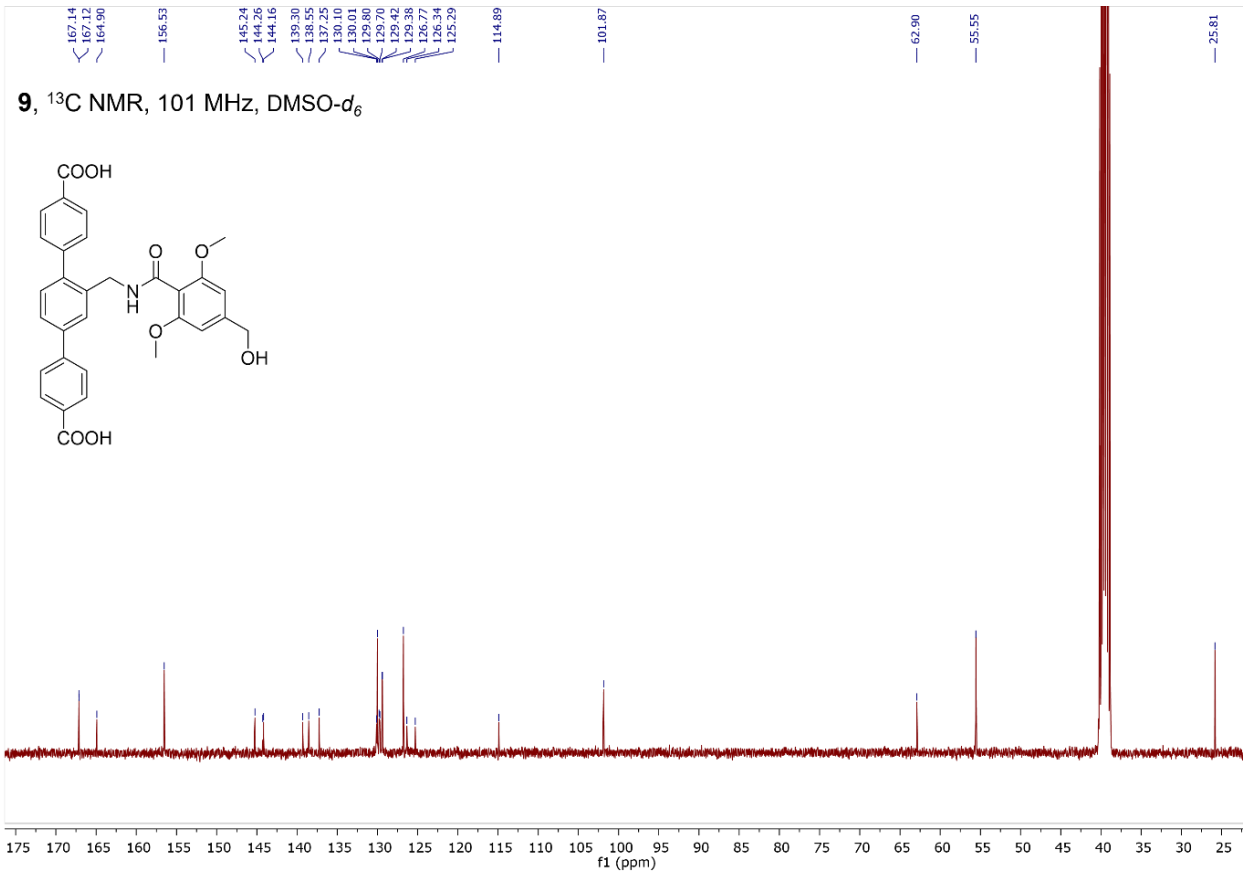

Figure 5-16. ^{13}C NMR spectrum of $H_2TP\text{-}OH$.

Dimethyl 2'-((4-(hydroxymethyl)-2,6-dimethoxybenzamido)methyl)-[1,1':4',1''-terphenyl]-4,4''-dicarboxylate (9). Compound **8** (500 mg, 0.730 mmol) was added to tetrabutylammonium fluoride solution in THF (1M, 5 mL) and stirred at room temperature for 2 hours. 10 mL saturated NH_4Cl solution was added and THF was removed via rotary evaporation. White precipitate was filtered and washed with water to produce compound **9** (395 mg, 0.694 mmol, 95%). ^1H NMR (400 MHz, Chloroform-d) δ 8.16 – 8.11 (m, 4H), 7.97 (d, J = 12.9 Hz, 1H), 7.75 (dd, J = 8.5, 2.3 Hz, 2H), 7.64 – 7.59 (m, 1H), 7.53 – 7.45 (m, 2H), 7.37 (dd, J = 7.9, 3.3 Hz, 1H), 6.56 (s, 2H), 5.96 (t, J = 6.3 Hz, 1H), 4.81 – 4.64 (m, 4H), 3.96 (d, J = 3.1 Hz, 6H), 3.73 (s, 6H). ^1H NMR (400 MHz, DMSO-d_6) δ 8.63 (t, *J* = 5.9 Hz, 1H), 8.09 (dd, *J* = 12.7, 7.9 Hz, 4H), 7.98 (s, 1H), 7.88 (d, *J* = 8.0 Hz, 2H), 7.74 (d, *J* = 8.1 Hz, 1H), 7.63 (d, *J* = 7.9 Hz, 2H), 7.41 (d, *J* = 7.8 Hz, 1H), 6.63

(s, 2H), 5.27 (s, 1H), 4.49 (s, 2H), 4.37 (d, *J* = 5.8 Hz, 2H), 3.90 (d, *J* = 4.4 Hz, 6H), 3.62 (s, 6H). ^{13}C NMR (101 MHz, DMSO-*d*$_6$) δ 166.08, 166.04, 164.88, 156.51, 145.24, 144.64, 144.51, 139.23, 138.43, 137.28, 130.12, 129.87, 129.59, 129.23, 128.65, 128.56, 126.93, 126.37, 125.35, 114.87, 101.87, 62.89, 55.56, 52.24, 52.21, 40.15. HR-MS (ESI, positive mode): *m/z* calc'd for $C_{33}H_{32}NO_8$ $[M+H]^+$: 570.2128, found 570.2111.

Dimethyl (S)-2'-((4-(((((4,11-diethyl-4-hydroxy-3,14-dioxo-3,4,12,14-tetrahydro-1H-pyrano[3',4':6,7]indolizino[1,2-b]quinolin-9-yl)oxy)carbonyl)oxy)methyl)-2,6-dimethoxybenzamido)methyl)-[1,1':4',1''-terphenyl]-4,4''-dicarboxylate (Me$_2$TP-SN). Compound **10** (500 mg, 0.878 mmol), 4-nitrophenyl chloroformate (442 mg, 2.195 mmol), TEA (366 μL, 2.634 mmol) were combined in dry DCM (30 mL) under Ar and stirred for 1 day at room temperature. The resulting solution was quenched with 5 mL H_2O and extracted with DCM, dried over Na_2SO_4, filtered, concentrated by rotary evaporation, and then dried completely under vacuum to produce dimethyl 2'-((2,6-dimethoxy-4-((((4-nitrophenoxy)carbonyl)oxy)methyl)benzamido)methyl)-[1,1':4',1"-terphenyl]-4,4"-dicarboxylate (**10**), which was used directly in the next step without purification.

To a solution of **10** (500 mg, 0.681 mmol) in DCM (20 mL) was added SN38 (668 mg, 1.702 mmol) and TEA (284 μL, 2.043 mmol); the resulting mixture was stirred at room temperature for 1 day before being washed with H_2O and extracted with DCM (3x20 mL). The organic phases were combined, dried over Na_2SO_4, filtered, concentrated by rotary evaporation, dissolved in minimal DCM, and purified via large TLC plate chromatography (5% MeOH in DCM) to give Me$_2$TP-SN (134 mg, 0.136 mmol, 20%). ^{1}H NMR (400 MHz, Chloroform-*d*) δ 8.24 (d, *J* = 9.2 Hz, 1H), 8.13 (ddd, *J* = 10.2, 6.1, 2.8 Hz, 4H), 7.99 (d, *J* = 1.9 Hz, 1H), 7.91 (d, *J* = 2.6 Hz, 1H), 7.78 – 7.74 (m, 2H), 7.74 – 7.69 (m, 4H), 7.64 (s, 1H), 7.64 – 7.60 (m, 2H), 7.50 (d, *J* = 8.3 Hz, 2H),

7.42 (d, *J* = 7.9 Hz, 1H), 6.65 (s, 2H), 6.07 (t, *J* = 6.0 Hz, 1H), 5.73 (d, *J* = 16.3 Hz, 1H), 5.26 (d, *J* = 11.3 Hz, 4H), 4.77 (d, *J* = 6.1 Hz, 2H), 3.95 (d, *J* = 2.4 Hz, 6H), 3.75 (s, 6H), 3.14 (q, *J* = 7.7 Hz, 2H), 1.89 (ddt, *J* = 16.9, 14.2, 7.1 Hz, 2H), 1.38 (t, *J* = 7.7 Hz, 3H), 1.03 (t, *J* = 7.3 Hz, 3H) (**Figure 5-17)**; ^{13}C NMR (101 MHz, $CDCl_3$) δ 174.00, 167.09, 165.58, 157.77, 157.74, 153.40, 152.33, 150.31, 149.88, 147.65, 146.90, 145.54, 145.36, 145.10, 140.67, 140.05, 139.67, 139.30, 137.72, 136.46, 132.48, 131.75, 131.00, 130.72, 130.36, 130.24, 129.99, 129.25, 129.22, 127.56, 127.52, 127.44, 127.24, 127.13, 126.99, 126.12, 124.72, 118.84, 116.13, 114.26, 104.32, 98.24, 72.89, 70.61, 66.47, 56.25, 52.34, 52.32, 49.51, 41.60, 31.75, 23.32, 14.13, 7.96 (**Figure 5-18)**. HR-MS (ESI, positive mode): *m/z* calc'd for $C_{56}H_{50}N_3O_{14}$ $[M+H]^+$: 988.3293, found 988.3273.

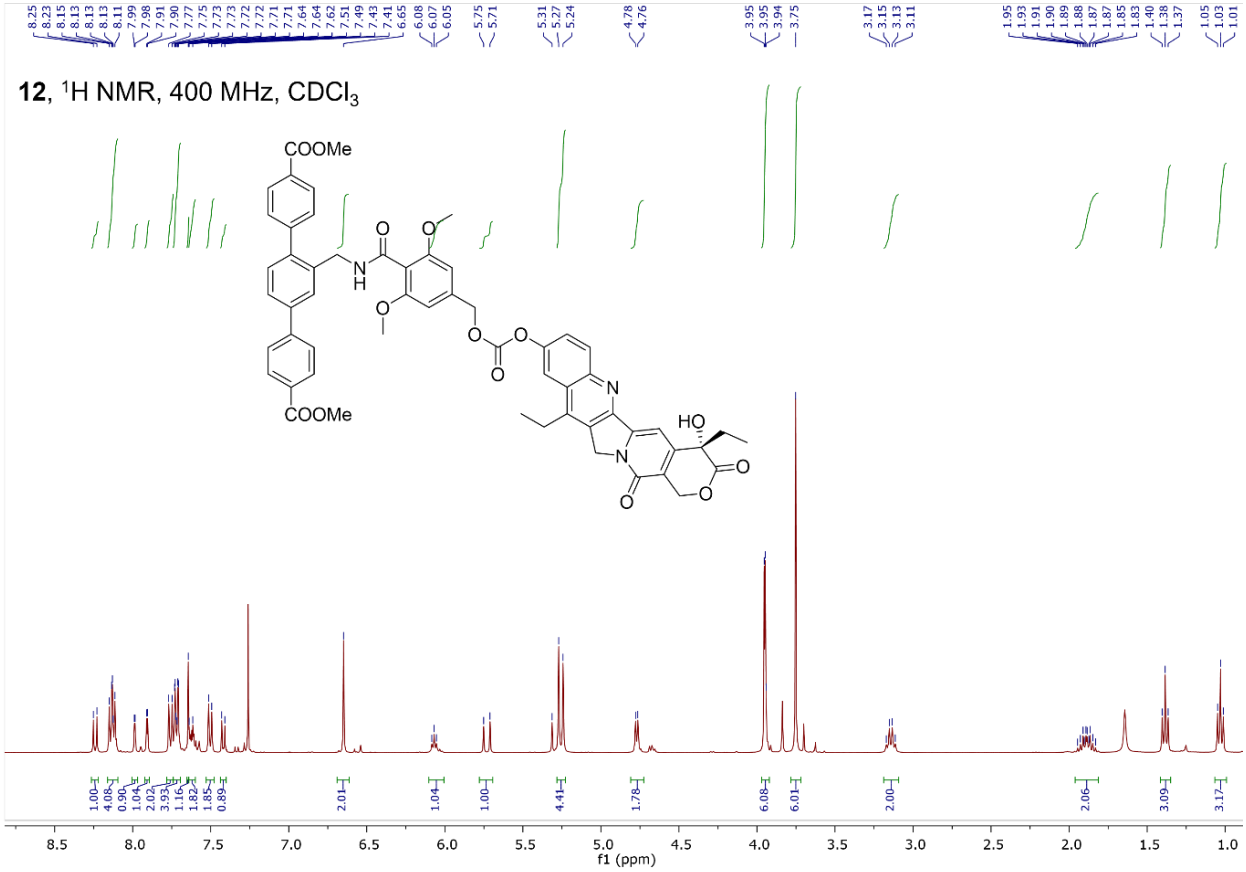

Figure 5-17. ^{1}H NMR spectrum of Me_2TP-SN.

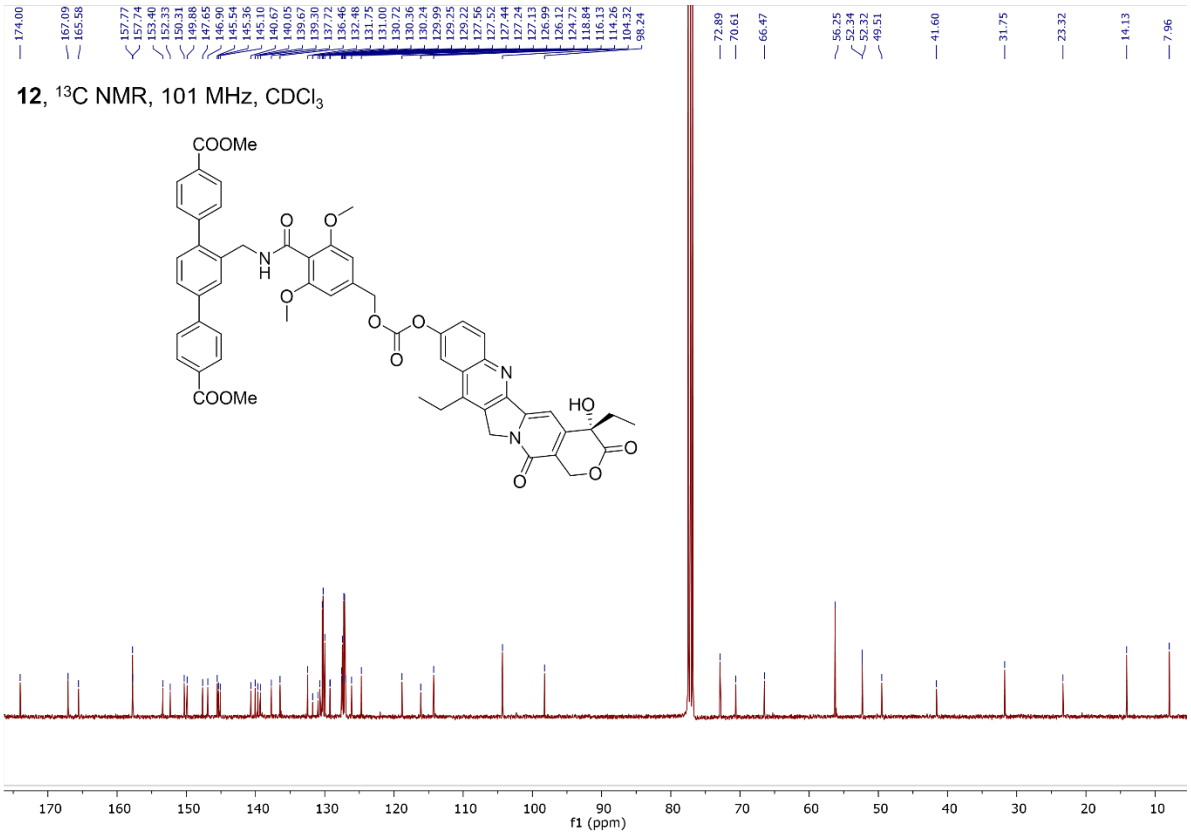

Figure 5-18. ^{13}C NMR spectrum of Me_2TP-SN.

(S)-4,11-diethyl-4-hydroxy-3,14-dioxo-3,4,12,14-tetrahydro-1H-pyrano[3',4':6,7]indolizino[1,2-b]quinolin-9-yl (3,5-dimethoxybenzyl) carbonate (**MeO-SN**)**.** Compound **1** (500 mg, 2.972 mmol), 4-nitrophenyl chloroformate (1.497 g, 7.430 mmol), TEA (1.240 mL, 8.916 mmol) were combined in dry DCM (50 mL) under Ar and stirred for 1 day at room temperature. The resulting solution was quenched with 5 mL H_2O and extracted with DCM, dried over Na_2SO_4, filtered, concentrated by rotary evaporation, and then dried completely under vacuum to produce dimethyl 3,5-dimethoxybenzyl (4-nitrophenyl) carbonate (**11**), which was used directly in the next step without purification.

To a solution of **11** (500 mg, 1.500 mmol) in DCM (30 mL) was added SN38 (1471 mg, 3.750 mmol) and TEA (626 μL, 4.500 mmol); the resulting mixture was stirred at room temperature for 1 day before being washed with H_2O and extracted with DCM (3 x 20 mL). The organic phases

were combined, dried over Na_2SO_4, filtered, concentrated by rotary evaporation, dissolved in minimal DCM, and purified via column chromatography to give MeO-SN (264 mg, 0.450 mmol, 30%).^{1}H NMR (400 MHz, $CDCl_3$) δ 8.25 (d, *J* = 9.2 Hz, 1H), 7.92 (d, *J* = 2.6 Hz, 1H), 7.68 (s, 1H), 7.65 (dd, *J* = 9.2, 2.6 Hz, 1H), 6.61 (d, *J* = 2.3 Hz, 2H), 6.47 (t, *J* = 2.3 Hz, 1H), 5.74 (d, *J* = 16.4 Hz, 1H), 5.30 (d, *J* = 16.5 Hz, 1H), 5.26 (d, *J* = 3.6 Hz, 4H), 3.82 (s, 6H), 3.15 (q, *J* = 7.7 Hz, 2H), 1.88 (dq, *J* = 17.0, 7.1 Hz, 2H), 1.39 (t, *J* = 7.7 Hz, 3H), 1.03 (t, *J* = 7.4 Hz, 3H) (**Figure 5-19**). ^{13}C NMR (101 MHz, $CDCl_3$) δ 173.93, 161.23, 157.72, 153.41, 151.89, 150.38, 150.10, 147.10, 146.56, 146.09, 136.73, 132.03, 127.60, 127.55, 125.08, 119.01, 114.27, 106.44, 100.87, 98.68, 72.90, 70.80, 66.43, 55.58, 49.57, 31.77, 23.40, 14.10, 7.96 (**Figure 5-20)**. HR-MS (ESI, positive mode): *m/z* calc'd for $C_{32}H_{31}N_2O_9$ $[M+H]^+$: 587.2030, found 587.2009.

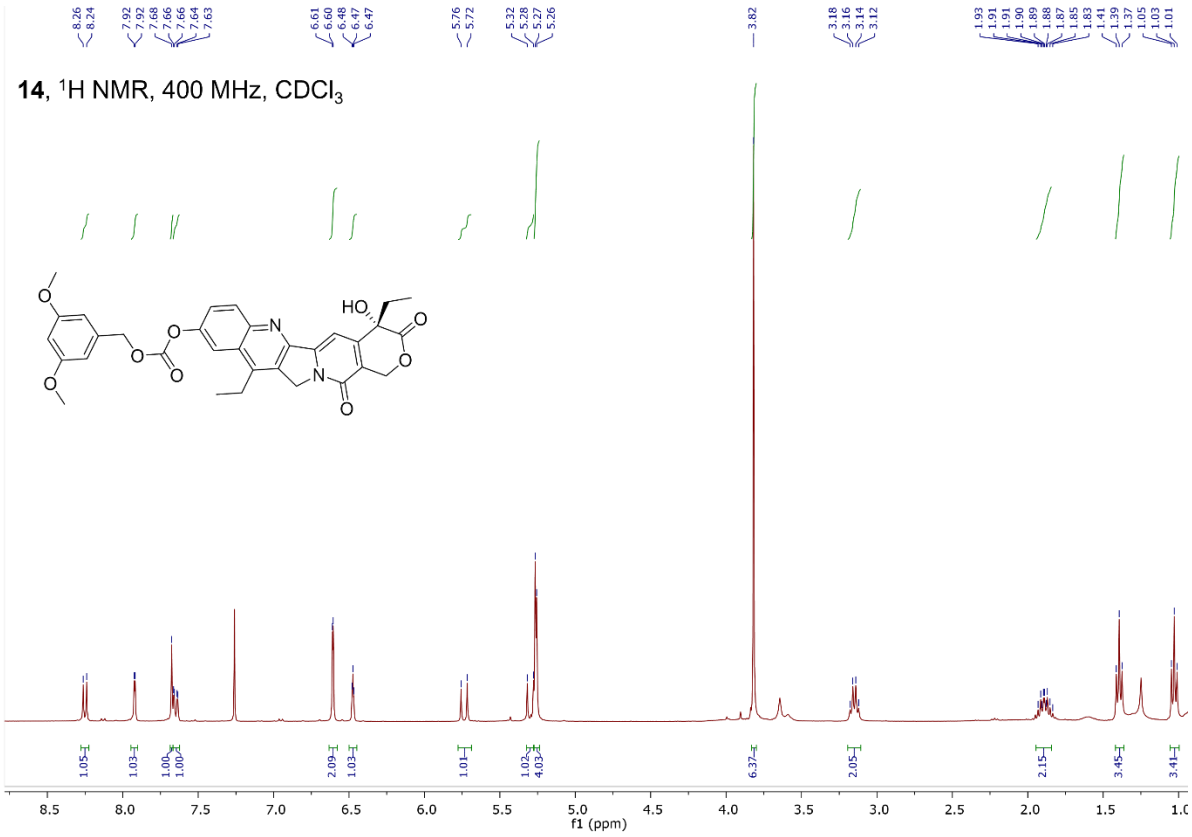

Figure 5-19. ^{1}H NMR spectrum of MeO-SN.

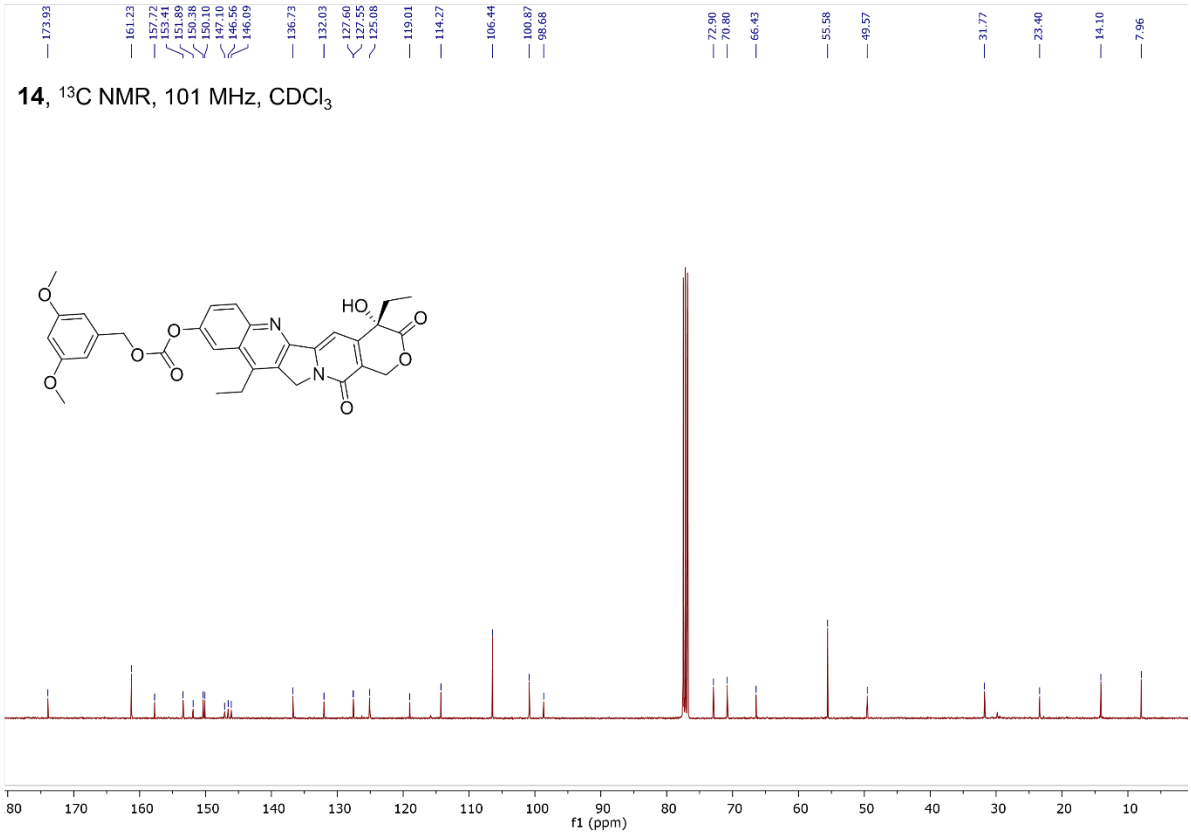

Figure 5-20. ^{13}C NMR spectrum of MeO-SN.

5.4.2. MOF synthesis and characterization

Synthesis of Hf-TP-OH. $HfCl_4$ and H_2TP-OH were separately dissolved in DMF at a concentration of 2 mg/mL. 500 μL $HfCl_4$ solution and 500 μL H_2TP-OH were then combined in a 1-dram vial with the addition of 1 μL trifluoracetic acid and 5 μL water as modulators. The mixture was heated in an oven at 80 °C for 1 day, after which the white precipitate was collected by centrifugation and sequentially washed with DMF, 1% triethylamine (TEA) in ethanol (EtOH) (v/v), and EtOH to afford Hf-TP-OH in 88% yield based on H_2TP-OH.

Synthesis of Hf-TP-SN via post-synthetic modification. 10 mL Hf-TP-OH was washed with dry acetonitrile (CAN) twice and dispersed in ACN with a ligand concentration of 3.0 mM. 4-nitrophenyl chloroformate (15.1 mg, 75 μmol), and TEA (12.5 μL, 90 μmol) were then added, and the solution was stirred for 2 days to afford Hf-TP-NO_2 nMOF. The mixture was then centrifuged,

washed with ACN for 3 times and redispersed in ACN before the addition of SN38 (11.8 mg, 30 μmol) and TEA (6.3 μL, 45 μmol); the solution was then stirred for 2 more days. The as-synthesized Hf-TP-SN was washed with 10% dimethyl sulfoxide (DMSO) in ACN 6 times and dispersed in EA for storage.

Digestion of Hf-MOFs for UV-Vis spectroscopic measurements. 50 μL Hf-TP-OH or Hf-TP-SN solution, 900 μL DMSO and 50 μL H_3PO_4 were mixed and sonicated for 1 hour and let stand overnight, after which the mixture was diluted to a proper concentration for UV-Vis measurement. The absorbance of H_2TP-OH at 304 nm was used to calculate the concentration of H_2TP-OH in Hf-TP-OH or Hf-TP-SN after comparison with the standard curve of H_2TP-OH in DMSO, while the absorbance of SN38 at 390 nm was used to calculate the concentration of SN38 in Hf-TP-SN after comparison with the standard curve of SN38 in DMSO.

Digestion of Hf-TP-SN for quantification of SN38 by LC-MS. 100 μL 1M $NaHCO_3$ solution was added to 100 μL Hf-TP-SN dispersion in water (total SN concentration: 100 μM). The mixture was sealed and sonicated for 20 minutes, after which 100 μL PBS (200 mM, pH 4.0) was added to adjust the pH to 7. 100 μL saturated NaCl solution and 150 μL ethyl acetate (EA) were then added before vortexing the mixture for 1 minute. The EA layer after centrifugation was analyzed with LC-MS. For HPLC, absorption of SN38 at 380 nm was used to calculate the concentration of free SN38 after comparison with the standard curve of SN38 in EA. For LC-MS, extracted ion chromatogram (EIC) at m/z value of 393.1450 was used to calculate the concentration of free SN38 after comparison with the standard curve of SN38 in EA.

Stability of Hf-TP-SN in PBS. Hf-TP-SN was dispersed in 1 mL PBS (1 mM) with a Hf concentration of 5.2 mM. 200 uL suspension was taken after incubation for 1, 2, 4, 8, and 24 hours and centrifuged for PXRD measurement.

Total ROS generation in test tubes. Total ROS generation under irradiation was detected by the 2',7'-dichlorodihydrofluorescein (DCFH) assay following reported procedures.[46] 1 mL DCFH-DA (1mM) in DMSO was hydrolyzed by 4 mL NaOH (0.01 M) solution in the dark for 30 minutes and stopped by adding 20 mL PBS (25 mM, pH 7.4). The freshly-prepared DCFH was then added to the PBS suspension (pH 7, 10 mM) of Hf-TP-OH or Hf-TP-SN at the same Hf concentration. In the final mixture, the concentration of DCFH was 10 μM while the concentration of Hf was 40 μM. The PBS solution with the same DCFH concentration served as a blank control. 100 μL of each suspension was added to 96-well plates (n = 6) and then irradiated with X-ray at 0, 1, 2, 3, 5, or 10 Gy, respectively. The fluorescence signal (em. 520/20 nm) was collected with a Synergy HTX microplate reader (ex. 485/20 nm).

Hydroxyl radical generation in test tubes. Hydroxyl radical (·OH) generation under irradiation was detected by the APF assay. APF assay was added to the PBS suspension of Hf-TP-OH or Hf-TP-SN at the same Hf concentration. In the final mixture, the concentration of APF was 5 μM while that of Hf was 40 μM. The PBS solution with the same APF concentration served as a blank control. 100 μL of each suspension was added to 96-well plates (n = 6) and then irradiated with X-ray at 0, 1, 2, 3, 5, or 10 Gy, respectively. The fluorescence signal (em. 520/20 nm) was collected with a Synergy HTX microplate reader (ex. 485/20 nm).

Hydroxyl radical triggered SN38 release in test tubes. Hf-TP-SN or MeO-SN was dispersed in H_2O at the same concentration of total SN38 (100 μM). $FeCl_3$, (+)-Sodium L-ascorbate, $Na_2(EDTA)\cdot 2H_2O$ (ethylenediaminetetraacetic acid, disodium salt dihydrate) was firstly dissolved in water to reach a concentration of 10 mM separately (10.5 mM for $Na_2(EDTA)\cdot 2H_2O$). Then, 100 μL of each solution and 50 μL H_2O_2 (200 mM in H_2O) was added to Hf-TP-SN or MeO-SN solution to generate hydroxyl radical in situ and to trigger the release of SN38. For control group,

only H_2O_2 was added. After 8h incubation at room temperature, additional 100 μL 1M $NaHCO_3$ was added to Hf-TP-SN to digest the nMOF, after which the mixture was sealed and sonicated for 20 minutes before the addition of 100 μL PBS (200 mM, pH 4) to adjust the pH to 7. 100 μL saturated NaCl solution and 150 μL ethyl acetate (EA) were added before vortexing the Hf-TP-SN or MeO-SN mixture for 1 minute. The EA layer after centrifugation was analyzed by LC-MS.

X-ray triggered release in test tubes. Hf-TP-SN or MeO-SN were dispersed in H_2O (10 mM, pH = 7.4) at the same concentration of total SN38 (100 μM). 100 μL Hf-TP-SN or MeO-SN suspension was irradiated with 10 Gy X-ray. 100 μL 1M $NaHCO_3$ was added to Hf-TP-SN to digest the nMOF, after which the mixture was sealed, sonicated for 20 minutes, and sat 15h before the addition of 100 μL PBS (200 mM, pH 4.0) to adjust the pH to 7. 100 μL saturated NaCl solution and 150 μL ethyl acetate (EA) were added before vortexing the Hf-TP-SN or MeO-SN mixture for 1 minute. The EA layer after centrifugation was analyzed by HPLC.

5.4.3. *In vitro* experiments

Dark toxicity. CT26 cells were cultured in RPMI-1640 medium supplemented with 10% fetal bovine serum, 1% HyClone penicillin-streptomycin 100X solution, and cultured in a humidified atmosphere containing 5% CO_2 at 37°C. The cytotoxicity of H_2TP-OH, Hf-TP-OH, and Hf-TP-SN on CT26 cells was detected by MTS assay. CT26 cells were seeded in 96-well plates at a density of 2500 cells/well. Different concentrations of H_2TP-OH, Hf-TP-OH and Hf-TP-SN were added and 24 hours later 10% (v/v) of MTS reagent was added to each well. 90 minutes later the absorbance of each well at 490 nm was read by a Synergy HTX plate reader to calculate cell viability.

Clonogenic assay. CT26 cells were seeded in 6-well plates at a density of 1.5×10^5 cells/well and cultured overnight. The cells were incubated with PBS, Hf-TP-OH, or Hf-TP-SN at an equivalent

metal concentration of 50 μM for 4 hours, and then irradiated with 0, 2, 4, 6 and 8 Gy X-ray (n = 3). The cells were washed with PBS twice and then trypsinized to afford single cell suspensions. The cells were counted and diluted, then 200 cells were seeded in each well of 6-well plates and cultured in 2 mL medium for another 7 days. Then, the plates were rinsed once with PBS, fixed by 4% paraformaldehyde for 20 minutes, and washed with PBS twice at room temperature. After that, the 6-well plates were scanned with IncuCyte S3 in the whole well mode with a 4× objective. The colonies were identified with IncuCyte 2021A software in a cellular resolution and the confluence was used as a parameter to calculate the plating efficiency (PE) and surviving fraction (SF):

$$PE = \text{Confluence}\ (0\ Gy, PBS)/\text{Cell \#}\ (0\ Gy, PBS)$$

$$SF\ (D, MOF) = \text{Confluence}\ (D, MOF)/\text{Cell \#}\ (D, MOF)\times \text{PE}$$

Where D was the radiation dose and Cell # (*D, MOF*) was the number of cells seeded for a certain radiation dose D and a certain treatment group.

The dose modifying ratio at a 10% ($DMR_{10\%}$) was used as a parameter to assess radiosensitization effect and defined as the ratio of doses under reference conditions to produce a 10%[52]:

$$DMR_{10\%} = DMR_{10\%}\ (PBS) / DMR_{10\%}\ (MOF)$$

Hydroxyl radical generation. To demonstrate ·OH generation, CT26 cells were seeded in cell culture dishes at a density of 1.5×10^5 and cultured overnight. Hf-TP-OH was added at an equivalent Hf concentration of 50 μM and further incubated in a 37℃ incubator for 4 hours. The cells were washed with PBS solution 3 times and 1 mL cell culture medium containing with 10 μM HPF was added and incubated at 37℃ for another 30 minutes. Then the cells were irradiated with X-ray (3 Gy) and cultured in the cell incubator for another 24 h. After that, the cells were washed with PBS for three times and further incubated with Hoechst 33342 (10 μg mL^{-1}) in PBS

for 10 minutes in the cell incubator. Finally, the cells were washed with PBS 3 times and observed on a Leica Stellaris 8 confocal microscope.

Dark toxicity. The cytotoxicity of SN38 and Me_2TP-SN on CT26 cells were detected by MTS assay. CT26 cells were seeded in 96-well plates at a density of 2500 cells/well. Different concentrations of SN38 and Me_2TP-SN were added and 48 hours later, 10% (v/v) of MTS reagent was added to each well. 90 minutes later the absorbance of each well at 490 nm was read by a Synergy HTX plate reader to calculate cell viability.

Cellular uptake. The cellular uptake of Hf-TP-SN (Hf: 50 μM) was evaluated on CT26 cells. The cells were seeded in 6-well plates at a density of 2×10^5/well and cultured overnight. Hf-TP-SN was added at a Hf concentration of 50 μM into the medium (n = 3). The cells were incubated in a 37 ℃ incubator for 1, 2, and 6 hours. At each time point, the medium was aspirated, the cells were washed with PBS three times, collected by centrifugation, and counted with a hemocytometer. The cell pellets were digested with nitric acid for 24 h and the concentration of Hf was detected by ICP-MS.

ROS generation. To demonstrate the generation of ROS, CT26 cells were seeded in cell culture dishes at a density of 1.5×10^5 and cultured overnight. Hf-TP-SN or Hf-TP-OH was added at a Hf concentration of 50 μM and further incubated in a 37℃ incubator for 4 hours. The cells were washed with PBS solution 3 times and 1 mL cell culture medium containing with 30 μM DCFH-DA was added and incubated at 37℃ for another 30 minutes. Then the cells were irradiated with X-ray (3 Gy) and cultured in the cell incubator for another 24 h. After that, the cells were washed with PBS three times and further incubated with Hoechst 33342 (10 μg mL^{-1}) in PBS for 10 minutes. Finally, cells were washed with PBS 3 times and observed on a Leica Stellaris 8 confocal microscope.

DNA damage. For CLSM imaging, CT26 cells were seeded in cell culture dishes at a density of 1.5×10^5. The cells were treated in the same way as in the clonogenic assay. 24 hours after radiation, the cells were washed with PBS and fixed with 4% paraformaldehyde at room temperature for 20 minutes. The cells were again rinsed with PBS, blocked and permeabilized with 5% FBS + 0.3% Triton-X in PBS at room temperature for 1 hour. After blocking, cells were incubated with the γ-H2AX primary antibody (1:500) in 1% BSA + 0.3% Triton-X in PBS at room temperature for 1 hour. The cells were then washed with PBS and incubated with the Alexa Fluor 488 conjugated secondary antibody (1:3000) in 1% BSA + 0.3% Triton-X in PBS at room temperature for 1 hour. Afterwards, the cells were washed with PBS and further incubated with Hoechst 33342 (10 μg mL^{-1}) in PBS for 10 minutes at 37 °C to visualize cell nuclei, respectively. Finally, cells were washed with PBS 3 times and observed on a Leica Stellaris 8 confocal microscope.

Apoptotic cell death. To quantify apoptosis, CT26 cells were seeded in 6-well plates at a density of 1.5×10^5/well and cultured overnight. Hf-TP-OH or Hf-TP-SN was added at an equivalent metal concentration of 50 μM for 4 hours and irradiated with X-ray (3 Gy). 24 hours later, the cells were washed with PBS, trypsinized to afford single cell suspensions, cells were stained with the dead cell apoptosis kit with annexin V Alexa Fluor 488 & PI following the manufacturer's protocol and resuspended in the binding buffer for flow cytometric analysis (Annexin-V in FITC channel, PI in PE-dazzle 594 channel).

5.4.4. *In vivo* experiments

Anti-cancer efficacy. BALB/c mice (6-8 weeks) were obtained from Charles River Laboratories, Inc (USA) and bred in house at the animal facility at the University of Chicago. The study protocol was reviewed and approved by the Institutional Animal Care and Use Committee (IACUC) at the University of Chicago. To evaluate the in vivo therapeutic efficacy, CT26 tumor models were

established on BALB/c mice by inoculating 2 × 10^6 cells/mouse subcutaneously onto the right flanks at day 0, respectively. When CT26 tumors reached ~85 mm^3, the mice were randomized for treatments. PBS, irinotecan, Hf-TP, or Hf-TP-SN was intratumorally injected with an equivalent metal dose of 0.5 μmol in 20 μL PBS and SN38 dose of 0.047 μmol in 20 μL PBS. The dose of irinotecan was 0.047 μmol in 20 μL PBS. 6-8 hours later, the mice were anaesthetized with 2.5% (v/v) isoflurane/O_2 and mounted onto the X-Rad 225 irradiator. The CT26 tumors were irradiated with 2 Gy X-ray/fraction for 3 consecutive days. The length and width of tumor tissues were measured with an electronic caliper (tumor volume = length × $width^2/2$) and body weights were monitored with an electronic scale. At the endpoint of the experiments, the mice were euthanized, and the tumors and major organs were sectioned for hematoxylin-eosin (H&E) staining to evaluate general toxicity. The tumor growth inhibition index (TGI) was defined as the equation below:[13]

$$TGI = 1 - \frac{\frac{T_e}{T_s} \Big/ \frac{C_e}{C_s}}{1 - \frac{C_s}{C_e}}$$

where T_e, T_s, C_e, and C_s represent average tumor volumes of treated mice at endpoint, treated mice at starting-point, control mice at endpoint and control mice at starting-point, respectively.

Immunohistochemistry analysis. To evaluate DNA damage and tumor proliferation after different treatments, a group of CT26-bearing mice were established and treated in the same way as in antitumor efficacy experiments. The mice were euthanized one day after the last irradiation. The tumors were excised and fixed in 4% PFA for 48 h and 70% ethanol for 1 day. The tissues were embedded in paraffin, sectioned and stained for H&E, γ-H2AX, Ki67 and TUNEL by Human Tissue Resource Center at the University of Chicago. Briefly, the slides were deparaffinized and rehydrated using xylenes and serial dilutions of ethanol to distilled water. Then the slides were treated with antigen retrieval buffer (Leica Biosystems, AR9640) and heated in a steamer at 97°C

for 20 minutes. After washing with tris-buffered saline, the slides were incubated with primary γ-H2AX antibody (1:400) or primary Ki67 antibody (Thermo Fisher Scientific, Clone# SP6, 1:400) at room temperature for 1 hour in a wet chamber. The slides were washed with tris-buffered saline, then γ-H2AX and Ki67 slides were incubated with anti-rabbit-polymer (Bond Polymer Refine Detection, Leica Biosystems, DS9800) for 30 minutes at room temperature. The antigen-antibody binding was detected with the 3,3′-Diaminobenzidine (DAB) (DAKO, K3468) system. Tissue sections were then immersed in hematoxylin for counterstaining and covered with cover glasses. The slides were scanned on a CRi Pannoramic SCAN 40× whole slide scanner by Integrated Light Microscopy Core at the University of Chicago. The images were analyzed with QuPath-0.2.3 software.

5.5. References

(1) Horcajada, P.; Gref, R.; Baati, T.; Allan, P. K.; Maurin, G.; Couvreur, P.; Férey, G.; Morris, R. E.; Serre, C., Metal–Organic Frameworks in Biomedicine. *Chem. Rev.* **2012,** *112* (2), 1232-1268.

(2) McKinlay, A. C.; Morris, R. E.; Horcajada, P.; Férey, G.; Gref, R.; Couvreur, P.; Serre, C., BioMOFs: Metal–Organic Frameworks for Biological and Medical Applications. *Angew. Chem. Int. Ed.* **2010,** *49* (36), 6260-6266.

(3) Yang, J.; Yang, Y.-W., Metal–Organic Frameworks for Biomedical Applications. *Small* **2020,** *16* (10), 1906846.

(4) Ge, X.; Wong, R.; Anisa, A.; Ma, S., Recent development of metal-organic framework nanocomposites for biomedical applications. *Biomaterials* **2022,** *281*, 121322.

(5) Sun, Y.; Zheng, L.; Yang, Y.; Qian, X.; Fu, T.; Li, X.; Yang, Z.; Yan, H.; Cui, C.; Tan, W., Metal–Organic Framework Nanocarriers for Drug Delivery in Biomedical Applications. *Nano-Micro Lett.* **2020,** *12* (1), 103.

(6) Horcajada, P.; Chalati, T.; Serre, C.; Gillet, B.; Sebrie, C.; Baati, T.; Eubank, J. F.; Heurtaux, D.; Clayette, P.; Kreuz, C.; Chang, J.-S.; Hwang, Y. K.; Marsaud, V.; Bories, P.-N.; Cynober, L.; Gil, S.; Férey, G.; Couvreur, P.; Gref, R., Porous metal–organic-framework nanoscale carriers as a potential platform for drug delivery and imaging. *Nat. Mater.* **2010,** *9* (2), 172-178.

(7) Horcajada, P.; Serre, C.; Maurin, G.; Ramsahye, N. A.; Balas, F.; Vallet-Regí, M.; Sebban, M.; Taulelle, F.; Férey, G., Flexible Porous Metal-Organic Frameworks for a Controlled Drug Delivery. *J. Am. Chem. Soc.* **2008,** *130* (21), 6774-6780.

(8) Orellana-Tavra, C.; Baxter, E. F.; Tian, T.; Bennett, T. D.; Slater, N. K. H.; Cheetham, A. K.; Fairen-Jimenez, D., Amorphous metal–organic frameworks for drug delivery. *Chem. Commun.* **2015,** *51* (73), 13878-13881.

(9) Teplensky, M. H.; Fantham, M.; Li, P.; Wang, T. C.; Mehta, J. P.; Young, L. J.; Moghadam, P. Z.; Hupp, J. T.; Farha, O. K.; Kaminski, C. F.; Fairen-Jimenez, D., Temperature Treatment of Highly Porous Zirconium-Containing Metal–Organic Frameworks Extends Drug Delivery Release. *J. Am. Chem. Soc.* **2017,** *139* (22), 7522-7532.

(10) Orellana-Tavra, C.; Marshall, R. J.; Baxter, E. F.; Lázaro, I. A.; Tao, A.; Cheetham, A. K.; Forgan, R. S.; Fairen-Jimenez, D., Drug delivery and controlled release from biocompatible metal–organic frameworks using mechanical amorphization. *J. Mater. Chem. B* **2016,** *4* (47), 7697-7707.

(11) He, C.; Lu, K.; Liu, D.; Lin, W., Nanoscale Metal–Organic Frameworks for the Co-Delivery of Cisplatin and Pooled siRNAs to Enhance Therapeutic Efficacy in Drug-Resistant Ovarian Cancer Cells. *J. Am. Chem. Soc.* **2014,** *136* (14), 5181-5184.

(12) Sun, C.-Y.; Qin, C.; Wang, C.-G.; Su, Z.-M.; Wang, S.; Wang, X.-L.; Yang, G.-S.; Shao, K.-Z.; Lan, Y.-Q.; Wang, E.-B., Chiral Nanoporous Metal-Organic Frameworks with High Porosity as Materials for Drug Delivery. *Adv. Mater.* **2011,** *23* (47), 5629-5632.

(13) Luo, T.; Nash, G. T.; Jiang, X.; Feng, X.; Mao, J.; Liu, J.; Juloori, A.; Pearson, A. T.; Lin, W., A 2D Nanoradiosensitizer Enhances Radiotherapy and Delivers STING Agonists to Potentiate Cancer Immunotherapy. *Adv. Mater.* **2022,** *34*, 2110588.

(14) Morris, W.; Briley, W. E.; Auyeung, E.; Cabezas, M. D.; Mirkin, C. A., Nucleic Acid–Metal Organic Framework (MOF) Nanoparticle Conjugates. *J. Am. Chem. Soc.* **2014,** *136* (20), 7261-7264.

(15) Zhao, N.; Yan, L.; Zhao, X.; Chen, X.; Li, A.; Zheng, D.; Zhou, X.; Dai, X.; Xu, F.-J., Versatile Types of Organic/Inorganic Nanohybrids: From Strategic Design to Biomedical Applications. *Chem. Rev.* **2019,** *119* (3), 1666-1762.

(16) Zhou, Z.; Vázquez-González, M.; Willner, I., Stimuli-responsive metal–organic framework nanoparticles for controlled drug delivery and medical applications. *Chem. Soc. Rev.* **2021,** *50* (7), 4541-4563.

(17) Wang, Y.; Yan, J.; Wen, N.; Xiong, H.; Cai, S.; He, Q.; Hu, Y.; Peng, D.; Liu, Z.; Liu, Y., Metal-organic frameworks for stimuli-responsive drug delivery. *Biomaterials* **2020,** *230*, 119619.

(18) Li, Y.; Teng, X.; Wang, Y.; Yang, C.; Yan, X.; Li, J., Neutrophil Delivered Hollow Titania Covered Persistent Luminescent Nanosensitizer for Ultrosound Augmented Chemo/Immuno Glioblastoma Therapy. *Adv. Sci.* **2021,** *8* (17), 2004381.

(19) Li, Y.; Teng, X.; Yang, C.; Wang, Y.; Wang, L.; Dai, Y.; Sun, H.; Li, J., Ultrasound Controlled Anti-Inflammatory Polarization of Platelet Decorated Microglia for Targeted Ischemic Stroke Therapy. *Angew. Chem. Int. Ed.* **2021,** *60* (10), 5083-5090.

(20) Zhang, C.; Wang, X.; Liu, G.; Ren, H.; Li, J.; Jiang, Z.; Liu, J.; Lovell, J. F.; Zhang, Y., Metal coordination micelles for anti-cancer treatment by gene-editing and phototherapy. *J. Controlled Release* **2023,** *357*, 210-221.

(21) Liu, G.; Jiang, Z.; Lovell, J. F.; Zhang, L.; Zhang, Y., Design of a Thiol-Responsive, Traceless Prodrug with Rapid Self-Immolation for Cancer Chemotherapy. *ACS Appl. Bio Mater.* **2021,** *4* (6), 4982-4989.

(22) Kilian, H. I.; Pradhan, A. J.; Jahagirdar, D.; Ortega, J.; Atilla-Gokcumen, G. E.; Lovell, J. F., Light-Triggered Release of Large Biomacromolecules from Porphyrin-Phospholipid Liposomes. *Langmuir* **2021,** *37* (36), 10859-10865.

(23) Lu, S.; Hao, D.; Xiang, X.; Pei, Q.; Xie, Z., Carboxylated paclitaxel prodrug nanofibers for enhanced chemotherapy. *J. Controlled Release* **2023,** *355*, 528-537.

(24) Hao, D.; Meng, Q.; Jiang, B.; Lu, S.; Xiang, X.; Pei, Q.; Yu, H.; Jing, X.; Xie, Z., Hypoxia-Activated PEGylated Paclitaxel Prodrug Nanoparticles for Potentiated Chemotherapy. *ACS Nano* **2022,** *16* (9), 14693-14702.

(25) Lu, S.; Xia, R.; Wang, J.; Pei, Q.; Xie, Z.; Jing, X., Engineering Paclitaxel Prodrug Nanoparticles via Redox-Activatable Linkage and Effective Carriers for Enhanced Chemotherapy. *ACS Appl. Mater. Interfaces* **2021,** *13* (39), 46291-46302.

(26) Spring, B. Q.; Bryan Sears, R.; Zheng, L. Z.; Mai, Z.; Watanabe, R.; Sherwood, M. E.; Schoenfeld, D. A.; Pogue, B. W.; Pereira, S. P.; Villa, E.; Hasan, T., A photoactivable multi-inhibitor nanoliposome for tumour control and simultaneous inhibition of treatment escape pathways. *Nat. Nanotechnol.* **2016,** *11* (4), 378-387.

(27) Xie, J.; Gonzalez-Carter, D.; Tockary, T. A.; Nakamura, N.; Xue, Y.; Nakakido, M.; Akiba, H.; Dirisala, A.; Liu, X.; Toh, K.; Yang, T.; Wang, Z.; Fukushima, S.; Li, J.; Quader, S.; Tsumoto, K.; Yokota, T.; Anraku, Y.; Kataoka, K., Dual-Sensitive Nanomicelles Enhancing Systemic Delivery of Therapeutically Active Antibodies Specifically into the Brain. *ACS Nano* **2020,** *14* (6), 6729-6742.

(28) Liu, J.; Saw, R. E.; Kiang, Y. H., Calculation of Effective Penetration Depth in X-Ray Diffraction for Pharmaceutical Solids. *J. Pharm. Sci.* **2010,** *99* (9), 3807-3814.

(29) Dawson, L. A.; Sharpe, M. B., Image-guided radiotherapy: rationale, benefits, and limitations. *Lancet Oncol.* **2006,** *7* (10), 848-858.

(30) Verellen, D.; Ridder, M. D.; Linthout, N.; Tournel, K.; Soete, G.; Storme, G., Innovations in image-guided radiotherapy. *Nat. Rev. Cancer* **2007,** *7* (12), 949-960.

(31) Barker, H. E.; Paget, J. T. E.; Khan, A. A.; Harrington, K. J., The tumour microenvironment after radiotherapy: mechanisms of resistance and recurrence. *Nat. Rev. Cancer* **2015,** *15* (7), 409-425.

(32) Yang, C.; Yang, Y.; Li, Y.; Ni, Q.; Li, J., Radiotherapy-Triggered Proteolysis Targeting Chimera Prodrug Activation in Tumors. *J. Am. Chem. Soc.* **2023,** *145* (1), 385-391.

(33) Ding, Z.; Guo, Z.; Zheng, Y.; Wang, Z.; Fu, Q.; Liu, Z., Radiotherapy Reduces N-Oxides for Prodrug Activation in Tumors. *J. Am. Chem. Soc.* **2022,** *144* (21), 9458-9464.

(34) Quintana, J. M.; Arboleda, D.; Hu, H.; Scott, E.; Luthria, G.; Pai, S.; Parangi, S.; Weissleder, R.; Miller, M. A., Radiation Cleaved Drug-Conjugate Linkers Enable Local Payload Release. *Bioconjugate Chem.* **2022,** *33* (8), 1474-1484.

(35) Tuo, W.; Renault, J.-P.; Rajpal, A.; Pin, S.; Le Gall, T.; Taran, F., Radiation-Responsive Benzothiazolines as Potential Cleavable Fluorogenic Linkers for Drug Delivery. *Chem. Eur. J.* **2023,** *n/a* (n/a), e202300358.

(36) Takakura, H.; Matsuhiro, S.; Inanami, O.; Kobayashi, M.; Saita, K.; Yamashita, M.; Nakajima, K.; Suzuki, M.; Miyamoto, N.; Taketsugu, T.; Ogawa, M., Ligand release from silicon

phthalocyanine dyes triggered by X-ray irradiation. *Org. Biomol. Chem.* **2022,** *20* (36), 7270-7277.

(37) Guo, Z.; Hong, H.; Zheng, Y.; Wang, Z.; Ding, Z.; Fu, Q.; Liu, Z., Radiotherapy-Induced Cleavage of Quaternary Ammonium Groups Activates Prodrugs in Tumors. *Angew. Chem. Int. Ed.* **2022,** *61* (34), e202205014.

(38) Fu, Q.; Li, H.; Duan, D.; Wang, C.; Shen, S.; Ma, H.; Liu, Z., External-Radiation-Induced Local Hydroxylation Enables Remote Release of Functional Molecules in Tumors. *Angew. Chem. Int. Ed.* **2020,** *59* (48), 21546-21552.

(39) Lu, K.; He, C.; Guo, N.; Chan, C.; Ni, K.; Lan, G.; Tang, H.; Pelizzari, C.; Fu, Y.-X.; Spiotto, M. T.; Weichselbaum, R. R.; Lin, W., Low-dose X-ray radiotherapy–radiodynamic therapy via nanoscale metal–organic frameworks enhances checkpoint blockade immunotherapy. *Nat. Biomed. Eng.* **2018,** *2* (8), 600-610.

(40) Xu, Z.; Ni, K.; Mao, J.; Luo, T.; Lin, W., Monte Carlo Simulations Reveal New Design Principles for Efficient Nanoradiosensitizers Based on Nanoscale Metal–Organic Frameworks. *Adv. Mater.* **2021,** *33* (40), 2104249.

(41) Zhen, W.; Weichselbaum, R. R.; Lin, W., Nanoparticle-Mediated Radiotherapy Remodels the Tumor Microenvironment to Enhance Antitumor Efficacy. *Adv. Mater.* **2022,** *n/a* (n/a), 2206370.

(42) Li, Y.; Xie, M.; Jones, J. B.; Zhang, Z.; Wang, Z.; Dang, T.; Wang, X.; Lipowska, M.; Mao, H., Targeted Delivery of DNA Topoisomerase Inhibitor SN38 to Intracranial Tumors of Glioblastoma Using Sub-5 Ultrafine Iron Oxide Nanoparticles. *Adv. Healthc. Mater.* **2022,** *11* (14), 2102816.

(43) Bottero, V.; Busuttil, V. r.; Loubat, A. s.; Magné, N.; Fischel, J.-L.; Milano, G. r.; Peyron, J.-F. o., Activation of Nuclear Factor κB through the IKK Complex by the Topoisomerase Poisons SN38 and Doxorubicin: A Brake to Apoptosis in HeLa Human Carcinoma Cells1. *Cancer Res.* **2001,** *61* (21), 7785-7791.

(44) Ni, K.; Lan, G.; Chan, C.; Quigley, B.; Lu, K.; Aung, T.; Guo, N.; La Riviere, P.; Weichselbaum, R. R.; Lin, W., Nanoscale metal-organic frameworks enhance radiotherapy to potentiate checkpoint blockade immunotherapy. *Nat. Commun.* **2018,** *9* (1), 2351.

(45) Chu, J.; Ke, F.-S.; Wang, Y.; Feng, X.; Chen, W.; Ai, X.; Yang, H.; Cao, Y., Facile and reversible digestion and regeneration of zirconium-based metal-organic frameworks. *Commun. Chem* **2020,** *3* (1), 5.

(46) Ju, E.; Dong, K.; Chen, Z.; Liu, Z.; Liu, C.; Huang, Y.; Wang, Z.; Pu, F.; Ren, J.; Qu, X., Copper(II)–Graphitic Carbon Nitride Triggered Synergy: Improved ROS Generation and Reduced Glutathione Levels for Enhanced Photodynamic Therapy. *Angew. Chem. Int. Ed.* **2016,** *55* (38), 11467-11471.

(47) Halliwell, B.; Gutteridge, J. M. C.; Aruoma, O. I., The deoxyribose method: A simple "test-tube" assay for determination of rate constants for reactions of hydroxyl radicals. *Anal. Biochem.* **1987,** *165* (1), 215-219.

(48) Wang, L.; Xia, J.; Fan, H.; Hou, M.; Wang, H.; Wang, X.; Zhang, K.; Cao, L.; Liu, X.; Ling, J.; Yu, H.; Wu, X.; Sun, J., A tumor microenvironment responsive nanosystem for chemodynamic/chemical synergistic theranostics of colorectal cancer. *Theranostics* **2021,** *11* (18), 8909-8925.

(49) Fan, L.; Peng, G.; Sahgal, N.; Fazli, L.; Gleave, M.; Zhang, Y.; Hussain, A.; Rassool, F.; Qi, J., Abstract 1981: Histone demethyalase JMJD1A promotes the DNA damage response of prostate cancer cells. *Cancer Res.* **2016,** *76* (14_Supplement), 1981-1981.

(50) Xia, D.; Hang, D.; Li, Y.; Jiang, W.; Zhu, J.; Ding, Y.; Gu, H.; Hu, Y., Au–Hemoglobin Loaded Platelet Alleviating Tumor Hypoxia and Enhancing the Radiotherapy Effect with Low-Dose X-ray. *ACS Nano* **2020,** *14* (11), 15654-15668.

(51) Fracaroli, A. M.; Furukawa, H.; Suzuki, M.; Dodd, M.; Okajima, S.; Gándara, F.; Reimer, J. A.; Yaghi, O. M., Metal–Organic Frameworks with Precisely Designed Interior for Carbon Dioxide Capture in the Presence of Water. *J. Am. Chem. Soc.* **2014,** *136* (25), 8863-8866.

(52) Ni, K.; Lan, G.; Chan, C.; Duan, X.; Guo, N.; Veroneau, S. S.; Weichselbaum, R. R.; Lin, W., Ultrathin Metal-Organic-Layer Mediated Radiotherapy–radiodynamic Therapy. *Matter* **2019,** *1* (5), 1331-1353.

Chapter 6. Mixed-Ligand Nanoscale MOFs for X-ray-Mediated Synergistic Radiotherapy–radiodynamic Therapy and Chemotherapy

6.1. Introduction

To improve the therapeutic effects and reduce the non-specific toxicity of traditional chemotherapeutics,[1-2] many nanotherapeutic systems have been designed to release active drugs using stimuli such as reactive oxygen species (ROS), enzymes, temperature, and light.[3-4] These stimuli-responsive nanotherapeutics undergo specific activation at the target site to release the pharmacologically active drugs.[5-7] In particular, ROS-responsive nanotherapeutics have emerged as a preferred antitumor strategy[8-10] as the ROS concentration in the tumor tissue is significantly higher than that in normal organs.[11] Various ROS-responsive drug delivery systems with photodynamic effect or chemodynamic effect have been developed to enable ROS-triggered drug release.[12-14] However, the photodynamic effect relies on visible to near-infrared photons which cannot penetrate deeply into most tumor tissues whereas the chemodynamic effect relies on unusually high ROS concentrations in mouse tumors which may not be present in human tumors.[15-18] In addition, existing stimuli-responsive nanotherapeutics tend to have inefficient drug loading and premature release of active drugs. Thus, there is a critical need for biocompatible ROS-responsive nanotherapeutics which can be selectively triggered to increase intratumoral ROS level for localized and on-demand release of active drugs in tumors for enhanced antitumor efficacy.[19]

Radiotherapy (RT) has provided important curative and palliative treatments to more than half of all cancer patients with tissue-penetrating ionizing radiations to kill cancer cells by directly inducing DNA damage or indirectly generating ROS to decompose biomolecules and disrupt the redox balance.[20-22] RT is essentially tumor-agnostic and provides an ideal stimulus to activate ROS-responsive prodrugs. As described in previous chapters, nanoscale metal–organic

frameworks (nMOFs)[23-25] have shown exciting potential in RT and drug delivery because of their unique advantages including highly porous structures, high surface areas, good biocompatibility, and molecular tunability.[26-28] In particular, our group reported Hf-DBP (DBP = bis(p-benzoato)porphyrin) nMOF-mediated radiotherapy–radiodynamic therapy (RT–RDT) in 2018.[29] Under X-ray irradiation, electron-dense Hf_{12} SBUs not only enhance hydroxyl radical (·OH) generation for RT, but also transfer energy to neighboring photosensitizing DBP ligands to generate $^1O_2$ for RDT. Thus, Hf-DBP provides an ideal nanoplatform for designing nanotherapeutics by incorporating a high loading of ROS-responsive prodrugs into the framework.

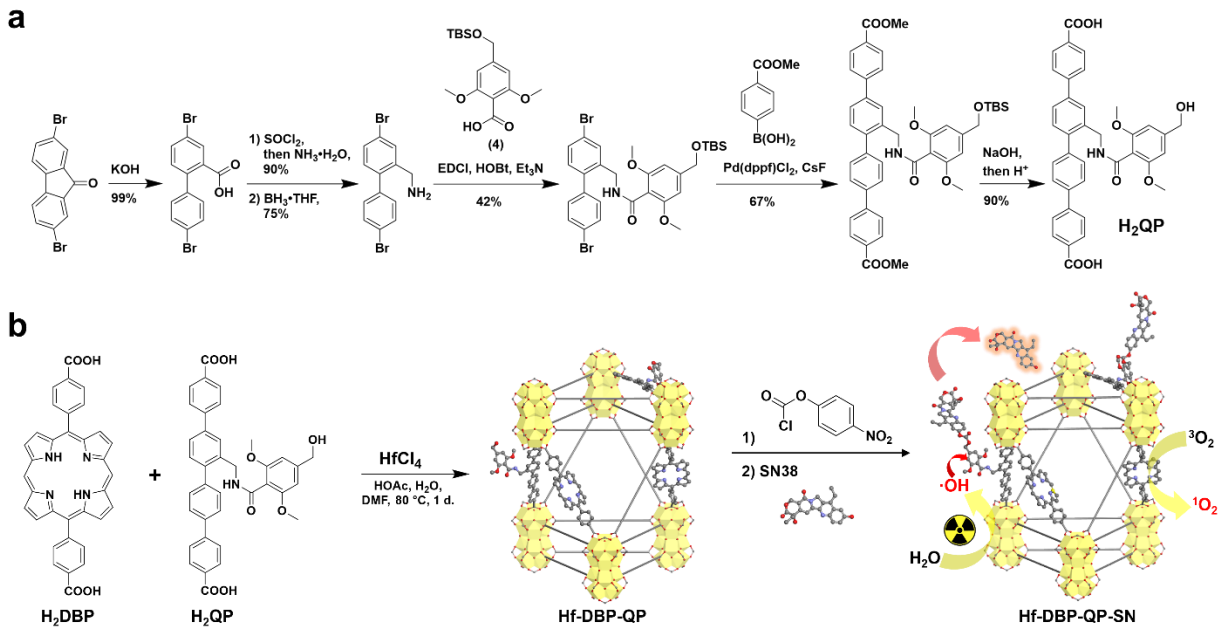

Figure 6-1. Synthesis of Hf-DBP-QP-SN and proposed mechanism of action. (a) Synthesis of H_2QP ligand. (b) Synthesis of Hf-DBP-QP and its post-synthetic modification with SN38 to afford Hf-DBP-QP-SN along with the proposed mechanism for X-ray triggered release of SN38 for synergistic RT–RDT and chemotherapy.

In this chapter, we designed a novel quaterphenyl dicarboxylate ligand (QP-SN) conjugated with 7-ethyl-10-hydroxycamptothecin (SN-38, an active metabolite of irinotecan)[30] via a ·OH responsive 3,5-dimethoxylbenzyl carbonate linkage. With a similar length as DBP ligand (19.3 vs

19.2 Å), QP-SN was introduced to Hf-DBP nMOF with photosensitizing DBP ligands to form a novel multi-functional mixed-ligand Hf-DBP-QP-SN nMOF. In addition to Hf-DBP mediated RT–RDT process for enhanced radiation damage, Hf-DBP-QP-SN achieved tumor-selective chemotherapy via a cascade of ·OH generation from electron-dense Hf_{12} SBUs[31], hydroxylation of the 3,5-dimethoxylbenzyl carbonate at ortho positions, and subsequent 1,4-elimination to release SN38.[32] Under the irradiation of X-rays, Hf-DBP-QP-SN effectively suppressed tumor growth due to synergistic tumor-targeted RT–RDT and chemotherapy (**Figure 6-1**).

6.2. Results and discussion

6.2.1. Synthesis and characterization of Hf-DBP-QP-SN

The 5,15-di (p-benzoato)porphyrin ligand (H_2DBP) was synthesized following reported procedures.[33] The quaterphenyl dicarboxylic acid (H_2QP) with 3,5-dimethoxyl benzyl alcohol was synthesized from 2,7-dibromo-9*H*-fluoren-9-one (**12**) in 6 steps via intramolecular ring-opening, amide formation with ammonia, borane reduction, amide coupling with 4-(((*tert*-butyldimethylsilyl)oxy)methyl)-2,6-dimethoxybenzoic acid, Suzuki coupling with (4-(methoxycarbonyl)phenyl)boronic acid, and base-catalyzed hydrolysis. The mixed-ligand nMOF, Hf-DBP-QP, was synthesized solvothermally by heating a mixture of $HfCl_4$, H_2DBP, H_2QP (with similar length as H_2DBP), acetic acid, and water in *N, N*-dimethylformamide at 80 °C for 1 day. Finally, Hf-DBP-QP was postsynthetically modified by treatment with 4-nitrophenyl chloroformate followed by SN38 to afford Hf-DBP-QP-SN with SN38 conjugated to the QP ligand via a hydroxyl radical-responsive 3,5-dimethoxyl benzyl carbonate linkage.[32]

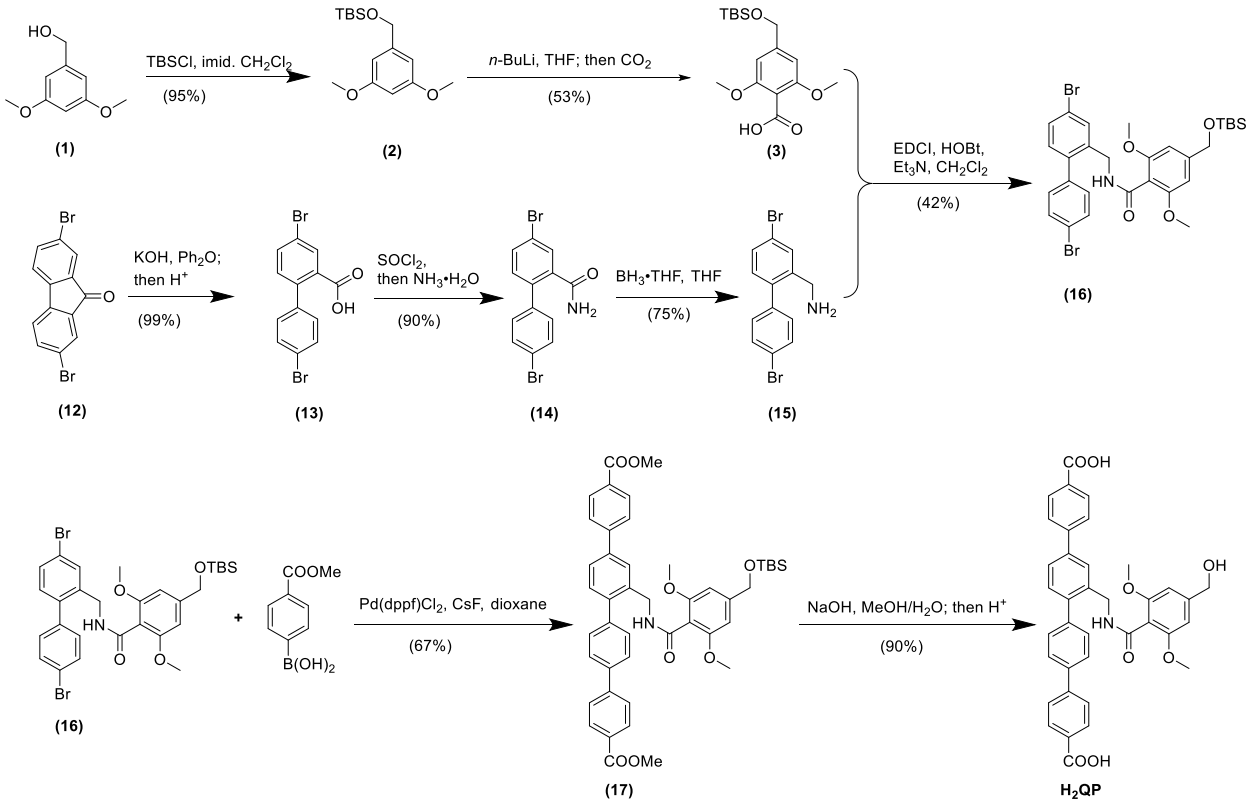

Scheme 6-1. Synthesis of H_2QP.

Hf-DBP-QP displayed a similar nanoplate morphology as previously reported Hf-DBP with a diameter of ~ 120 nm and a thickness of ~20 nm by transmission electron microscopy (TEM, **Figure 6-1a**). After postsynthetic modification, Hf-DBP-QP-SN retained the nanoplate morphology without obvious variation of diameters (**Figure 6-1b**). The number-averaged sizes of Hf-DBP-QP and Hf-DBP-QP-SN were measured to be 81 ± 3 nm and 96 ± 3 nm (**Figure 6-1c**), respectively, while their ζ-potentials were -18.4 ± 0.8 mV and -21.7 ± 0.5 mV (**Figure 6-1d**), respectively, by dynamic light scattering (DLS).

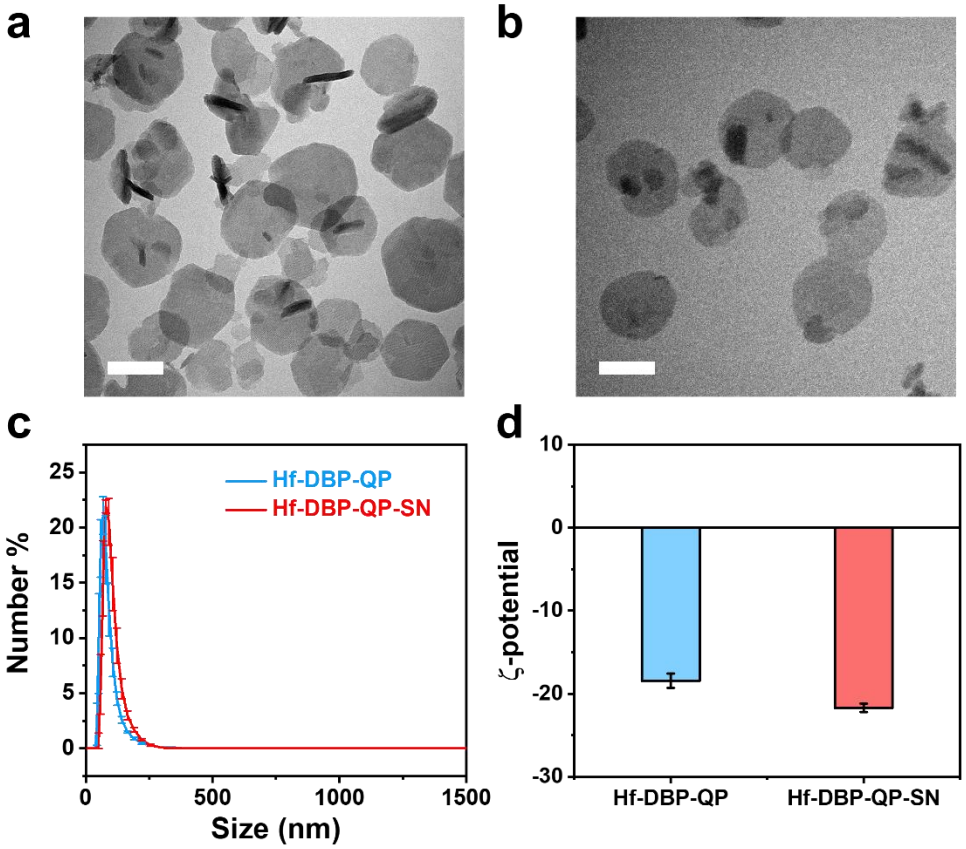

Figure 6-2. TEM and DLS characterization. TEM images of (a) Hf-DBP-QP and (b) Hf-DBP-QP-SN. Scale bars: 100 nm. (c) Number-averaged sizes and (d) ζ-potentials of Hf-DBP-QP and Hf-DBP-QP-SN.

Powder X-ray diffraction (PXRD) studies showed both Hf-DBP-QP and Hf-DBP-QP-SN displayed similar patterns as Hf-DBP, corresponding to the Hf_{12}-nMOF structure with $Hf_{12}(\mu_3\text{-}O)_8(\mu_3\text{-}OH)_8(\mu_2\text{-}OH)_6$ SBUs and linear dicarboxylate ligands in a *hcp* topology (**Figure 6-3a**).[34] Moreover, Hf-DBP-QP-SN retained its crystallinity after incubation in PBS (1mM, pH 7.4) for 24 hours (**Figure 6-3b**), suggesting the good stability of Hf-DBP-QP-SN in physiologically relevant environments.

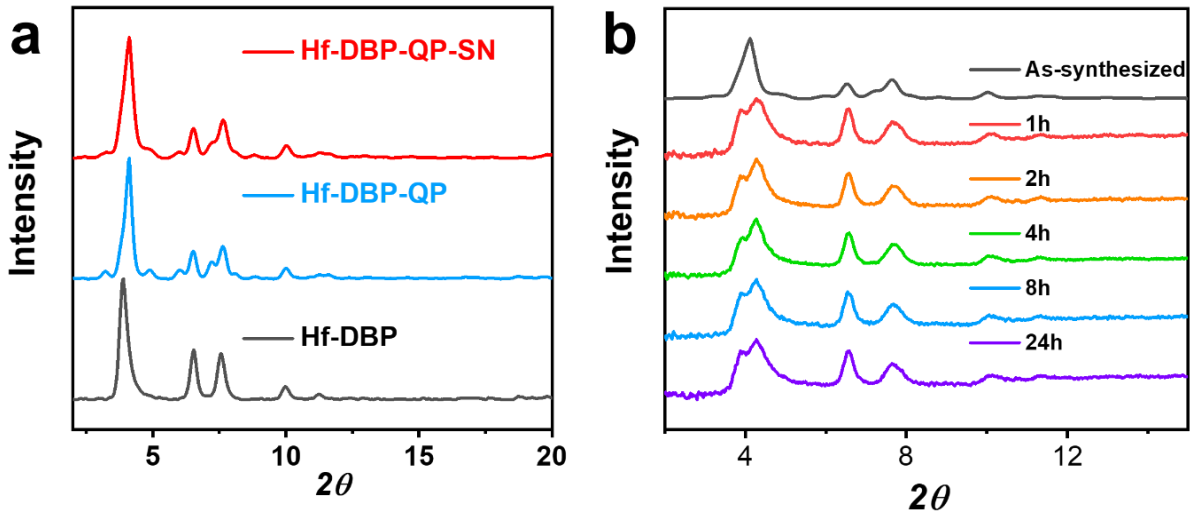

Figure 6-3. Crystallinity and stability of Hf-DBP-QP-SN. (a) PXRD patterns of Hf-DBP, Hf-DBP-QP and Hf-DBP-QP-SN MOF. (b) PXRD patterns of Hf-DBP-QP-SN freshly prepared and dispersed in PBS for 1, 2, 4, 8 and 24 hours.

UV-Vis spectroscopic analysis of digested Hf-DBP-QP determined the QP/DBP ratio to be 3.29 (**Figure 6-4**) by comparing the absorbance of QP and DBP ligands with their standard curves (**Figure 6-5**), which was consistent with the QP/DBP ratio (3.55) used in the synthesis.

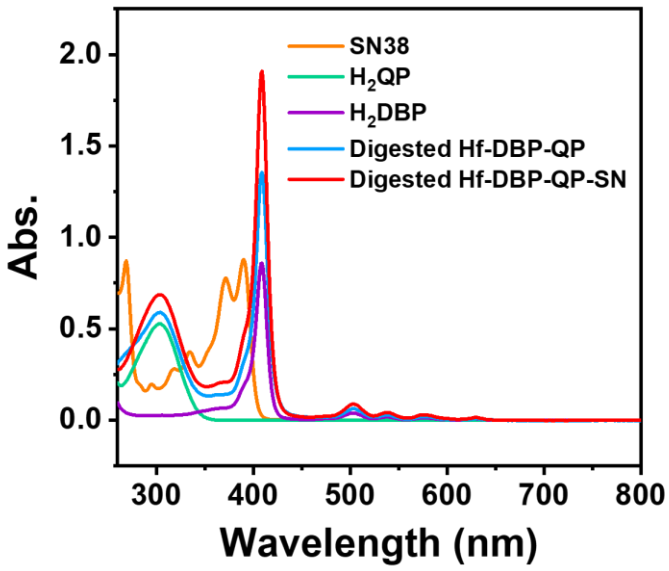

Figure 6-4. UV-Vis spectra of SN38, H_2QP, and H_2DBP and digested Hf-DBP-QP and Hf-DBP-QP-SN in DMSO.

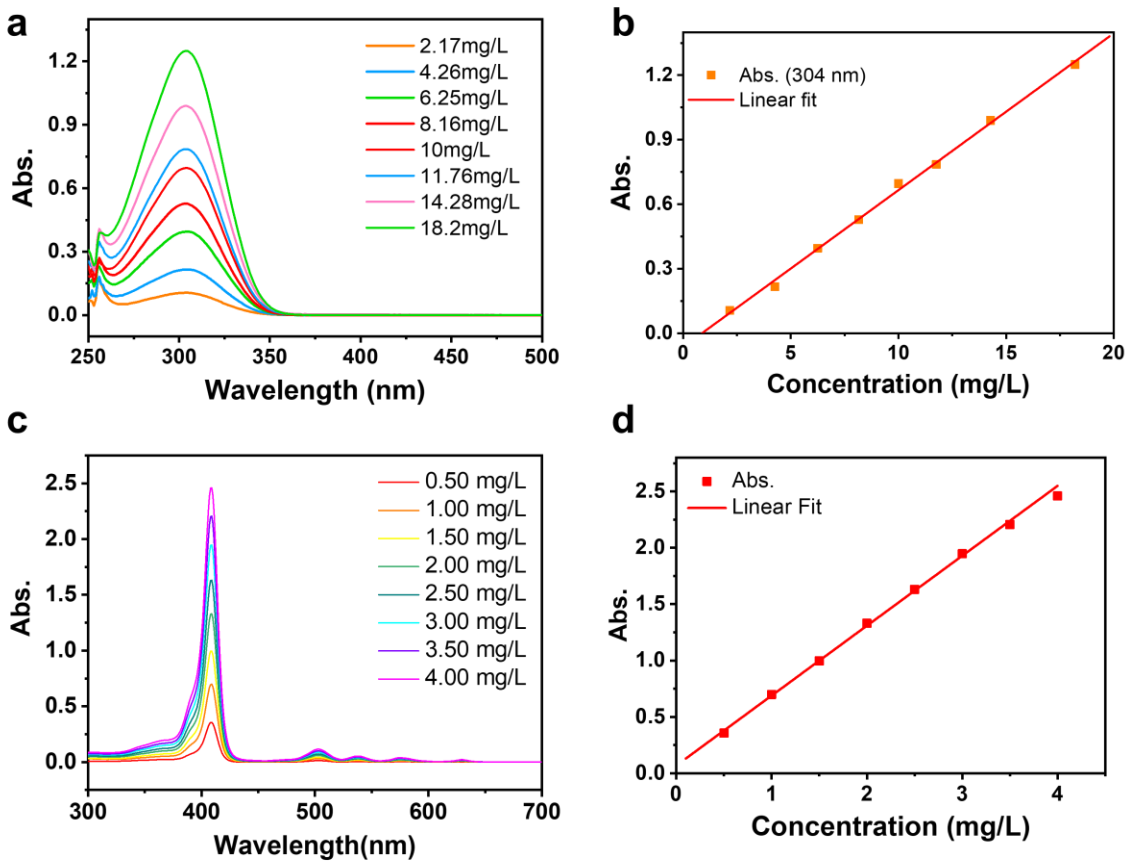

Figure 6-5. UV-Vis standard curves for quantification. UV-vis absorption spectra of (a) H_2QP and (c) H_2DBP and the fitted standard curves of (b) H_2QP and (d) H_2DBP.

The total loading of SN38 was quantified by high performance liquid chromatography (HPLC) after digesting Hf-DBP-QP-SN in 10% trifluoracetic acid in EA, indicating ~25% of QP ligands were conjugated with SN38. Liquid chromatography-mass spectrometry (LC-MS) analysis indicated the trapping of 1.5% free SN38 (relative to total SN38) in the pores after digesting Hf-DBP-QP-SN using $NaHCO_3$ and extraction with ethyl acetate. After determining the Hf content by inductively coupled plasma-mass spectrometry (ICP-MS), the formula of Hf-DBP-QP-SN was determined to be $Hf_{12}(\mu_3\text{-}O)_8(\mu_3\text{-}OH)_8(\mu_2\text{-}OH)_6(QP\text{-}SN)_{0.88}(QP)_{2.74}(DBP)_{1.36}(OH)_{8.04}(H_2O)_{8.04}(SN38)_{0.01}$.

A molecular counterpart, Me_2QP-SN, was synthesized from compound **17** using the same synthetic route to support the post-synthetic modification and to examine the toxicity of the prodrug (Schemes 6-2). Because of low aqueous solubility of Me_2QP-SN, we synthesized MeO-SN from compound **1** and used it as a homogeneous control (Scheme 5-3).

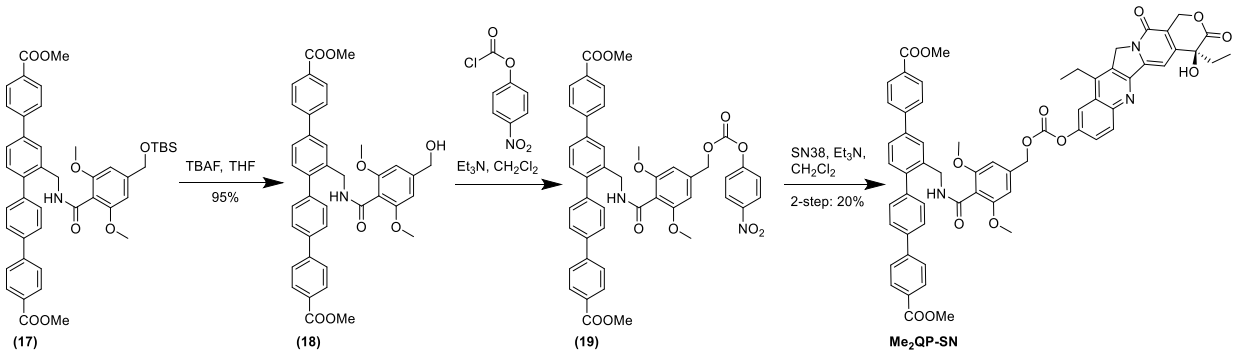

Scheme 6-2. Synthesis of Me_2QP-SN.

6.2.2. ROS generation and triggered release of SN38

To confirm the proposed mechanism of chemotherapy via X-ray triggered release of SN38 via RT–RDT (**Figure 6-6a**), we first evaluated ROS generation by DCFH assay[35] and ·OH generation by aminophenyl fluorescein (APF) assay. The ·OH signals in PBS, Hf-DBP, Hf-DBP-QP, and Hf-DBP-QP-SN groups all increased linearly with X-ray doses. Hf-DBP-QP and Hf-DBP enhanced ·OH generation by 20% and 21%, respectively, over PBS (**Figure 6-6b**), while Hf-DBP-QP-SN consumed ·OH significantly to reduce ·OH generation by 13% from PBS group. In terms of total ROS, the relative enhancements of Hf-DBP and Hf-DBP-QP over PBS were 76% and 21%, respectively (**Figure 6-6c**), while Hf-DBP-QP-SN was comparable with PBS. The reduced ROS and hydroxyl radical signals from Hf-DBP-QP-SN are likely due to the consumption of ·OH by the 3,5-dimethoxylbenzyl carbonate linkage to release SN38, while the incorporation of DBP ligand significantly improved total ROS signal by generating singlet oxygen through the RDT process.[36-37]

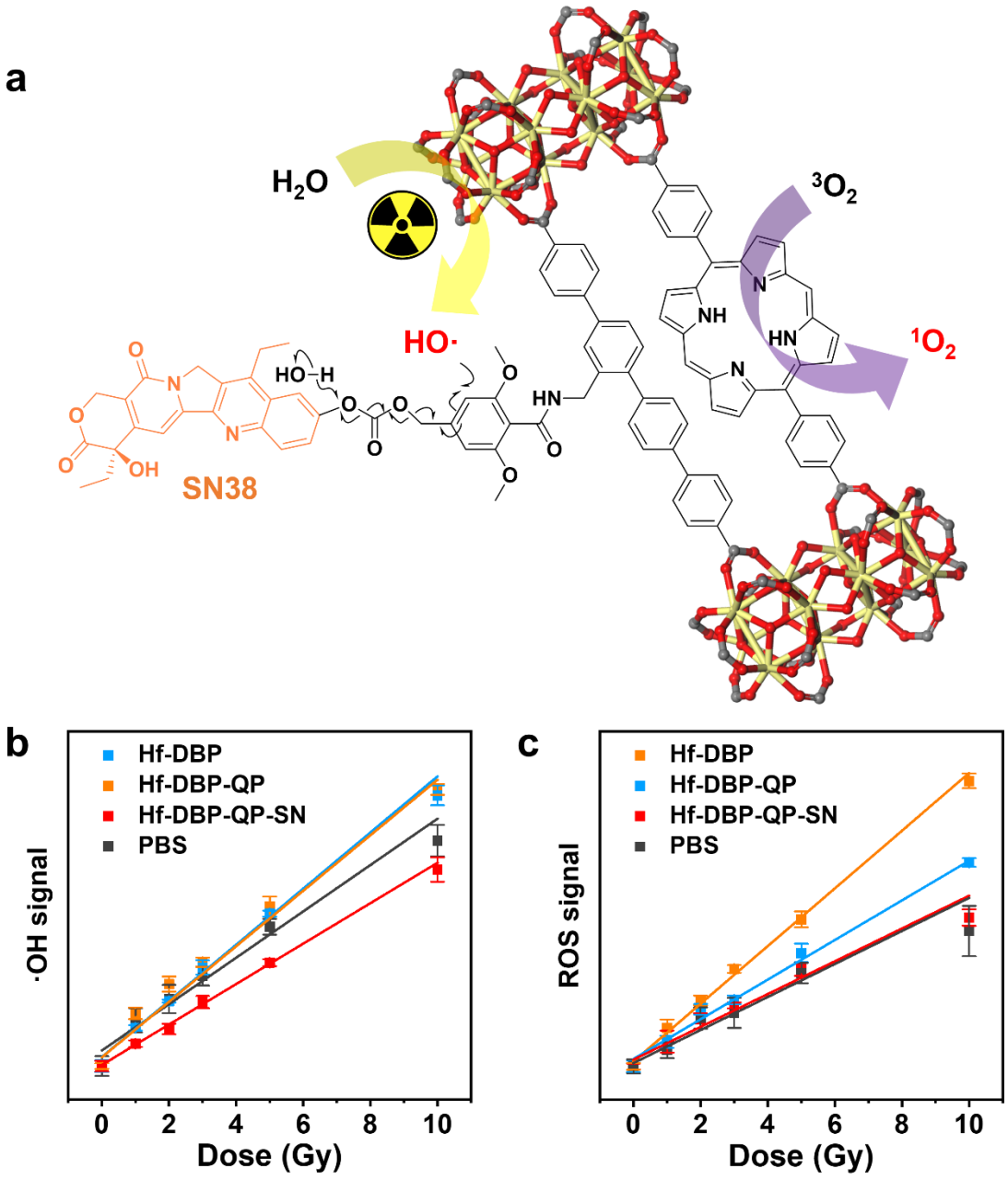

Figure 6-6. Release mechanism and ROS generation in test tubes. (a) Mechanism for X-ray triggered release of SN38 from Hf-DBP-QP-SN via RT–RDT. (b) Hydroxyl radical signals and (c) total ROS signals of PBS, Hf-DBP, Hf-DBP-QP, and Hf-DBP-QP-SN by APF assay and DCFH assay, respectively, after different doses of X-ray radiation (n = 6). Hf concentration was 40 μM.

Next, LC-MS analyses were used to evaluate the release of SN38. Hf-DBP-QP-SN released ~3.3% of total SN38 after 10 Gy X-ray irradiation, which was 13-fold higher than SN38 released

from MeO-SN under identical conditions (**Figures 6-7a**), suggesting that electron-dense Hf_{12} SBUs could serve as radiosensitizers to enhance ·OH generation for the triggered release of SN38 via hydroxylation of the 3,5-dimethoxylbenzyl carbonate followed by 1,4-elimination (**Figure 6-6a**). The successful release of SN38 was supported by using ·OH generated via the Fenton reaction;[38] Hf-DBP-QP-SN showed 14.8-fold higher SN38 release than MeO-SN under this condition (**Figures 6-7b**) due to better dispersity of the SN38 prodrug in the nMOF.

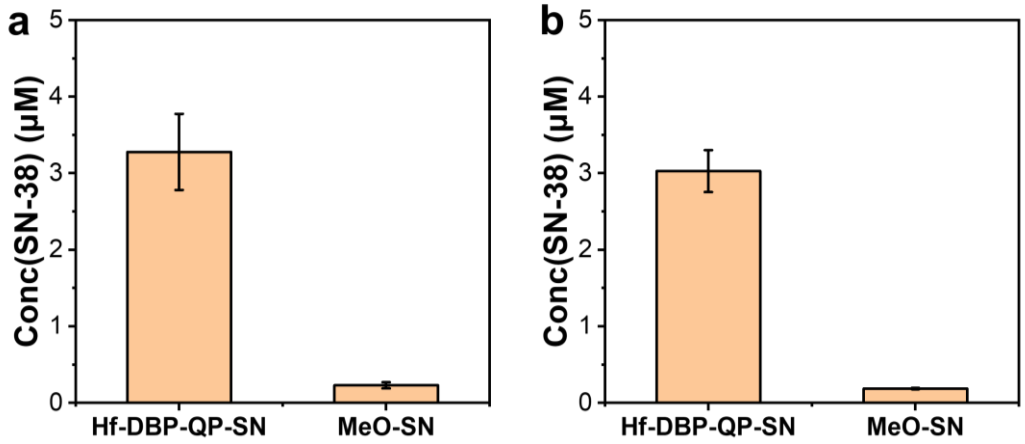

Figure 6-7. Concentration of SN38 released from MeO-SN or Hf-DBP-QP-SN (d) after 10 Gy X-ray irradiation or (e) after reacting with ·OH generated by the Fenton reaction. Starting MeO-SN or Hf-DBP-QP-SN concentration was 100 μM.

6.2.3. *In vitro* experiments

The cytotoxicity of H_2QP ligand and Hf-DBP-QP was assessed by 3-(4,5-dimethylthiazol-2-yl)-5-(3-carboxymethoxyphenyl)-2-(4-sulfo-phenyl)-2H-tetrazolium (MTS) assay on CT26 cells. No obvious toxicity was observed at a Hf concentration of up to 200 μM or at a H_2QP concentration of up to 60.33 μM (**Figure 6-8**). This result suggests the biocompatibility of the mixed-ligand Hf-DBP-QP nMOF.

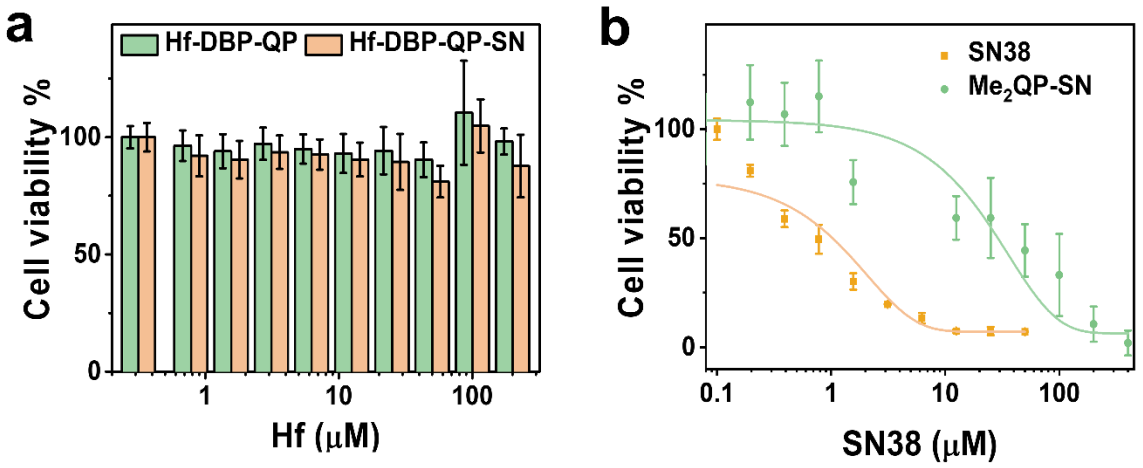

Figure 6-8. Cell viability of CT26 cells after incubation with (a) Hf-DBP-QP, Hf-DBP-QP-SN, (b) SN38, or Me_2QP-SN.

Compared with the strong toxicity of SN38 with a low half maximal inhibitory concentration (IC_{50}) value of 0.994 μM (**Figure 6-8b**),[39] Me_2QP-SN showed less toxicity with a IC_{50} value of 28.95 μM (**Figure 6-8b**), while Hf-DBP-QP-SN showed no obvious toxicity (**Figure 6-8a**) at a Hf concentration of up to 300 μM (corresponding to 22.3 μM SN38 in Hf-DBP-QP-SN). This result shows that Me_2QP-SN and Hf-DBP-QP-SN serve as novel prodrugs with low intrinsic toxicity.

We next determined the uptake of the prepared nMOFs by cancer cells. CT26 cells were incubated with Hf-DBP-QP-SN for 1, 2, 6, 8 and 12 h, and cellular content of Hf was detected by ICP-MS (**Figure 6-9a**). CT26 cells showed efficient uptake of Hf-DBP-QP-SN in a time-dependent manner.

DCFH-DA was then utilized to detect the generation of ROS in cancer cells. Flow cytometry analysis results showed that Hf-DBP-QP generated 1.62-fold higher ROS signals than PBS group under the radiation of 3 Gy X-ray (**Figure 6-9b**). Stronger ROS generation by Hf-DBP-

QP was supported by confocal laser scanning macroscopy (CLSM) imaging (**Figure 6-10**). This result suggests efficient ROS generation by Hf-DBP-QP via the RT–RDT process.

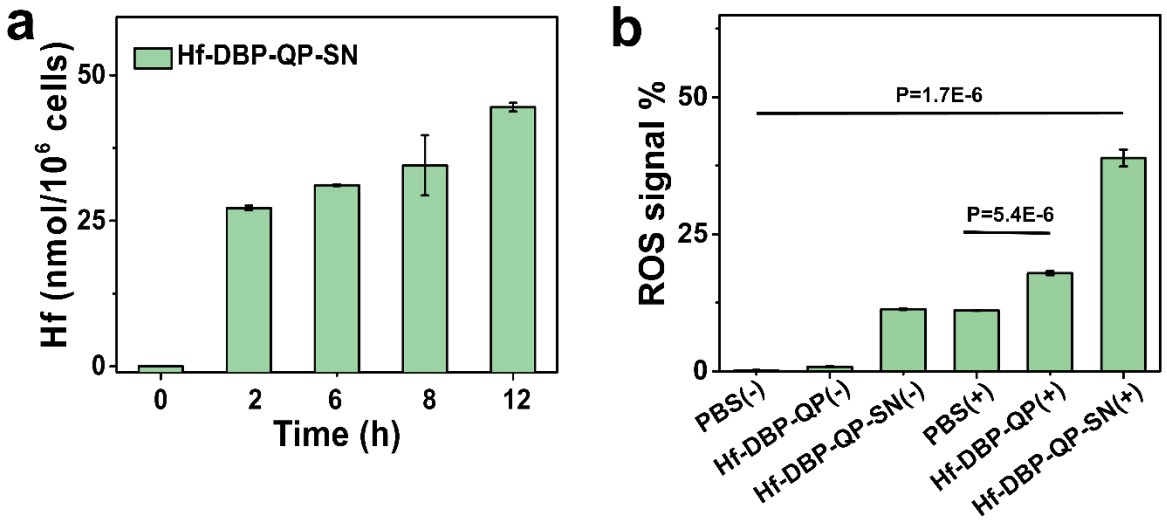

Figure 6-9. (a) Time-dependent cellular uptake of Hf-DBP-QP-SN as quantified by ICP-MS. (b) Total ROS generation in CT26 cancer cells after different treatments as probed by DCFH-DA and quantified by flow cytometry. The X-ray dose was 3 Gy.

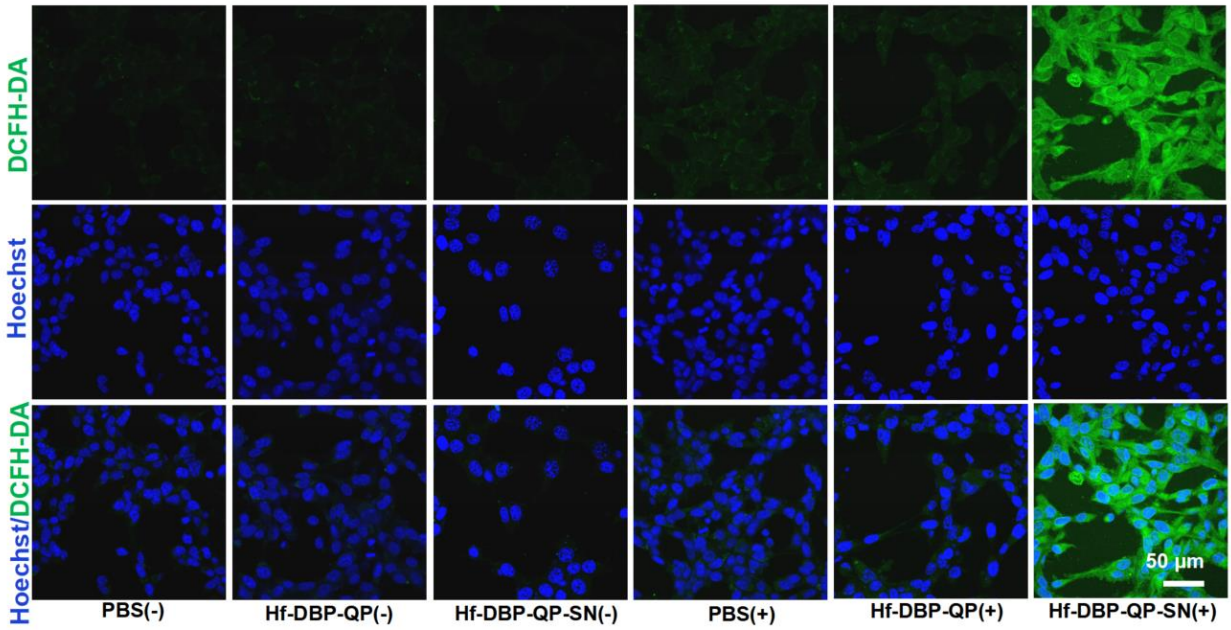

Figure 6-10. CLSM images of CT26 cells stained by DCFH-DA (green) and Hoechst (blue).

Hydroxyphenyl fluorescein (HPF), a specific probe of ·OH, was used to demonstrate the intracellular generation of ·OH. As shown in **Figure 6-11**, Hf-DBP-QP generated more ·OH than PBS under X-ray irradiation, which supported X-ray-triggered SN38 release from Hf-DBP-QP-SN.

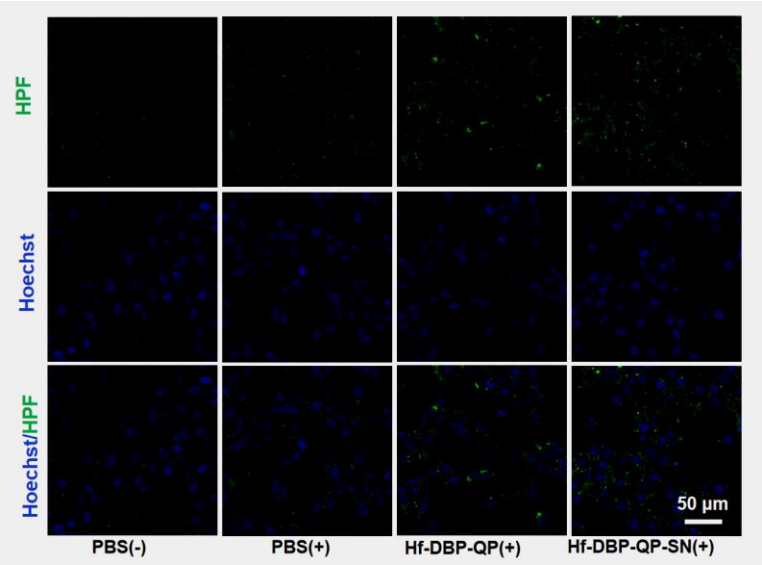

Figure 6-11. CLSM images of CT26 cells stained by HPF (green) and Hoechst (blue).

Hf-DBP-QP-SN(+) generated 38.9% ROS^+ cells, which was 2.17-fold higher than Hf-DBP-QP(+) (17.9%, **Figure 6-12**). This difference could be caused by the oxidative pressure by released SN38 molecules.[40]

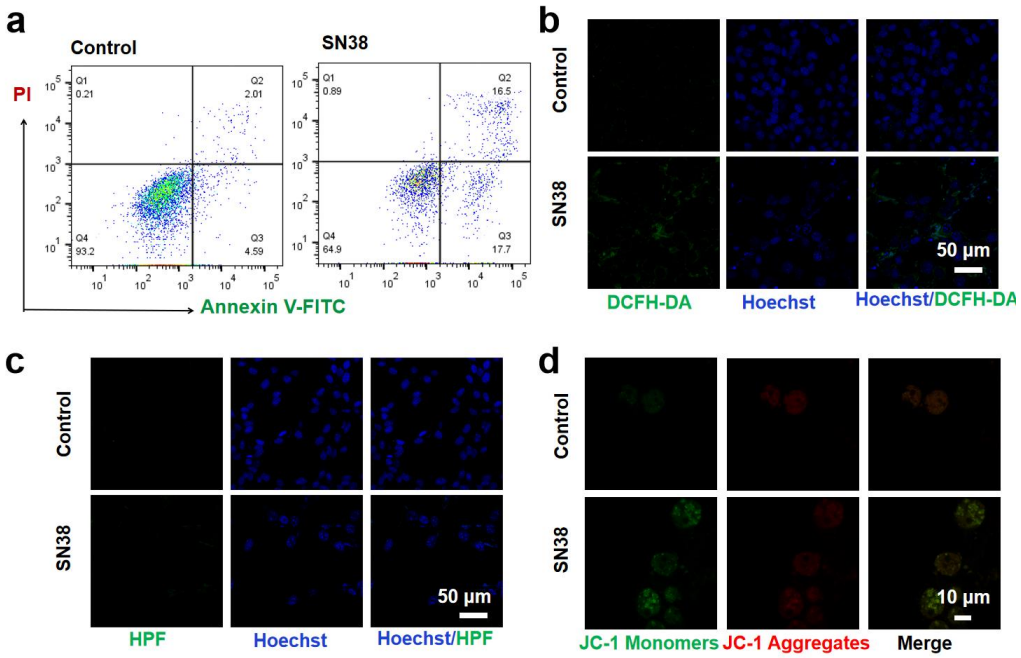

Figure 6-12. (a) Flow cytometric analysis of CT26 cells treated with or without SN38. (b) CLSM images showing ROS generation (probed by DCFH-DA) in CT26 cells after incubation with SN38. (c) CLSM images showing ·OH generation (probed by HPF) in CT26 cells after incubation with SN38. (d) CLSM images showing mitochondria membrane potentials (probed by JC-1).

Clonogenic assays were conducted to determine the radio-enhancement effects.[41] At the same Hf concentration of 50 μM mM, Hf-DBP-QP and Hf-DBP-QP-SN exhibited long-term anti-proliferative effect with a radiation enhancement factor (REF_{10}) of 1.147, and 2.52, respectively (**Figure 6-13a&b**). The radioenhancement of Hf-DBP-QP likely resulted from RT–RDT process, while higher radioenhancing effect of Hf-DBP-QP-SN was likely due to the synergistic effect between RT–RDT and chemotherapy resulted from the released SN38 triggered by ·OH.

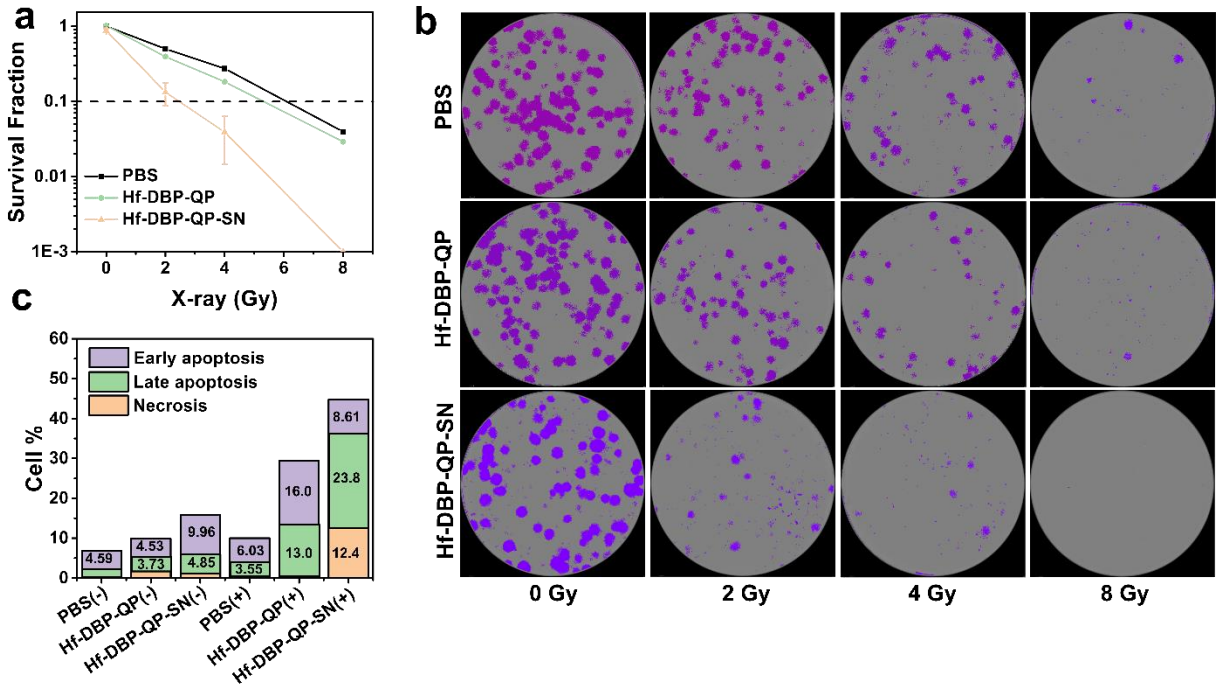

Figure 6-13. Clonogenic assay and immunogenetic cell death. (a) Clonogenic assays showing radioenhancement of Hf-DBP-QP and Hf-DBP-QP-SN on CT26 cells upon the radiation of different doses of X-rays (n=3). (b) Respective images of colony formation of CT26 cells after treated with Hf-DBP-QP or Hf-DBP-QP-SN followed by 250 kVp X-ray irradiation. (c) Quantification of early apoptotic, late apoptotic, and necrotic CT26 cells after incubation with Hf-DBP-QP or Hf-DBP-QP-SN with or without X-ray radiation (X-ray dose: 3 Gy).

Flow cytometry was used to assay the exposure of phosphatidylserine (PS) of CT26 cells by annexin V/propidium iodide (PI) apoptosis staining (**Figure 6-13c**). Compared with PBS(-) and PBS(+) groups, Hf-DBP-QP(+) treatment gave an obviously increased ratio of early and late apoptotic cells (29%), suggesting effective radioenhancement effect of Hf-DBP-QP. Hf-DBP-QP-SN(+) treatment showed a remarkable increase of necrosis, early and late apoptosis (44.81%), supporting the successful release of the SN38 to result in a higher proportion of apoptotic and necrotic cells than Hf-DBP-QP(+) treatment.

DNA damage was measured by γ-H2AX assay (**Figure 6-14**). Hf-DBP-QP(+) treatment showed stronger red fluorescence than PBS(+) treated cells, suggesting the RT–RDT process could

effectively lead to more DNA damage. Hf-DBP-QP-SN(+) treated cancer cells showed much stronger DNA damage than Hf-DBP-QP(+) treated cells, likely due to DNA damage by released SN38. Taken together, Hf-DBP-QP-SN(+) treatment effectively generated ROS through the RT–RDT process and caused oxidative stress by the released SN38.

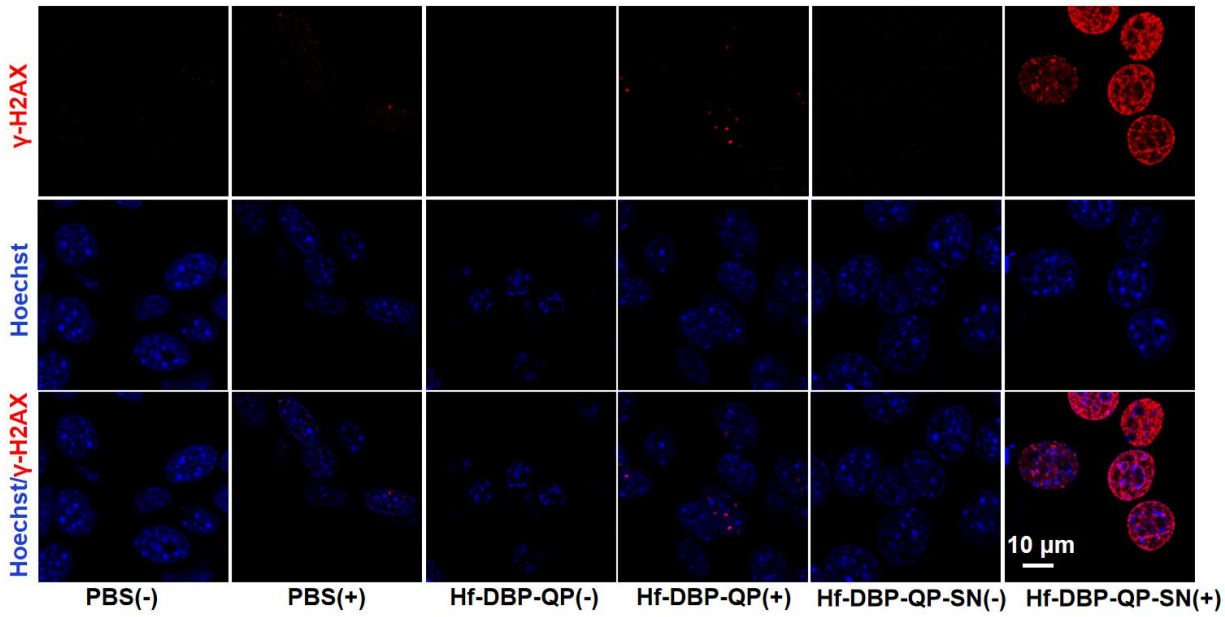

Figure 6-14. CLSM images of treated CT26 cells for γ-H2AX assay (scale bar: 10 μm).

6.2.3. *In vitro* experiments

The CT26 tumor model was established on BALB/c mice by inoculating 2×10^6 cells/mouse subcutaneously onto the right flanks. When the volume of CT26 tumors reached ~105 mm^3, the mice were randomized into six groups (n = 5) to receive PBS(-), Hf-DBP-QP-SN(-) (0.5 μmol Hf and 0.037 μmol SN38), PBS(+), irinotecan(+) (a prodrug of SN38: 0.037 μmol), Hf-DBP-QP(+), or Hf-DBP-QP-SN(+) treatment. Hf-DBP-QP-SN(-) exhibited no obvious tumor inhibition effect, supporting low toxicity of the nMOF nanotherapeutics. Irradiation of CT26 tumors with 2 Gy X-ray by 3 fractions moderately inhibited tumor growth with a tumor growth inhibition index

(TGI) of 0.474, while Hf-DBP-QP(+) enhanced tumor growth inhibition with a TGI of 0.744. Irinotecan(+) exhibited a TGI of 0.641 due to the additive effect of radiotherapy and chemotherapy. Importantly, Hf-DBP-QP-SN(+) treatment gave an impressive TGI of 0.935 (**Figure 6-15a**), demonstrating the synergistic effect between RT–RDT and chemotherapeutic effect of SN38 released from Hf-DBP-QP-SN in the tumors.

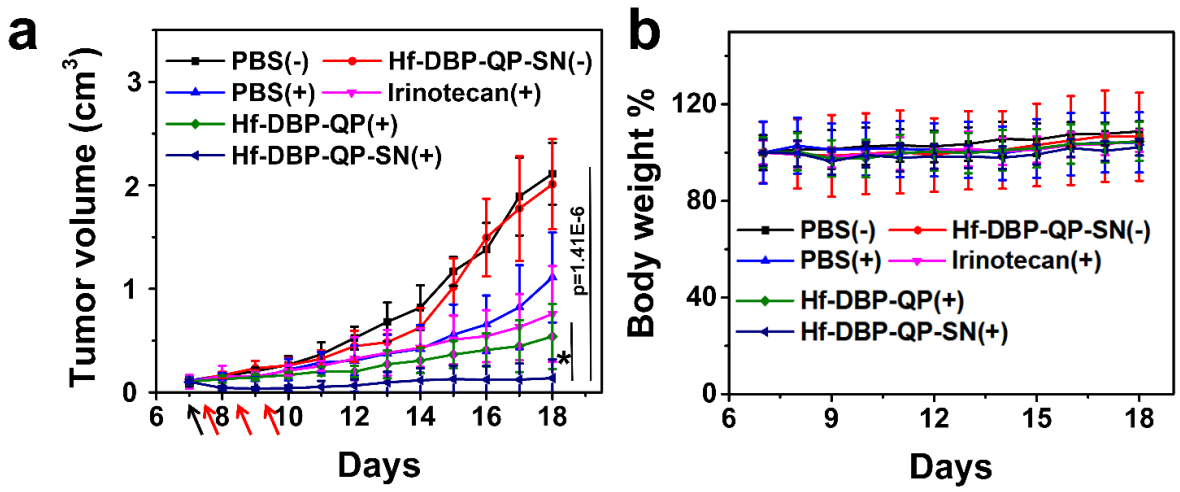

Figure 6-15. (a) Growth curves of CT26 tumors in BALB/c mice after different treatments (*n* = 5). Black arrow indicates i.t. injection and red arrows indicate X-ray radiation. (b) Relative body weights of CT26 tumor-bearing BALB/c mice after different treatments.

The therapeutic effects of Hf-DBP-QP-SN(+) and control groups were also evaluated by analyzing tumor slices by hematoxylin and eosin (H&E) and TdT-mediated dUTP nick end labeling (TUNEL) staining (**Figure 6-16**). In the Hf-DBP-QP-SN(-) group, no damaged or apoptotic cancer cells were observed, suggesting insignificant premature release of SN38 in the absence of X-ray irradiation. In the PBS(+) group, only a small percentage of damaged cancer cells and TUNEL positive cells were observed, while Hf-DBP-QP(+) treatment reduced the number of viable cancer cells and increased TUNEL positive cells. Hf-DBP-QP-SN(+) treatment led to the most damaged and TUNEL positive cells, supporting the synergistic antitumor effects

from RT–RDT and chemotherapy from released SN38. γ-H2AX and Ki67 staining further demonstrated that Hf-DBP-QP-SN(+) effectively induced the strongest DNA damage and inhibited tumor proliferation while greatly reducing systemic toxicity of traditional chemotherapeutic drugs.

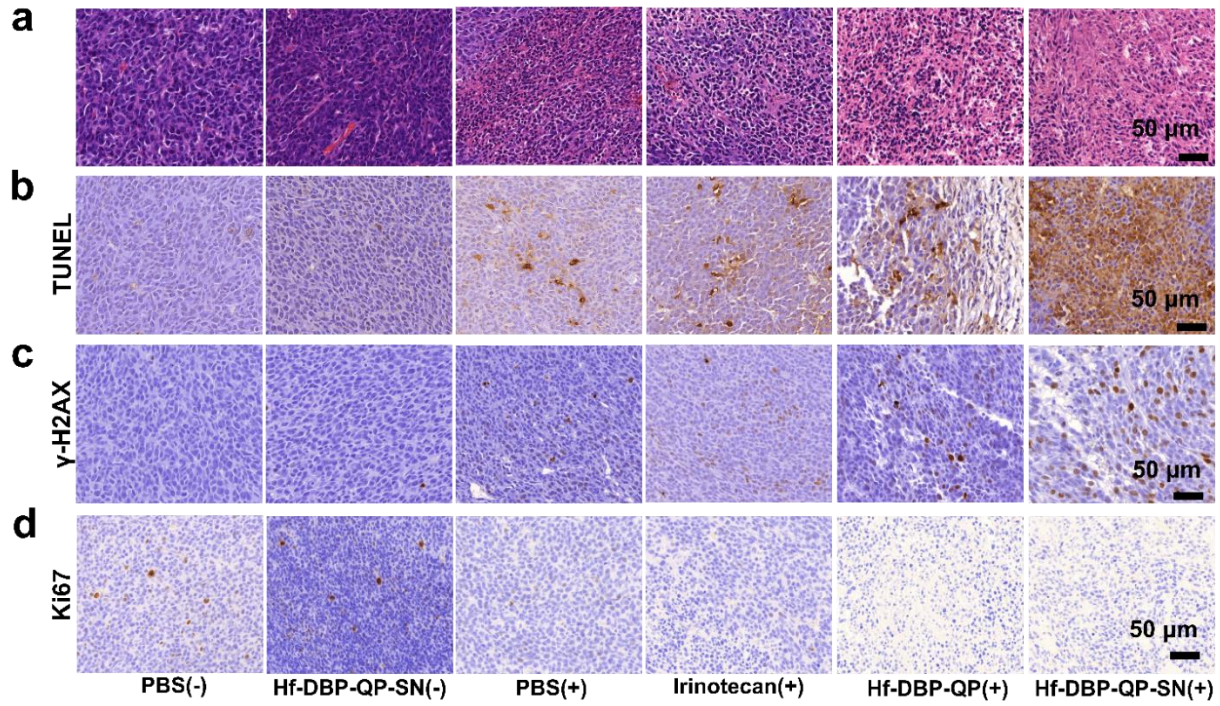

Figure 6-16. (a) H&E, (b) TUNEL, (c) γ-H2AX and (d) Ki67 staining of excised CT26 tumors at day 1 after the last X-ray radiation (scale bar: 50 μm).

Importantly, the mice in all treatment groups showed similar and steady body weight growth patterns (**Figure 6-15b**), suggesting the lack of toxicity from these treatments. The treatments did not cause any histological abnormality in major organs (**Figure 6-17**), further supporting the safety of Hf-DBP-QP-SN(+) treatment. Finally, Hf-DBP-QP-SN(+) treatment significantly increased the median survival to 38 days from 29 days for Hf-DBP-QP(+) treatment (**Figure 6-18**). For comparison, PBS(+) only modestly increased mouse median survival to 21 days from 18 days for PBS(-). These results showed that Hf-DBP-QP-SN served as an efficient

radioenhancer and a novel nanotherapeutics for X-ray triggered release of SN38 for tumor-targeted and synergistic RT–RDT and chemotherapy without causing systemic toxicity.

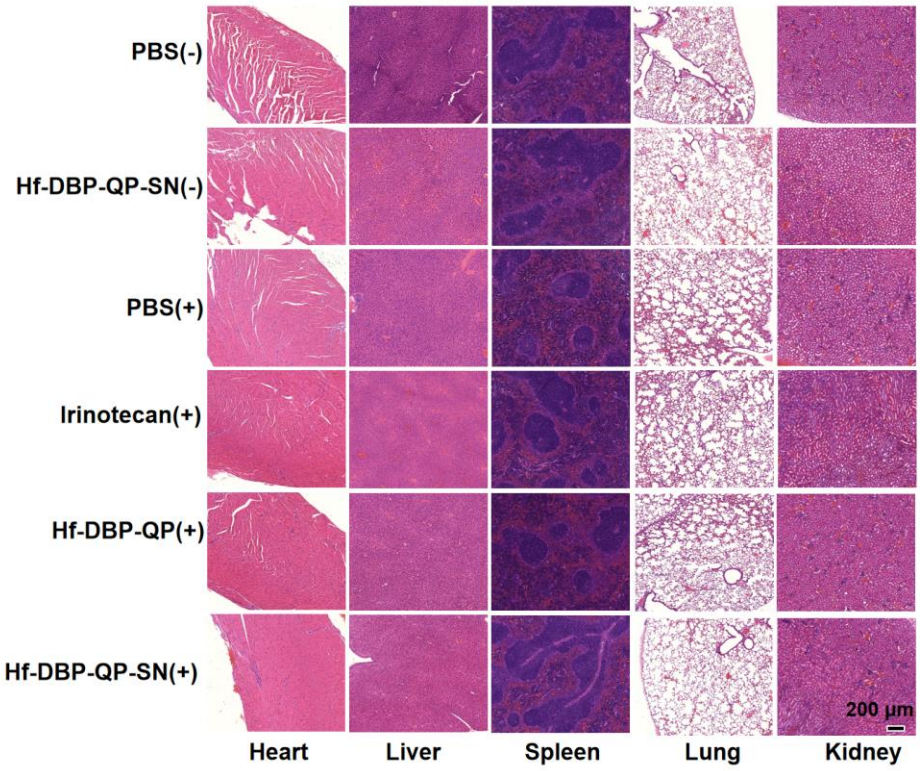

Figure 6-17. H&E staining of hearts, livers, spleens, lungs, and kidneys of CT26 tumor-bearing BALB/c mice after different treatments (scale bar: 200 μm).

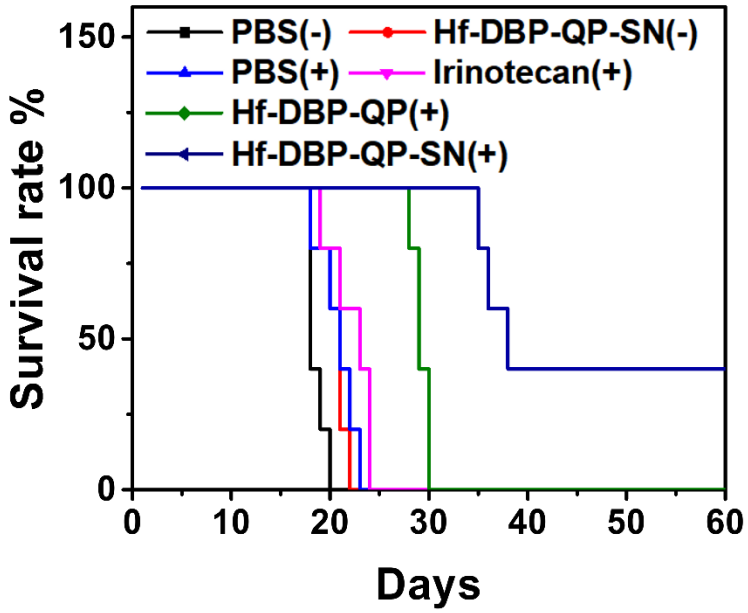

Figure 6-18. Survival rate of CT26 tumor-bearing BALB/c mice after different treatments.

6.4. Methods

6.4.1. Synthesis of H_2QP and Me_2QP-SN

(4,4'-Dibromo-[1,1'-biphenyl]-2-yl)methanamine (15). 2,7-Dibromo-9*H*-fluoren-9-one (**12**, 6 g, 17.8 mmol) and KOH (15.6 g, 0.278 mol) were dissolved in diphenyl ether (Ph_2O, 80 mL) and heated at 120 °C for 18 hrs. After the solution was cooled to room temperature, concentrated HCl (21.5 mL) was added dropwise to adjust the pH to 1-2. The precipitate was collected via filtration and washed with H_2O to remove excess KCl and then hexane to remove excess Ph_2O, and finally dried under vacuum to give 4,4'-dibromo-[1,1'-biphenyl]-2-carboxylic acid (**13**, 6.32 g, 17.8 mmol, 99%). ^{1}H NMR (400 MHz, $CDCl_3$): δ 8.10 (d, *J* = 2.2 Hz, 1H), 7.69 (dd, *J* = 8.2, 2.1 Hz, 1H), 7.55 – 7.50 (m, 2H), 7.23 – 7.15 (m, 3H);^{13}C NMR (101 MHz, $CDCl_3$) δ 168.92, 141.21, 139.09, 135.25, 133.76, 132.67, 131.49, 130.16, 129.87, 123.35, 122.23, 121.72, 119.03. HR-MS (ESI, positive mode): *m/z* calc'd for $C_{13}H_9Br_2O_2$ $[M-H]^-$: 354.8798, found 354.8835.

$SOCl_2$ (15 mL) was added to compound **13** (6.32 g, 17.8 mmol) and the mixture was refluxed at 80 °C for 6 h to produce 4,4'-dibromo-[1,1'-biphenyl]-2-carbonyl chloride. The unreacted $SOCl_2$ was removed by distilling under reduced pressure. 25-28% NH_3• H_2O (100 mL) was added slowly to 4,4'-dibromo-[1,1'-biphenyl]-2-carbonyl chloride with vigorous stirring overnight. The resulting solution was filtered with water (to remove any NH_4Cl salt) and hexane before being dried under vacuum to afford 4,4'-dibromo-[1,1'-biphenyl]-2-carboxamide (**14**, 5.67 g, 15.9 mmol, 90%). ^{1}H NMR (400 MHz, chloroform-d): δ 7.88 (d, *J* = 2.1 Hz, 1H), 7.63 (dd, *J* = 8.3, 2.1 Hz, 1H), 7.59 – 7.54 (m, 2H), 7.33 – 7.28 (m, 2H), 7.21 (d, *J* = 8.2 Hz, 1H), 5.49 (s, 1H), 5.27 (s, 1H); ^{13}C NMR (101 MHz, $CDCl_3$) δ 169.41, 138.03, 137.58, 136.21, 133.82, 132.16, 132.00, 130.36, 122.92, 122.28. HR-MS (ESI, positive mode): *m/z* calc'd for $C_{13}H_{10}Br_2NO$ $[M+H]^+$: 355.9109, found 355.9111.

Compound **14** (5.67 g, 15.9 mmol) was dissolved in 1M BH_3 in THF (56.0 mL, 56 mmol) and stirred at reflux for 24 h before being quenched with concentrated HCl (6 mL). The solution was refluxed for 2 more hours, cooled to room temperature, and basified by addition of saturated Na_2CO_3 to pH = ~10. The solution was then partitioned with water (15 mL) and AcOEt (30 mL) to separate the organic phase from the aqueous phase, extracted with CH_2Cl_2 (3 × 30 mL). The combined organic phase was dried with Na_2SO_4, filtered, condensed via rotary evaporation, and then purified by silica gel column chromatography to give (4,4'-dibromo-[1,1'-biphenyl]-2-yl)methanamine (**15**, 4.07 g, 11.9 mmol, 75%)**.** ^{1}H NMR (400 MHz, chloroform-d): δ 7.68 (s, 1H), 7.59 - 7.53 (m, 2H), 7.47 - 7.41 (m, 1H), 7.23 - 7.16 (m, 2H), 7.07 (d, *J* = 8.2 Hz, 1H), 3.78 (s, 2H); ^{13}C NMR (101 MHz, $CDCl_3$) δ 139.05, 138.96, 131.71, 131.60, 131.19, 130.76, 130.02, 122.26, 121.87, 43.85. HR-MS (ESI, positive mode): *m/z* calc'd for $C_{13}H_{12}Br_2N$ $[M+H]^+$: 341.9316, found 341.9313.

4-(((*tert*-Butyldimethylsilyl)oxy)methyl)-N-((4,4'-dibromo-[1,1'-biphenyl]-2-yl)methyl)-2,6-dimethoxybenzamide (16). Compound **3** (1.20 g, 3.68 mmol), 1-(3-dimethylaminopropyl)-3-ethylcarbodiimide hydrochloride (EDCI, 0.846 g, 4.42 mmol), hydroxybenzotriazole (HOBt, 0.596 g, 4.42 mmol), TEA (615 uL, 4.42 mmol), and compound **15** (1.255 g, 3.68 mmol) were combined in CH_2Cl_2 (70 mL). The resulting mixture was degassed and then stirred at room temperature for 12 h. The reaction mixture was then partitioned between EA and water, and the aqueous layer was extracted with EA twice. The combined organic phase was then dried over Na_2SO_4, filtered, concentrated by rotary evaporation, and separated with column chromatography to give compound **16** (1.00 g, 1.54 mmol, 42%). ^{1}H NMR (400 MHz, chloroform-d): δ 7.89 (d, *J* = 2.0 Hz, 1H), 7.60 - 7.51 (m, 2H), 7.44 (dd, *J* = 8.1, 2.1 Hz, 1H), 7.23 - 7.15 (m, 2H), 7.08 (d, *J* = 8.1 Hz, 1H), 6.56 (t, *J* = 0.8 Hz, 2H), 5.94 (t, *J* = 6.1 Hz, 1H), 4.72 (t, *J* = 0.8 Hz, 2H), 4.56 (d, *J* = 6.2 Hz, 2H), 3.87 (d, *J* = 1.1 Hz, 6H), 0.95 (d, *J* = 1.1 Hz, 9H), 0.11 (d, *J* = 1.1 Hz, 6H); ^{13}C NMR (101 MHz, $CDCl_3$) δ 166.02, 157.39, 145.28, 138.76, 138.44, 138.07, 131.63, 131.21, 130.75, 130.63, 130.12, 122.27, 121.90, 113.79, 101.24, 64.78, 55.90, 40.90, 30.94, 25.89, 18.40, -5.23. HR-MS (ESI, positive mode): *m/z* calc'd for $C_{29}H_{36}Br_2NO_4Si$ $[M+H]^+$: 650.0760, found 650.0795.

Dimethyl 2''-((4-(((*tert*-butyldimethylsilyl)oxy)methyl)-2,6-dimethoxybenzamido)methyl)-[1,1':4',1'':4'',1'''-quaterphenyl]-4,4'''-dicarboxylate (17). To compound **16** (1.00 g, 1.54 mmol) was added (4-(methoxycarbonyl)phenyl)boronic acid (0.832 g, 4.62 mmol), CsF (0.702 g, 4.62 mmol), [1,1′-bis(diphenylphosphino)ferrocene]dichloropalladium(II) ($Pd(dppf)Cl_2$, 0.113 g, 0.154 mol), and the solid mixture was degassed followed by the addition of degassed dioxane (30 mL). The resulting solution was stirred at 90 °C under N_2 for 3 days. The mixture was filtered before the removal of dioxane under reduced pressure, extracted with EA, and purified by column

chromatography to yield compound **17** (0.784 g, 1.03 mmol, 67%)**.** ^{1}H NMR (400 MHz, chloroform-d): δ 8.13 (ddd, *J* = 8.2, 6.5, 1.6 Hz, 4H), 7.99 (s, 1H), 7.78 - 7.74 (m, 2H), 7.61 (dt, *J* = 7.9, 1.6 Hz, 1H), 7.54 - 7.45 (m, 2H), 7.41 (dd, *J* = 7.9, 1.4 Hz, 1H), 6.53 (s, 2H), 6.05 (t, *J* = 6.3 Hz, 1H), 4.76 (d, *J* = 5.9 Hz, 2H), 4.70 (s, 2H), 3.99 - 3.92 (m, 6H), 3.70 (d, *J* = 1.6 Hz, 6H), 0.98 - 0.88 (m, 9H), 0.15 - 4 (m, 6H); ^{13}C NMR (101 MHz, $CDCl_3$) δ 233.82, 232.85, 224.23, 212.11, 211.99, 211.87, 207.34, 206.84, 206.34, 205.93, 203.37, 197.33, 197.04, 196.92, 196.70, 195.90, 195.86, 194.11, 193.96, 193.84, 193.74, 192.73, 180.80, 168.13, 131.56, 122.68, 118.99, 108.25, 97.75, 92.70, 85.20, 61.57. HR-MS (ESI, positive mode): *m/z* calc'd for $C_{45}H_{50}NO_8Si$ $[M+H]^+$: 760.3306, found 760.3311.

2''-((4-(hydroxymethyl)-2,6-dimethoxybenzamido)methyl)-[1,1':4',1'':4'',1'''-quaterphenyl]-4,4'''-dicarboxylic acid (H_2QP). To compound **17** (1 g, 1.32 mmol) was added NaOH (5.28 g, 132 mmol) and MeOH and H_2O in a 1:1 ratio (20 mL: 20 mL). The resulting mixture was stirred at 40 °C for 1 day, acidified with 1M HCl to pH = 1-2, filtered, washed with water and methanol, and dried under vacuum to afford **H_2QP** (0.728 g, 1.18 mmol, 90%). ^{1}H NMR (400 MHz, DMSO-d_6) δ 13.00 (s, 2H), 8.65 (t, *J* = 6.0 Hz, 1H), 8.11 – 8.03 (m, 4H), 7.98 (d, *J* = 1.9 Hz, 1H), 7.93 – 7.81 (m, 6H), 7.73 (dd, *J* = 7.9, 2.0 Hz, 1H), 7.62 – 7.56 (m, 2H), 7.43 (d, *J* = 7.9 Hz, 1H), 6.64 (s, 2H), 5.29 (t, *J* = 5.8 Hz, 1H), 4.49 (d, *J* = 5.1 Hz, 2H), 4.44 (d, *J* = 5.9 Hz, 2H), 3.63 (s, 6H). ^{13}C NMR (101 MHz, DMSO-d_6) δ 167.15, 166.07, 164.94, 156.58, 156.54, 145.23, 144.68, 144.24, 143.87, 139.85, 139.71, 139.61, 138.21, 138.04, 138.00, 137.81, 137.41, 137.37, 130.19, 130.02, 129.90, 129.88, 129.73, 128.57, 127.03, 127.00, 126.89, 126.84, 126.73, 126.15, 125.27, 114.94, 101.89, 62.91, 55.57, 55.54, 52.20. HR-MS (ESI, positive mode): *m/z* calc'd for $C_{37}H_{32}NO_8$ $[M+H]^+$: 618.2128, found 618.2120.

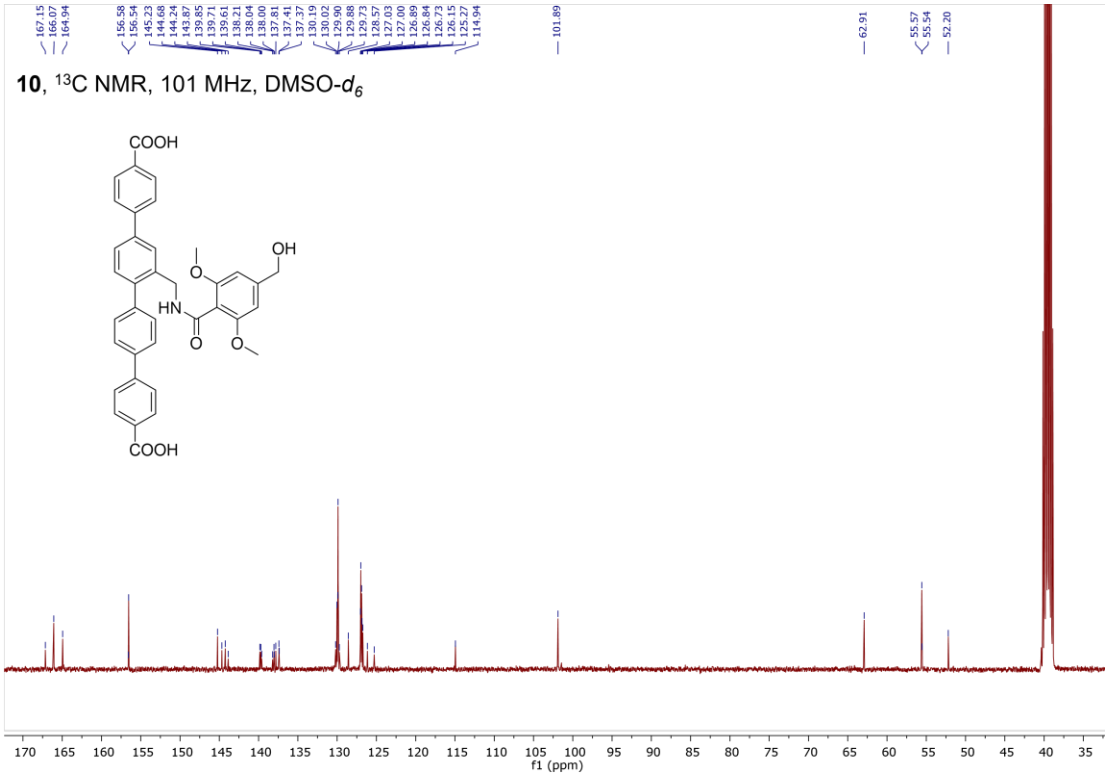

Figure 6-19. ^{13}C NMR spectrum of H_2QP.

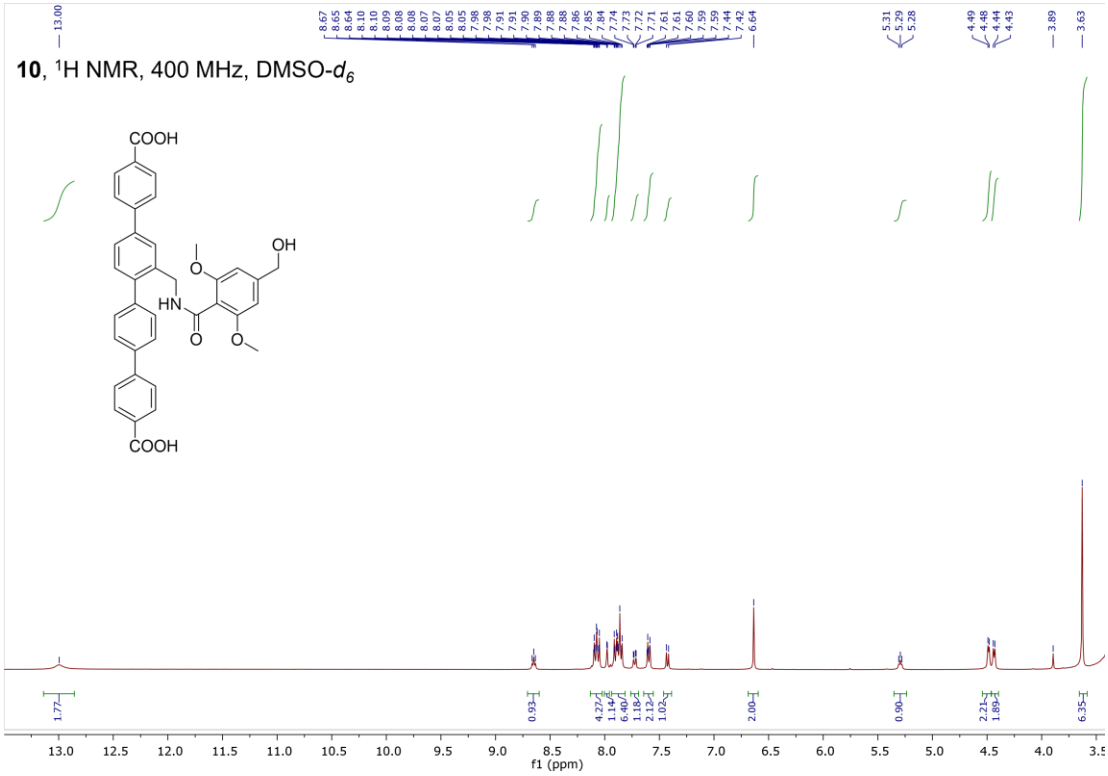

Figure 6-20. ^{1}H NMR spectrum of H_2QP.

dimethyl (*S*)-2''-((4-(((((4,11-diethyl-4-hydroxy-3,14-dioxo-3,4,12,14-tetrahydro-1*H*-pyrano[3',4':6,7]indolizino[1,2-*b*]quinolin-9-yl)oxy)carbonyl)oxy)methyl)-2,6-dimethoxybenzamido)methyl)-[1,1':4',1'':4'',1'''-quaterphenyl]-4,4'''-dicarboxylate (Me$_2$QP-SN). Compound **9** (1.0 g, 1.32 mmol) was added tetrabutylammonium fluoride solution in THF (1M, 5 mL) and stirred at room temperature for 2 h. 10 mL saturated NH_4Cl solution was added and THF was removed via rotary evaporation. White precipitate was filtered and washed with water to produce dimethyl 2''-((4-(hydroxymethyl)-2,6-dimethoxybenzamido)methyl)-[1,1':4',1'':4'',1'''-quaterphenyl]-4,4'''-dicarboxylate (**18**, 0.809 g, 1.25 mmol, 95%). ^{1}H NMR (400 MHz, DMSO-d_6) δ 8.65 (t, *J* = 6.0 Hz, 1H), 8.09 (dd, *J* = 11.5, 8.2 Hz, 4H), 7.98 (d, *J* = 2.0 Hz, 1H), 7.93 (d, *J* = 8.2 Hz, 2H), 7.88 (d, *J* = 7.9 Hz, 4H), 7.77 – 7.69 (m, 1H), 7.60 (d, *J* = 8.0 Hz, 2H), 7.43 (d, *J* = 7.9 Hz, 1H), 6.63 (s, 2H), 5.29 (t, *J* = 5.7 Hz, 1H), 4.49 (d, *J* = 5.7 Hz, 2H), 4.43 (d, *J* = 6.0 Hz, 2H), 3.89 (s, 6H), 3.62 (s, 6H). ^{13}C NMR (101 MHz, DMSO-d_6) δ 166.14, 165.02, 156.58, 145.27, 144.72, 144.28, 139.88, 139.75, 138.09, 137.86, 137.43, 130.25, 129.93, 128.60, 127.08, 127.04, 126.94, 126.18, 125.33, 114.95, 101.93, 62.95, 55.62, 52.26. HR-MS (ESI, positive mode): *m/z* calc'd for $C_{39}H_{36}NO_8$ $[M+H]^+$: 646.2441, found 646.2440.

Compound 18 (500 mg, 0.774 mmol), 4-nitrophenyl chloroformate (390 mg, 1.94 mmol), TEA (322 μL, 2.322 mmol) were combined in dry DCM (30 mL) under Ar and stirred for 1 day at RT. The resulting solution was quenched with 5 mL H_2O and extracted with DCM, dried over Na_2SO_4, filtered, concentrated by rotary evaporation, and then dried completely under vacuum to afford dimethyl 2''-((2,6-dimethoxy-4-((((4-nitrophenoxy)carbonyl)oxy)methyl)benzamido)methyl)-[1,1':4',1'':4'',1'''-quaterphenyl]-4,4'''-dicarboxylate (**19**), which was used directly in the next step without purification. HR-MS (ESI, positive mode): *m/z* calc'd for $C_{46}H_{39}N_2O_{12}$ $[M+H]^+$: 811.2505, found 811.2542.

To a mixture of **19** in DCM (20 mL) was added SN38 (589 mg, 1.500 mmol) and TEA (250 μL, 1.80 mmol); the resulting mixture was stirred at room temperature for 1 day before being washed with H_2O and extracted with DCM (3 × 20 mL). The organic phases were combined, dried over Na_2SO_4, filtered, concentrated by rotary evaporation, dissolved in minimal DCM, and purified via thin layer chromatography (5% MeOH in DCM) to give Me_2QP-SN (0.165 g, 0.155 mmol, 20%). ^{1}H NMR (400 MHz, Chloroform-*d*) δ 8.27 (d, *J* = 9.2 Hz, 1H), 8.14 (ddd, *J* = 8.5, 6.4, 1.9 Hz, 5H), 7.99 (d, *J* = 1.9 Hz, 1H), 7.93 (d, *J* = 2.6 Hz, 1H), 7.79 – 7.75 (m, 2H), 7.72 (dt, *J* = 8.6, 1.9 Hz, 4H), 7.68 (s, 1H), 7.67 – 7.60 (m, 2H), 7.53 – 7.49 (m, 2H), 7.43 (d, *J* = 7.9 Hz, 1H), 6.65 (s, 2H), 6.02 (t, *J* = 6.0 Hz, 1H), 5.75 (d, *J* = 16.4 Hz, 1H), 5.31 (d, *J* = 16.3 Hz, 1H), 5.27 (d, *J* = 3.1 Hz, 4H), 4.77 (d, *J* = 6.0 Hz, 3H), 3.96 (d, *J* = 1.9 Hz, 7H), 3.76 (s, 7H), 3.64 (s, 2H), 3.16 (q, *J* = 7.7 Hz, 3H), 2.26 – 2.18 (m, 3H), 1.38 (d, *J* = 7.7 Hz, 2H), 1.04 (t, *J* = 7.4 Hz, 3H), 0.91 – 0.85 (m, 3H). ^{13}C NMR (101 MHz, CDCl3) δ 174.00, 167.09, 165.58, 157.77, 157.74, 153.40, 152.33, 150.31, 149.88, 147.65, 146.90, 145.54, 145.36, 145.10, 140.67, 140.05, 139.67, 139.30, 137.72, 136.46, 132.48, 131.75, 131.00, 130.72, 130.36, 130.24, 129.99, 129.25, 129.22, 127.56, 127.52, 127.44, 127.24, 127.13, 126.99, 126.12, 124.72, 118.84, 116.13, 114.26, 104.32, 98.24, 72.89, 70.61, 66.47, 56.25, 52.34, 52.32, 49.51, 41.60, 31.75, 23.32, 14.13, 7.96. HR-MS (ESI, positive mode): *m/z* calc'd for $C_{62}H_{54}N_3O_{14}$ $[M+H]^+$: 1064.3606, found 1064.3596.

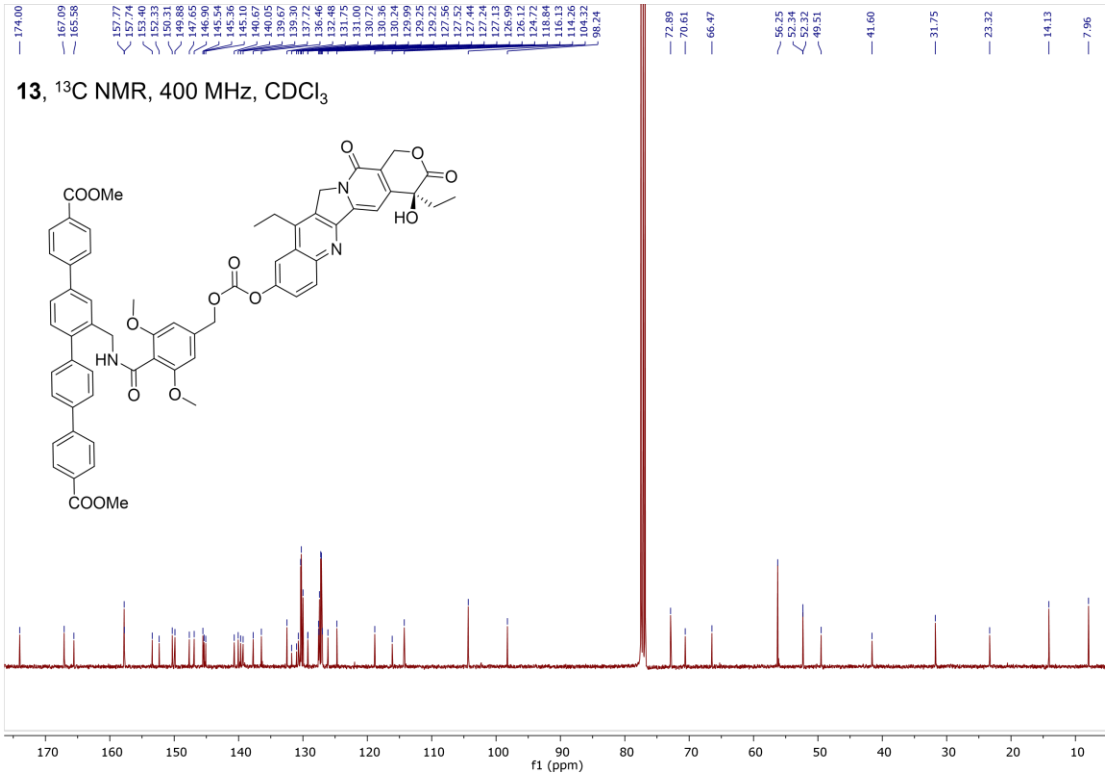

Figure 6-21. ^{13}C NMR spectrum of Me_2QP-SN.

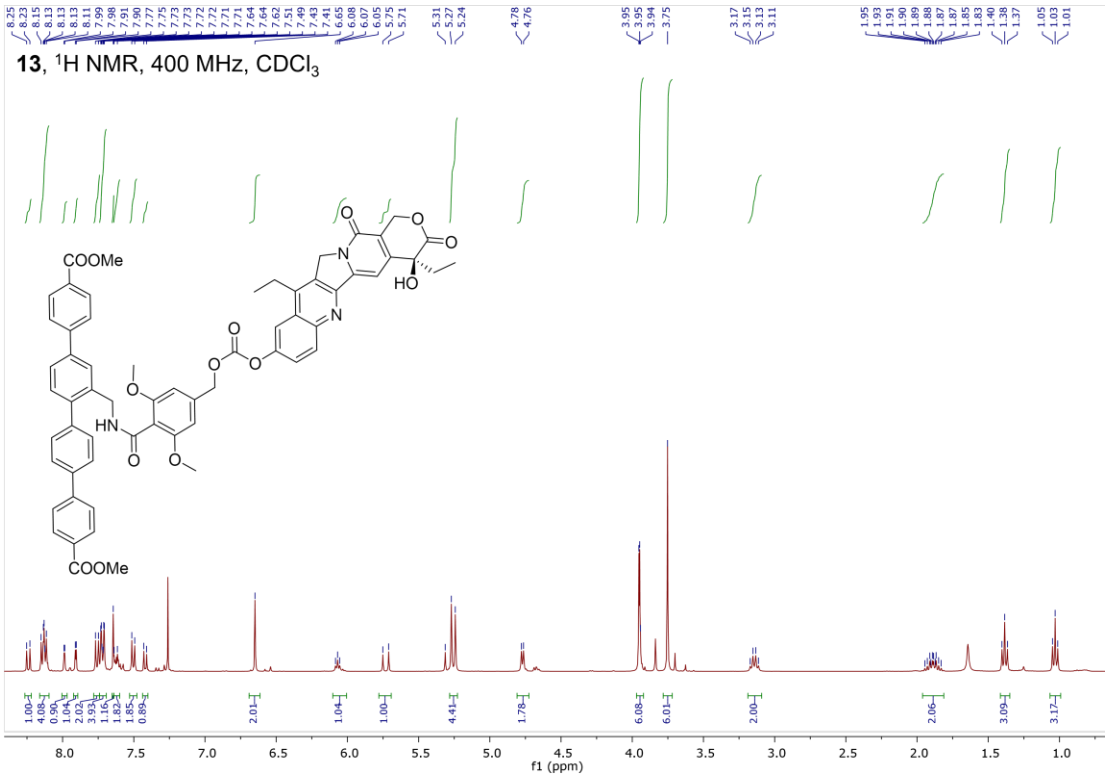

Figure 6-22. ^{1}H NMR spectrum of Me_2QP-SN.

6.4.2. Synthesis and characterization of Hf-DBP-QP-SN

Synthesis of Hf-DBP-QP. $HfCl_4$, H_2DBP and H_2QP-OH were separately dissolved in DMF at a concentration of 2, 3.5 and 3.5 mg/mL, respectively. 500 μL $HfCl_4$ solution, 100 μL H_2DBP and 400 μL H_2QP-OH were then combined in a 1-dram vial with the addition of 55 μL acetic acid and 5 μL water as modulators. The mixture was heated in an oven at 80 ^oC for 2 days. The purple precipitate was collected by centrifugation and sequentially washed with DMF, 1% triethylamine (TEA) in ethanol (EtOH) (v/v), and EtOH, and then dispersed in EtOH for storage.

Synthesis of Hf-DBP-QP-SN. 10 mL Hf-DBP-QP was washed with dry acetonitrile (ACN) twice and dispersed in ACN with a QP concentration of 2.0 mM. 4-Nitrophenyl chloroformate (10.1 mg, 50 μmol), and TEA (8.3 μL, 60 μmol) were then added, and the solution was stirred for 2 days to afford Hf-DBP-QP-NO_2 nMOF. The mixture was then centrifuged, washed with ACN three times and redispersed in ACN before the addition of SN38 (7.9 mg, 20 μmol) and TEA (4.2 μL, 30 μmol); the solution was then stirred for 2 more days. The as-synthesized Hf-DBP-QP-SN was washed with 10% dimethyl sulfoxide (DMSO) in ACN 6 times and dispersed in EA for storage.

MOF Digestion for UV-Vis Spectroscopic Measurement. 50 μL Hf-DBP-QP or Hf-DBP-QP-SN solution, 900 μL DMSO, and 50 μL H_3PO_4 were mixed and sonicated for 1 h. The mixture was diluted to a proper concentration for UV-Vis measurement. The absorption of H_2QP at 304 nm was used to calculate the concentration of H_2QP-OH in Hf-DBP-QP after comparison with the standard curve of H_2QP-OH in DMSO while the absorption of H_2DBP at 408 nm was used to calculate the concentration of H_2DBP in Hf-DBP-QP or Hf-DBP-QP-SN after comparison with the standard curve of H_2DBP in DMSO.

Digestion of Hf-DBP-QP-SN for Quantification of SN38 by HPLC. 10 μL Hf-DBP-QP-SN dispersion in EA (Hf concentration of ~1.5 mM) and 100 μL TFA/EA mixture (v/v=1:9) was combined and sonicated for 15min. The supernatant was obtained by centrifugation and analyzed by HPLC. The absorption of SN38 at 380 nm was used to calculate the concentration of SN38 after comparison with the standard curve of SN38 in EA.

Digestion of Hf-DBP-QP-SN for Quantification of SN38 by LC-MS. 100 μL 1M $NaHCO_3$ solution was added to 100 μL Hf-DBP-QP-SN dispersion in PBS (SN concentration of approximately 100 μM). The mixture was sealed and sonicated for 20 min. 100 μL saturated NaCl solution and 150 μL ethyl acetate (EA) were added and the mixture was vortexed for 1 min. The EA layer after centrifugation was analyzed by LC-MS.

Stability Test of Hf-DBP-QP-SN in PBS. Hf-DBP-QP-SN was dispersed in 1 mL PBS (1 mM) with a Hf concentration of 5 mM. 200 uL suspension was taken after incubation for 1, 2, 4, 8, and 24 h and centrifuged for PXRD measurement.

Total ROS Generation in Test Tubes. Total ROS generation under irradiation was detected by the 2',7'-dichlorodihydrofluorescein (DCFH) assay. 1 mL DCFH-DA (1mM) in DMSO was hydrolyzed by 4 mL NaOH (0.01 M) solution in the dark for 30 minutes and stopped by adding 20 mL PBS (25 mM, pH 7.4). The freshly-prepared DCFH was then added to the PBS suspension (pH 7, 10 mM) of Hf-DBP, Hf-DBP-QP or Hf-DBP-QP-SN at the same Hf concentration. In the final mixture, the concentration of DCFH was 5 μM while the concentration of Hf was 40 μM. The PBS solution with the same DCFH concentration served as a blank control. 100 μL of each suspension was added to 96-well plates (n = 6) and then irradiated with X-ray at 0, 1, 2, 3, 5, or 10 Gy, respectively. The fluorescence signal (em. 520/20 nm) was collected with a Synergy HTX microplate reader (ex. 485/20 nm).

Hydroxyl radical generation in Test Tubes. Hydroxyl radical (·OH) generation under irradiation was detected by the APF assay. APF assay was added to the PBS suspension of Hf-DBP, Hf-DBP-QP or Hf-DBP-QP-SN at the same Hf concentration. In the final mixture, the concentration of APF was 5 μM while that of Hf was 40 μM. The PBS solution with the same APF concentration served as a blank control. 100 μL of each suspension was added to 96-well plates (n = 6) and then irradiated with X-ray at 0, 1, 2, 3, 5, or 10 Gy, respectively. The fluorescence signal (em. 520/20 nm) was collected with a Synergy HTX microplate reader (ex. 485/20 nm).

Hydroxyl Radical Triggered SN38 Release in Test Tubes. Hf-DBP-QP-SN or MeO-SN was dispersed in H_2O at the same concentration of total SN38 (100 μM). $FeCl_3$, (+)-Sodium L-ascorbate, $Na_2(EDTA)\cdot 2H_2O$ (ethylenediaminetetraacetic acid, disodium salt dihydrate) was firstly dissolved in water to reach a concentration of 10 mM separately (10.5 mM for $Na_2(EDTA)\cdot 2H_2O$). Then, 100 μL of each solution and 50 μL H_2O_2 (200 mM in H_2O) was added to Hf-DBP-QP-SN or MeO-SN solution to generate hydroxyl radical in situ and to trigger the release of SN38. For control group, only H_2O_2 was added. After 8h incubation at room temperature, additional 100 μL 1M $NaHCO_3$ was added to Hf-DBP-QP-SN to digest the nMOF, after which the mixture was sealed and sonicated for 20 minutes before the addition of 100 μL PBS (200 mM, pH 4) to adjust the pH to 7. 100 μL saturated NaCl solution and 150 μL ethyl acetate (EA) were added before vortexing the Hf-DBP-QP-SN or MeO-SN mixture for 1 minute. The EA layer after centrifugation was analyzed by LC-MS.

X-ray Triggered Release in Test Tube. Hf-DBP-QP-SN or MeO-SN were dispersed in H_2O (10 mM, pH = 7.4) at the same concentration of total SN38 (100 μM). 100 μL Hf-DBP-QP-SN or MeO-SN suspension was irradiated with 10 Gy X-ray. 100 μL 1M $NaHCO_3$ was added to Hf-DBP-QP-SN to digest the nMOF, after which the mixture was sealed, sonicated for 20 minutes,

and sat 15h before the addition of 100 μL PBS (200 mM, pH 4.0) to adjust the pH to 7. 100 μL saturated NaCl solution and 150 μL ethyl acetate (EA) were added before vortexing the Hf-DBP-QP-SN or MeO-SN mixture for 1 min. The EA layer after centrifugation was analyzed by LC-MS.

6.4.3. *In vitro* experiments

Dark Toxicity. CT26 cells were cultured in RPMI-1640 medium supplemented with 10% fetal bovine serum (VWR, USA, filtered), 1% HyClone Penicillin-Streptomycin 100X solution (Cytiva, USA), and cultured in a humidified atmosphere containing 5% CO_2 at 37°C. Mycoplasma was tested on a regular basis by MycoAlert detection kit (Lonza Nottingham, Ltd.).

The cytotoxicity of H_2QP ligand, Hf-DBP-QP and Hf-DBP-QP-SN on CT26 cells were detected by MTS assay. CT26 cells were seeded in 96-well plates at a density of 2500 cells/well. Different concentrations of Hf-DBP-QP-SN were added and 24 hours later 10% (v/v) of MTS reagent was added to each well. 90 minutes later the absorbance of each well at 490 nm was read by a Synergy HTX plate reader to calculate cell viability.

The cytotoxicity of SN38 and Me_2QP-SN on CT26 cells were detected by MTS assay. CT26 cells were seeded in 96-well plates at a density of 2500 cells/well. Different concentrations of SN38 or Me_2QP-SN were added and 48 hours later 10% (v/v) of MTS reagent was added to each well. 90 minutes later the absorbance of each well at 490 nm was read by a Synergy HTX plate reader to calculate cell viability.

Cellular Uptake. CT26 cells were seeded in 6-well plates at a density of 2×10^5/well and cultured overnight. Hf-DBP-QP (Hf: 50 μM) and Hf-DBP-QP-SN (Hf: 50 μM) was added at an equivalent metal concentration into medium (n = 3) and incubated for 1, 2, 3, 4 and 6 hours in a 37 ºC incubator. At each time point, the medium was aspirated, the cells were washed with PBS for three

times, collected by centrifugation, and counted with a hemocytometer. Then, the uptake of Hf-DBP-QP and Hf-DBP-QP-SN were detected on an LSR-Fortessa 4-15 HTS at the Cytometry and Antibody Technology Facility at the University of Chicago and analyzed by FlowJo software (Tree Star, USA).

Intracellular ROS Generation. To demonstrate the generation of total ROS, CT26 cells were seeded in the cell culture dishes at a density of 1.5×10^5 and cultured overnight. Hf-DBP-QP-SN or Hf-DBP-QP was added at an equivalent metal concentration of 50 μM and further incubated in a 37 ºC incubator for 4 hours. The cells were washed with PBS solution for 3 times and 1 mL cell culture medium containing with 20 μM DCFH-DA was added and incubated at 37 ºC for another 30 min. Then, the cells were irradiated with X-ray (3 Gy) and continued to be cultured in the cell incubator for another 12 h. After that, cells were washed by PBS for three times and collected by centrifugation and counted with a hemocytometer. Then, the generation of total ROS was detected on an LSR-Fortessa 4-15 HTS and analyzed by FlowJo software.

To demonstrate the generation of total ROS, CT26 cells were seeded in the cell culture dishes at a density of 1.5×10^5 and cultured overnight. Hf-DBP-QP-SN or Hf-DBP-QP was added at an equivalent metal concentration of 50 μM and further incubated in a 37 ºC incubator for 4 hours. The cells were washed with PBS solution for 3 times and 1 mL cell culture medium containing with 30 μM DCFH-DA was added and incubated at 37 ºC for another 30 min. Then the cells were irradiated with X-ray (3 Gy) and continued to be cultured in the cell incubator for another 24 h. After that, cells were washed by PBS for three times and further incubated with Hoechst 33342 (10 μg mL^{-1}) in PBS for 10 min in the cell incubator. Finally, cells were washed by PBS 3 times and observed on a Leica Stellaris 8 confocal microscope at the Integrated Light Microscopy Facility at the University of Chicago and analysis was done with Image J software (NIH, USA).

The generation of ·OH in cancer cells was also detected according to the similar method as above. Typically, CT26 cells were seeded in the cell culture dishes at a density of 1.5×10^5 and cultured overnight. Hf-DBP-QP-SN or Hf-DBP-QP was added at an equivalent metal concentration of 50 μM and further incubated in a 37 ºC incubator for 4 hours. The cells were washed with PBS solution for 3 times and 1 mL cell culture medium containing with 10 μM HPF was added and incubated at 37℃ for another 30 min. Then the cells were irradiated with X-ray (3 Gy) and continued to be cultured in the cell incubator for another 24 h. After that, cells were washed by PBS for three times and further incubated with Hoechst 33342 (10 μg mL^{-1}) in PBS for 10 min in the cell incubator. Finally, cells were washed by PBS for 3 times and observed on a Leica Stellaris 8 confocal microscope at the Integrated Light Microscopy Facility at the University of Chicago and analysis was done with Image J software.

Apoptotic Cell Death. To quantify the apoptosis, CT26 cells were seeded in 6-well plates at a density of 2×10^5/well and cultured overnight. Hf-DBP-QP or Hf-DBP-QP-SN was added at an equivalent metal concentration of 50 μM for 4 hours and irradiated with X-ray (3 Gy). 24 hours later, the cells were washed with PBS, trypsinized to afford single cell suspensions, The cells were stained with the dead cell apoptosis kit with annexin V Alexa Fluor 488 & PI and resuspended in the binding buffer for flow cytometric analysis (Annexin-V in FITC channel, PI in PE-dazzle 594 channel).

Clonogenic Assay. RT250 orthovoltage X-ray machine model (Philips, USA) with fixed setting at 250 kVp, 15 mA and a built-in 1 mm Cu filter was used for X-ray irradiation in test tube and *in vitro* experiments. CT26 cells were seeded in 6-well plates at a density of 1.5×10^5 cells/well and cultured overnight. The cells were incubated with PBS, Hf-DBP-QP, or Hf-DBP-QP-SN at an equivalent metal concentration of 50 μM for 4 hours, and then irradiated with 0, 2, 4, 6 Gy X-ray

(n = 3). The cells were washed with PBS twice and then trypsinized to afford single cell suspensions. The cells were counted and diluted, then 200 cells were seeded in each well of 6-well plates and cultured in 2 mL medium for another 7 days. When an appropriate colony size was observed, the plates were rinsed once with PBS, fixed by 4% paraformaldehyde for 20 minutes at room temperature, and washed with PBS once. The 6-well plates were then scanned and analyzed with IncuCyte S3 (Essen BioScience) at Cellular Screening Center at the University of Chicago in the whole well mode with a 4× objective. The colonies were identified with IncuCyte 2021A software in a cellular resolution and the confluence was used as a parameter to calculate the plating efficiency (PE)and surviving fraction (SF):

$$PE = \frac{Confluence\ (0\ Gy, PBS)}{Cell\#\ (0\ Gy, PBS)} \qquad SF(D, MOF) = \frac{Confluence\ (D, MOF)}{Cell\#\ (D, MOF) \times PE}$$

Where was the radiation dose and was the number of cells seeded for a certain radiation dose D and a certain treatment group.

The dose modifying ratio at a 10% ($DMR_{10\%}$) was used as a parameter to assess radiosensitization effect and defined as the ratio of doses under reference conditions to produce a 10% SF:

$$DMR_{10\%} = \frac{D_{PBS}}{D_{MOF}}$$

DNA Damage. For CLSM imaging, CT26 cells were seeded in cell culture dishes at a density of 1.5×10^5 . The cells were treated in the same way as in the clonogenic assay. 24 hours after radiation, the cells were washed with PBS and fixed with 4% paraformaldehyde at room temperature for 20 minutes. The cells were again rinsed with PBS, blocked and permeabilized with 5% FBS + 0.3% Triton-X in PBS at room temperature for 1 hour. After blocking, the cells were incubated with the γ-H2AX primary antibody (1:500) in 1% BSA + 0.3% Triton-X in PBS at 4 °C overnight. The

cells were then washed with PBS and incubated with the Alexa Fluor 488 conjugated secondary antibody (1:3000) in 1% BSA + 0.3% Triton-X in PBS at room temperature for 1 hour. Afterwards, the cells were washed with PBS and further incubated with Hoechst 33342 (10 μg mL^{-1}) in PBS for 10 min at 37 ^{o}C to visualize cell nuclei, respectively. Finally, cells were washed by PBS for 3 times and observed on a Leica Stellaris 8 confocal microscope.

6.4.4. *In vivo* experiments

Anti-cancer Efficacy. X-RAD 225 image-guided biological irradiator (Precision X-ray Inc., USA) was used with voltage at 225 kVp, current at 13 mA, a 0.3 mm Cu filter, and a 15 mm collimator for animal therapy. The X-ray dose rate of X-RAD 225 was 0.04167 Gy/second. BALB/c mice (6-8 weeks) were obtained from Charles River Laboratories, Inc (USA) and bred in house at the animal facility at the University of Chicago. The study protocol was reviewed and approved by the Institutional Animal Care and Use Committee (IACUC) at the University of Chicago. To evaluate the in vivo therapeutic efficacy of Hf-DBP-QP-SN, CT26 tumor model was established on BALB/c mice by inoculating 2×10^6 cells/mouse subcutaneously onto the right flanks at day 0, respectively. When CT26 tumors reached to ~105 mm^3, the mice were randomized for irradiation treatment. PBS, Hf-QP, or Hf-DBP-QP-SN was intratumorally injected with an equivalent metal dose of 0.5 μmol and SN38 dose of 0.0373 μmol in 20 μL PBS (n = 5). 6-8 hours later, the mice were anaesthetized with 2.5% (v/v) isoflurane/O_2 and mounted onto the X-Rad 225 irradiator. The CT26 tumors were irradiated with 2 Gy X-ray/fraction for 3 consecutive days. The length and width of tumor tissues were measured with an electronic caliper (tumor volume = length × $width^2$/2) and body weights were monitored with an electronic scale. At the endpoint of the experiments, the mice were euthanized, and the tumors and major organs were sectioned for hematoxylin-eosin

(H&E) staining to evaluate general toxicity. The tumor growth inhibition index (TGI) was defined as the equation below:

$$TGI = (1 - \frac{\frac{T_e}{T_s} / \frac{C_e}{C_s}}{1 - \frac{C_s}{C_e}}) \times 100\%$$

where T_e, T_s, C_e, and represent average tumor volumes of treated mice at endpoint, treated mice at starting-point, control mice at endpoint and control mice at starting-point, respectively.

Immunohistochemistry Analysis. The histological slides were scanned on a CRi Pannoramic SCAN 40x whole slide scanner by Integrated Light Microscopy Core at the University of Chicago. To evaluate DNA damage and tumor proliferation after different treatments, a group of CT26-bearing mice were established and treated in the same way as described above, but euthanized one day after the last irradiation. The tumors were excised and fixed in 4% PFA for 48 h and 70% ethanol for 1 day. The tissues were embedded in paraffin, sectioned and stained for H&E, γ-H2AX, Ki67 and TUNEL by Human Tissue Resource Center at the University of Chicago. Briefly, the slides were deparaffinized and rehydrated using xylenes and serial dilutions of ethanol to distilled water. Then the slides were treated with antigen retrieval buffer (Leica Biosystems, AR9640) and heated in a steamer over 97°C for 20 minutes). After washing with tris-buffered saline, the slides were incubated with primary γ-H2AX antibody (1:400) or primary Ki67 antibody (Thermo Fisher Scientific, Clone# SP6, 1:400) at room temperature for 1 hour in a wet chamber. The slides were washed with tris-buffered saline, then γ-H2AX and Ki67 slides were incubated with anti-rabbit-polymer (Bond Polymer Refine Detection, Leica Biosystems, DS9800) for 30 minutes at room temperature. The antigen-antibody binding was detected with the 3,3′-Diaminobenzidine (DAB) (DAKO, K3468) system. Tissue sections were then immersed in hematoxylin for counterstaining and covered with cover glasses. The slides were scanned on a CRi Pannoramic SCAN 40× whole

slide scanner by Integrated Light Microscopy Core at the University of Chicago and analyzed with the QuPath-0.2.3 software.

6.5. References

(1) Johnstone, T. C.; Suntharalingam, K.; Lippard, S. J., The Next Generation of Platinum Drugs: Targeted Pt(II) Agents, Nanoparticle Delivery, and Pt(IV) Prodrugs. *Chem. Rev.* **2016,** *116* (5), 3436-3486.

(2) Chabner, B. A.; Roberts, T. G., Chemotherapy and the war on cancer. *Nat. Rev. Cancer* **2005,** *5* (1), 65-72.

(3) Xu, X.; Zeng, Z.; Ding, X.; Shan, T.; Liu, Q.; Chen, M.; Chen, J.; Xia, M.; He, Y.; Huang, Z.; Huang, Y.; Zhao, C., Reactive oxygen species-activatable self-amplifying Watson-Crick base pairing-inspired supramolecular nanoprodrug for tumor-specific therapy. *Biomaterials* **2021,** *277*, 121128.

(4) Zhang, Y.; Xu, C.; Yang, X.; Pu, K., Photoactivatable Protherapeutic Nanomedicine for Cancer. *Adv. Mater.* **2020,** *32* (34), 2002661.

(5) Abet, V.; Filace, F.; Recio, J.; Alvarez-Builla, J.; Burgos, C., Prodrug approach: An overview of recent cases. *Eur. J. Med. Chem.* **2017,** *127*, 810-827.

(6) Zubrod, C. G., Selective Toxicity of Anticancer Drugs: Presidential Address1. *Cancer Res.* **1978,** *38* (12), 4377-4384.

(7) Albert, A., Chemical aspects of selective toxicity. *Nature* **1958,** *182*, 421-423.

(8) Dong, X.; Brahma, R. K.; Fang, C.; Yao, S. Q., Stimulus-responsive self-assembled prodrugs in cancer therapy. *Chem. Sci.* **2022,** *13* (15), 4239-4269.

(9) Hao, Y.; Chen, Y.; He, X.; Yu, Y.; Han, R.; Li, Y.; Yang, C.; Hu, D.; Qian, Z., Polymeric Nanoparticles with ROS-Responsive Prodrug and Platinum Nanozyme for Enhanced Chemophotodynamic Therapy of Colon Cancer. *Adv. Sci.* **2020,** *7* (20), 2001853.

(10) Chu, B.; Qu, Y.; He, X.; Hao, Y.; Yang, C.; Yang, Y.; Hu, D.; Wang, F.; Qian, Z., ROS-Responsive Camptothecin Prodrug Nanoparticles for On-Demand Drug Release and Combination of Chemotherapy and Photodynamic Therapy. *Adv. Funct. Mater.* **2020,** *30* (52), 2005918.

(11) Zhen, W.; An, S.; Wang, S.; Hu, W.; Li, Y.; Jiang, X.; Li, J., Precise Subcellular Organelle Targeting for Boosting Endogenous-Stimuli-Mediated Tumor Therapy. *Adv. Mater.* **2021,** *33* (51), 2101572.

(12) Luo, C.; Sun, J.; Liu, D.; Sun, B.; Miao, L.; Musetti, S.; Li, J.; Han, X.; Du, Y.; Li, L.; Huang, L.; He, Z., Self-Assembled Redox Dual-Responsive Prodrug-Nanosystem Formed by Single Thioether-Bridged Paclitaxel-Fatty Acid Conjugate for Cancer Chemotherapy. *Nano Lett.* **2016,** *16* (9), 5401-5408.

(13) Zhou, F.; Feng, B.; Wang, T.; Wang, D.; Cui, Z.; Wang, S.; Ding, C.; Zhang, Z.; Liu, J.; Yu, H.; Li, Y., Theranostic Prodrug Vesicles for Reactive Oxygen Species-Triggered Ultrafast

Drug Release and Local-Regional Therapy of Metastatic Triple-Negative Breast Cancer. *Adv. Funct. Mater.* **2017,** *27* (46), 1703674.

(14) Guo, Z.; Hong, H.; Zheng, Y.; Wang, Z.; Ding, Z.; Fu, Q.; Liu, Z., Radiotherapy-Induced Cleavage of Quaternary Ammonium Groups Activates Prodrugs in Tumors. *Angew. Chem. Int. Ed.* **2022,** *61* (34), e202205014.

(15) Zhang, W.; Hu, X.; Shen, Q.; Xing, D., Mitochondria-specific drug release and reactive oxygen species burst induced by polyprodrug nanoreactors can enhance chemotherapy. *Nat. Commun.* **2019,** *10* (1), 1704.

(16) Li, X.; Lovell, J. F.; Yoon, J.; Chen, X., Clinical development and potential of photothermal and photodynamic therapies for cancer. *Nat. Rev. Clin. Oncol.* **2020,** *17* (11), 657-674.

(17) Pham, T. C.; Nguyen, V.-N.; Choi, Y.; Lee, S.; Yoon, J., Recent Strategies to Develop Innovative Photosensitizers for Enhanced Photodynamic Therapy. *Chem. Rev.* **2021,** *121* (21), 13454-13619.

(18) Yang, B.; Chen, Y.; Shi, J., Reactive Oxygen Species (ROS)-Based Nanomedicine. *Chem. Rev.* **2019,** *119* (8), 4881-4985.

(19) Yang, K.; Yang, Z.; Yu, G.; Nie, Z.; Wang, R.; Chen, X., Polyprodrug Nanomedicines: An Emerging Paradigm for Cancer Therapy. *Adv. Mater.* **2022,** *34* (6), 2107434.

(20) Vaidya, S. P.; Patra, M., X-rays Actuate Anticancer Drugs: Opening New Vistas in Prodrug Therapy. *ChemBioChem* **2021,** *22* (21), 2998-3000.

(21) Zhen, W.; Weichselbaum, R. R.; Lin, W., Nanoparticle-Mediated Radiotherapy Remodels the Tumor Microenvironment to Enhance Antitumor Efficacy. *Adv. Mater.* **2023,** *35* (21), 2206370.

(22) Pan, Y.; Tang, W.; Fan, W.; Zhang, J.; Chen, X., Development of nanotechnology-mediated precision radiotherapy for anti-metastasis and radioprotection. *Chem. Soc. Rev.* **2022,** *51* (23), 9759-9830.

(23) Wang, D.; He, I. W.; Liu, J.; Jana, D.; Wu, Y.; Zhang, X.; Qian, C.; Guo, Y.; Chen, X.; Bindra, A. K.; Zhao, Y., Missing-Linker-Assisted Artesunate Delivery by Metal–Organic Frameworks for Synergistic Cancer Treatment. *Angew. Chem. Int. Ed.* **2021,** *60* (50), 26254-26259.

(24) Lismont, M.; Dreesen, L.; Wuttke, S., Metal-Organic Framework Nanoparticles in Photodynamic Therapy: Current Status and Perspectives. *Adv. Funct. Mater.* **2017,** *27* (14), 1606314.

(25) McKinlay, A. C.; Morris, R. E.; Horcajada, P.; Férey, G.; Gref, R.; Couvreur, P.; Serre, C., BioMOFs: Metal–Organic Frameworks for Biological and Medical Applications. *Angew. Chem. Int. Ed.* **2010,** *49* (36), 6260-6266.

(26) Simon-Yarza, T.; Giménez-Marqués, M.; Mrimi, R.; Mielcarek, A.; Gref, R.; Horcajada, P.; Serre, C.; Couvreur, P., A Smart Metal–Organic Framework Nanomaterial for Lung Targeting. *Angew. Chem. Int. Ed.* **2017,** *56* (49), 15565-15569.

(27) Alyami, M. Z.; Alsaiari, S. K.; Li, Y.; Qutub, S. S.; Aleisa, F. A.; Sougrat, R.; Merzaban, J. S.; Khashab, N. M., Cell-Type-Specific CRISPR/Cas9 Delivery by Biomimetic Metal Organic Frameworks. *J. Am. Chem. Soc.* **2020,** *142* (4), 1715-1720.

(28) Haddad, S.; Abánades Lázaro, I.; Fantham, M.; Mishra, A.; Silvestre-Albero, J.; Osterrieth, J. W. M.; Kaminski Schierle, G. S.; Kaminski, C. F.; Forgan, R. S.; Fairen-Jimenez, D., Design of a Functionalized Metal–Organic Framework System for Enhanced Targeted Delivery to Mitochondria. *J. Am. Chem. Soc.* **2020,** *142* (14), 6661-6674.

(29) Lu, K.; Aung, T.; Guo, N.; Weichselbaum, R.; Lin, W., Nanoscale Metal–Organic Frameworks for Therapeutic, Imaging, and Sensing Applications. *Adv. Mater.* **2018,** *30* (37), 1707634.

(30) Ramesh, M.; Ahlawat, P.; Srinivas, N. R., Irinotecan and its active metabolite, SN-38: review of bioanalytical methods and recent update from clinical pharmacology perspectives. *Biomed. Chromatogr.* **2010,** *24* (1), 104-123.

(31) Lan, G.; Ni, K.; Veroneau, S. S.; Song, Y.; Lin, W., Nanoscale Metal–Organic Layers for Radiotherapy–Radiodynamic Therapy. *J. Am. Chem. Soc.* **2018,** *140* (49), 16971-16975.

(32) Fu, Q.; Li, H.; Duan, D.; Wang, C.; Shen, S.; Ma, H.; Liu, Z., External-Radiation-Induced Local Hydroxylation Enables Remote Release of Functional Molecules in Tumors. *Angew. Chem. Int. Ed.* **2020,** *59* (48), 21546-21552.

(33) Lu, K.; He, C.; Lin, W., Nanoscale Metal–Organic Framework for Highly Effective Photodynamic Therapy of Resistant Head and Neck Cancer. *J. Am. Chem. Soc.* **2014,** *136* (48), 16712-16715.

(34) Lu, K.; He, C.; Guo, N.; Chan, C.; Ni, K.; Lan, G.; Tang, H.; Pelizzari, C.; Fu, Y.-X.; Spiotto, M. T.; Weichselbaum, R. R.; Lin, W., Low-dose X-ray radiotherapy–radiodynamic therapy via nanoscale metal–organic frameworks enhances checkpoint blockade immunotherapy. *Nat. Biomed. Eng.* **2018,** *2* (8), 600-610.

(35) Ju, E.; Dong, K.; Chen, Z.; Liu, Z.; Liu, C.; Huang, Y.; Wang, Z.; Pu, F.; Ren, J.; Qu, X., Copper(II)–Graphitic Carbon Nitride Triggered Synergy: Improved ROS Generation and Reduced Glutathione Levels for Enhanced Photodynamic Therapy. *Angew. Chem. Int. Ed.* **2016,** *55* (38), 11467-11471.

(36) Zhong, X.; Wang, X.; Zhan, G.; Tang, Y. a.; Yao, Y.; Dong, Z.; Hou, L.; Zhao, H.; Zeng, S.; Hu, J.; Cheng, L.; Yang, X., NaCeF4:Gd,Tb Scintillator as an X-ray Responsive Photosensitizer for Multimodal Imaging-Guided Synchronous Radio/Radiodynamic Therapy. *Nano Lett.* **2019,** *19* (11), 8234-8244.

(37) Liu, J.; Hu, F.; Wu, M.; Tian, L.; Gong, F.; Zhong, X.; Chen, M.; Liu, Z.; Liu, B., Bioorthogonal Coordination Polymer Nanoparticles with Aggregation-Induced Emission for Deep Tumor-Penetrating Radio- and Radiodynamic Therapy. *Adv. Mater.* **2021,** *33* (9), 2007888.

(38) Halliwell, B.; Gutteridge, J. M. C.; Aruoma, O. I., The deoxyribose method: A simple "test-tube" assay for determination of rate constants for reactions of hydroxyl radicals. *Anal. Biochem.* **1987,** *165* (1), 215-219.

(39) Li, Y.; Xie, M.; Jones, J. B.; Zhang, Z.; Wang, Z.; Dang, T.; Wang, X.; Lipowska, M.; Mao, H., Targeted Delivery of DNA Topoisomerase Inhibitor SN38 to Intracranial Tumors of Glioblastoma Using Sub-5 Ultrafine Iron Oxide Nanoparticles. *Adv. Healthc. Mater.* **2022,** *11* (14), 2102816.

(40) Bottero, V.; Busuttil, V. r.; Loubat, A. s.; Magné, N.; Fischel, J.-L.; Milano, G. r.; Peyron, J.-F. o., Activation of Nuclear Factor κB through the IKK Complex by the Topoisomerase Poisons SN38 and Doxorubicin: A Brake to Apoptosis in HeLa Human Carcinoma Cells1. *Cancer Res.* **2001,** *61* (21), 7785-7791.

(41) Franken, N. A. P.; Rodermond, H. M.; Stap, J.; Haveman, J.; van Bree, C., Clonogenic assay of cells in vitro. *Nat. Protoc.* **2006,** *1* (5), 2315-2319.